

## ABSTRACT

Title of Dissertation:           GEOPHYSICAL EXPLORATION  
  OF TERRESTRIAL AND  
  LUNAR VOLCANIC FIELDS

Ernest Robert Bell, Jr.  
Doctor of Philosophy, 2021

Dissertation directed by:       Associate Professor, Nicholas C. Schmerr  
  Department of Geology

Planetary analogs are environments representative of current or past conditions on other planetary bodies. My research uses terrestrial volcanic fields as lunar analogs to conduct geophysical studies on the subsurface structure of cinder cones, lava flows, and lava tubes, as well as understand terrestrial field methods for application to lunar surface exploration.

As part of this research, I relate the magnetic anomalies produced by lava tubes to their location and geomorphology. By comparison of magnetic anomalies against synthetic predictions, I derive a relationship between the terrestrial magnetic anomalies and underlying tube geometry. The model is shown to predict terrestrial lava tube magnetic anomalies, and adjusting for the lunar magnetic environment, anomalies resulting from tubes on the Moon.

Active source seismic experiments performed by Apollo astronauts were used to determine lunar tectonic and volcanic structure at depth. Terrestrial geophysical analogs are useful for understanding the Apollo results, and for improving the quality

of future lunar seismic studies. I use seismic refraction to attempt to identify subsurface continuation of locally mapped faults beneath lava flows and cinder deposits to examine their association to cinder cone vent chains. However, due to high seismic energy attenuation, my analysis was unable to resolve displacement of stratigraphic layers indicative of fault locations. The seismic attenuation properties of the field area were able to be characterized. I then analyze the Apollo 17 Lunar Seismic Profiling Experiment (LSPE) data and an Apollo LSPE equivalent terrestrial data set to provide insights into the subsurface imaging potential for a terrestrial equivalent array in the Taurus-Littrow Valley on the Moon.

Finally, I insert active seismic refraction into a previously executed simulated human lunar rover mission where the traverse route and associated science station locations omitted geophysical studies. Data from these lines are used to create 1-D seismic velocity profiles to examine subsurface structural trends and geophysical features of the field area. The seismic fieldwork and analysis are related to similar activities performed by the Apollo 14 & 16 crews to highlight similarities in issues encountered with both terrestrial and lunar field operations, and discuss considerations for future human lunar surface science.

GEOPHYSICAL EXPLORATION  
OF TERRESTRIAL AND LUNAR VOLCANIC FIELDS

by

Ernest Robert Bell, Jr.

Dissertation submitted to the Faculty of the Graduate School of the  
University of Maryland, College Park, in partial fulfillment  
of the requirements for the degree of  
Doctorate of Philosophy  
2021

Advisory Committee:

Associate Professor Nicholas Schmerr, Chair  
Dr. Jacob Bleacher  
Associate Professor Vedran Lekic  
Assistant Professor Mong-Han Huang  
Professor Jessica Sunshine

© Copyright by  
Ernest Robert Bell, Jr.  
2021

## Preface

Very few goals are ever accomplished alone, and mine most certainly have not. I owe much to many. The greatest adventures are those you undertake as a team, and space exploration strongly highlights this adage. Growing up in a small rural town in Pennsylvania in the 1980's, adventures seemed endless. My days were spent exploring the countryside, and nights watching the stars. I became intently interested in human space exploration at a very early age, and remember watching the first space shuttle launch. The Moon landings were still relatively fresh in society's mind, and I recall hearing that someone from my generation would be the first to walk on Mars. This inspired me to earn a degree in engineering and pursue a career in space exploration. Again, adventures abounded. I've worked at multiple NASA centers, conducted testing with rocket fuel, flown zero-gravity flights, practiced spacewalks, trained astronauts, worked countless shifts in Mission Control as an EVA flight controller to assemble the International Space Station, and led operations teams during simulated lunar missions. I was then inspired to combine my engineering and operations expertise with the science of geology to help with the coordination that will be required to successfully execute a return to human lunar surface exploration. What an adventure that will be. This has led me to UMD, and the experiences conducting lunar analog geophysical fieldwork and analyzing the resulting data. I look forward to applying my combined span of knowledge to be a part of the team to continue the quest of space and planetary exploration. Adventures await.

Ad lunam! Ad astra!

## Foreword

Portions of this dissertation are being prepared for submission to peer-reviewed journals as follows:

Chapter 2 is being prepared as:

Bell, E., Schmerr, N., Young, K., Esmaili, S., Garry, W. B., Jazayeri, S., Kruse, S., Richardson, J., Whelley, P. (2021). Field Mapping and Modeling of Terrestrial Lava Tube Magnetic Anomalies as an Analog for Lunar Lava Tube Exploration and Prospecting. *Journal of Geophysical Research: Planets*.

Chapter 3 is being prepared as:

Bell, E., Schmerr, N., Bleacher, J., Porter, R., Burdick, S., Rees, S., Richardson, J., West, J., Young, K. (2021). Seismic Refraction Study Within the San Francisco Volcanic Field as an Analog Comparison to Apollo 17 Lunar Seismic Profiling Experiment. *Journal of Geophysical Research: Planets*.

Chapter 4 is being prepared as:

Bell, E., Schmerr, N., Bleacher, J., Porter, R., Young, K., Burdick, S., Pettit, D. (2021). Active Seismic Studies on Lunar Traverses, An Example Based on a NASA Analog Human Lunar Mission. *Acta Astronautica*.

## **Dedication**

To:

my grandparents, for their inspiration

my parents, for their encouragement

my sister, for her strength

my wonderful wife, for her love and support

my son & best buddy, for his optimism & heart

## **Acknowledgements**

I would like to thank the following funding sources and support under which I was able to conduct my research: The NASA Planetary Science and Technology Through Analog Research (PSTAR) grant NNX15AL87G supporting geophysical lunar analog studies. The NASA TubeX team, NASA PSTAR grant NNX16AK11G, and the Goddard Instrument Field Team supporting investigation of field technologies and strategies for lava tube exploration. The Ann G. Wylie Dissertation Fellowship for supporting the final stages of my dissertation writing. The Earth-Systems Science Interdisciplinary Center (ESSIC) for providing travel funds.

I would also like to thank my advisor, Nick. I am extremely grateful for your time, patience, guidance, friendship, and willingness to help and provide me with indispensable experiences to be successful throughout my graduate research, and into the future. Thank you for the opportunity to expand my horizons. Ad lunam. Ad astra.

# Table of Contents

Preface .....	ii
Foreword.....	iii
Dedication.....	iv
Acknowledgements .....	v
Table of Contents .....	vi
List of Tables .....	viii
List of Figures.....	ix
List of Abbreviations.....	xiii
1 Introduction .....	1
1.1 Research Overview & Objectives .....	1
1.2 Volcanic Structures .....	1
1.2.1 Terrestrial Volcanic Features & Structures .....	1
1.2.2 Lunar Volcanism .....	5
1.3 Use of Magnetic & Seismic Research Methods .....	7
1.4 Analogs for Lunar Surface Science & Exploration .....	11
2 Field Mapping and Modeling of Terrestrial Lava Tube Magnetic Anomalies as an Analog for Lunar Lava Tube Exploration and Prospecting.....	14
2.1 Abstract.....	14
2.2 Introduction and Background.....	15
2.2.1 Volcanism and Lava Tubes .....	15
2.2.2 Lunar Lava Tubes.....	19
2.2.3 Terrestrial and Lunar Magnetic Studies .....	21
2.3 Geologic Setting: Lava Beds National Monument.....	25
2.3.1 Lava Beds National Monument.....	25
2.3.2 Description of Incline, Skull, & Ship Caves .....	30
2.4 Modoc Crater Lava Tube Field Data.....	32
2.4.1 Ground Level Magnetic Survey .....	32
2.4.2 Three-dimensional Laser (LiDAR) Surveys .....	33
2.5 Data Processing and Analysis .....	34
2.5.1 Initial Data Processing.....	34
2.5.2 Magnetic Modeling .....	37
2.5.3 Calculation of Magnetic Gradients.....	39
2.6 Discussion & Interpretation of Results.....	42
2.6.1 Relating Magnetic Anomaly to Tube Geomorphology .....	42
2.6.2 Validation of Magnetic Anomaly to Geomorphic Relationship.....	46
2.6.3 Interpretation and Utility of Magnetic Gradient Analysis.....	53
2.6.4 Comparisons of Lava Tube Magnetic Surveys and Models.....	54
2.6.5 Implications for Lunar Lava Tubes .....	59
2.7 Conclusions .....	64
2.8 Acknowledgments .....	65
3 Seismic Refraction Study Within the San Francisco Volcanic Field as an Analog Comparison to Apollo 17 Lunar Seismic Profiling Experiment .....	66
3.1 Abstract.....	66
3.2 Introduction and Background.....	67

3.2.1	Volcanic fields as Lunar Analogs.....	67
3.2.2	Geology of the SFVF.....	71
3.2.3	Taurus-Littrow Valley & Apollo 17.....	78
3.2.4	Active Seismic Exploration.....	81
3.2.5	SFVF Study as a Taurus-Littrow Valley / Apollo 17 Analog.....	84
3.3	Experimental Arrangements and Execution.....	86
3.3.1	SFVF Seismic Refraction Experiment.....	86
3.3.2	Nodal Seismic Lines Pair 1, Vent V5704.....	89
3.3.3	Nodal Seismic Lines Pair 2, Vent V6735.....	91
3.4	Data Processing and Analysis Methods.....	92
3.4.1	Dataset and Data Processing.....	92
3.4.2	Power Spectral Density Analysis.....	95
3.4.3	2-D Inversion.....	97
3.5	Results.....	102
3.5.1	Evaluation of Seismic Velocity Profiles & Power Spectral Density.....	102
3.5.2	Apollo 17 LSPE Re-evaluation.....	103
3.5.3	Evaluation of SFVF Experiment as an Apollo 17 LSPE Analog.....	107
3.6	Discussion.....	116
3.6.1	SFVF 2-D Seismic Velocity Profiles.....	116
3.6.2	Re-evaluation and Interpretation of Apollo 17 LSPE Analysis.....	117
3.6.3	SFVF Experiment as an Analog to Apollo 17 LSPE.....	119
3.7	Conclusions.....	121
3.8	Acknowledgments and Data Location.....	124
4	Active Seismic Studies on Lunar Traverses, An Example Based on a NASA Analog Human Lunar Mission.....	125
4.1	Abstract.....	125
4.2	Introduction, Motivation, and Background.....	126
4.3	Experimental Setup and Data.....	135
4.4	1-D Seismic Inversion.....	140
4.5	Results.....	143
4.6	Interpretation and Discussion.....	148
4.7	Conclusions.....	158
4.8	Acknowledgements.....	160
5	Conclusions and Application to Human Lunar Exploration.....	161
5.1	Overview.....	161
5.2	Summary of Conclusions with Operational Considerations.....	162
5.2.1	Chapter 2 Summary & Lunar Surface Survey Considerations.....	162
5.2.2	Chapter 3 Summary & Considerations for Crew-Robotic Synergy ..	164
5.2.3	Chapter 4 Summary & Considerations for Lunar Geophysics.....	167
5.3	Continued Research: Human Lunar Surface Exploration.....	169
	Appendices.....	170
	Bibliography.....	209

## List of Tables

<b>Table 2.1:</b> Summary of lava tube geomorphology .....	30
<b>Table 2.2:</b> For Incline, Skull, and Ship lava tube caves the following values are provided based on calculated and observed data. A) The median of the maximum negative magnetic anomaly over the lava tube. B) The median observed ceiling depth for the lava tube. C) The apparent radius (r) for 1) the calculated apparent radius based on the median maximum negative magnetic anomaly and the median observed ceiling depth, 2) the actual observed median apparent radius, and 3) the ratio of the two. D) The ratio of the observed apparent radius to the depth to the lava tube ceiling. E) The observed median ½ width. F) The observed median ½ height. G) The mean magnetic anomaly from 1) within the tube perimeter, 2) the overall region of observation over the lava tube, and 3) the ratio of these two which quantifies the magnetic signal to magnetic background variation. ....	50
<b>Table 3.1:</b> Summary of select properties of nodal seismic lines, and associated volcanic vents and faults shown in Figure 3.1A. (Billingsley, Priest, & Felger, 2007; Ulrich & Bailey, 1987) .....	87
<b>Table 3.2:</b> List of initial conditions, constraints, and static returns for the SFVF nodal seismic line pairs 1 and 2 refraction analysis. ....	99
<b>Table 3.3:</b> Wavelength scaled distances of SFVF nodal data.....	112
<b>Table 3.4:</b> Quantity of Apollo 17 LSPE EP-to-geophone pairs for each of the SFVF equivalent distances, with the three data points available in the SFVF data highlighted in gray. ....	113
<b>Table 4.1:</b> Details of geophone lines. Left to right, the line number as designated in this study, latitude & longitude of first and last source location, maximum offset distance (negative distance) from first geophone, maximum offset distance (positive distance) from final geophone, maximum change in elevation between first and last source locations, and the percentage of first arrival picks that were able to be selected. ....	140
<b>Table 4.2:</b> Surface context and physiographic location descriptions for the nineteen geophone line locations. Color coded by physiographic descriptions. ....	144
<b>Table 4.3:</b> Statistical details and interpretation of seismic velocity layers. All values in m/s. Column definitions are, Range: seismic layer designation; Min. & Max. Vel.: minimum and maximum velocities of layer; Mean: mean of the velocity range; SD: standard deviation of the velocity range; Median: median of the velocity range; Mode: mode of the velocity range; Interpretation: geophysical interpretation of the velocity range with descriptions provided in the section 4.6 Interpretation and Discussion; Reference Velocity Range: expected P-wave seismic velocity based on previous studies; *Watkins, 1965; **Kring, 2017. ....	146

## List of Figures

- Figure 2.1:** A) Aerial view of Lava Beds National Monument (LBNM) showing location of Modoc Crater lava tube complex, and the location of our field study area indicated with yellow box. B) LBNM location in northern California. Background aerial LBNM image credit: USGS National Elevation Dataset, from north 42 west 122 tile. C) Image of Marius Hills Hole, a collapsed pit suspected to lead to a lava tube on the Moon. Hole diameter is approximately 65 m. Image scale equal to horizontal scale bar. Image credit: LROC NAC M114328462R (NASA/GSFC/Arizona State University).....27
- Figure 2.2:** A) Schematic depiction of the Modoc Crater lava tube complex field area in yellow box from Figure 2.1. Locations of the three analyzed caves (Incline, Skull, & Ship) are noted in bold text. B) View looking out of Incline Cave towards the collapsed trench at the western entrance. Photograph credit: Jacob Richardson. C) View from inside of Skull Cave looking towards the cave entrance to the west. The floor is littered with significant ceiling and wall collapses. C) View from inside of Ship Cave looking west towards the cave entrance. The floor is lined by large meter-scale basaltic blocks collapsed from the ceiling and walls. For reference, ~1.8 m tall person, is circled in sub-figures B, C, and D. ....29
- Figure 2.3:** Ground level surface magnetic anomaly survey of a portion of the Modoc Crater lava tube system. Lava tube subsurface perimeters are shown in the black outlines. Collapse pits are indicated by broken red lines, and the magnetically inferred location of an unexplored subsurface tube is in broken black lines. Magnetic field is reported relative to the local background [50,685 nT at Skull Cave segment, and 50,541 for all other segments], and the colorbar saturates to white at +2500 and black at -2000 nT. Background aerial image credit: USGS National Elevation Dataset, from north 42 west 122 tile.....33
- Figure 2.4:** Orthographic view of LiDAR point cloud models of Incline (A), Skull (B), & Ship (C) caves for the corresponding outlined perimeters shown in black in the aerial plots of the observed magnetic anomalies (subplots D, E, & F), and the modelled magnetic anomalies (subplots G, H, & I) for the same recorded portions of the lava tube caves. ....35
- Figure 2.5:** Normalized magnetic gradient plots for both the observed (left column) and modeled (right column) magnetic anomaly plots of Incline (A & D), Skull (B & E), and Ship (C & F) lava tube caves respectively. LiDAR derived lava tube perimeters are outlined in white. Magnetic gradients plotted are normalized to the highest gradient (nT/m) calculated for each figure. ....41
- Figure 2.6:** Schematic representation, of lava tube geometry deconstruction used for geomorphic versus geophysical relationship analysis between the lava tube geomorphology and the magnetic anomaly, used for this study. ....42
- Figure 2.7:** The relationship between the observed lava tube total field magnetic anomalies and the LiDAR-derived non-dimensional geometric ratio. A linear least squares regression (broken black line) was used to determine the equivalent magnetic

susceptibility. Figure A: All observed 1-meter slice data points for Ship (green triangles), Incline (blue circles), and Skull (orange squares) caves. Equivalent magnetic susceptibility of  $0.166 \pm 0.007$ . Figure B: Median of the observed data for every 0.125 geometric ratio increment. Error bars show one standard deviation from the median. Equivalent magnetic susceptibility of  $0.155 \pm 0.023$ . .....45

**Figure 2.8:** The relationship between the modeled lava tube total field magnetic anomalies and the LiDAR-derived non-dimensionalized geometric ratio. A linear least squares regression (broken black line) was used to determine the equivalent magnetic susceptibility. Figure A: All modeled 1-meter slice data points for Ship (green triangles), Incline (blue circles), and Skull (orange squares) caves. Equivalent magnetic susceptibility of  $0.175 \pm 0.002$ . Figure B: Median of the modeled data for every 0.125 geometric ratio increment. Error bars show one standard deviation from the median. Equivalent magnetic susceptibility of  $0.168 \pm 0.014$ . .....48

**Figure 2.9:** Magnetic anomalies and gradients for theoretical double tube models at Skull Cave location. Figure A: Plot of magnetic anomalies from application of magnetic susceptibility of 0.155. Figure B: Magnetic gradient plot normalized to the highest gradient (nT/m) calculated. ....58

**Figure 2.10:** Plot of theoretical lava tube magnetic anomaly strength versus the geometric ratio for lava tubes based on remanent magnetic properties, simulating lunar equivalent lava tube signatures. The four lines represent: 1) the lowest anticipated remanent magnetic anomalies based on remanent strength of Apollo samples (dashed blue line); 2) lower bound for lunar swirl required magnetic strength (green circle line); 3) upper bound for lunar swirl required magnetic strength (yellow cross-hatched line); and 4) terrestrial equivalent remanent magnetic strength sampled from Mount Etan, Italy (purple dotted line). The Marius Hills example based on known ceiling thickness and depth to floor at the Marius Hills Hole, with assumed oval lava tube cross-section with 2 to 1 ratio of width to height resulting in a geometric ratio of 0.57 is plotted crossing each of these lines at red asterisk. ....63

**Figure 3.1:** A) Aerial overview of the SFVF fieldsite showing locations of our seismic refraction nodal lines in relation to volcanic cinder cone vents, known and inferred local faults, and major geologic units (adopted from Billingsley et al. (2007)). B) Aerial overview of the Apollo 17 mission site and LSPE hardware in relation to major geologic units and features within the Taurus-Littrow Valley (Haase et al., 2018; Wolfe & Scott, 1977). ....70

**Figure 3.2:** A) Notional cross-section beneath seismic refraction nodal line 1A showing subsurface graben feature based on this study’s seismic refraction analysis. B) Inferred cross-section of major sub-regolith units of the Taurus-Littrow Valley (TLV) showing in-filled graben feature with relative positions of Apollo 17 landing site and LSPE hardware looking west. TLV cross-section adapted from illustration by Wolfe, et al. (1975) and modified. ....76

**Figure 3.3:** Example of typical seismic wave move out and first arrivals picks. Source located at 490 m, designated by red star. Receiver nodes located at each of the distances noted on y-axis. First arrival picks designated with vertical red lines. Note maximum pick distance from source to receiver was 130 m between 490 m (source) and 360 m (receiver) positions. Trace data amplitudes are normalized to maximum amplitude per

trace, and clipped to prevent overlapping other traces. Trace data from nodes not shown shows only the background noise, and no perceptible source waves.....94

**Figure 3.4:** Power spectral density estimate plots characterizing the SFVF study area. A) Background noise for the study area using data from Line 1A (blue) and Line 2A (red). Earth background high (solid black line) and low noise (dashed black line) models are included for reference. B & D) Show the power spectral density plots for at each of the 51 nodes for a shot performed at shot location 16 (490 m position) on Lines 1A & 2A. Each of the 51 nodes is shown as a different colored line. C & E) Spectrograms showing the attenuation of the shot energy from shot location 16 (490 m position) as it moves out along both Lines 1A & 2A respectively. Power/frequency scale saturates at -130 dB as this is the point that the noise background (equivalent to the earth new high noise model) is greater than the signal.....96

**Figure 3.5:** Schematic overview of seismic refraction reversible Markov chain Monte Carlo algorithm iteration. ....98

**Figure 3.6:** Mean misfit profiles from saved ensemble iterations of 2D Bayesian analysis inversions for each of the four nodal lines. Inversions were saved every 100 iterations. ....100

**Figure 3.7:** Results from the 2D inversion for the SFVF refraction surveys. The mean P-wave velocity of the ensemble is shown in A, C, E, and G, while the standard deviation of the ensemble is shown in B, D, E, and H for each refraction line respectively. The white dashed line indicates the deepest modelled penetration of the seismic rays recorded by the nodes. Velocity scale is the same for the four velocity panels, and the four standard deviation panels as indicated by the color bars. ....101

**Figure 3.8:** Plots A and B show the 1-D seismic velocity profiles for the Apollo 17 LSPE TLV data as calculated by this ‘Analog-study’; Cooper and Kovach, 1974; and Heffels et al., 2017. For this ‘Analog study’, the solid red profile is the best fit discrete steps velocity model; solid black profile is the mean velocity model; and the gray dot-dash lines are the one sigma standard deviation from the mean model. A) Upper 50 m of TLV subsurface, based results from EPs 2 & 3. B) Upper 600 m, based on results using EPs 2, 3, 4, 5, 6, & 8. ....106

**Figure 3.9:** Comparison of typical seismic characteristics of the SFVF and the Apollo 17 LSPE data used for SFVF Apollo 17 LSPE equivalency analysis. Plots A, B, & C are SFVF data and D, E, & F are Apollo 17 LSPE data (DARTS Seismology at ISAS/JAXA, 2019). From top to bottom of each column, the figures contain representative data for Power Density Spectrum, Spectrogram, and Seismogram plots. Frequency resolution for the SFVF data is 1000 Hz, and for the LSPE data is 235 Hz. A red circle-X on the seismograms indicates examples of the picks for the P-wave first arrival..... 108

**Figure 3.10:** Four sets of plots (A-B, C-D, E-F, G-H) show the 1-D velocity profiles for the SFVF full data set (plots A, C, E, H); and the 1-D velocity profiles for the SFVF LSPE equivalent data set (plots B, D, F, H); of the four seismic refraction nodal lines (1A, 1B, 2A, 2C) shown in Figure 1A. ....115

**Figure 4.1:** Overview of SFVF field area, showing geologic units as defined by Skinner & Fortezzo (2013) for the NASA Desert RATS lunar rover traverse simulation. Map

modified to show science stations (blue and yellow dots, geophone lines from this study (red lines denoted as Gph #), geographic grouping locations (denoted as Loc. A thru F), pseudo-transect grouping alignments (orange line), and suggest ideal geophysical transects (dashed blue lines). Locations A-F, and pseudo-transect and suggested transect lines, are discussed in the Sections 4.6 & 4.7, and Figure 4.7. .... 134

**Figure 4.2:** Geometry of typical geophone line array employed. Geophones indicated at blue triangles. Source locations indicated as red dots. .... 135

**Figure 4.3:** Example seismic wave move-out plot of seismic wave arrivals for each of the 24 geophone receivers for study geophone line #7. Individual waves are normalized against their maximum. Y-axis indicates location of the 24 geophone receivers (0 m equal to first geophone). X-axis indicates time from shot occurrence. Red star is location of shot. Blue circles indicate example picks of first arrivals. On individual waves, black fill indicates positive and red fill indicates negative arrivals. .... 138

**Figure 4.4:** Travel time picks, average velocity model, and example seismic ray paths. A) Plot of all 3,447 travel time picks from all nineteen geophone lines, along with best fit travel time model. Scatter of arrival time picks is representative of the range of subsurface structure encountered across the nineteen geophone line locations. B) Seismic velocity model of best fit travel time model from A. C) Theoretical seismic ray paths for the P-waves traveling in model B. Note rays bottom at between 40 and 50 m, providing confidence in the velocity models to 50 m depth. .... 139

**Figure 4.5:** Schematic overview of seismic refraction Markov chain Monte Carlo inversion algorithm iteration. .... 142

**Figure 4.6:** Histogram of velocities from all 19 geophone line refraction analysis ensembles. Velocity ranges shown by colored regions and designated as 1 thru 7. Statistical details and interpretations listed in Table 4.3. Velocity range designations and colors match those used in the Figure 4.7 mean seismic velocity plots, and used for interpretations and discussion in Section 4.6. .... 145

**Figure 4.7:** Study geophone line #'s (Gph) 1 thru 19, 1-D seismic velocity profiles of mean and standard deviations for the mean velocity organized according to geographic locations along one pseudo-transect, six geographic location groups (Location A thru F), or individual positions. Depth and velocity scales are the same for all plots. .... 147

## **List of Abbreviations**

ASE – Active Seismic Experiment  
EVA – Extravehicular Activity  
GPS – Global Positioning System  
LBNM – Lava Beds National Monument  
LiDAR – Light Detection and Ranging  
LSPE – Lunar Seismic Profiling Experiment  
MHH – Marius Hills Hole  
NASA – National Aeronautics and Space Administration  
PEG – Portable Energy Generator  
RATS – Research and Technology Studies  
PASSCAL – Portable Array Seismic Studies of the Continental Lithosphere  
PSE – Passive Seismic Experiment  
SFVF – San Francisco Volcanic Field  
TLV – Taurus-Littrow Valley

# **1 Introduction**

## ***1.1 Research Overview & Objectives***

The research presented in this dissertation has two aims. It is designed to address both the scientific as well as operational categories of the use of planetary analogs. My first objective is the characterization of the subsurface structure of cinder cones, lava flows, and lava tubes found within the San Francisco Volcanic Field (SFVF), CA and Lava Beds National Monument (LBNM) field sites. For this research, I use magnetic surveys and analysis to characterize the morphologic structure of lava tubes, and active seismic refraction methods to analyze the near subsurface structure associated with monogenetic volcanoes. Then by analog, I extend this terrestrial research to similar studies on the lunar surface. The second objective of my dissertation research is to relate the terrestrial geophysical field techniques and methods to the strategies for human lunar surface science operations.

## ***1.2 Volcanic Structures***

### ***1.2.1 Terrestrial Volcanic Features & Structures***

Volcanism is known to be ubiquitous throughout the terrestrial and icy planetary bodies of the solar system (Frankel, 1996; Sigurdsson, Houghton, McNutt, Rymer, & Stix, 2015). The processes involved with it are of key importance to the creation and evolution of these planetary bodies. On Earth, one of the most frequent forms of volcanic vents results in the creation of cinder cones, which are generally of a basaltic composition and located in groups, or fields, on the periphery of larger strato- or shield-volcanos (de Silva & Lindsay, 2015; Settle, 1979; Valentine & Connor, 2015; Wood,

1980). Basalt also lends itself to the formation of lava tubes due to its high liquidus temperature and low viscosity (Dragoni, Piombo, & Tallarico, 1995; Greeley, 1987; Peterson & Swanson, 1974a; Valerio, Tallarico, & Dragoni, 2008). Indications of the existence of both cinder cones and lava tubes have also been found on the Lunar surface (Chappaz et al., 2017; Greeley, 1971a; Hong, Yi, & Kim, 2014; Kaku et al., 2017; McGetchin & Head, 1973; Robinson et al., 2012; Sauro et al., 2020; Wagner & Robinson, 2014).

On the Earth volcanic fields of cinder cones tend to form on the flanks of major volcanoes or can occur in flat terranes with large associated lava flows. Volcanic fields are defined as multiple volcanoes, from just a few to thousands, within a specific age range, that can span several million years, and within a geographically defined area, although there is some subjectivity to the definition for each specific case (Valentine & Connor, 2015). Generally, each of the volcanic vents produce less than 1 km<sup>3</sup> of erupted basalt (Valentine & Connor, 2015). These fields generally occur in extensional tectonic settings, but are also known to form in other tectonic regimes such as convergent and transitional regimes (Le Corvec, Spörli, Rowland, & Lindsay, 2013). The formation and evolution of cinder cone volcanic fields are tied to the origin and composition of the melt that is erupted onto the surface during their formation in combination with the subsurface structure (Wood, 1980). The dynamical sources of melt forming these volcanic fields on Earth include hotspots, subduction zone melt, crustal delamination, or lithosphere to asthenospheric shearing (Valentine & Connor, 2015). These sources of melt originate in the upper mantle at depths between 50 to 150 km (Valentine & Connor, 2015). In cinder cone volcanic fields the cones are formed by eruptions consisting of a combination of effusive and explosive eruptive

components (Valentine & Connor, 2015). Each of these individual vents locations are the surface terminus for a magmatic pathway from a dike system controlled by the local tectonic stresses and/or pre-existing fracture structure (Le Corvec et al., 2013). During the lifetime of a volcanic field, the eruptive volume fluxes can range from less than 0.5 to 800 km<sup>3</sup>/Ma (Valentine & Connor, 2015).

The cinder cones within these volcanic fields range from 10's to 100's of meters in height, and 100's to 1000's of meters in basal diameter, usually not exceeding 2000 m. (Reynolds, Brown, Thordarson, & Llewellyn, 2016; Settle, 1979; Wood, 1980) Monogenetic cinder cones volcanoes are generally cone shaped volcanic vents with a bowl-shaped crater constructed of cinders (or scoria) and volcanic bombs that are generally basaltic in composition. Generally, it has been found that the final volume of a cinder cone forms within 12 days or initial eruption. The total duration of eruptions last for an average of 30 days, although some have continued to erupt for several years, such as Paricutin in Mexico (Wood, 1980).

It has been noted that cinder cone vents within a volcanic field can have visual linear alignments between vent locations. This has been noted at various locations on the Earth, including Jorullo and Paricutin, Mexico, (Cebriá, Martín-Escorza, López-Ruiz, Morán-Zenteno, & Martiny, 2011; Connor, 1987, 1990), the cinder cones of the Tolbachick, Russia volcanic complex (Valentine & Connor, 2015), Paiute Ridge, NV (Valentine & Krogh, 2006), at the R-K fissure eruption in North Iceland (Reynolds et al., 2016), East Grants Ridge, NM (Keating, Valentine, Krier, & Perry, 2008), the Springville Volcanic Field, AZ (Connor, Condit, Crumpler, & Aubele, 1992), as well as the San Francisco Volcanic Field, AZ (Le Corvec et al., 2013). Work by Le Corvec, Spörli, Rowland, & Lindsay (2013) showed that in all but one volcanic field they

studied there were preferential alignment headings. These alignments are due to a combination of pre-existing faults, tectonic stress level, and magma pressure (Le Corvec et al., 2013).

During a volcanic eruption, flowing lava can develop a type of cave, called a lava tube (Greeley, 1971b; Keszthelyi, 1995; Peterson, Holcomb, Tilling, & Christiansen, 1994; Sakimoto, Crisp, & Baloga, 1997). Lava tubes form when a flow of lower viscosity lava, typically mafic in composition, develops a solidified surface while maintaining a fluid interior. This solidified surface provides an insulating layer for the molten lava that continues to flow underneath (Greeley, 1972; Hon, Kauahikaua, Denlinger, & Mackay, 1994; Peterson & Swanson, 1974). Once molten lava drains from the enclosed interior, a hollow lava tube is left behind within the solidified lava. Lava tubes can have significant impact on the lava flow distances and geometries through their insulating characteristics allowing transport of molten lava beyond that which would be possible from channel fed flows (Calvari & Pinkerton, 1998).

There are two primary mechanisms that can form lava tubes. They are via surface solidification of the skin of a pahoehoe lava flow, or through the “roofing over” of an established lava flow channel. Roofing over can occur from several processes. These processes include the welding of crust formations across a channel, the stagnation of a solidified sheet on top of the flow, or the accretion of the levees inward until they connect over the lava flow (Dragoni et al., 1995; Greeley, 1971b; Hong et al., 2014; Peterson & Swanson, 1974a; Rowland & Walker, 1990). On the Earth, lava tubes range in sizes from meter scale to 10s of meters in diameter (Calvari & Pinkerton, 1998, 1998, 1999; Greeley, 1971b), whereas on the Moon, evidence and theoretical structural

analysis points to tubes with widths of 100s or 1000s or meters across (Blair et al., 2017; Greeley, 1971a; Robinson et al., 2012).

### ***1.2.2 Lunar Volcanism***

Throughout the solar system, volcanism plays an important part in the evolution of planetary bodies, such as the Earth and Moon (as well as Mars, Venus, and larger satellites including icy moons), by helping to transfer internal heat to the surface, specifically on terrestrial planets and moons (Frankel, 1996; Wilson, 2009). For the Moon, the bulk of volcanism ceased by approximately 2 billion years ago, as the body has cooled to the point where any melt is likely greater than 1000 km deep, in the final few hundred kilometers of the mantle (Frankel, 1996). However, there is evidence of some more recent volcanism found in small isolated locations identified at irregular mare patches (IMP) which may have erupted within the past 100 million years (Braden et al., 2014). Despite the length of billions of years since the cessation of the majority of lunar volcanic activity, with the exception of these small IMP eruptions, evidence of past volcanism is found across the lunar surface (Frankel, 1996; Head, 1976; McGetchin & Head, 1973; Wilson, 2009; Wilson & Head, 1981). Features on the lunar surface that are remnants of periods of active volcanism include the mare flood basalts, vents, cones, scarps, rilles, and collapsed pits.

On the Moon cinder cone style basaltic volcanic vents have been found in locations comparable to terrestrial volcanic fields. It has been noted that similar to volcanic fields on Earth, on the Moon volcanic vents can be found in both area groupings as well as linear alignments (Weitz & Head, 1999). The Taurus Littrow Valley contains multiple cinder cone vents and associated deposits, as observed from orbit during the Apollo 15

missions (National Aeronautics and Space Administration, 1972a). The Marius Hills region is another region known to contain a variety of volcanic features (rilles, pyroclastic deposits, and lava flows) and vent types (domes, spatter, and cinder) which are basaltic in nature. This includes the largest known grouping of cinder cones on the Moon. The cones in this region are generally less than 3 km in diameter and less than 300 m in relief (Weitz & Head, 1999).

The Marius Hills region is also suspected to contain lava tubes, (Haruyama et al., 2009; Robinson et al., 2012; Wagner & Robinson, 2014). Modern scientific discussion as to the existence and formation of lunar lava tubes date back to the Apollo era, when Greeley (1971b) suggested that rille and rille-like structures are results of lava channels, or partially collapsed lava tubes. More recently, there have been multiple pits identified on the lunar surface which, due to the lack of ejecta or volcanic deposits, appear to be collapsed roofs of either lava tubes or magma chambers, as opposed to impact craters or volcanic vents (Robinson et al., 2012). The first of these collapsed pits was discovered in the Marius Hills region within a rille formed during a high-discharge effusive eruption (Haruyama et al., 2009; Robinson et al., 2012; Wagner & Robinson, 2014). This specific pit is estimated to be approximately 65 m in diameter and has a depth from surface of 80 m to 90 m, with a roof thickness of approximately 20 m to 25 m (Haruyama et al., 2009; Robinson et al., 2012). Since the initial discovery of the Marius Hills Hole, there have been over 200 pits identified from Lunar Reconnaissance Orbiter observations (Wagner & Robinson, 2014). These pits are located at various mare and melt pond regions including Mare Ingenii, Mare Tranquillitatis, King pond bridge, and the Copernicus pond pit. It is thought that these pits likely provide access to lava tube systems as well as to emptied near surface magma chambers.

### **1.3 Use of Magnetic & Seismic Research Methods**

Geophysical research methods include the use of a number of techniques. For my research of geologic structures found within volcanic fields, magnetic and active source seismology surveys are the two primary methods used for data collection and subsequent analysis. In Chapter 2, I discuss my use of magnetometry at LBNM to passively survey the signatures at ground level of the anomalies, created by lava tubes, in the magnetic field of the lava flows within which the lava tubes reside. Secondly, I use active source seismic refraction surveys to inform on the 1-D and 2-D stratigraphic velocity structure beneath survey lines within the SFVF. This is the geophysical method I use for the research I describe in Chapter 3, where I attempt to resolve local fault planes intersecting cinder cones vents in the SFVF, and equate the method to possible lunar surface research. I again use the method of active source seismology for my research described in Chapter 4, where I used this method to determine the near-surface velocity structure at point locations along a simulated human lunar traverse, within the SFVF. The originally conducted simulated lunar traverse did not include geophysical studies as part of the simulation. This enabled me to demonstrate the increase in geologic/geophysical understanding of the study area gained by including even non-geographically-prioritized geophysical data collection within lunar geologic observation and sample collection traverses.

Magnetic surveys use the technique known as magnetometry to measure and map the strength of a magnetic field, which can be used to locate magnetic anomalies and characterize the magnetic environment (Burger, Sheehan, & Jones, 2006). Within volcanic fields these surveys can be used to locate various buried geologic structures associated with basaltic lava flows, or magmatic pathways due to the magnetic

properties afforded basalt largely from the magnetite and Fe content. Magnetometry surveys generally use one of two variations of an instrument known as a magnetometer, either a flux-gate or a proton-precession magnetometer. Flux-gate magnetometers measures the relative changes in the magnetic field, but are able to provide these changes in the total field, as well as the horizontal and vertical components (Burger et al., 2006). Proton-precession magnetometers measure only the total magnetic field intensity (Burger et al., 2006). Proton-precession magnetometers are most commonly used in fieldwork due to their ease of use, no requirements for leveling or determining of sensor orientation as needed by flux-gate versions, and operational reliability. Both versions of magnetometers can provide to at least 1 nT of precision (Burger et al., 2006).

Terrestrial field survey operations with magnetometers can be performed via airborne platforms or walking surveys on the surface, with higher resolution being obtained closer to the ground. For the research included in my dissertation, walking surveys were performed to gain high resolution magnetic strength data which mimics the most likely possibility for obtaining similar data on the Moon where aeromagnetic surveys, other than at orbital altitudes, are not practical to perform in the airless environment. These consist of carrying a proton-precession magnetometer on a backpack frame mount with the sensor at an elevation of approximately 2 m above the ground. The magnetometer continuously recorded both the total field as well as GPS located position while carried across pre-determined routes to systematically cover individual lines or areas of interest. It does not provide gradient or vector magnetic field.

Magnetometry is useful for mapping the magnetic signature of rock units and features within the sub-surface of Earth, of both the continents and seafloors (Hinze & Hood, 1998; Klitgord, Huestis, Mudie, & Parker, 1975; Minty, Milligan, Luyendyk, & Mackey, 2003). Examples of the use of magnetic mapping and analysis techniques with regards to volcanic features include the identification and modeling of a buried volcanic crater in the Amargosa Desert, NV (George et al., 2014), as well as detecting the location of active lava tubes based on the intensity of the magnetic field produced by flowing lava (Budetta & Negro, 1995). Also, a geophysical study by the Central Federal Lands Highway Division of lava tubes structure beneath roads within the LBNM included magnetic transects of previously emplaced lava tubes concluded that anomalies determined through magnetic surveys could be used to interpret locations of lava tubes (Meglich, Williams, Hodges, & DeMarco, 2003) Magnetic studies have also been conducted on the Moon, although not of lava tubes. These include orbital surveys that began with Russian spacecraft in 1959 (Dolginov, Eroshenko, Zhuzgov, & Pushkov, 1966; Dolginov, Yeroshenko, Zhuzgov, & Pushkov, 1963), and continued with the Explorer 35 U.S. spacecraft (Dyal & Gordon, 1973) to look for evidence of lunar magnetic dipole, of which one was not found. The Apollo program continued the study of the magnetic properties of the Moon through use of both portable and stationary surface magnetometers (Dyal & Gordon, 1973). The results of the surface data indicated a range in magnetic intensity from 30 nT to 313 nT, and corroborated the lack of existence of a lunar dipole (Dyal & Gordon, 1973).

The second geophysical method I am exploiting for my research is active seismic refraction surveys. This method relies on the analysis of the travel time between source and receiver of seismic waves traveling down into the subsurface and refracting back

towards the surface upon encountering the interface between layers with different seismic velocities (Burger et al., 2006). These surveys provide the ability for 1-D, 2-D, and 3-D inversion analysis to visualize the subsurface layers and structure, assuming a structure of increasing seismic velocity with depth, and are routinely used for various geophysical surveys on Earth. Examples of terrestrial seismic refraction surveys include the Pacific to Arizona Crustal Experiment that included observations high velocity regions that were interpreted as igneous intrusions associated with the volcanic centers of the SFVF (Durrani, Doser, Keller, & Hearn, 1999), a 46 kilometer long 2-D survey that provided positive identification of fault locations within the San Andreas Fault zone (Hole, Ryberg, Fuis, Bleibinhaus, & Sharma, 2006). During the Apollo missions active seismic studies on the order of 10s of meters to kilometers were conducted. Shorter, 90 meter, three geophone lines, were conducted with crew initiated seismic sources during both the Apollo 14 and Apollo 16 missions (National Aeronautics and Space Administration, 1971a; National Aeronautics and Space Administration, 1972b). The data from these geophone lines was used to resolve to depths of approximately 38 m (National Aeronautics and Space Administration, 1971b; National Aeronautics and Space Administration, 1972c). The Apollo 17 mission setup a larger scale active seismic experiment, four geophone array, with explosive sources set at distances up to about 3 km (National Aeronautics and Space Administration, 1973a; National Aeronautics and Space Administration, 1973b). Results from the Apollo 17 experiment from the explosive sources provided a 1-D seismic velocity model of the Taurus-Littrow Valley's upper 500 m (Heffels, Knapmeyer, Oberst, & Haase, 2017; Kovach, Robert & Watkins, Joel, 1973b, 1973a; National Aeronautics and Space Administration, 1973b).

#### **1.4 Analogs for Lunar Surface Science & Exploration**

The Apollo missions demonstrated that geophysical tools are of importance to planetary surface exploration, and helped to dramatically increase our knowledge of the lunar environment, surface, and interior structure. However, these missions are the only experience we have of humans performing fieldwork on a planetary body other than Earth. The total duration on the surface was relatively limited, with a total of only about 300 hours on the surface for the six missions which landed (National Aeronautics and Space Administration, 1969b; National Aeronautics and Space Administration, 1970; National Aeronautics and Space Administration, 1971a; National Aeronautics and Space Administration, 1971c; National Aeronautics and Space Administration, 1972b; National Aeronautics and Space Administration, 1973a). Of that time, the crew was only outside of the lunar lander performing extravehicular activities for about 80 hours, of which only a portion was spent actually conducting geologic or geophysical fieldwork (National Aeronautics and Space Administration, 1969b; National Aeronautics and Space Administration, 1970; National Aeronautics and Space Administration, 1971a; National Aeronautics and Space Administration, 1971c; National Aeronautics and Space Administration, 1972b; National Aeronautics and Space Administration, 1973a).

In order to optimize the execution of future human lunar surface exploration of field geophysical activities, the use of terrestrial analogs, representative environments of locations on other planetary bodies, is key. On the Earth terrestrial volcanic fields provide established analogs for studying subsurface structures similar to those found on the Moon (Bell et al., 2018; Bleacher et al., 2015; Garry & Bleacher, 2011; Heldmann et al., 2015; L  veill  , 2010). These analogs can be used for the study of the

geophysical features, as well as the methods and protocols for lunar surface operations. By conducting scientific studies of geophysical analogs of lunar locations, researchers are able to anticipate probable findings from similar studies on the Moon. Scientists can also use the terrestrial studies to appropriately scale experiments to the lunar environment and to set minimum requirements for sufficient data coverage for addressing geophysical questions. Operationally, the use of lunar analogs provides the ability to examine the techniques and methods used by geophysicists (or other scientific disciplines) in conducting their fieldwork. This provides the opportunity to understand items such as the evolution of field plans, standard practices, hardware utilization, anomaly recognition and resolution, and addressing serendipitous targets of opportunity.

Historically, from a human space exploration standpoint, locations such as SFVF were used for preparing the teams of scientists, engineering, operations, crew, and management personnel for executing the Apollo lunar missions (Lofgren, Horz, & Eppler, 2011; Phinney, 2015). Preparation included geologic training exercises to educate the crews and ground support teams on the methods and skills needed for conducting field geology. Also, simulations of mission activities, such as instrument deployments, field observations, and geologic sampling, were performed (Lofgren et al., 2011; Phinney, 2015). During these exercises each discipline (scientists, operations, and engineering) would provide expertise in their specialties, providing for cross-discipline training and feedback resulting in increased efficiency for mission activities (Lofgren et al., 2011; Phinney, 2015). More recently these same locations were used to prepare for future human lunar exploration through a series of studies and mission simulations by NASA, known as Desert Research and Technology Studies (RATS).

These tests evolved from engineering evaluations of prototype spacesuits and geologic hardware to a full multi-week lunar mission simulation (Ross, Kosmo, & Janoiko, 2013).

Overall, lunar analog locations on Earth hold an important role in the scientific advancement of knowledge of the Moon by providing a proving ground for scientific study of lunar locations and mission training that result in the optimization of limited human lunar mission resources to efficiently obtain necessary field data. The research executed for this dissertation specifically adds to this advancement by exploring how to use geophysical methods to study lava tubes and lava flows in volcanic fields that are geomorphological, and presumably geophysical analogs to lunar volcanic fields.

For this research I used 1) a high resolution magnetic survey to detect and examine the processes of formation and evolution of lava tubes (Chapter 2), 2) refraction surveys transects perpendicular to the local fault strike to characterize the alignment geometry of cinder cones vents, a question postulated for both the Earth and Moon (Chapter 3), 3) a detailed set of seismic surveys that reveal the velocity structure within and beneath lava flows, and illustrate the heterogeneity found within a cinder cone field, that may potentially provide insight to analogous locations on the Moon (Chapter 4), and 4) the development of operational strategies for human scientific exploration of the lunar surface based upon lessons learned from these terrestrial field investigations (Chapter 5). The research described in this dissertation is only possible due to the extensive investigations, fieldwork, analysis, and efforts by the giants who have gotten us to this point.

## **2 Field Mapping and Modeling of Terrestrial Lava Tube Magnetic Anomalies as an Analog for Lunar Lava Tube Exploration and Prospecting**

### ***2.1 Abstract***

Lava tubes are a commonplace feature on the terrestrial planets, and knowledge of tube size and location informs on lava flow processes. Future exploration of lava tubes on the Moon can provide access to geologic environments that likely remain unaltered from their emplacement billions of years ago. Lunar lava tubes may also provide astronauts protection from thermal extremes, meteoroid impacts, and radiation. We demonstrate how magnetometry is useful for determining the geometry and extent of lava tubes on the Earth and Moon, by relating the magnetic anomalies produced by lava tubes to their location and geomorphology. Using a proton-precession total field magnetometer, we magnetically surveyed an area of more than 100,000 m<sup>2</sup>, with cross-tube linear traverses spaced at 3 m to 5 m, perpendicularly to an approximately 1000 m length of the Lava Beds National Monument (California, USA) Modoc Crater lava tube complex. The observed magnetic anomalies of the sections known as Incline, Skull, and Ship Caves were compared against synthetic predictions, and the sensitivity of the magnetic anomalies to the tube geometry were used to derive a basic relationship between the two. We use our model of terrestrial lava tube magnetic anomalies, and adjusting for the lunar magnetic environment, to predict the signature of anomalies resulting from tubes on the Moon. High-resolution magnetic identification and characterization of lava tubes will be essential for informing future scientific investigations of tubes and for human exploration and utilization of tube space.

## ***2.2 Introduction and Background***

### ***2.2.1 Volcanism and Lava Tubes***

Volcanism is the surface expression of internal heat advected from a planetary interior to the surface. Volcanism and associated lava flows are ubiquitous throughout the terrestrial bodies of the solar system, and volcanic activity plays an important part in the formation and evolution of planets (Frankel, 1996; Sigurdsson et al., 2015), moons (Greeley, 1971a; Head, 1976) and large asteroids (Williams et al., 2014; Wilson & Keil, 1996). During a volcanic eruption, flowing lava can develop a type of cave, called a lava tube (Greeley, 1971b; Keszthelyi, 1995; Peterson, Holcomb, Tilling, & Christiansen, 1994; Sakimoto, Crisp, & Baloga, 1997). Lava flow development and geometry are a result of several variables including effusion rate, cooling rate, eruption duration, chemistry, as well as the presence of lava tubes. Previous research indicates that the formation of lava tubes, with the insulating characteristics they provide, aid in the transportation of lava away from its originating volcanic vent (Hon et al., 1994; Keszthelyi, 1995; Pieri & Baloga, 1986; Self et al., 1996; Walker, 1973). Lava tubes enhance the lava flow transport distances and geometries, extending the reach of lava flows by many kilometers beyond the distances of channel-fed lava flows (Calvari & Pinkerton, 1998; Keszthelyi & Self, 1998).

Lava tubes form when a flow of lower viscosity lava, typically mafic in composition, develops a solidified surface while maintaining an interior of flowing fluid lava. The formation mechanisms by which the surface solidification of the molten lava can occur in general includes the solidification of the skin of an inflating pahoehoe lava flow or the roofing over of an established lava flow channel, but in all cases this

hardened surface provides an insulating layer for the molten lava that continues to flow underneath (Greeley, 1972; Hon, Kauahikaua, Denlinger, & Mackay, 1994; Peterson & Swanson, 1974). In the cases where the roof becomes structurally capable of supporting itself, and the molten lava drains from the enclosed interior, a hollow lava tube, or cave, is left behind within the solidified lava flow.

In the case of lava tube formation from an inflating lava flow, the flow front will consist of a series of overlapping lobes of lava that fuse and cool to form the roof of the lava tube (Greeley, 1971b; Peterson et al., 1994). This mechanism generally occurs in slow moving lava flows and result in irregular constructs in comparison to tubes forming from continuous surface crusts (Greeley, 1971c). With this formation mechanism the surface skin of these lava tubes essentially cools and solidifies in place in comparison to some mechanisms of roofing of lava flow channels. These pahoehoe types of lava tube formations also have significantly more irregularity to their flow paths due to the unconstrained nature of the spreading of toes of the lava flow (Peterson et al., 1994).

Lava tubes originating from channel flows can be the result of several formation mechanisms. One possibility is for crust to solidify along the channel edges via cooling and then grow towards the centerline of the channel, progressing downstream in a V-shape, essentially zippering over the channel (Greeley, 1971b; Peterson et al., 1994). Another possibility, in channels with stable flow, is for the flow surface to develop a scum or crust. This initial roof thickens from either periodic overflow of flowing lava onto the surface, or from an accretion of cooling lava on the underside of the surface layer, to the point of becoming structurally stable (Greeley, 1971b; Peterson et al., 1994). A third, similar formation mechanism to the previous, essentially constructs a

roof from previously solidified crustal plates which have broken loose and been transported downstream. As these plates meet, they lock and fuse to the channel sides as well as to each other to create a roof across the channel (Greeley, 1971b; Peterson et al., 1994). These roof forming plates are therefore randomly orientated with respect to their orientation during cooling. A final process that can result in the creation of a lava tube from a channel occurs in more turbulent lava flows. In this case, the turbulence results in splashing, spattering, and lava overflow which create levees along the edges of the channel. These levees continue to conglomerate in an arch over the channel from each side, where they can eventually meet and fuse to form the roof of the lava tube (Greeley, 1971b; Peterson et al., 1994).

It is probable that subsequent eruptions result in multiple lava flows running through or above previously formed lava tubes. When these new lava flows coincide with previously formed lava tubes, they may impact the tube geometry by either elongating the tube cross-sections or constructing a vertical stacking of multiple lava tubes on top of one another (Greeley, 1971b; Peterson et al., 1994). Internally, tubes may exhibit multiple levels that are indicative of when a flow resumed within a pre-existing lava tube, but did not completely flood the previous tube, thus allowing for crusting of the new flow at an intermediate level within the established tube (Peterson et al., 1994; Peterson & Swanson, 1974b). The follow-on flows may also impact the current structure of a lava tube by causing a collapse of the tube, or by simply increasing the thickness of the roof. Long lived tubes covered by multiple lava flows tend to lack evidence from which to determine the initial lava tube formation process, due to thermal erosion and annealing producing a surface glaze on most internal surfaces that hide growth structures (Peterson et al., 1994).

Many characteristic morphological features and structural modifications are found on or within lava tubes, including skylights, collapse features, and internal bridges or multiple levels/tubes. Skylights and collapse features are locations along the tube where the cave roof did not form or has been removed, forming holes, pits, or trenches with steep vertical walls in the local landscape (Arnold, 1986; Greeley, 1987). Skylights are defined as locations where the tube surface did not fully solidify, while collapse features are indicative that a portion of the tube has failed or slumped back into the tube. If lava tubes are not observed during formation, both of these types of openings are particularly important for recognizing the existence of a lava tube and are the primary morphology used for locating and tracing the paths of lava tubes (Piombo, Di Bari, Tallarico, & Dragoni, 2016).

Terrestrial planets elsewhere in the solar system are known to contain similar pit craters features associated with basaltic lava flows. These pit craters have been located on the lunar surface (Greeley, 1971a; Haruyama et al., 2009; Kaku et al., 2017), as well as on the surface of Mars (Bleacher et al., 2017; Crown, Berman, Scheidt, & Hauber, 2019; Cushing, Titus, Wynne, & Christensen, 2007; Zhao, Huang, Kraft, Xiao, & Jiang, 2017). In some cases on the Moon these pits are indicative of more extensive subsurface void spaces that are interpreted as lava tubes based upon corroborating geophysical gravity (Wagner & Robinson, 2014) and radar sounding observations (Haruyama et al., 2017; Kaku et al., 2017).

### ***2.2.2 Lunar Lava Tubes***

Modern scientific discussion of the existence and formation of lunar lava tubes dates back to the NASA Apollo era (Greeley, 1971a). It has been suggested that both Hadley Rille as well as rille and rille-like structures within the Marius Hills region are lava channels or partially collapsed lava tubes. (Greeley, 1971b; Hurwitz, Head, & Hiesinger, 2013; Keszthelyi, 1995; Roberts & Gregg, 2019). One specific example is the Marius Hills Hole, shown in Figure 2.1A, which appears to be a collapsed pit leading to a lava tube within Rille A of the Marius Hills region on the Moon (Robinson et al., 2012). In addition, there have been over 150 pit craters identified from the Lunar Reconnaissance Orbiter (LRO) data (Robinson et al., 2012; Wagner & Robinson, 2014). These pits are located at various mare and melt pond regions including Mare Ingenii, Mare Tranquillitatis, King pond bridge, and the Copernicus pond pit. Due to the lack of ejecta or volcanic deposits these pits appear to be either skylights or collapsed roofs of lava tubes and magma chambers, (Head & Wilson, 2017; Robinson et al., 2012). While most of these pits are likely shallow (<10 m), it is probable that several provide access to lava tube systems (Wagner & Robinson, 2014) as well as to emptied near-surface magma conduits (Halliday, 1998; Robinson et al., 2012).

The first of these pits was discovered in the Marius Hills region. This specific pit, known as the Marius Hills Hole (MHH), shown in Figure 2.1C, is an average 65 m in diameter and has a depth from lunar surface of between 80 m to 88 m, with an original roof thickness of at least 40 m (Haruyama et al., 2009; Robinson et al., 2012; Wagner & Robinson, 2014). A large number of sinuous rilles are located within the Marius Hills region, including the 32+ km long rille, Rille A, on which the MHH pit is located. It is projected that this rille contains a lava tube with a width of 370-meter-wide based

on the observed dimensions and depth of the MHH, and an estimated tensile strength of 6.9 MPa and density of 2500 kg/m<sup>3</sup> for the basalt (Haruyama et al., 2009). This estimated width results in a plausible lava tube geometry for this location that is greater than the diameter of the MHH and less than the approximately 500-meter-wide rille (Haruyama et al., 2009). Recent lunar orbital missions further support the interpretation that the MHH leads to a lunar lava tube. First, gravity data from the GRAIL spacecraft was used to determine that the Marius Hill region contains several lines of mass deficit, including one that intersects the MHH (Chappaz et al., 2017). This was followed by radar evidence from the SELENE Lunar Radar Sounder of a cave-like void extending from the MHH (Kaku et al., 2017).

Future lunar exploration has the potential to lead to permanent human occupation of the Moon's surface. Beyond the increased scientific understanding of lunar volcanic and lava flow processes gained from the study of lava tubes, it is also possible that the lava tubes could become ideal locations for human lunar bases. They could afford human bases protection from radiation, extreme temperatures, and meteor impacts (Horz, 1985; Wendel, 2017). It is feasible that some lunar lava tubes are orders of magnitude larger than their terrestrial counterparts. Structural analysis shows that they may be up to several kilometers in diameter, which is on the scale of sinuous rilles found on the Moon (Blair et al., 2017). For these reasons, pit craters have been identified as a high-priority landing target (Jawin et al., 2019).

There exists a critical need for determining methods for locating and characterizing lava tubes to enhance the scientific and operational outcomes of future robotic and crewed missions. Areas to consider for searching for lunar lava tubes include locations extending from apparent collapse pits and along rilles. Other locations to search include

areas containing lunar swirls, where the lines of the magnetic fields of lava tubes may be responsible for the variation in albedo in these regions (Hemingway & Tikoo, 2018), and may follow the lines of high or low magnetic gradient.

However, methods for locating lava tubes on the moon are, in general, neither thorough nor systematic. A standard method is to map the distribution of surface identified holes or other features (i.e. skylights or collapses) to trace the pathway of lava tubes (Crown et al., 2019; Piombo et al., 2016). However, without a technique to probe the subsurface, there is no way to ensure the route of the lava tube, that the tube drained, or that the subsurface void space has not collapsed between skylights. Geophysical tools (gravity, magnetometry, ground penetrating radar, etc.) have all proved promising for detection and mapping of lava tubes on Earth and elsewhere (Esmaeili et al., 2020; J Haruyama et al., 2017; Mallozzi, 2019; Meglich et al., 2003; Miyamoto et al., 2005). Here we specifically focus on using the analysis of magnetic signatures as a method to remotely detect lava tubes and characterize their geometry. Magnetic data is relatively easy to collect at ground level over a lava tube, and should provide the sensitivity to distinguish the lack material associated with the void of the lava tube within magnetically enriched basaltic lava flows.

### ***2.2.3 Terrestrial and Lunar Magnetic Studies***

Magnetic methods have long been used to measure and map the patterns of rock units with a magnetic signature (George et al., 2014; Tanaka, Shoemaker, Ulrich, & Wolfe, 1986), or in the case of tubes, detecting the lack of magnetic signal from a cavity or void space against a rock with a magnetic signal (Burger et al., 2006; Mallozzi, 2019; Meglich et al., 2003). Magnetic techniques have adequate resolution to reveal various

subsurface magmatic intrusions on Earth (George et al., 2014; Negro & Ferrucci, 1998), and have provided magnetic maps of the continents and seafloor (Hinze & Hood, 1998; Klitgord et al., 1975; Minty et al., 2003).

The magnetic properties of the Moon were first explored in orbit by various Russian spacecraft beginning in 1959 with Luna 1, followed by Luna 2 and Luna 10 (Dolginov, Eroshenko, Zhuzgov, & Pushkov, 1966; Dolginov, Yeroshenko, Zhuzgov, & Pushkov, 1963; Dyal & Gordon, 1973). The United States performed magnetic measurements on Explorer 35 (Dyal & Gordon, 1973). All of these lunar orbiting spacecraft carried magnetometers and searched for a lunar magnetic dipole field, which proved to be undetectable. Additionally, Luna 10's objective included studying the effect of Earth's magnetosphere tail in the vicinity of the Moon. The results could not establish an extension of Earth's magnetosphere to distances of sixty Earth radii, but they did record magnetic highs that indicated the possibility of lunar paleofield (Dolginov et al., 1966).

During the Apollo program, surface magnetometers were used, including stationary locations on Apollo 12, 14, 15, and 16, as well as portable units on Apollo 14 and 16 (Dyal & Gordon, 1973). The results of the seven data points recorded by the handheld units on Apollo 14 and 16 show a variation in absolute magnetism from 40 nT to 313 nT, with a maximum gradient of 370 nT/km in Descartes and 54 nT/km in the Fra Mauro (Dyal & Gordon, 1973). Additionally, the combination of Apollo results indicated a lack of evidence for a current global dipole. The observed magnetism is interpreted to originate from thermo-remanence from a field, that may have been as large as 100,000 nT, existing three to four billion years ago (Dyal & Gordon, 1973). The Apollo stationary surface magnetometer units, with readings varying from 5 nT to

313 nT, corroborate the analysis of the portable units, indicating primarily regional magnetic sources versus the presence of a global dipole field (Dyal & Gordon, 1973).

More recently, the Lunar Prospector orbiting spacecraft recorded the distribution and strengths of magnetic anomalies on the lunar surface (Binder, 1998). Many of these anomalies are suspected to be associated with ejecta material (Hood et al., 2001). There is also some correlation between a group of magnetic anomalies, on the nearside, with the Rima Sirsalis extensional graben, that would support the theory that the sources of the anomalies are subsurface igneous intrusions (Hood et al., 2001; Srnka, Hoyt, Harvey, & McCoy, 1979). Recently, Hemingway & Tikoo (2018) discussed the possibility of lunar lava tubes accounting for the existence of lunar swirls. They postulated that lunar lava tubes may have provided the mechanism for increased magnetic anomalies of the surrounding basalts by imparting a thermoremanent or thermochemical remanent magnetization.

Although there is no current lunar dynamo, a long lived global magnetic field of greater than 5000 +/- 2000 nT has been shown to have existed until at least 2.5 billion years ago (Ga) (Tikoo et al., 2017). This timeframe includes the period of the major basin forming events and lunar volcanism which occurred between approximately 3.8 to 2.5 Ga (Head, 1976). From studies of lunar samples returned during the Apollo missions it is known that, although different from Earth, the Moon contains sufficient compositional percentage of ferromagnetic material to provide observable magnetic signatures (Nagata, Fisher, & Schwerer, 1974). The composition includes both metallic iron, Fe-Ni-Co alloy dominated by Fe, and kamacite, with the kamacite theorized to be partially of meteoric origin. Studies have found that lunar samples can contain thermoremanent magnetization (Doell, Grommé, Thorpe, & Senftle, 1970; Runcorn et

al., 1970). Although the lunar magnetic field may have been an order of magnitude less than the Earth's current magnetic field during the period of time of the majority of lunar volcanism, the presence of a magnetic field of approximately 5000 nT on the Moon would have provided the mechanism for the basalt forming lunar lava tubes to acquire a remanent magnetic signature of sufficient intensity ( $> 1$  nT) during emplacement to be observable today.

Lava tubes produce magnetic anomalies due to the void space they create within the lava flows within which they reside. Basaltic lava flows are inherently magnetic due to containing appropriate mineralogy to have both remanent and induced magnetic properties. The remanent magnetic properties are set in the ferromagnetic matrix of the basalt during cooling below the Curie point, the temperature below which materials lock-in a permanent magnetic set, if cooling within a magnetic field, such as the Earth's, or the past lunar, dipole magnetic fields.

However, there are few examples of research that has been conducted on the correlation of lava tube magnetic anomalies to the mapping the lava tube locations or to their specific physical geomorphic characteristics. Terrestrial examples included validating the use of magnetometry for determining the presence of a lava tube under a roadway within Lava Beds National Monument (LBNM) (Meglich et al., 2003), as well as attempts to track lava flows within active lava tubes, using thermomagnetic effects, during the 1991-1993 Mount Etna eruption (Budetta & Negro, 1995). Both studies showed that magnetometry can provide details on lava tube location, depth, and size. However, a more general model that relates these features to tubes of different geometries remains to be developed. This is because magnetic signatures are modeled with non-unique solutions, and the complexity of natural lava tube systems can

potentially mask their signature without a sufficiently high-resolution survey over the tube structure.

Here we develop a relationship between tube geometry and magnetic signature of the lava tube by combining a systematic magnetic survey and ground truth provided by Light Detection and Ranging (LiDAR) scans of tube geometry. We then apply our model to make predictions for the magnetic signatures of lava tubes expected elsewhere, specifically the Moon. To date there has not been a dedicated study of the correlation of magnetic data to lava tube locations and morphology on either the Earth or the Moon. Our study of a tube system on Earth is designed to fill the gap by connecting high-resolution ( $\sim \leq 5$  m scale) ground-level magnetic signatures over a lava tube with ground-truthed subsurface lava tube morphology to test if a scaling relationship can be used to infer lava tube structures elsewhere in the solar system. These results are expected to have practical application in the research of lava tubes for both in terrestrial lava fields and for future lunar exploration.

## ***2.3 Geologic Setting: Lava Beds National Monument***

### ***2.3.1 Lava Beds National Monument***

In this study we specifically focus on terrestrial lava tubes, with Lava Beds National Monument (LBNM), CA, USA, shown in Figure 2.1, as our fieldsite, and relate our results to lunar lava tube structures. The LBNM encompasses a multitude of lava tubes, lava flows, and cinder cone volcanic vents that are associated with the Medicine Lake shield volcano (Figure 2.1). The Medicine Lake volcano is located near the border of California and Oregon and is the largest volcano in the region (Larson &

Larson, 1990) covering an area of over 1125 square kilometers within the Cascade Range (National Park Service, 2017). Volcanic eruptions have occurred here for over the past 500,000 years, resulting in over 200 volcanic vents that are likely connected to multiple magma chambers (National Park Service, 2017).

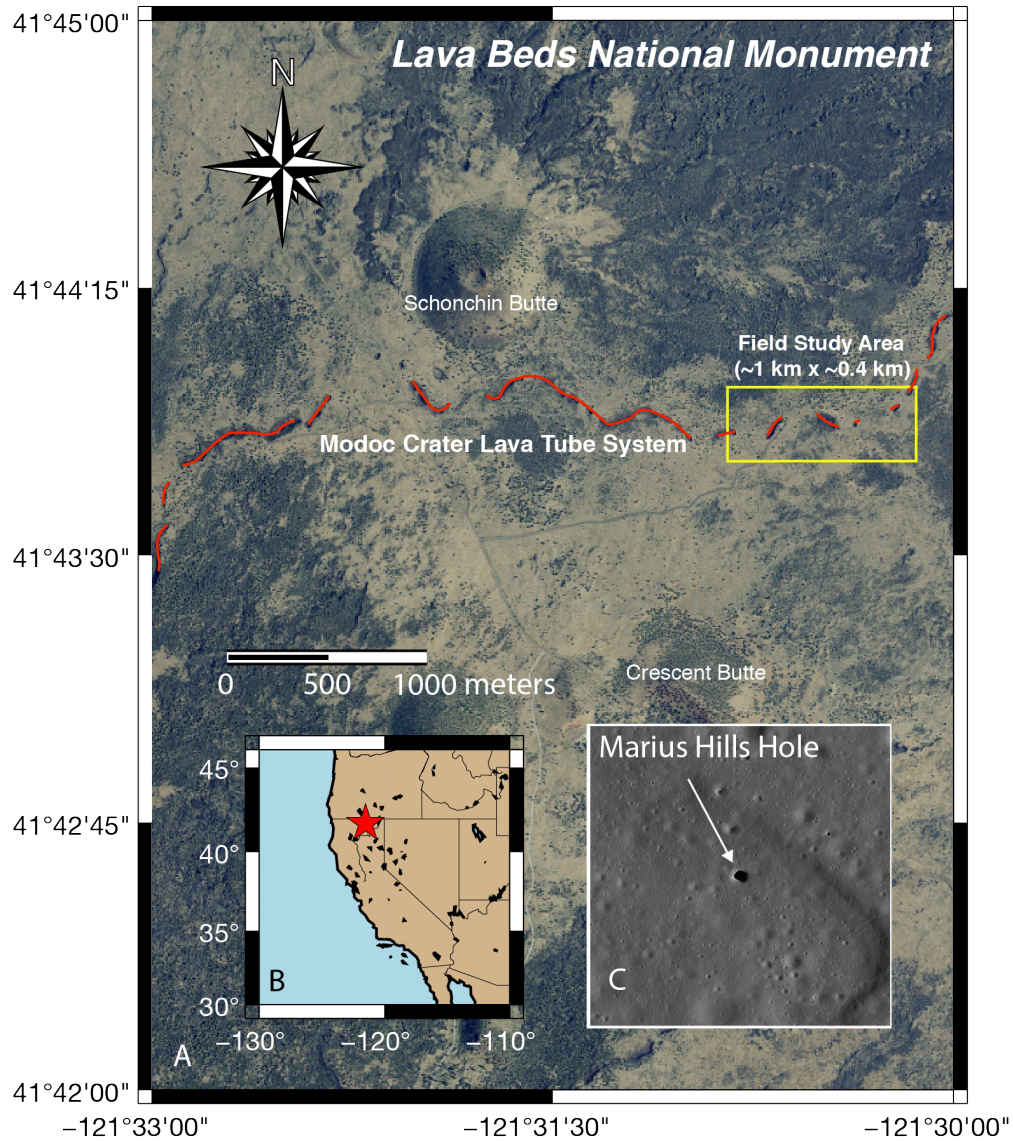


**Figure 2.1:** A) Aerial view of Lava Beds National Monument (LBNM) showing location of Modoc Crater lava tube complex, and the location of our field study area indicated with yellow box. B) LBNM location in northern California. Background aerial LBNM image credit: USGS National Elevation Dataset, from north 42 west 122 tile. C) Image of Marius Hills Hole, a collapsed pit suspected to lead to a lava tube on the Moon. Hole diameter is approximately 65 m. Image scale equal to horizontal scale bar. Image credit: LROC NAC M114328462R (NASA/GSFC/Arizona State University)

Most of the lava tubes found within LBNM are from basaltic flows that occurred between 40,000 and 30,000 years ago from the Mammoth and Modoc volcanic craters on the southern border of the monument. Approximately 11,000 years ago, lower viscosity lava flows created a number of caves including those analyzed in this study.

The most recent lava flows occurred at 900 to 1,100 years ago in the southeast corner of the monument (Arnold, 1986; Larson & Larson, 1990). In total, over 30 lava flows are contained within the LBNM, stemming from periodic eruptions every few hundred to several tens of thousands of years (National Park Service, 2017).

LBNM contains the greatest number of lava tube cave entrances, over 200, within the continental United States (Larson & Larson, 1990). The resulting intact lava tube caves range in length from just a few meters to approximately 7000 m of surveyed passageways. The complexity of the tube systems also varies from simple single passageways to multiple vertical levels and/or interwoven horizontal branches. Many of the more notable caves within the Monument have infrastructural improvements, specifically relocation of some ceiling collapses to create clear pathways and the installation of ladders for public access, but the tubes do retain their primary morphologic features and structural characteristics (Larson & Larson, 1990). Our study centers on the lava tube caves Incline, Skull, and Ship Caves; these are adjacent intact sections of the Modoc Crater lava tube network (Figure 2.2). A summary of characteristic qualities of these three lava tube caves is provided in Table 2.1. The Modoc Crater network of lava tubes is approximately 16 km in length and is interpreted to be formed by a roofed over trench lava flow (DeDecker, 2014). Our survey of the Modoc Crater tube network begins with the intact portion of Incline, situated just west of a collapsed trench leading to Skull Cave. The survey then restarts after continuing eastward of Skull Cave on the east side of a large collapse pit feature over several intact lava tube caves Cave, Robin, Ship, and White Lace. The final portion of the survey extends over an inaccessible, and unnamed, portion of the lava tube complex separated from White Lace Cave by another collapsed pit feature. The total magnetic survey

covers an area of over 100,000 m<sup>2</sup>, along approximately 1000 m of the Modoc Crater lava tube network (Figure 2.2A).

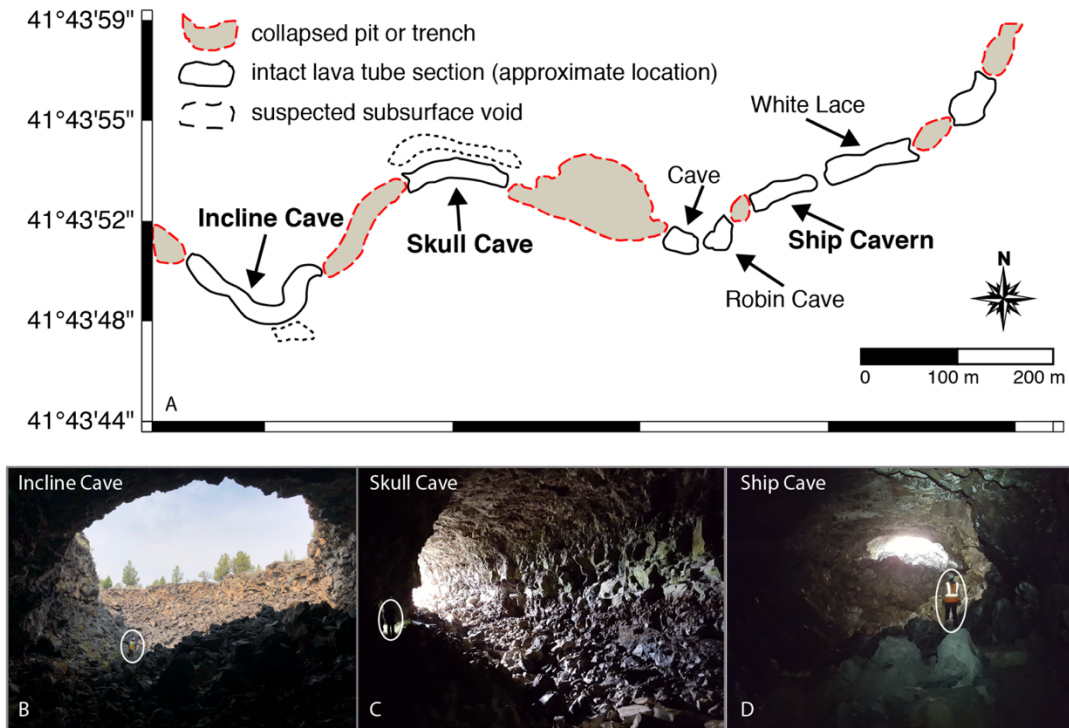


**Figure 2.2:** A) Schematic depiction of the Modoc Crater lava tube complex field area in yellow box from Figure 2.1. Locations of the three analyzed caves (Incline, Skull, & Ship) are noted in bold text. B) View looking out of Incline Cave towards the collapsed trench at the western entrance. Photograph credit: Jacob Richardson. C) View from inside of Skull Cave looking towards the cave entrance to the west. The floor is littered with significant ceiling and wall collapses. C) View from inside of Ship Cave looking west towards the cave entrance. The floor is lined by large meter-scale basaltic blocks collapsed from the ceiling and walls. For reference, ~1.8 m tall person, is circled in sub-figures B, C, and D.

**Table 2.1:** Summary of lava tube geomorphology

	<b>Accessible Length (m)</b>	<b>Height of Primary Section (m)</b>	<b>Width of Primary Section (m)</b>	<b>Ceiling Depth of Primary Section (m)</b>
<b>Incline Cave</b>	>130	1-10	1-30	5-24
<b>Skull Cave</b>	>180	5-20	5-20	6-35
<b>Ship Cave</b>	>100	6-7	12-19	7-15

### ***2.3.2 Description of Incline, Skull, & Ship Caves***

Incline Cave is a single-level cave located at the western extent of a collapsed trench that connects Incline and Skull Caves. Incline is approximately 130 m in length starting with an oval-shaped cross-section, approximately 10 m high by 30 m wide, at its western opening. The depth below ground surface to the ceiling of Incline Cave increases from 5 m at this opening to approximately 24 m at its eastern extent where it connects to the trench leading to Skull Cave. Along this transect from western end to eastern end the cross-sectional area decreases to just a few square meters. The interior consists of extensive blocks, of meter scale, collapsed from the walls and ceilings. The reduction in cross-sectional area is partly due to increasing collapse within the tube from west to east. It is possible to enter/exit Incline Cave at either the western and eastern ends, however the eastern location is difficult to locate and access amongst the large boulders of the collapsed trench. The western opening is easily located and can be seen in Figure 2.2B.

Skull Cave is approximately 180 m in length, with a maximum depth below ground surface to the ceiling of about 36 m. Skull Cave is an exceptionally large diameter (~18-

20 m), multi-level lava tube. It was likely formed via the process of ‘roofing over’ of a trench filled lava flow that formed this specific network of lava tubes. The intact portion of the tube we surveyed is located between two collapsed trenches, both of greater than 120 m in length. The trench to the west, or “upstream”, of Skull Cave, is approximately 23 m wide, and the downstream trench to the east is approximately 40 to 50 m wide. The depth-to-ceiling is between approximately 6 m to 8 m from the western entrance until about 115 m into the cave, at which point it increases rapidly in depth as the cave constricts and drops to a lower level with a depth-to-ceiling of 30 m to 35 m below ground level. Inside, Skull Cave’s upper-most level ends some 125 m inside, just beyond a collapse into the lower levels. This collapse was possibly caused by thermal erosion of the floor of the upper level by flowing lava. The second level then continues further on, with descending access to a third level. This third, and lowest known level extends back in the direction of the cave entrance from its access point within the Skull Cave complex. Morphologic features within the tube include extensive collapsed ceiling and wall blocks of meter scale, some of which exhibit examples of solidified pahoehoe flow and rope features (Arnold, 1986; Larson & Larson, 1990). Additionally, at the furthest reaches of Skull Cave, there is a breach on the south side of the tube where basaltic cinders have penetrated into the tube itself. The opening to Skull Cave, looking towards the entrance at the collapsed trench between it and Incline Cave, is shown in Figure 2.2C.

Ship Cave is located further downstream from Skull Cave and is separated from Skull Cave by first an exceptionally large collapsed trench, ~40 m to 50 m wide and ~100 m long (west to east). Proceeding east, there are two small intact but unconnected portions of the Modoc Crater tube system. The first known simply as Cave, and the

second known as Robin Cave. Ship Cave is accessed to their east via a roughly circular, ~24-m diameter collapsed pit positioned between it and Robin Cave. Ship Cave is a relatively large intact portion of the tube system of fairly consistent cross-section, ~19 m wide by 7 m high at the entrance and gradually constricting down to a width of 12 m and height of 6 m at the farthest extent. The depth-to-ceiling is ~7 m to 8 m near the entrance, dropping to ~15 m as one progresses into the cave. The furthest reach appears to be blocked by a combination of collapse and solidified basaltic flow. As in Skull Cave, the internal geomorphic features consist of significant collapse of the ceiling and wall lining resulting in meter scale blocks covering the floor. Figure 2.2D provides a picture of the internal view of Ship Cave, looking west towards its entrance.

## ***2.4 Modoc Crater Lava Tube Field Data***

### ***2.4.1 Ground Level Magnetic Survey***

To record the total magnetic strength above the lava tube complex, we used a GEM Systems (Geophysical Electromagnetic Systems) GSM-19 Overhauser magnetometer during two separate field seasons in May 2017 and September 2018 (GEM Systems, Inc., 2008). The magnetometer system acquired the total magnetic field strength at a resolution of 0.2 nT with an absolute accuracy of 1 nT at 5 Hz (GEM Systems, Inc., 2008). The magnetometer was deployed 2 m above the ground on a boom attached to a non-magnetic backpack. The magnetic data was collected by performing ground level magnetic surveys with continuous data acquisition, acquired at 5 Hz. Carried at walking speed, this corresponded to an average along-track spacing of < 0.2 m between readings. Parallel lines were walked perpendicular to the tube direction as determined from U.S. Geological Survey Maps (Waters, Donnelly-Nolan, & Rogers, 2010), and

were pre-mapped on a handheld GPS unit at 2-meter to 4-meter intervals. We typically extended the lines ~20 m to 50 m to either side of the estimated location of the walls of the lava tube being surveyed. The GPS location for each data point was also recorded. In total we magnetically surveyed approximately 100,000 m<sup>2</sup> along an approximately 1000-meter length of the Modoc Crater Lava Tube complex (Figure 2.3) (Bell et al., 2020, 2018). Some areas, such as north of Ship Cave were not surveyed due hazardous walking conditions and/or obstruction by dense vegetation.

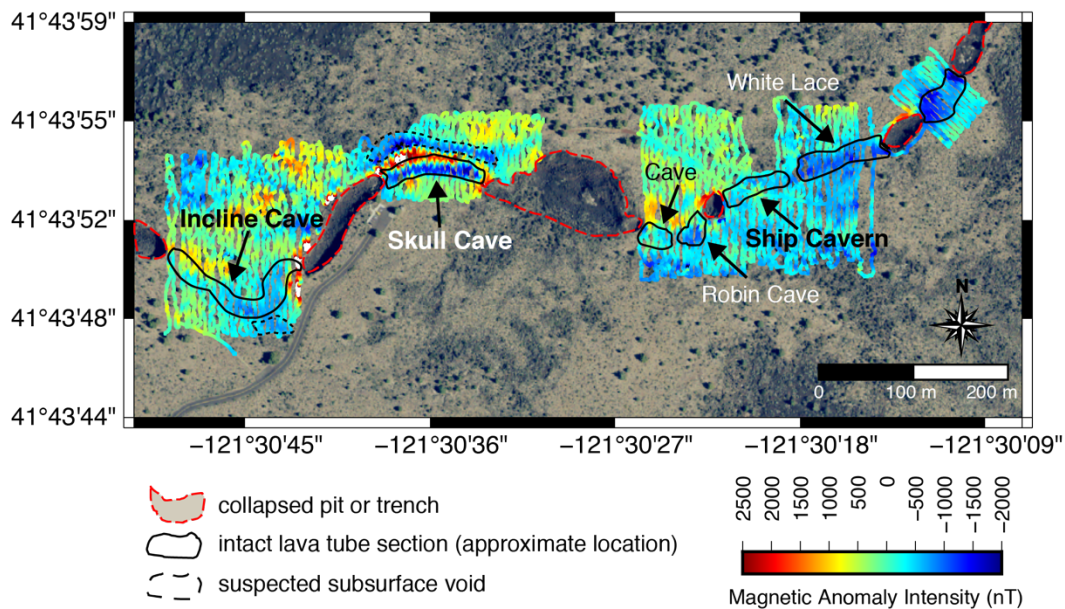


**Figure 2.3:** Ground level surface magnetic anomaly survey of a portion of the Modoc Crater lava tube system. Lava tube subsurface perimeters are shown in the black outlines. Collapse pits are indicated by broken red lines, and the magnetically inferred location of an unexplored subsurface tube is in broken black lines. Magnetic field is reported relative to the local background [50,685 nT at Skull Cave segment, and 50,541 for all other segments], and the colorbar saturates to white at +2500 and black at -2000 nT. Background aerial image credit: USGS National Elevation Dataset, from north 42 west 122 tile.

#### 2.4.2 Three-dimensional Laser (LiDAR) Surveys

Multiple Light Detection and Ranging (LiDAR) 3-D surveys were completed of both the interior of the lava tubes and the overlying ground surface topography with a Riegl Vz-400 tripod mounted terrestrial laser scanner (Garry, Whelley, Shiro,

Rowland, & Bleacher, 2017; Whelley, et al., 2018). The LiDAR data captures sub-centimeter geomorphologic details of the interiors and ground level topography. Data from outside of the tube were geo-located using a pair of high accuracy differential GPS receivers. LiDAR data from the tube interiors, where GPS satellite lock was not possible, were then merged with outside scans in RiSCAN Pro 2.8 software. The resulting point cloud provides geometry, locations, and distances from the surface to any feature of interest and a three-dimensional map of the interior of the lava tube with a cm-accurate relation to the ground surface topography. The high-resolution LiDAR data scans were produced for the three intact tube portions, Incline, Skull, and Ship Caves shown in Figure 2.4, Subplots A, B, and C.

## ***2.5 Data Processing and Analysis***

### ***2.5.1 Initial Data Processing***

To remove the background magnetic field of the Earth we used the International Geomagnetic Reference Field (IGRF) model from the NOAA National Center for Environmental Information (NCEI) Magnetic Field Calculators for the total magnetic field intensity for LBNM on the days of the surveys. The total field average was 50685 nT for the May 1, 2017 observations around Skull Cave, and 50541 nT for the September 6-8, 2018 observations of Incline and Ship Caves (National Geophysical Data Center, 2020). Figure 2.3 presents the resulting magnetic anomaly map created from the observed ground level magnetic survey of our field area portion of the Modoc Carter Lava Tube complex after these corrections were applied.

We concluded that corrections for diurnal variations did not need to be applied to our dataset owing to the low diurnal variation during the data acquisition time relative

to the overall background magnetic variation across the lava flow itself. We evaluated the average diurnal variation in the total Earth magnetic field recorded at the three USGS Geomagnetic Observatories (Fresno, CA; Newport, WA; & Tucson, AZ) closest to LBNM during the dates overlapping our magnetic surveys. The largest diurnal variation gradient was 7.5 nT per hour over 2 hours and 17 minutes, on September 7, 2018, during a portion of the Ship Cave magnetic survey. For the same location the background variation due to the lava flow is +/-281 nT, which is also the lowest background variation of the three lava tubes. For the rest of the data collection, the largest diurnal variation was between 2 and 4 nT per hour.

For our magnetic analysis of Incline, Skull, and Ship Caves, we sub-selected the data points from the areas surrounding each respective tube (Figure 2.4). Data points

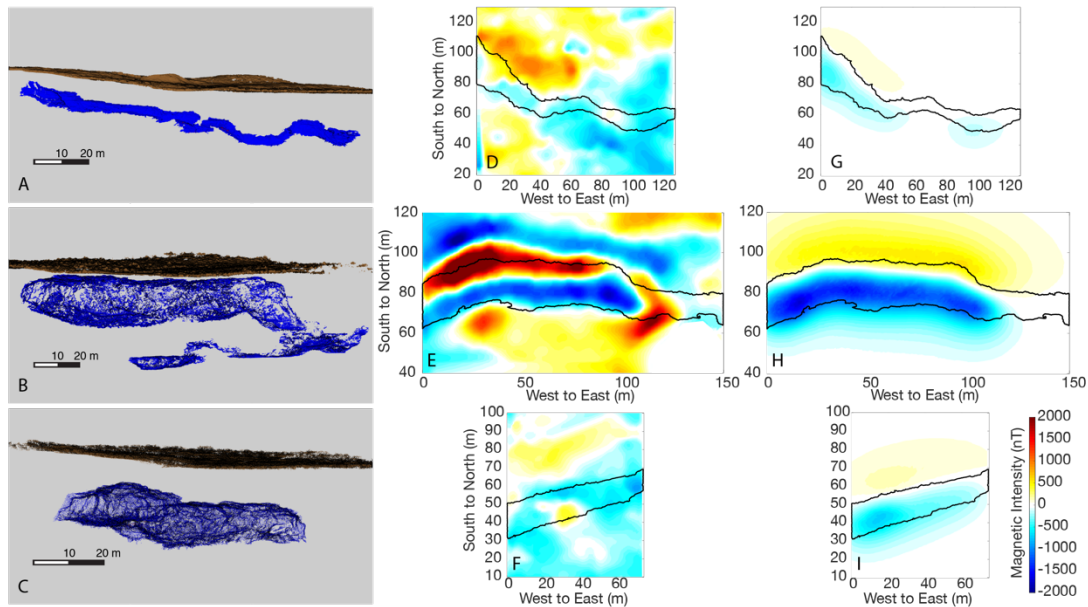


**Figure 2.4:** Orthographic view of LiDAR point cloud models of Incline (A), Skull (B), & Ship (C) caves for the corresponding outlined perimeters shown in black in the aerial plots of the observed magnetic anomalies (subplots D, E, & F), and the modelled magnetic anomalies (subplots G, H, & I) for the same recorded portions of the lava tube caves.

were then interpolated onto a regular 1-by-1-meter grid and smoothed by performing a 5-by-5-meter median filter, selected due to the original 3 to 5 m spacing of the survey lines. We then removed the median observed background magnetic anomaly of -13.15 nT created by the basaltic lava flows surrounding the lava tubes from the NOAA NCEI model. This resulted in our final smoothed and filtered plots of the magnetic anomalies for each of the three lava tubes at approximately 2 m above ground level. These plots are shown in Figures 2.4D, E, & F.

The original sub-centimeter LiDAR point cloud surveys were down-sampled to 10-centimeter point-spacing. This provided manageable file sizes to sub-select the portion of the surface topography and lava tube LiDAR point clouds contained within the volume directly below a rectangular area overlaying each lava tube. Figure 2.4, Subplots A, B, and C shows the three-dimensional LiDAR point cloud models for Incline, Skull, and Ship Caves. From these reduced LiDAR point clouds, we generated finite point models, with regular spacing, for use in calculating theoretical 2-D magnetic anomalies from the lava tubes and surface topography. For each of the lava tubes, a 3D grid was defined with 1-m spacing between points in the east-west direction (along the general longitudinal axis of the lava tube), 0.25m spacing in the north-south direction, and 0.25m spacing in the vertical direction. Then from the LiDAR data each point on the grid was defined as being either inside or outside the lava tube. For the surface topography, the elevations of the LiDAR surface topography were interpolated onto the same 1-m east-west and 0.25 m north-south grid. These uniform grids allowed for the construction of parameterized finite element models of desired resolution.

### ***2.5.2 Magnetic Modeling***

The 3D-grid point models described above were used to create forward models of the expected magnetic signatures of the lava tubes. In these regularized models we assigned rectangular prismatic dimensions of 1.0 m x 0.25 m x 0.25 m, in X, Y, and Z directions to each point on the grid. We then assume the surrounding basalt is homogeneous and assigned a constant magnetic susceptibility of 0.155 to all prisms inside the lava tube, for reasons described below.

As we do not have an independent constraint on induced versus remanent magnetism, we set the remanent magnetism to zero, and performed the initial analysis assuming an effective magnetic susceptibility accounts for both the induced and remanent magnetism. For this, we prescribed the Earth's field direction at LBNM, with magnetic inclination  $64.7^\circ$  and declination  $14.3^\circ$ . The equivalent magnetic susceptibility value of 0.155 was derived from our results described below in the Discussion section. We applied properties only to the prisms inside the lava tube void to minimize the required number of prismatic elements and reduce the forward modeling computational time. The resulting amplitudes were then phase shifted by  $180^\circ$  (multiplied by -1) to determine the proper magnetic anomaly signature produced from the absence of basaltic material in the lava tube void. This method also removed the edge effects that would be caused by modeling a block of basalt with a lava tube void in it.

Our prismatic element model was then processed with a modified version of the "GRAV\_MAG\_PRISM" Matlab® script to compute the magnetic signature of these rectangular prismatic elements (Bongiolo, Souza, Ferreira, & Castro, 2013). The

Matlab code generates the synthetic 2-dimensional ground surface magnetic signature, at a desired elevation, with the magnetic anomaly strength for a surface observer at each point being the summation of all the elements in the model. For our models the final results are equivalent to the lava tubes' magnetic anomalies as observed from 2 m above the ground.

To reduce computational requirements, the code originally assumes that all of the prismatic bodies are located beneath a flat surface at  $Z=0$ . The expression that is derived for the total magnetic anomaly produced by a rectangular prismatic body, equation 33 as shown and detailed in (Bongiolo et al., 2013), is Equation 1.

$$\Delta T(x, y, 0) = G_1 \ln F_1 + G_2 \ln F_2 + G_3 \ln F_3 + G_4 \ln F_4 + G_5 \ln F_5 \quad (1)$$

In Equation 1,  $\Delta T$  is the total field anomaly at  $z=0$ , and the constants  $G_1$ ,  $G_2$ ,  $G_3$ ,  $G_4$ , &  $G_5$  are a combination of the magnetization vector, direction cosines of magnetization, and the directive cosines of the geomagnetic field environment as described in (Bongiolo et al., 2013). The constants  $F_1$ ,  $F_2$ ,  $F_3$ ,  $F_4$ , &  $F_5$  are a representation of the coordinates of the vertices of each prismatic element used to locate each prism within the geomagnetic field (Bongiolo et al., 2013). Together they are used to calculate the total magnetic field created by each individual prismatic element. These individual results for each prism are then combined to determine the total magnetic intensity at each point on the surface ( $Z=0$ ). We introduced a modification into the Matlab script that accounts for the variation in elevation of the actual surface topography above the lava tubes. Our script modification provides for a better synthetic magnetic anomaly signature with which to compare our field observations. The modification sets the highest elevation of the ground surface, for the area being

analyzed, equal to  $Z=0$ . The rest of the points in both the ground topography and lava tube point clouds are then vertically referenced to this location. The difference between the  $Z=0$  elevation and the maximum elevation at each X-Y location in the regularized ground topography point cloud is then calculated, creating a 2-dimensional matrix of the topographic variation for the area above the lava tube. This vertical topographic variation difference is then removed from the depth to each of the regularized lava tube point cloud points for each X-Y position. Essentially this adjusts the depths of all the lava tube prisms towards the surface to their same absolute depths below what would be a flat plane located at the  $Z=0$  location of the ground topography, where:

$$h_{equivalent} = h_{maximum} - h_{topography} \quad (2)$$

Implementing this modification results in additional computations for each X-Y location to determine the modified depth,  $h_{(equivalent)}$ , to each of the lava tube prisms, but creates a magnetic signature across a flat plane at  $Z=0$  that accounts for the relative depth of the lava tube beneath the actual undulating topography located above the lava tube. The final resulting aerial magnetic anomaly maps for our models of the three lava tubes, Incline, Skull, and Ship Caves, are shown in Figure 2.4, Subplots G, H, and I.

### ***2.5.3 Calculation of Magnetic Gradients***

Along with the previously described analysis, a final evaluation of both the observed as well as the synthetic model, was to calculate and plot the horizontal gradients of the mapped magnetic anomalies shown in Figure 2.4. Calculating of magnetic gradients is one method used to examine magnetic survey data to determine the geometry of the source of a magnetic anomaly by outlining edges with the resulting

gradient maxima or minima (Ferreira, de Souza, de B. e S. Bongiolo, & de Castro, 2013). The magnetic gradients for our study are calculated by applying a standard sobel operator (Duda, Hart, & Stork, 1973; Sobel, 2014) which is a weighted sum of adjacent pixels, or points, regularly used to detect edges in image processing. It first calculates the latitudinal and longitudinal components of the gradient at each of the points on the magnetic anomaly map. The gradient magnitude is then computed by taking the square root of the sum of the squares of the components at each data point for the magnetic anomaly map. For the edges, the values outside the boundary of the magnetic anomaly map are assumed to be equal to the nearest anomaly map value.

The resulting magnetic gradient plots are shown in Figure 2.5. Notice in the plots of the observed magnetic anomaly data, the Skull Cave (Figure 2.5B) perimeter is clearly outlined by lines of minimum magnetic gradient, whereas Incline Cave (Figure 2.5A) and Ship Cave (Figure 2.5C) perimeters are obscured by additional gradient lines from localized anomalies. In the plots of the magnetic gradients from the modeled magnetic anomaly data, the LiDAR derived outline of the tube perimeters of all three lava tubes are consistently ~5 m south of the minimum magnetic gradients, seen in Figures 2.5D, E, and F.

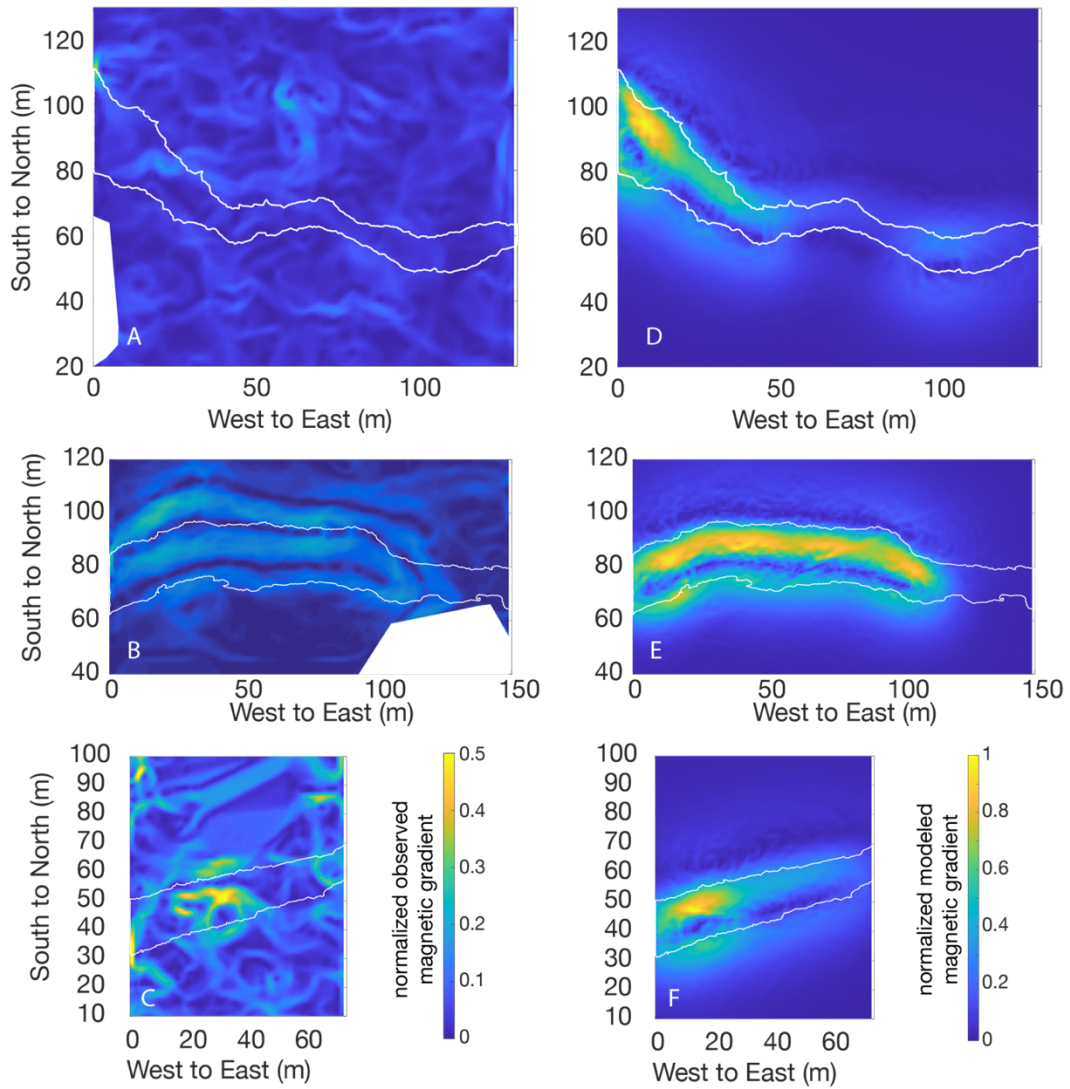


**Figure 2.5:** Normalized magnetic gradient plots for both the observed (left column) and modeled (right column) magnetic anomaly plots of Incline (A & D), Skull (B & E), and Ship (C & F) lava tube caves respectively. LiDAR derived lava tube perimeters are outlined in white. Magnetic gradients plotted are normalized to the highest gradient (nT/m) calculated for each figure.

## 2.6 Discussion & Interpretation of Results

### 2.6.1 Relating Magnetic Anomaly to Tube Geomorphology

In simplest terms, the magnetic signature of a lava tube is analogous to that of a buried cylindrical rod at depth, where the rod represents the void space produced by the lava tube. The derivation for determining the total field magnetic anomaly  $\Delta F$ , in nanaotesla; located directly above the longitudinal centerline of an infinite cylindrical magnet, with magnetic susceptibility  $k$ , equivalent radius  $r$  in meters, cross-sectional area  $A$  in meters squared, buried beneath a ceiling of thickness  $t$  in meters, with a depth to center of the rod of  $t+r$ , where  $r$  is the radius of the cylinder in meters; shown in Figure 2.6, is given by Gay (1965), to be (Eq. 3):

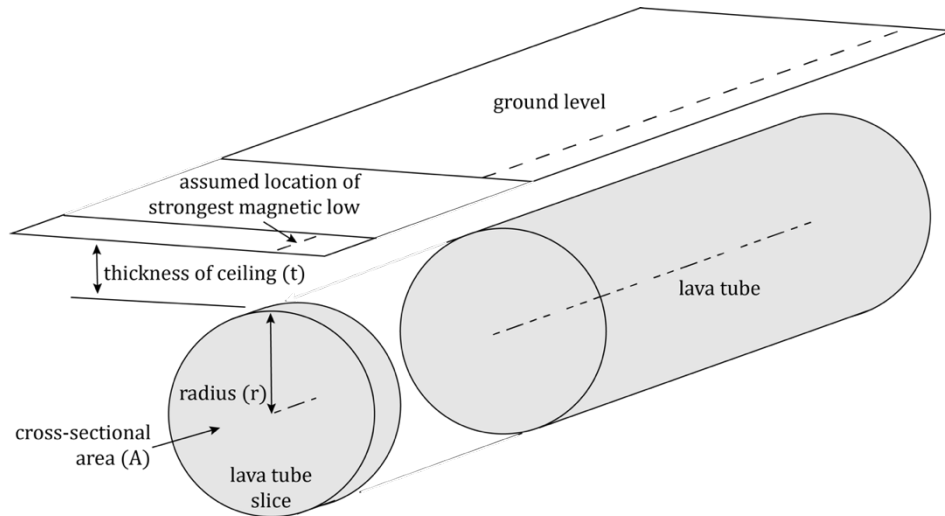


**Figure 2.6:** Schematic representation, of lava tube geometry deconstruction used for geomorphic versus geophysical relationship analysis between the lava tube geomorphology and the magnetic anomaly, used for this study.

$$\Delta F = \frac{k}{4\pi} \left( \frac{2T' \sin I_o \cos(2I'_o - 180)}{\sin I'_o} \right) \frac{A}{(t + r)^2} \quad (3)$$

where,

$$T'_o = \frac{T_o \sin I_o}{\sin I'_o} \quad (4)$$

and,

$$\tan I'_o = \frac{\tan I_o}{\sin \alpha} \quad (5)$$

In this  $T_o$  is the Earth's magnetic field in nT,  $I_o$  is the true inclination, and  $\alpha$  is the strike of the lava tube. For our purposes, the radius  $r$ , of the observed lava tubes, is defined to be an apparent radius of the lava tubes based on the average of the height and width of the lava tube:

$$r = \frac{1}{2} \left( \frac{1}{2} height + \frac{1}{2} width \right) \quad (6)$$

Assuming the inclination and strike of the lava tube remain constant at  $64.7^\circ$ , for the location of LBNM ,and  $90^\circ$ , as an approximate position for the lava tubes in this study, respectively, and setting the Earth's magnetic field equal to the average of the field on the days of the field surveys (50613 nT), we define constant  $C_1$ , Equation 7, which accounts for the geographic location and relative geometric position of the lava tube.

$$C_1 = \left( \frac{2T'_o \sin I_o \cos(2I'_o - 180)}{\sin I'_o} \right) \quad (7)$$

For our analysis, we divided each lava tube into 1-meter cross-sectional slices along the west-to-east running longitudinal length. For each slice, across the regularly spaced lava tube point cloud models of the observed lava tubes, we determined the

geometric ratio of the cross-sectional area ( $A$ ) to the apparent depth to center ( $t + r$ ) of the lava tube. For each of these cross-sectional slices, the strongest observed negative magnetic anomaly  $\Delta F$  from the smoothed interpolated data, within the borders of the lava tube walls was determined. The minimum magnetic anomaly versus the geometric ratio of the observed data was then plotted for all three Modoc Crater lava tube system segments studied; Incline, Skull, and Ship Caves; and can be seen in Figure 2.7A. This data was then binned at 0.125 increments of the geometric ratio, along the X-axis, with the median for each of these bin groupings plotted in Figure 2.7B along with the one standard deviation error from the median for each bin. For these scatter plots, the best fit least squares linear regression line for a zero intercept was determined. As would be predicted by Equation 3 for a void within a lava flow, we observe an overall negative linear relationship between the strongest observed negative magnetic anomaly and an increase in the geometric ratio of lava tube depth to cross-sectional area. This suggests that it is probable that the tube anomaly is contributing to the variation we observed at the Modoc study region.

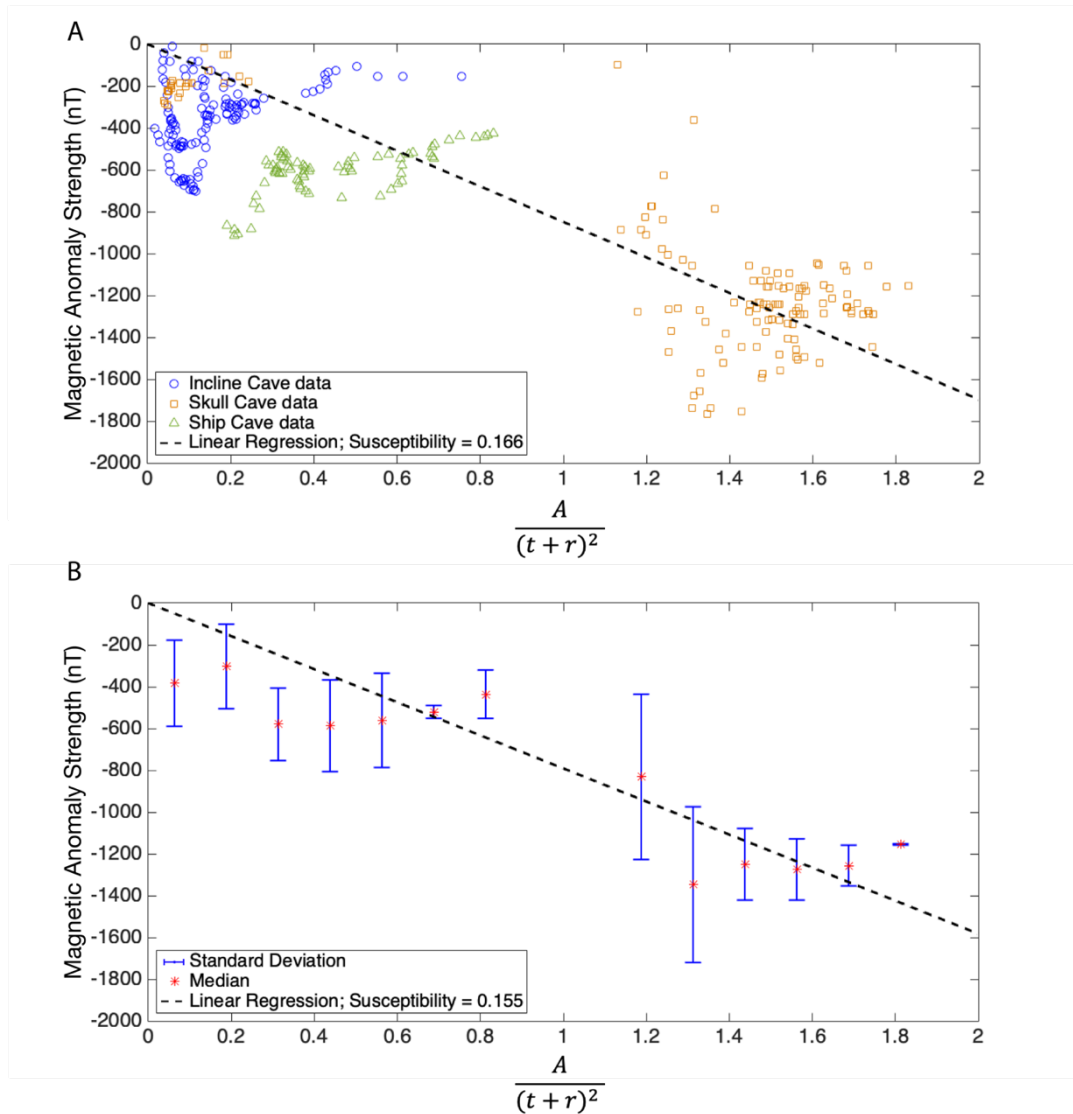


**Figure 2.7:** The relationship between the observed lava tube total field magnetic anomalies and the LiDAR-derived non-dimensional geometric ratio. A linear least squares regression (broken black line) was used to determine the equivalent magnetic susceptibility. Figure A: All observed 1-meter slice data points for Ship (green triangles), Incline (blue circles), and Skull (orange squares) caves. Equivalent magnetic susceptibility of  $0.166 \pm 0.007$ . Figure B: Median of the observed data for every 0.125 geometric ratio increment. Error bars show one standard deviation from the median. Equivalent magnetic susceptibility of  $0.155 \pm 0.023$ .

The slope of this linear relationship is related to the equivalent magnetic susceptibility for the family of lava tubes in the Modoc Crater lava tube system. Equivalent magnetic susceptibility is defined in this sense as the combination of the unknown true susceptibility and unidentified thermo-remanent magnetization into a

single apparent susceptibility parameter. For this calculation, we set the magnetic susceptibility ( $k$ ) and the constant  $\left(\frac{C_1}{4\pi}\right)$  equal to the slope of the plotted data and solve for the apparent magnetic susceptibility ( $k$ ) as follows in Equation 8.

$$k = \frac{4\pi}{C_1} \frac{\delta(\Delta F)}{\delta\left(\frac{A}{(t+r)^2}\right)} \quad (8)$$

This analysis results in an apparent magnetic susceptibility of  $0.166 \pm 0.007$  for the scatter plot of all data points in Figure 2.7 A. Using the median data, Figure 2.7 B, we calculate an equivalent magnetic susceptibility of  $0.155 \pm 0.023$ . The calculated apparent magnetic susceptibility is well with the range of measured susceptibilities for basaltic lava flows, that can range of up to 0.4 S.I. (Budetta & Negro, 1995). The recovered apparent susceptibility of 0.155 was used for all our forward models.

### ***2.6.2 Validation of Magnetic Anomaly to Geomorphic Relationship***

Forward magnetic anomaly models that used the 3-dimensional LiDAR point cloud representations of Incline, Skull, and Ship lava tubes allowed us to test the sensitivity of our magnetic anomaly to geomorphic relationship using the assumption of a known apparent magnetic susceptibility for the region. If apparent magnetic susceptibility of the lava, and the spatial variation in the total field magnetic anomaly are known, then the result shows that a suspected underlying lava tube geometry can be bounded, and subsurface cavity space inferred.

Per our assumption of relating the full magnetic anomaly to an apparent induced magnetism, we set the remanent magnetism to zero. We then perform the modeling

based purely on an apparent magnetic susceptibility value of  $0.155 \pm 0.023$  determined from observed geometric ratio vs. magnetic strength analysis. The resulting 2-dimensional aerial magnetic anomaly maps are shown in Figure 2.4G, H, & I. The geomorphic analysis performed on the observed data (results in Figure 2.7) was repeated on the results of our modeled lava tubes, with plots of this analysis shown in Figure 2.8. These model results show good agreement to the observed data analysis, returning an apparent magnetic susceptibility of  $0.168 \pm 0.014$ , Figure 2.8B, versus  $0.155 \pm 0.023$ . A difference of 8%, with overlapping error margins. This difference is likely a combination in the differences between true geometries and the simple cylindrical model, as well as unaccountable variations in the actual lava flow itself. This demonstrates that an observed lava tube magnetic anomaly behaves as the cylindrical theoretical model predicts it should in a natural lava tube system, as long as the observed magnetic signal is above the background variation.

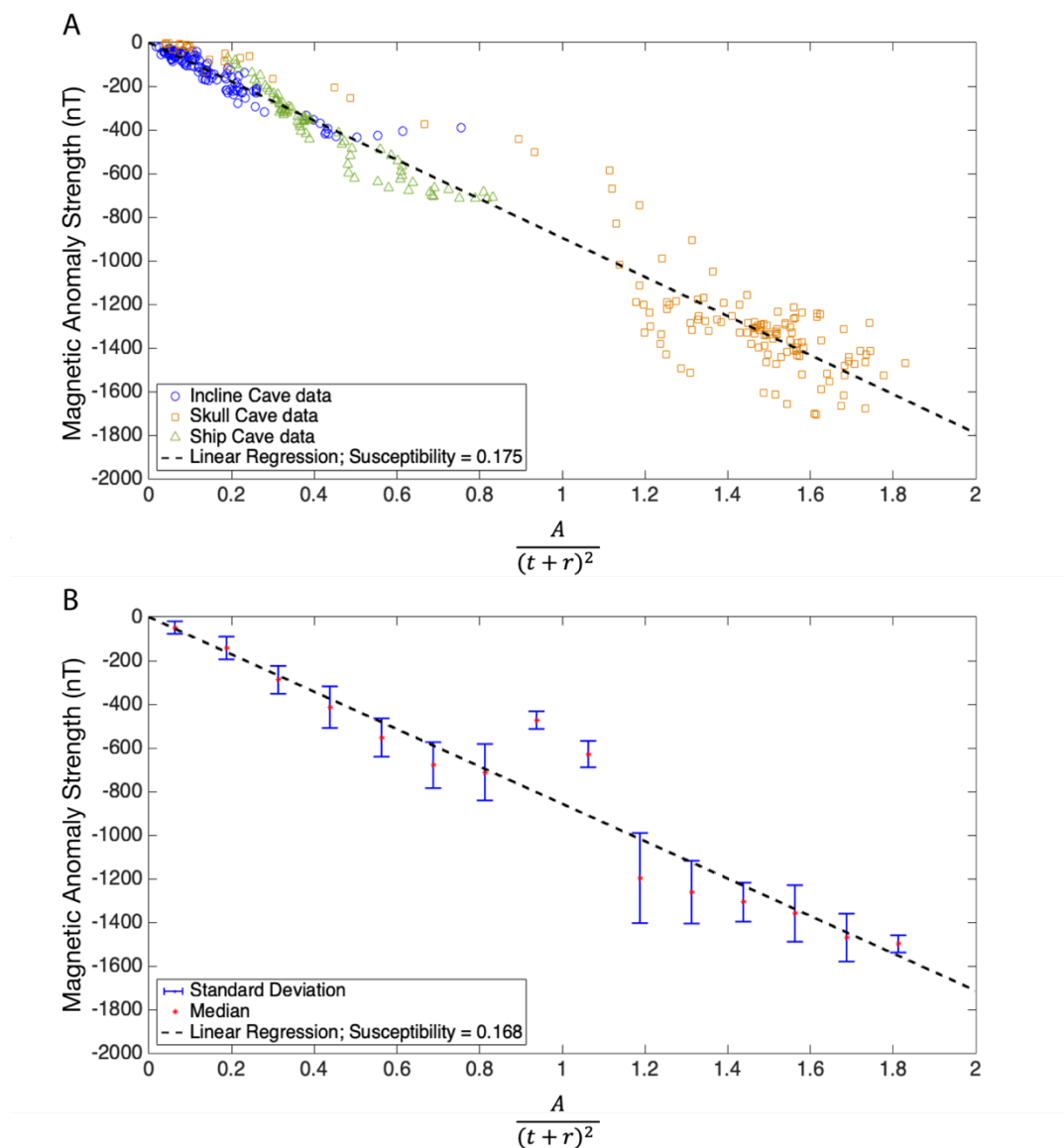


**Figure 2.8:** The relationship between the modeled lava tube total field magnetic anomalies and the LiDAR-derived non-dimensionalized geometric ratio. A linear least squares regression (broken black line) was used to determine the equivalent magnetic susceptibility. Figure A: All modeled 1-meter slice data points for Ship (green triangles), Incline (blue circles), and Skull (orange squares) caves. Equivalent magnetic susceptibility of  $0.175 \pm 0.002$ . Figure B: Median of the modeled data for every 0.125 geometric ratio increment. Error bars show one standard deviation from the median. Equivalent magnetic susceptibility of  $0.168 \pm 0.014$ .

The practical capability acquired from this magnetic to geometric relationship for lava tubes is to use magnetic anomalies to help envelope the possible geometric ratio of lava tubes. With the addition of one independently acquired geometric constraint on

a lava tube (depth to ceiling), along with the local magnetic properties of the lava, it is possible to envelope the range of lava tube geometries based on a surface map of the magnetic anomaly created by a lava tube with sufficient signal to noise ratio.

For example, the depth to lava tube ceiling, or in other words the overburden thickness, can be acquired either from visual inspection of a lava tube at a collapsed pit, or via other geophysical field methods such as ground penetrating radar (Esmaeili et al., 2020; Miyamoto et al., 2005). Using this depth, along with a field determination of the magnetic properties (i.e. susceptibility), the apparent cross-sectional radius for a lava tube, can then be calculated.

To demonstrate calculating an apparent lava tube radius we used the data from Incline, Skull, and Ship Caves. We used the medians of the strongest negative magnetic anomalies ( $\Delta F$ ) and of the tube ceiling thickness ( $t$ ) based on all perpendicular slices used in the geomorphic to magnetic analysis, given in Table 2.2 rows 1 and 2. Along with this data, we use the apparent magnetic susceptibility of 0.155 which we calculated for our field section of the Modoc Crater lava tube complex. Then, rearranging Equation 3, we solve for the apparent lava tube radius ( $r$ ), provided in Table 2.2 row 3, that would be required to create the median strongest negative magnetic anomaly. Table 2.2 row 5 then provides the ratio of observed median (Table 2.2 row 4) to this calculated apparent radius (Table 2.2 row 3), with 1 being an exact fit.

**Table 2.2:** For Incline, Skull, and Ship lava tube caves the following values are provided based on calculated and observed data. A) The *median of the maximum negative magnetic anomaly* over the lava tube. B) The *median observed ceiling depth* for the lava tube. C) The *apparent radius (r)* for 1) the calculated apparent radius based on the median maximum negative magnetic anomaly and the median observed ceiling depth, 2) the actual observed median apparent radius, and 3) the ratio of the two. D) The ratio of the observed apparent radius to the depth to the lava tube ceiling. E) The observed median  $\frac{1}{2}$  width. F) The observed median  $\frac{1}{2}$  height. G) The mean magnetic anomaly from 1) within the tube perimeter, 2) the overall region of observation over the lava tube, and 3) the ratio of these two which quantifies the magnetic signal to magnetic background variation.

		<b>Incline Cave</b>	<b>Skull Cave</b>	<b>Ship Cave</b>
<b>Median Max Negative Magnetic Anomaly (nT)</b>		-345	-1177	-605
<b>Median Observed Ceiling Depth (t) (m)</b>		12.60	4.2	10.2
<b>Apparent Radius (r)</b>	<b>Calculated (m)</b>	7.5	9.3	9.9
	<b>Observed Median (m)</b>	3.9	9.1	6.4
	<b>Ratio: Observed / Calculated</b>	0.52	0.98	0.65
<b>Ratio: Observed Apparent Radius (r) / Depth (t)</b>		0.31	2.17	0.63
<b>Observed Median <math>\frac{1}{2}</math> Width (m)</b>		5.5	10.6	8.8
<b>Observed Median <math>\frac{1}{2}</math> Height (m)</b>		2.3	7.5	4.1
<b>Mean Magnetic Anomaly</b>	<b>Within Tube Perimeter (nT) (signal)</b>	-161±306	-29±1095	-364±287
	<b>Overall Tube Area (nT) (background variation)</b>	44±421	92±784	-250±282
	<b>Signal to Background Variation</b>	0.73	1.40	1.02

The results of this example for a first order approximation of the apparent radius of the three lava tubes provide insight into trends to guide continued research in this area. The first of these trends is to examine the median observed apparent radius (Table 2.2 row 4) with respect to the median observed ceiling depth (Table 2.2 row 2). The ratio of these two dimensions is listed in Table 2.2, row 6. It results in a trend of increasing ratio from Incline, to Ship, to Skull Caves. The second of these trends is from a comparison of the signal to background variation for each lava tube location. For this comparison, we first calculated the means and standard deviation from the observed data for the fieldsite above and extending approximately two to three width of the lava tube to represent normal variation in the magnetic signal in the site location,

defined as the noise (Table 2.2 row 10). We then assumed the ground level area outlined by the extents of the lava tube to represent the magnetic signature presented from the lava tube itself, defined as the signal (Table 2.2 row 9). The resulting signal-to-background variation ratio is provided in Table 2.2 row 11. Again, we see an increasing trend from Incline, to Ship, to Skull Caves for the signal-to-noise ratio. Both of these trends match the increasing trend of better fit for the apparent radius from our example, in Table 2.2 row 5, where a result of 1 would be an exact fit of the calculated lava tube apparent radius with respect to the observed median. This quantifies the understanding that small deep lava tubes are difficult to resolve, whereas large shallow tubes have ideal signal-to-background-variation and geometric ratios for locating.

It is likely that the tube signal and background variation are both partially dependent on the formation process and evolution of lava flows in the area which likely introduce background variation into the system that is not explicitly addressed in this research. For instance, a lava tube formation mechanism of either coalescing of previously solidified rafted plates, already cooled below the Curie point, may result in a final lava tube roof constructed of essentially individually remanently magnetized plates with random orientations resulting in a lack of a uniform magnetic background signature. This would add noise on the scale of meters to tens of meters on top of the tube's magnetic signature which may then lie below this variation. Similarly, the lava tube formation processes by construction of arches from border levees along turbulent flow can be envisioned to result in individual spatter components cooling below the Curie point, and then having a physical change in orientation due to the addition of additional spatter as the arch is created. Pahoehoe and stable channel flow surface solidification processes can be envisioned to result in less physical orientation

rearrangement after a remanent magnetic set as it cools below the Curie point, thus these would be expected to have relatively large spatial coherency. However, even these formation processes can have changes in positioning as they cool due to changes in channel flow depth, or inflation/deflation of pahoehoe lobes, which could still result in adding to the complexity of the magnetic background variation, albeit less than from construction transport processes. Follow-on flows after the original construction of a lava tube could be envisioned to impact the magnetic signature as they potentially alter location of previously emplaced basalt, or increase the ceiling thickness with randomly orientate blocks of a'a' basalt on the scale of size of the magnetic measurements. Finally, the impact of the roughness (or blockiness) of the lava flow surface, along with possible unknown and therefore unaccounted for void spaces in the lava tube ceilings during the formation evolution can result in increased complexity in the magnetic background variation. The roughness and voids will create a multitude of induced magnetic fields that will interact in a non-uniform fashion which increase the magnetic background variation. These impacts to the magnetic background variation would be more pronounced in lava tubes with smaller apparent radius to depth ratios such as Incline and Ship Caves, and these details are not accounted for in the resolution used for constructing these models.

Overall, these trends show that the Skull Cave segment produces magnetic anomalies of significant magnitude above the background variation that allow us to reliably determine the overall radius of the lava tube. This signal to noise (background variation) for Skull Cave is likely amplified primarily because the ratio of radius to ceiling depth for Skull Cave is three to seven times larger than for Incline and Ship Caves. This higher ratio at Skull Cave results in the tube producing a magnetic anomaly

that is not lost in the magnetic background variation from the lava flow and lava tube formation processes.

### ***2.6.3 Interpretation and Utility of Magnetic Gradient Analysis***

As described in the analysis section, the 2-dimensional gradients of the ground level magnetic signatures for the three lava tubes were also investigated, and are shown in Figure 2.5. For each of the model results (Figures 2.5D, E, & F) this analysis shows well-defined lines of minimal gradients that track the outlines of the lava tube perimeter, with a slight offset to the north, likely due to the magnetic inclination at LBNM of 64.7°.

Conversely, for the observed magnetic gradients at Incline and Ship Caves (Figure 2.5A and C), there is very little to no area in which gradient lines are associated with the location of the actual lava tubes. This is again likely due to the ratio of the apparent radius to depth for these caves being too low for the magnetic signature of the cave to overcome the magnetic background variation. As previously discussed, this background variation is likely due to small-scale magnetic fields from the various lava flow surface blocks and small void spaces in the lava tube ceiling interacting in a non-uniform fashion, and overriding the magnetic gradient created from the perimeter of the lava tubes.

However, the observed, higher apparent radius to depth ratio, Skull Cave data (Figure 2.5B) does show three distinct lines of minimal gradient. The southern two of these lines align with the locations of the actual Skull Cave walls, similar to the modeled results. There is a slight variation of the northern of these two lines (center line of the three) aligning perfectly with the northern wall of Skull Cave versus being

slightly offset to the north as seen in the results from the modeled data (Figure 2.5E). This position of the center line of minimal magnetic gradient may be affected by a second significant negative magnetic anomaly parallel, to the north, of the one produced by Skull Cave. This additional negative magnetic anomaly may be compressing the positive magnetic anomaly field lines, from the Skull Cave anomaly, slightly to the south which would account for this variation. The third line, furthest north, of minimal magnetic gradient in the observed Skull Cave data analysis is also due to this second negative magnetic anomaly, which is produced by an as yet unknown source.

One item of note from the results of Skull Cave is that these magnetic gradient lines have the potential to be used for an initial estimate of the width of the lava tube. For example, the width based on the observed magnetic gradient plot can be estimated to be approximately 20 m across, which is of similar order to the true median observed width of 21.2 m (based on Table 2.2 row 7). We can then apply the  $\frac{1}{2}$  width of 10 m along with the calculated apparent radius of 9.3 m (Table 2.2 row 3) to equation 6 to calculate an a  $\frac{1}{2}$  height. The result of this calculation is a  $\frac{1}{2}$  height of 8.6 m. The observed median  $\frac{1}{2}$  height is 7.5 m, or a difference of 13%.

#### ***2.6.4 Comparisons of Lava Tube Magnetic Surveys and Models***

As can be seen on Figure 2.3, known intact lava tube sections correlate fairly well with recorded magnetic lows. In addition, there are several magnetic lows that appear to originate from unmapped tube locations. However, it is unconfirmed if a void space exists at these positions due a lack of accessibility into these areas. These regions of interest are labelled as “suspected subsurface void”.

When comparing the observed and modeled magnetic survey maps there are similarities as well as some variations between the two sets. This can be noticed by comparing the magnetic anomaly maps in Figure 2.4, as well as comparing the data points in the scatter plots of the magnetic anomalies vs tube geomorphology seen in Figures 2.7 and 2.8.

For Incline Cave (Figures 2.4D and G), similar locations for a magnetic high, albeit of different magnitudes, are seen on the north side of the tube outline in the 0 to 50-meter range of west to east. Also, the negative anomaly over the first 40 m of the modeled anomaly of Incline Cave match the location of a negative anomaly of similar strength and geographic location in the observed data. Despite these similarities, the modeled magnetic low for the remainder of the tube, from 40 m to 120 m, is approximately equal to or less than the background variation of the observed data, producing negative magnetic anomalies at ground level from 0 to -500 nT from the tube. For this easternmost 80 m of the tube, the ratio of the apparent tube radius to lava tube ceiling thickness significantly decreases providing an explanation for the lack of observed magnetic signature of Incline Cave in this region.

There is a similar effect seen in the comparison for Ship Cave (Figures 2.4F and I), although the tube has a signal-to-noise ratio of  $\sim 1.0$ . Specifically, the expected positive magnetic anomaly associated with the lava tube is present on the north side of the tube for both the observed and modeled data, albeit of a higher magnitude and further north in the observed data. Also, the observed data shows some negative anomalies over the tube location that are slightly above the background magnetic variability similar to the model, which suggests that the signal-to-noise ratio of the tube

versus the background is somewhat variable, i.e. there are a few places where the signal is noticeable above the background variation.

Skull Cave (Figures 2.4E and H) provides the most pronounced magnetic signature and best agreement between the observed and modeled magnetic maps. There are two strong negative anomalies running parallel to each other with a strong positive anomaly between them. The southern of these two anomalies, lying over the location of Skull Cave, matches very well with the strength of the modeled negative anomalies for this lava tube. The location of the observed positive anomaly also matches the location of a positive anomaly in the model, though the observed peak is ~four times the modeled magnitude. The other primary difference between the observed and modeled magnetic maps is the strong northern negative magnetic anomaly, which does not exist in the model results, but is the reason for additional lines of minimal magnetic gradient (Figure 2.5B) as discussed earlier. This second strong negative magnetic anomaly is a cause of interest as to its source.

At Skull Cave two approximately -1500 nT east-west parallel magnetically low anomalies, flank a ~1500+ high anomaly, as seen in Figure 2.4E. In Figures 2.2 and 2.3, it can clearly be seen that there is a collapsed pit just to the east of Skull Cave that is more than twice the width of Skull Cave and the other collapsed pits in this tube complex. This gives rise to the hypothesis that this location contained either a lava tube wider than the Skull Cave segment, or a second lava tube parallel to Skull Cave. If there was a second parallel lava tube, the northerly magnetically low anomaly may be the magnetic signature of an inaccessible lava tube parallel to Skull Cave.

To address this question, a simple model was created of two parallel lava tubes with surrounding magnetic susceptibility of 0.155. For this model, we duplicated the Skull Cave LiDAR survey to the north of its true location, at an offset of 40 m from the southern wall. This geometry separates the twin lava tubes with a wall thickness varying between approximately 15 m to 20 m. The results (Figure 2.9A) show a slight magnetic high between the twin lava tubes, with a negative magnetic anomaly above each tube. Additionally, there is a stronger magnetically high anomaly north of both lava tubes. The resulting magnetic gradient for this twin model, presented in Figure 2.9B, shows four distinct lines of minimal magnetic gradient, of which the southern three are similar to the three lines of minimal slope seen in the observed magnetic gradient in Figure 2.5B. Although not an exact match of the magnetic signature seen at Skull Cave, there are significant similarities, with the model's primary difference being the low amplitude of the positive magnetic anomaly between the two negative anomalies.

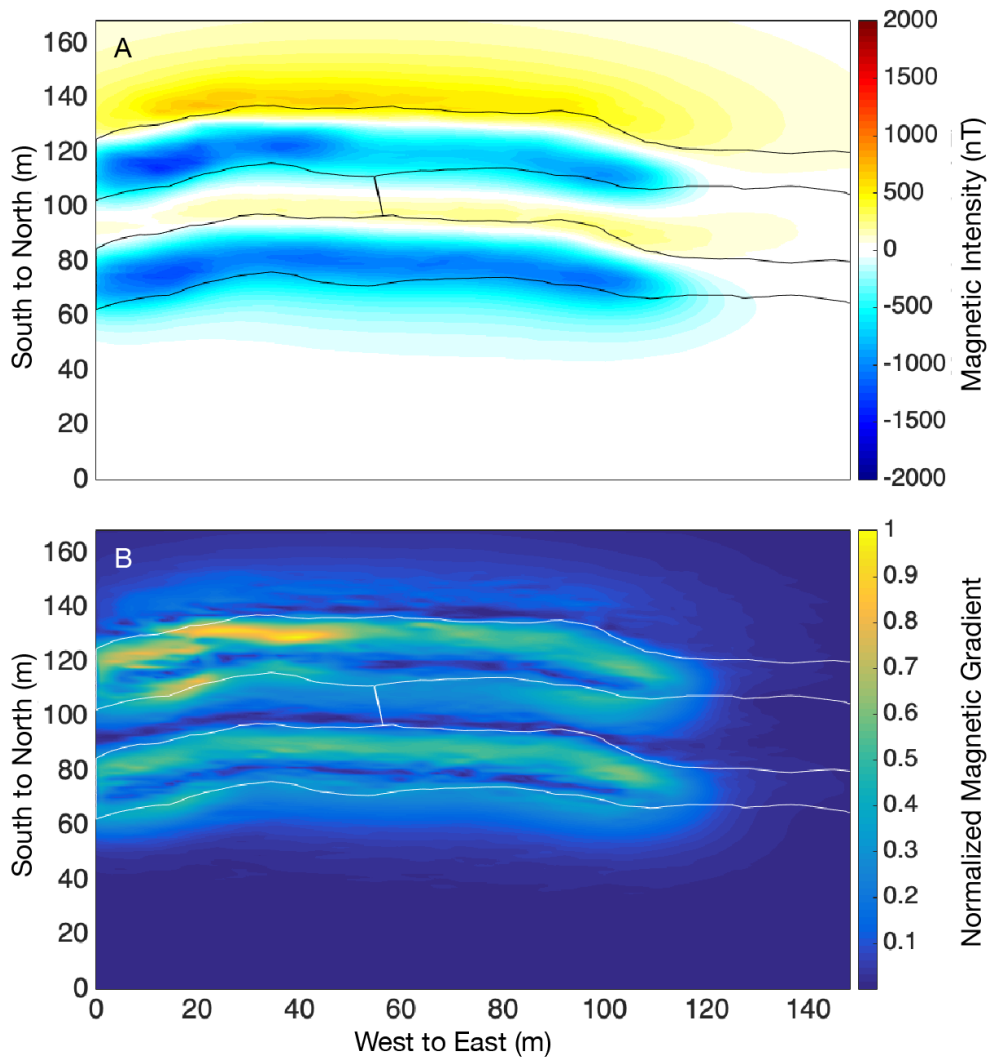


**Figure 2.9:** Magnetic anomalies and gradients for theoretical double tube models at Skull Cave location. Figure A: Plot of magnetic anomalies from application of magnetic susceptibility of 0.155. Figure B: Magnetic gradient plot normalized to the highest gradient (nT/m) calculated.

It is understood that magnetic modeling is a non-unique technique to analyze a potential field, and thus we cannot confirm the existence of a previously unknown, and inaccessible, parallel tube, of similar size, to Skull Cave. However, the negative magnetic anomaly north of Skull Cave coupled with the strong positive anomaly would suggest a complex history of formation at this location. This history may include a bifurcating branch parallel to Skull Cave, or additional thermal-magnetic or thermal-

chemical alterations to this segment of the Modoc Lava Tube System. (Garrick-Bethell & Weiss, 2010; Hemingway & Tikoo, 2018; Xu, Van der Voo, Peacor, & Beaubouef, 1997)

Future observations of this field site using additional geophysical techniques are warranted to aid in increasing the understanding of the formations in place. These analyses when combined with similar observations from other field sites have potential to offer new understanding into the lava flow processes and the extent to which lava tubes, and voids, exist within a lava flow.

### ***2.6.5 Implications for Lunar Lava Tubes***

There are several differences between the Moon and the terrestrial lunar analogs used in this study. For instance, the magnetic background variation found on the Moon's surface will need to be assessed at target study locations on the Moon, as the consistency and influence of the magnetic properties of the regolith covering the lunar surface are unknown on small high-resolution scales (1 to 10 meters) at the surface. Also, the impacts of the variations in strength and complexity throughout the evolution of the Moon's magnetic history during the period when possessed a magnetic field may have non-uniformly influenced the final remanent magnetism at various locations on the lunar surface during formations of lava tubes. Finally, the lack of a current lunar dipole magnetic field versus the ~50,000 nT Earth dipole results in a reliance on observations of these purely remanent magnetic signatures from the lunar surface to conduct analysis, versus Earth-based analysis which standardly assumes only induced magnetism.

Despite these differences, it is expected that the remanent magnetic signature of lunar lava flows can provide sufficient anomalies to detect candidate locations to search for lava tubes, as well as bound their internal geomorphology. For surveys conducted on the lunar surface, within 2 meters of the ground, magnetic anomalies are known to range from 5 to 313 nT from Apollo mission stationary and portable magnetometer observations, and surface-level anomalies are estimated to be  $> 500$  nT from Kaguya and Lunar Prospector observations (Dyal & Gordon, 1973; Tsunakawa, Takahashi, Shimizu, Shibuya, & Matsushima, 2015). Assuming a lunar lava tube magnetic anomaly is of the same relative order of magnitude with respect to the background variability as seen at Skull Cave (signal-to-noise ratio  $\sim 1.4$ ), the resulting magnetic anomaly would be in range of 10's to 100's of nT, which is well within the resolution capability of the current state of the art for magnetometers to resolve the lava tube structure. The biggest lunar lava tubes are theorized to be significantly larger, on the order of 100's to 1000's of meters in diameter, than their terrestrial counterparts (Blair et al., 2017). Thus, even ceilings as thick as 100 m would produce a ratio of lava tube apparent radius to ceiling thickness of one or greater, comparable to the 2.17 value for Skull Cave. The larger lunar dimensions will create lunar lava tube magnetic signatures with longer wavelengths relative to local background variability. Of the tubes studied here, Skull Cave, with its  $> 1$  ratio of apparent radius to ceiling thickness, is the best terrestrial analog for comparison to lunar lava tubes. With the addition of knowledge of the background magnetic variability on the Moon, added to the an understanding of the potential size and shape of lunar lava tubes, we can envelope the ability to detect the magnetic anomalies of lunar lava tube.

To develop lunar equivalent plots for magnetic anomaly verses lava tube geometric ratio as in Figures 2.7 and 2.8, we must convert the use of induced magnetism used in equation 8, to using the remanent magnetic property of the lunar basalt. To do this we begin with the equation of the total magnetic strength,  $j_T$ , being the summation of the induced magnetism,  $j_{oI}$ , and the remanent magnetism,  $j_{oR}$ , equation 9. For the terrestrial analysis of LBNM, we assumed that the remanent magnetism portion was zero and

$$j_T = j_{oI} + j_{oR} \quad (9)$$

calculated an apparent magnetic susceptibility. This apparent susceptibility accounted for both the induced as well as remanent portion, which cannot be separated without additional sample testing for the actual remanent magnetic properties of the basalt in the field site. Magnetic analysis is commonly combined in this fashion for terrestrial applications. In this equation, the induced magnetic strength,  $j_{oI}$ , is related to the magnetic susceptibility and the strength of the Earth's magnetic field at the location of interest, as seen in equation 10.

$$j_{oI} = \frac{k T_o 10^{-9}}{4\pi 10^{-7}} \quad (10)$$

If we assume that there is only remanent magnetism, as on the Moon, we can determine a relationship between the magnetic anomaly and the geometric ratio of cross-sectional area to depth to tube center similar to Equation 8, based on this remanent magnetic property. For this, we first set  $j_{oI} = j_{oR}$  then solve for the magnetic susceptibility,  $k$ . We then substitute the result into equation 8 and solve for the slope of the relationship of the magnetic anomaly to geometric ratio, equation 11. Known lunar

remanent magnetic properties can then be included as  $j_{oR}$  in equation 11, in lieu of the equivalent susceptibility used for the earlier terrestrial analysis.

$$\frac{\delta(\Delta F)}{\delta\left(\frac{A}{(t+r)^2}\right)} (\text{lunar equivalent}) = \frac{j_{oR}C_1}{T_o 10^{-2}} \quad (11)$$

From this relationship, we plot lunar equivalent magnetic anomaly versus lava tube geometric ratio, shown in Figure 2.10. We show lines for several assumed remanent magnetic strengths to attempt to bound the magnitude of the magnetic anomalies that may be observed on the lunar surface. The four lines represent remanent magnetism ( $j_{oR}$ ) of: 1) A minimum natural remanent magnetism of  $2.51e^{-5} \text{ Am}^2 \text{ kg}^{-1}$ , based on a study of the Apollo lunar basalt samples by (Cournède, Gattacceca, & Rochette, 2012), which equates to a remanent magnetic strength of 0.0788 A/m assuming a basaltic density of  $3140 \text{ kg m}^{-3}$  (Kiefer, Macke, Britt, Irving, & Consolmagno, 2012). 2 & 3) An estimated remanent magnetism at a lunar swirl region bounded by possible remanent magnetic strengths of 0.5 and 2.0 A/m (Hemingway & Tikoo, 2018). This range spans the possible remanent magnetic intensities that would provide the required magnetic strength to produce the anomalous optical lunar markings that are known as lunar swirls. 4) A natural remanent magnetism of 8 A/m representing an average terrestrial basalt sample based on the mean remanent magnetization of the Etnean lava flows of 1910 and 1950 (Negro & Ferrucci, 1998).

From Figure 2.10 we estimate the potential strength of a magnetic anomaly produced by a theoretical lunar lava tube. For this example, we extend the known dimensions of the ceiling thickness and void height at the Marius Hills Hole (MHH) collapsed pit (Figure 2.1C) into a lava tube of oval geometry with a width to height ratio of 2:1. Data from LRO shows the depth of this pit from the lunar surface is between 80 m to 88 m, and has an original ceiling thickness of at least 40 m (Haruyama

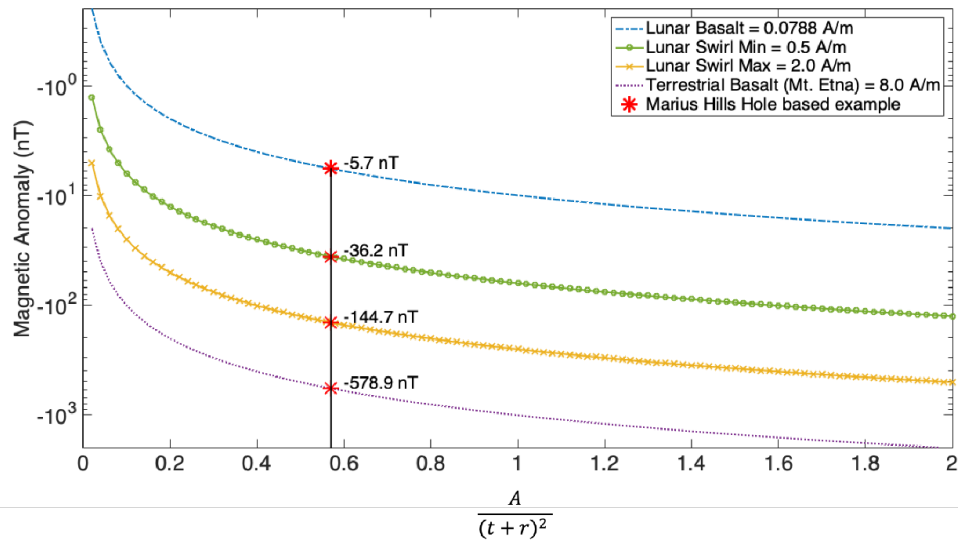


**Figure 2.10:** Plot of theoretical lava tube magnetic anomaly strength versus the geometric ratio for lava tubes based on remanent magnetic properties, simulating lunar equivalent lava tube signatures. The four lines represent: 1) the lowest anticipated remanent magnetic anomalies based on remanent strength of Apollo samples (dashed blue line); 2) lower bound for lunar swirl required magnetic strength (green circle line); 3) upper bound for lunar swirl required magnetic strength (yellow cross-hatched line); and 4) terrestrial equivalent remanent magnetic strength sampled from Mount Etan, Italy (purple dotted line). The Marius Hills example based on known ceiling thickness and depth to floor at the Marius Hills Hole, with assumed oval lava tube cross-section with 2 to 1 ratio of width to height resulting in a geometric ratio of 0.57 is plotted crossing each of these lines at red asterisk.

et al., 2009; Robinson et al., 2012; Wagner & Robinson, 2014). Assuming a ceiling thickness,  $t$ , of 40 m, a lava tube height of 44 m, and a width of 88 m results in an apparent radius (Equation 6) to ceiling thickness ratio of 0.75 and a geometric ratio of

$\frac{A}{(t+r)^2} = 0.57$ , which are between those for Ship and Skull caves in LBNM. Assuming

this geometric ratio, from Figure 2.10 the resulting lunar magnetic anomaly would be

approximately -5.7 nT in a low lunar remanent magnetism region, -36 to -145 nT in a lunar swirl area, or as high as -579 nT in a region with remanent magnetism similar to terrestrial basalt. Even the minimum 5.7 nT is observable via lunar surface magnetic surveys using today's technology. Therefore, assuming a magnetic background variability that is below the strength of the lava tube anomaly, the results can be applied to estimating the actual geometry of a lunar lava tube.

## **2.7 Conclusions**

We have shown that where the magnetic anomaly produced by a lava tube is above the magnetic background variation, or noise, the maximum negative magnetic anomaly produced by a lava tube follows the magnetic signature produced by a simple cylindrical model. For LBNM, these anomalies were detectable for lava tubes with larger apparent radii with shallower ceiling depths. With this model the magnetic minimum can be related to a non-dimensional geometric ratio that is based on the depth and cross-sectional dimensions of the lava tube. This model was validated using 3-dimensional LiDAR maps of lava tubes in LBNM.

The magnetic gradients produced at lava tubes in a high magnetic signal to background variation environment are shown to reveal the perimeter of lava tubes with large magnetic gradients, as seen at Skull Cave in LBNM. Use of this gradient analysis can constrain the width of a lava tube and, when coupled with the geometric ratio from the anomaly analysis, further constrain the dimensions of a lava tube. The gradient analysis may also be used to illuminate undiscovered lava tubes.

Finally, even with the lack of a current lunar dipole field, residual remanent magnetism could provide a way to detect lava tubes on the Moon. The magnetic

anomaly to geometric ratio model can be generalized to the Moon to predict the magnetic anomaly of a lunar lava tube, provided independent constraints on the geometry such as ceiling thickness, and magnetic properties. These methods have the potential to aid in the prospecting and evaluation of lunar lava tubes for the most desirable targets to continue additional robotic or human scientific investigation or for human utilization.

## **2.8 Acknowledgments**

This work was performed in coordination with the NASA TubeX team whose research investigating field technologies and strategies for lava tube exploration is supported by NASA PSTAR grant NNX16AK11G and the Goddard Instrument Field Team. Additional support was provided by the NASA PSTAR grant NNX15AL87G supporting geophysical analog studies.

Additionally, the authors would like to thank the staff and park rangers, including Randall Paylor, name and Katrina Smith, of Lava Beds National Monument, CA, USA for their support, expertise, and providing guidance and access to the lava tubes studied.

Also, many thanks to Patrick Whelley, Brent Garry, Kelsey Young, Jacob Richardson and Sarah Kruse, Sanaz Esmacili, and Sajad Jazayeri for a variety of items including collecting and processing the LiDAR data used in this study, as well as suggestions on the magnetic analysis.

### **3 Seismic Refraction Study Within the San Francisco Volcanic Field as an Analog Comparison to Apollo 17 Lunar Seismic Profiling Experiment**

#### **3.1 Abstract**

Terrestrial analog locations, such as the San Francisco Volcanic Field (SFVF), are used to refine geophysical field methods, data analysis, and interpretation of investigations of near-surface features on the Moon. Active source seismic experiments performed by Apollo astronauts were used to determine lunar tectonic and volcanic structure at depth. Terrestrial geophysical analogs are useful for understanding the Apollo results, and for improving the quality of future mission work. Here, we use seismic refraction at our study site in the San Francisco Volcanic Field (SFVF), a lunar tectonic and volcanic analog terrane, to identify subsurface continuation of locally mapped faults beneath the lava flows and cinder deposits to examine their association to cinder cone volcanic vent chains. We used 1-km long lines perpendicular to the strike of suspected faults to attempt to determine the geometry of faulting and if it continues beneath the volcanic deposits. Seismic lines were positioned on opposite sides of two cinder cone vents. However, our analysis was unable to detect vertical displacement of the stratigraphic layers that match the local fault strike due to the rapid attenuation of power across the source frequency range, resulting in the inability to analyze sufficient depth and details of the seismic layers to positively resolve the continuation of faults. Nevertheless, we were able to characterize the power spectral density relative to the Earth background noise models along with using the power spectral density from a single shot location at the center of a nodal line to display the decrease of body wave energy with distance. We then re-examined the Apollo 17 Lunar Seismic Profiling

Experiment (LSPE) data using the same methods, which shows that our results are consistent with previous studies. Finally, we analyzed an Apollo LSPE equivalent SFVF degraded data set. The results show a less robust model, resulting in insights into the subsurface imaging potential from a SFVF equivalent array in the Taurus-Littrow Valley.

## ***3.2 Introduction and Background***

### ***3.2.1 Volcanic fields as Lunar Analogs***

Terrestrial volcanic fields are used as scientific and operational analogs for the geophysical studies of features similar to those that have been, and will be, examined on the Moon. These terrestrial analog locations provide structures with geophysical and geologic properties that can be related to the basaltic volcanic environment of the Moon (Bell et al., 2018; Bleacher et al., 2015; Esmaeili et al., 2020; Garry & Bleacher, 2011; L veill , 2010). As analogs, they afford the ability to collect and analyze data similar to that expected from the same types of tests on the lunar surface, such as accomplished during the Apollo missions. For the Apollo missions, crews used terrestrial lunar analog locations to train on geologic observations, rock sampling protocols, and geophysical tests they would perform during their missions (National Aeronautics and Space Administration, 1969a; National Aeronautics and Space Administration, 1970; National Aeronautics and Space Administration, 1971a; National Aeronautics and Space Administration, 1972b). The geophysical training included preparation for conducting the active seismic experiments such as those included on Apollo 14, Apollo 16, and Apollo 17 (National Aeronautics and Space Administration, 1971a, p. 14;

National Aeronautics and Space Administration, 1972b, p. 16; National Aeronautics and Space Administration, 1973a).

For future lunar exploration missions, the proper experiment design based on the understanding of the geophysical characteristics of the near surface will be key to successfully executing lunar surface science operations and completing the subsequent data analysis similar to the accomplishments of the Apollo geologic research (National Aeronautics and Space Administration, 1971a, p. 14; National Aeronautics and Space Administration, 1972b, p. 16; National Aeronautics and Space Administration, 1973a). For example, the results of the Apollo active seismic studies provided data on the internal structure down to a depth of 460 m from Apollo 14, the thickness of regolith from Apollo 16, and a near-surface 1-dimensional seismic velocity structure of the Taurus-Littrow Valley (TLV) in the upper 2000 m from the Apollo 17 Lunar Seismic Profiling Experiment (LSPE) (Cooper, Kovach, & Watkins, 1974; National Aeronautics and Space Administration, 1971b; National Aeronautics and Space Administration, 1972c; National Aeronautics and Space Administration, 1973c). The probability of success of future lunar surface geophysical fieldwork can be improved by analog geophysical studies using the active seismic data collected within the San Francisco Volcanic Field (SFVF), AZ region adjacent to the SP Crater cinder cone.

The SFVF have been used in the past for the refinement of field techniques, data analysis methods, and interpretation of results for the exploration of similar locations on the lunar surface. Specifically for human spaceflight the SFVF was used as a geologic analog to the Moon for training Apollo crews in the 1960s and 70s (Lofgren et al., 2011; Ross et al., 2013). In 2010 the SFVF was the site of the NASA Desert Research and Technology Studies (RATS) campaign, simulating a multi-week human

lunar rover mission. Our specific fieldsite, shown in Figure 3.1A, constitutes a significant portion of the rover traverses and science stations from that simulation (Hörz et al., 2013).

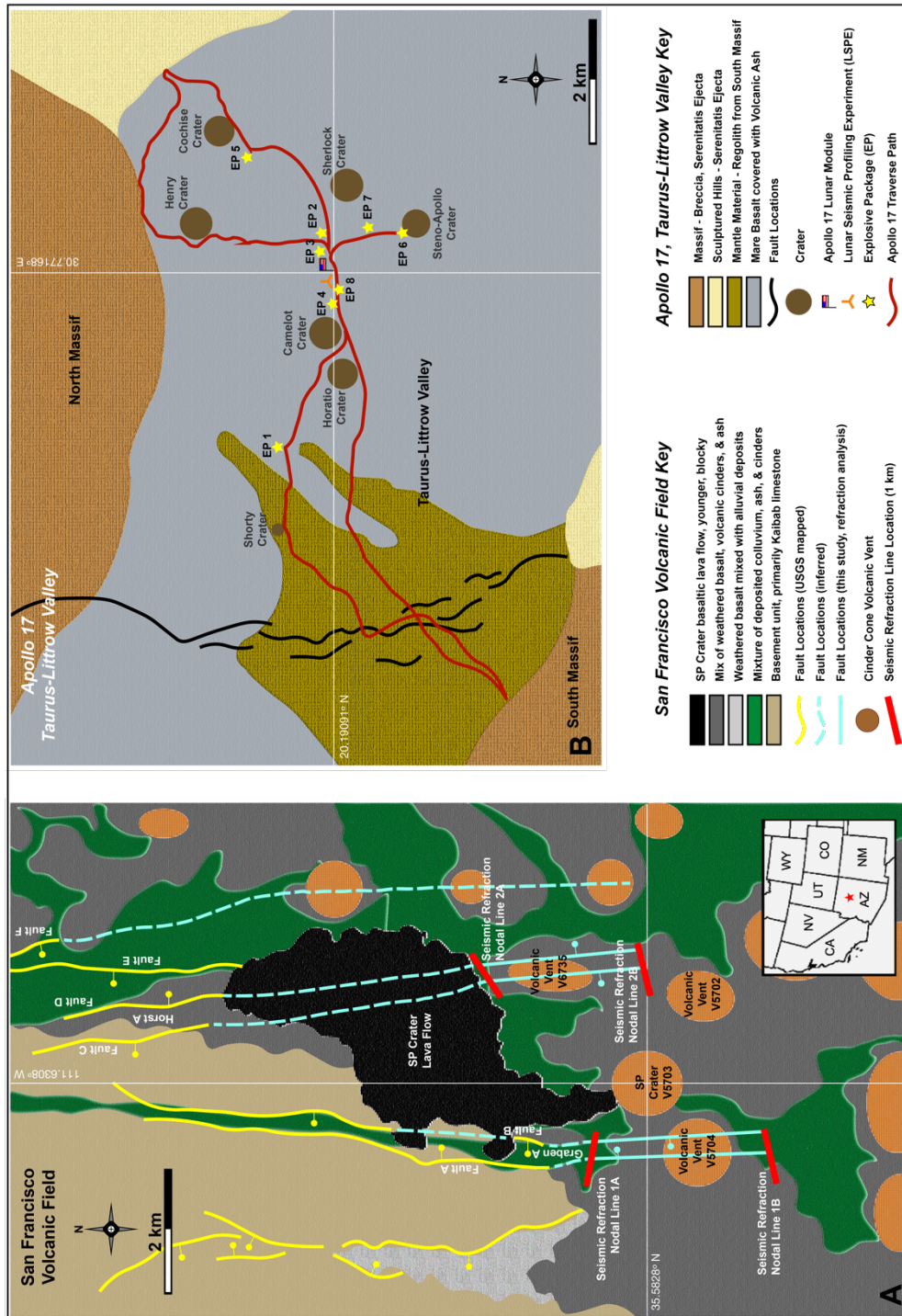


**Figure 3.1:** A) Aerial overview of the SFVF fieldsite showing locations of our seismic refraction nodal lines in relation to volcanic cinder cone vents, known and inferred local faults, and major geologic units (adopted from Billingsley et al. (2007)). B) Aerial overview of the Apollo 17 mission site and LSPE hardware in relation to major geologic units and features within the Taurus-Littrow Valley (Haase et al., 2018; Wolfe & Scott, 1977).

### ***3.2.2 Geology of the SFVF***

#### **3.2.2.1 Geologic Setting of the SFVF**

The SFVF is located at an ~2 km elevation, in the western United States, on the Colorado Plateau province, a physiographic region located within the current borders of Utah, Colorado, New Mexico, and Arizona (Pederson & Mackley, 2002). The Colorado Plateau is characterized by the classic Grand Canyon Sequence, consisting of a basement of Precambrian metamorphic rocks with a network of later-emplaced igneous intrusions. That crystalline basement is overlain by a thick sequence of Paleozoic and Mesozoic Era tropical sea sediments (limestone, sandstone, siltstone, and shales), subaerial deposits from streams and sand dunes (Flowers, 2010), and multiple unconformities. The Colorado Plateau was uplifted to its current elevation during late Cretaceous to mid-Tertiary period, with the exact timing and mechanism of uplift a matter of significant discussion (Bird, 1979; Thompson & Zoback, 1979; Morgan & Swanberg, 1985; Parsons & McCarthy, 1995; Spencer, 1996; McQuarrie & Chase, 2000; Moucha et al., 2008; Moucha et al., 2009; Roy, Jordan, & Pederson, 2009; Liu & Gurnis, 2010; Crow et al., 2011; Levander et al., 2011; Liu et al., 2011; Porter et al., 2017). Mechanisms that are hypothesized to have driven this uplift includes continental delamination (Bird, 1979), a thickened crust from mid-crustal flow (McQuarrie & Chase, 2000), heating of the lithosphere beneath the region (Roy et al., 2009), mantle convection at the plateau boundaries (Sine et al., 2008; van Wijk et al., 2010; Crow et al., 2011), and the addition of volatiles in the in the lithosphere (Humphreys et al., 2003; Jones, Mahan, Butcher, Levandowski, & Farmer, 2015; Porter et al., 2017). Flowers (2010), presents a review of these hypothesis, including the possibility of combinations of these mechanisms.

During the uplift of the Colorado Plateau, faulting in the region produced three regional fault systems in the SFVF; the Cataract Creek system running to the northwest, and the Mesa Butte system running to the northeast, which are shown in Figure 2 in Brumbaugh (2012); along with the Bright Angel fault system that lies to the northwest of the SFVF. The intersection of the Cataract Creek and Mesa Butte faults, approximately 26 km south-southwest of our field site, provides a focal point for both recent volcanic and seismic activity, and was the site of the 2009 earthquake swarm near Sunset Crater, located approximately 26 km south-southwest of our field site (Brumbaugh, Hodge, Linville, & Cohen, 2014). Analysis of this swarm activity concluded that it was likely a resultant of mid-to-lower crustal magmatic dike intrusion beneath the SFVF inflating in parallel to the northeast trending Mesa Butte Fault system (Brumbaugh et al., 2014).

Beginning in the mid-Tertiary period volcanic fields formed at the margins of the Colorado Plateau, with the interior of the plateau experiencing only low volume volcanic activity during this same period. This corresponds to the ignimbrite flareup that resulted from the rollback of the Farallon slab during the end of the Laramide orogeny. The three largest volcanic fields are the San Juan/Southern Rocky Mountain Volcanic Field (SJVF), the Mogollon-Datil Volcanic Field (MDVF), and the Marysvale Volcanic Field (MVF) (Dickinson, 2002; Humphreys, 1995; McQuarrie & Oskin, 2010; Nelson, Davidson, & Sullivan, 1992). The SFVF, on the southern margin, has the most recent volcanism on the Colorado Plateau. It was formed from predominately basaltic rock during the late-Tertiary and Quaternary periods (beginning in the late Miocene, ~6 Mya), approximately the last 6 to 8 million years ago (Mickus & Durrani, 1996). Stratigraphic K-Ar and  $^{40}\text{Ar}$ - $^{39}\text{Ar}$  dating has shown that this area

has been volcanically active for the past 780 kA, with volcanic events approximately every 15 kA (Conway et al., 1998). The most likely source for the basaltic magmas found in the SFVF is from mantle melt at the base of the lithosphere, while the limited rhyolitic and intermediate composition magmas of San Francisco Mountain is likely from crystal fractionation (Tanaka et al., 1986). The SFVF includes an area of approximately 4,800 square kilometers, containing over 600 volcanic vents, cinder cones, maars, and related lava flows (Tanaka et al., 1986). The basaltic cinder cones contained within the SFVF study region are associated with the San Francisco Mountain stratovolcano, which includes Humphrey's Peak. It has been previously noted that throughout the SFVF there is an apparent trend of cinder cone volcanic vents aligning with visually identifiable local faults associated with the primary fault systems of Cataract Creek and Mesa Butte (Conway et al., 1997; Tanaka et al., 1986).

Tanaka et al. (1986), used the remanent magnetism within over 600 samples from the SFVF, to show that volcanic activity within the SFVF has been steadily migrating in a north-eastern and eastern direction, with younger volcanism to the east. This north to north-east trend of movement in formation and reduction in age may be due to the relative movement of the North American plate, but has alternatively been associated with the progression of magma along the Mesa Butte fault system that trends in the same general direction (Tanaka et al., 1986). The movement of the centroid of the SFVF is broken down into two steps: 1) from roughly 5 Ma to 2.5 Ma, movement was in a northeastward direction, at a rate of approximately 1.2 cm/year; 2) at roughly 2.5 Ma, the direction of motion became mainly eastward, with the rate more than doubling to approximately 2.9 cm/year. During this same timeframe, the annual magma production increased nearly 20-fold, from approximately  $75 \times 10^{-6} \text{ km}^3/\text{year}$  to  $1,400 \times$

$10^{-6}$  km<sup>3</sup>/year, with a corresponding increase in the rate of basaltic eruptions. In the past 250,000 years the eruption rate has reduced to approximately  $180 \times 10^{-6}$  km<sup>3</sup>/year.

The SFVF volcanism is attributed to viscous heating due to shearing at the lithospheric base from the stress of asthenospheric flow, although the possibility of multiple heat sources cannot be completely dismissed (Tanaka et al., 1986). The necessary shear stress to cause this viscous heating is likely a result of an inhomogeneous “bump”, of roughly 35 km north to south, by 25 km west to east, at the base this interface (Tanaka et al., 1986). Beneath the SFVF a 6 km wide seismically low-velocity zone has been found in the mid-to-lower crust, at a depth of approximately 9 km to 34 km below sea level (Stauber, 1982), with a seismically high-velocity zone also located above, at an elevation of around 3 km below sea level (Durrani et al., 1999).

As stated earlier, within the SFVF there are three primary regional fault systems, the Cataract Creek system running to the northwest, and the Bright Angel and Mesa Butte systems running to the northeast (Brumbaugh et al., 2014). However, within our field site, the visually apparent local faults run in a generally north-south direction. These faults, and their suspected continuations are mapped in Figure 3.1A. The faults seen to the north of SP lava flow disappear to the south at the flow boundary. The faults on the west side of SP lava flow align to form a graben that drops approximately 14 m to 40 m in elevation dependent on location along the graben generating faults. These faults are suspected to continue south under an older basaltic lava flow which contacts the Kaibab limestone containing this graben feature at its northern extent. A cross-section of this graben feature, infilled by basalt is depicted in Figure 3.2A, representing the location beneath our seismic nodal line 1A, north of volcanic vent V5704. It is

hypothesized that these local faults continue south beneath the overlaying lava flows and that there is a likely correlation between the alignment and positions of the cinder cone vents and the locations of these local fault systems. These faults could have provided a pathway which aided in controlling the magmatic propagation to the surface.

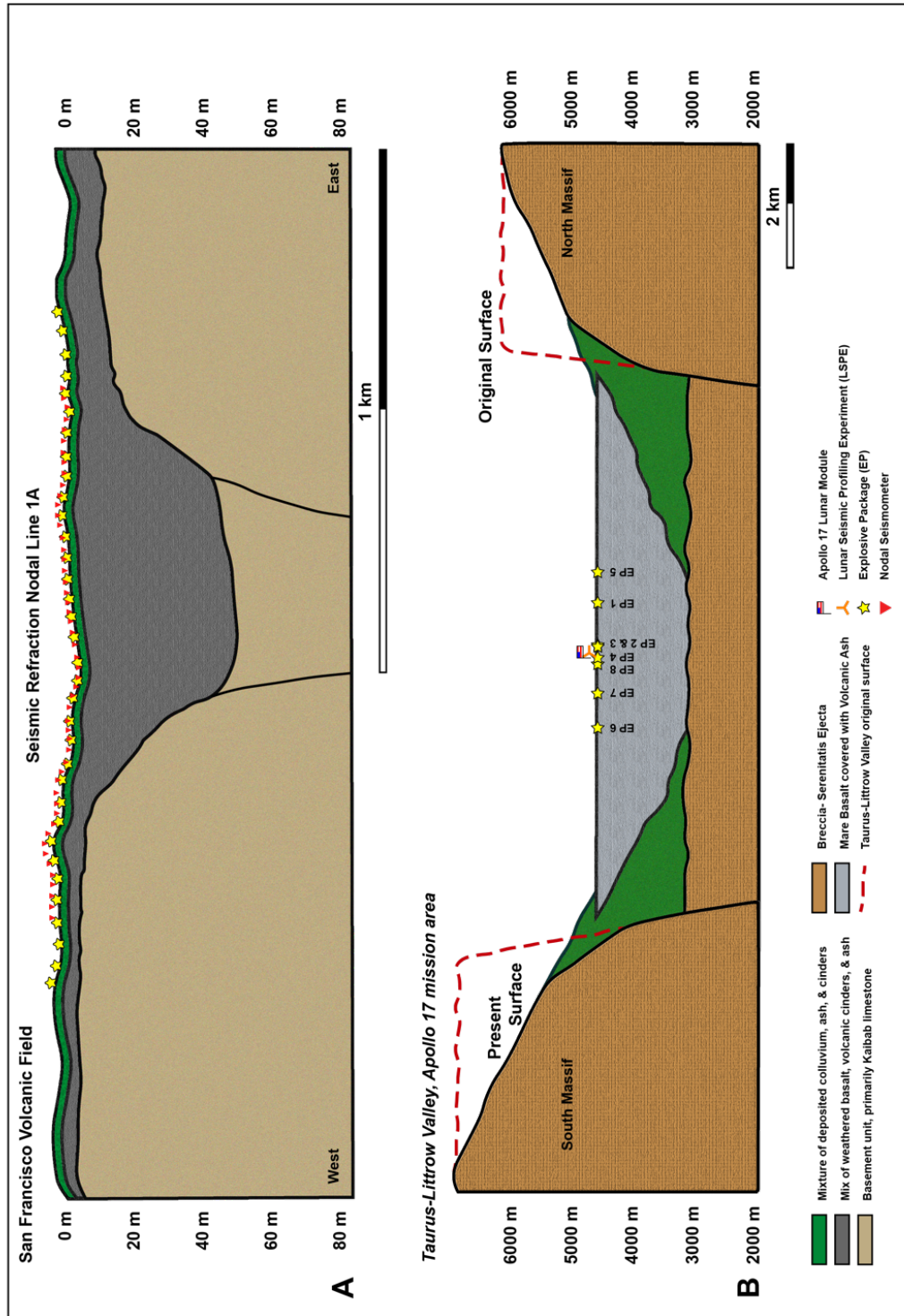


**Figure 3.2:** A) Notional cross-section beneath seismic refraction nodal line 1A showing subsurface graben feature based on this study's seismic refraction analysis. B) Inferred cross-section of major sub-regolith units of the Taurus-Littrow Valley (TLV) showing in-filled graben feature with relative positions of Apollo 17 landing site and LSPE hardware looking west. TLV cross-section adapted from illustration by Wolfe, et al. (1975) and modified.

### **3.2.2.2 Monogenetic Cinder Cone Field Vent Alignment of SFVF**

Tanaka et al. (1986), noted there is an apparent visual alignment between the cinder cone vents and known local faults within the SFVF. This connection is detected in other cinder cone fields as well, such as in Jorullo and Parícutin, Mexico, (Cebriá et al., 2011; Connor, 1987, 1990), the cinder cones of the Tolbachick, Russia volcanic complex (Valentine & Connor, 2015), Paiute Ridge, NV (Valentine & Krogh, 2006), at the R-K fissure eruption in North Iceland (Reynolds et al., 2016), East Grants Ridge, NM (Keating et al., 2008), as well as the Springville Volcanic Field, AZ (Connor et al., 1992). Le Corvec, Spörli, Rowland, & Lindsay (2013) completed an analysis of the spatial distribution and alignment of vent locations in 37 monogenetic volcanic fields. Their work found that in all but one field there were preferential alignment headings. These headings are due to either pre-existing faults, tectonic stress level, and magma pressure, or a combination of these factors (Le Corvec et al., 2013). It has been noted that vent locations can be oriented along the regional axis of compression, normal to the axis of least stress (Cebriá et al., 2011). However, vent alignment orientation can also be a result of magma ascent controlled by activation of older near-surface fractures, versus the direction of principal stress, for low magma flux fields (Valentine & Gregg, 2008).

Within the SFVF it has been noted that the cinder cone vents generally align parallel to visual surface expressions of either local or regional fault systems (Connor et al., 1992; Conway et al., 1997). These alignments within the SFVF do not necessarily correlate with the primary fault systems of Cataract Creek, Bright Angel, and Mesa Butte systems, which agrees with the findings by Le Corvec et al., (2013) of multiple

preferred alignment headings. The orientations include a group of nine vents aligning with the Mesa Butte fault line scarp from the southwest to the northeast, and three vents forming a parallel alignment approximately 1 kilometer to the northwest (Conway et al., 1997). The group of three vents is suggested to be the result of a dike propagation, channeled by the local fault system (Conway et al., 1997). The alignment of vent positions to possible local fault locations within these volcanic fields has been attributed to the local faults and fractures providing a more efficient near-surface pathway over the perpendicular axis to the least principle stress through which a propagating dike would have been ascending to that point (Valentine & Connor, 2015).

### ***3.2.3 Taurus-Littrow Valley & Apollo 17***

#### **3.2.3.1 Geologic Setting of Taurus-Littrow Valley, Apollo 17 Mission Site**

The TLV is one location on the Moon for which terrestrial locations such as the SFVF provide a geologic analog. The TLV was the landing site for the Apollo 17 mission. The Apollo 17 mission was the final manned mission to the lunar surface of the Apollo program. The mission landed in the TLV on December 11, 1972 for three days of operations, including 22 hour of surface extravehicular activity (EVA) exploration ((Schmitt, 1973)). The TLV mission landing site was located at the southeastern edge of Mare Serenitatis, located at 20 10' North and 30 46' East (National Aeronautics and Space Administration, 1973a).

The TLV provided the Apollo 17 crew access to the massifs of the North and South Taurus Mountains consisting of anorthositic highland material, along with the TLV filled with mare basalts, (Cooper et al., 1974) shown in Figure 3.1B. The massifs are a part of the ejecta deposits of the southern rim of the 740 km diameter Mare Serenitatis

mascon basin formation (Schmitt et al., 2017; Wolfe et al., 1981). Defining the TLV to the west is the Lee-Lincoln scarp, which is a thrust fault formed after the initial flooding of the valley as a result of the thermal contraction of the Moon combined with tidal effects from the Earth (Schmitt et al., 2017; Watters et al., 2010). To the east of the TLV are located the Sculptured Hills, which also extend up and around the north side of the North Massif. The Sculptured Hills were likely formed from Imbrium Basin ejecta after the formation of the TLV by the valley graben faulting (Schmitt et al., 2017; Spudis, Wilhelms, & Robinson, 2011). Within the Sculptured Hills are black ash fissures that indicate volatile-rich late pyroclastic eruptions from magma diverted to this area from the basaltic filled TLV (Schmitt et al., 2017). The TLV itself is a large graben feature, that has extended radially out from Mare Serenitatis, and was flooded to a depth of approximately 1400 m by basaltic lava flows from mare volcanism. The basaltic infill of the TLV ended approximately 3.7 Ga, after which pyroclastic glass beads were deposited across the valley floor. The initial graben valley was likely produced during the formation of the southern Serenitatis Basin, with a cross-section bounded by fault planes that were significantly steeper than the current sloping massifs (Wolfe et al., 1981). These steep sided faces collapsed into the graben valley, forming wedges of colluvium relatively early in the evolution of this region (Wolfe et al., 1981; Wolfe et al., 1975). A basaltic flow then filled the valley floor up the extents of the colluvium wedges (Wolfe et al., 1981; Wolfe et al., 1975). A cross-section of the Taurus-Littrow Valley, adapted from Wolfe et al. (1975) with the Apollo 17 landing site and LSPE hardware added, is shown in Figure 3.2B.

### 3.2.3.2 Apollo 17, Lunar Seismic Profiling Experiment

Prior to the arrival of the Apollo 17 crew, it was anticipated that potential sampling of basaltic rocks younger than 3.2 billion years in age would help to extend the understanding of the volcanic and thermal history of the Moon (National Aeronautics and Space Administration, 1973b). Additionally, the site was expected to potentially provided access within the TLV basin to some of the oldest non-metamorphosed lunar crust (Kirsten & Horn, 1974). From a geophysical perspective, the TLV provided the opportunity to use active seismic refraction techniques to examine the upper 5 to 10 kilometers of the lunar crust, including resolving details of the upper 500 m, which had not been previously examined. At the time of the Apollo 17 mission it was unknown if the seismic velocity increased smoothly or in discreet steps within this near surface region (Kovach, Robert & Watkins, Joel, 1973a).

The Apollo 17 mission objectives included the deployment of the LSPE. The LSPE was an active seismic refraction experiment that consisted of four geophone receivers, with eight explosive packages (EP) and the LM ascent stage as active sources. The crew deployed the LSPE as part of the Apollo Lunar Surface Experiments Package (ALSEP) to gather seismic data to analyze the seismic velocity profile of the near sub-surface. Relative locations of the lunar module, LSPE geophone array, and the EPs are shown in Figure 3.1B. (Kovach, Robert & Watkins, Joel, 1973a)

The four geophones for this experiment were a coil-magnet type with a natural resonant frequency of 7.5 Hz. They were positioned in a Y-shaped array, within the geometry of an equilateral triangle of 100 m on a side (Kovach, Robert & Watkins, Joel, 1973a). The EPs were placed at various bearings, and distances from 95 m up to 2900 m from the geophones. The lunar module (LM) ascent stage liftoff occurred

approximately 148 m from the geophone array, and the later impact of the discarded LM ascent stage occurred approximately 8.7 km from the geophones. The EPs varied in explosive weight from 57 grams to 2722 grams, and were detonated remotely from Earth between December 15th and 18th, 1972 after the crew had departed the lunar surface. (Kovach, Robert & Watkins, Joel, 1973a)

The results of the experiment were used to determine the seismic velocity profile of the upper 5 to 10 kilometers of the lunar crust, including resolving details of the upper 500 m. One particular objective of the experiment was to determine if the seismic velocity increased smoothly or in discreet steps within this near surface region (Heffels et al., 2017; Kovach, Robert & Watkins, Joel, 1973a, 1973b). The results of the LSPE showed that the seismic P-wave velocity increases in a step function in the upper 2.5 km of the TLV surface. The initial LSPE active seismic refraction analysis resulted in three layers with velocities of 280 m/s, 1130 m/s and 4000 m/s having corresponding interface depths of 264 m and 1187 m (Kovach, Robert & Watkins, Joel, 1973b, 1973a; National Aeronautics and Space Administration, 1973c). Further analysis determined a more refined model consisting of seismic layers of rapidly increasing velocities of 100 m/s, 327 m/s 960 m/s, and 4700 m/s at interface depths of 4 m, 32 m, 390 m, and 1385 m (Cooper et al., 1974). This velocity structure is indicative of a model of basaltic lava flows of varying fracture and compaction covering deeper anorthositic breccias (Cooper et al., 1974).

### ***3.2.4 Active Seismic Exploration***

Seismic exploration is a geophysical technique that is used to probe the layers of the subsurface by recognizing the variations in seismic velocities between

geophysically different layers. It is routinely used to determine 1-D, 2-D, or 3-D variation in the sub-surface structure for scientific and commercial applications on Earth, however only 1-D studies have been conducted on the lunar surface. The use of active seismic refraction field methods and analysis is commonly used to determine the depth and structure of the relatively upper portion of the subsurface (Burger et al., 2006). In general, seismic refraction lines of three to four times the maximum targeted exploration depth are required (Burger et al., 2006), and can be an effective method for attaining subsurface data for analyzing stratigraphy, locating resources, determining the geologic history (Brenquier, Coutant, Baudon, Doré, & Dietrich, 2006; Durrani et al., 1999; Meglich et al., 2003; Montgomery et al., 2017; Nakamura, Latham, & Dorman, 1982; Negro & Ferrucci, 1998; Tien-when & Inderwiesen, 1994).

A specific example of active seismic exploration on Earth includes the use of refraction analysis to define fault locations of the San Andreas fault zone by Hole, Ryberg, Fuis, Bleibinhaus, & Sharma (2006). In this study the team performed a 46-kilometer long linear seismic survey across the San Andreas Fault that consisted of 912 seismometers (Hole et al., 2006). These seismometers were spaced at 50-meter intervals with the exception of 25-meter intervals at the San Andreas Fault. A total of 63 explosive, borehole placed, charges were fired along the seismic line as the active sources (Hole et al., 2006). Two institutions independently completed refraction analysis of the data that resulted in two consistent velocity models down to a depth of 4 to 6 kilometers, which verified the robustness of the analysis. Interpretation of the seismic velocity models provided clear indications of lateral and vertical velocity heterogeneity that corresponded well to the locations of known fault positions (Hole et al., 2006). Although of significantly larger scale than our study, but with similar station

spacing, their methods of using active seismic refraction analysis and the interpretation of lateral and vertical velocity changes over a fault is the same technique we employed within our study of the SFVF to explore the near-surface for indications of local near-surface faults.

For lunar examples, the Apollo missions conducted both passive and active seismic experiments. The primary passive seismic experiment (PSE) was the establishment of a four-station lunar seismic array in an equilateral triangle geometry with 1100 kilometer spacing between the vertexes. This array was created by placement of seismometers at the Apollo 12, Apollo 14, Apollo 15, and Apollo 16 landing sites (Latham et al., 1973). Results from the PSE included determining the 1-D seismic velocity profile down to approximately 1000 km (Nakamura et al., 1982). Deep and shallow moonquakes were also characterized, with deep quakes recorded primarily between 800 and 1000 kilometers depth. Shallow Moonquakes were found to occur much less frequently and were located in the upper mantle, below the 58 kilometer crust/mantle interface (Nakamura et al., 1982). Additionally, the PSE data has been used to determine the depth of the Moon's core, which was found to begin with a fluid outer core at a radius of 330 km, and a solid inner core with a radius of 240 km (Weber, Lin, Garnero, Williams, & Lognonne, 2011).

The active experiments included small scale geophone setups on the Apollo 14, Apollo 16, and Apollo 17 missions. During Apollo 14 and Apollo 16, the active seismic experiment (ASE) consisted of three geophones placed linearly at 45-meter intervals, with a crew activated thumper used as the active source (National Aeronautics and Space Administration, 1971b; National Aeronautics and Space Administration, 1972c). For Apollo 14, the results of this experiment showed a two-layer model with near-

surface regolith material having a seismic velocity of 104 m/s down to a depth of 8.5 m, followed by a layer with a seismic velocity of 299 m/s that has an estimated depth from 38 m to 76 m (National Aeronautics and Space Administration, 1971b). Apollo 16 similarly found a two-layer model consisting of a regolith layer at 114 m/s down to a depth of 12.2 m followed by a layer with a velocity of 250 m/s of unknown thickness (National Aeronautics and Space Administration, 1972b).

### ***3.2.5 SFVF Study as a Taurus-Littrow Valley / Apollo 17 Analog***

Our study is conducted on a portion of the SFVF that is an approximately 50 km<sup>2</sup> area surrounding the SP Crater cinder cone, Figure 3.1A. This area of the SFVF is characterized by numerous cinder cone volcanoes, lava flows, rilles, and faults (Tanaka et al., 1986). Our active seismic refraction experiment is designed to explore our hypothesis of the correlation between the linear alignment of monogenetic cinder cone vents and the local fault system in our SFVF study area, using standard “terrestrial-based” seismic refraction field deployment methodology and data collection methods. We specifically focus on the positions of monogenetic cinder cone vents V5704 and V6735 with suspected underlying north-south running local faults. For this, we analyze the seismic velocity structure of the upper two hundred meters of the subsurface along four 1000-meter-long nodal seismic refraction lines, indicated as red lines in Figure 3.1A, which were deployed perpendicular to the suspected fault locations.

The seismic refraction fieldwork and analysis we applied to this problem is directly analogous to the analysis of near-surface lunar seismic and geophysical field data. Specifically, we can compare this to the LSPE conducted during Apollo 17 with respect to understanding the potential structure that could be resolved by an active source

seismic refraction experiment designed to target the larger TLV area. Specifically, it could help understand the hypothesized faults at the boundaries at the North and South Massifs that form the conjectured TLV graben. Although this lunar graben is of significantly larger scale than the terrestrial SFVF analog north of cinder cone vent V5704, and a geophysical study of it was not the objective of the seismic refraction experiments of Apollo 17, it does provide comparative context. Additionally, by use of the SFVF V5704 location as an analog we can begin to examine the seismic array geometry, using wavelength equivalency, that would be required on the lunar surface to examine the TLV graben feature to study the extent and geometry of near surface faults on the Moon.

The field methods used on the lunar surface and analysis of the seismic data from the LSPE are directly relatable to our terrestrial investigation in the SFVF. There are two areas of comparison that we examine. The first of these is a straight-forward re-analysis of the Apollo 17 LSPE data based on the updated locations provided by Heffels et al. (2017), using both our one-dimensional and two-dimensional Bayesian seismic analysis code. The objective of this exercise is to compare our updated results against those from the Heffels et al. (2017) study and the original analysis by Cooper et al. (1974) to determine if our technique using the updated array positions extracted similar seismic layers from the data. Our results are then directly relatable to a comparable analysis using our SFVF data downgraded to an Apollo 17 LSPE equivalent spacing of receivers and sources based on wavelength equivalency, given the very different seismic velocities on terrestrial and lunar materials, and differences in attenuation properties. The comparison of the results between the full SFVF data set compared to the SFVF LSPE equivalent data set provides the ability to understand the qualitative

difference in structural resolution of features that could be obtained with the use of a SFVF scaled array in the TLV.

### **3.3 Experimental Arrangements and Execution**

#### ***3.3.1 SFVF Seismic Refraction Experiment***

To study the subsurface expression of local faults beneath the SFVF, we deployed an active source seismic refraction experiment over a series of ~1 km long seismometer lines. The experiment made use of 51 individual Fairfield Zland 3C Nodal seismometers from the University of Maryland instrument pool, and the Propelled Energy Generator (PEG), an accelerated kinetic energy transfer system as an active source, borrowed from the Portable Array Seismic Studies of the Continental Lithosphere (PASSCAL) Instrument Center. The goal of our study was to create a series of 2-D seismic refraction profiles (Fig. 1A) to determine the local fault existence and geometry beneath lava flows of the SFVF. Active source lines pairs, Pair 1 and Pair 2, were positioned in parallel on opposite sides of two separate cinder cone vents (V5704 and V6735) (Ulrich & Bailey, 1987). We used the surface expression of nearby faults, labelled Faults A thru F on Figure 3.1A, to orient the lines approximately perpendicular to the strike of suspected faults lying beneath the cinder cone vents and surrounding emplaced lava flows. Table 3.1 provides a summary of the two pairs of seismic nodal lines, including descriptions of the faults and surface geology.

		Seismic Nodal Line Pair 1		Seismic Nodal Line Pair 2	
Seismic Refraction Line	Designation	1A	1B	2A	2B
	<b>Western End</b> UTM zone 12N	440995.143 3938904.477	441212.756 3935732.747	444245.065 3940325.974	444277.436 3937774.253
	<b>Eastern End</b> UTM zone 12N	441975.003 3938713.076	442196.1 3935904.694	445075.348 3940882.438	445242.654 3938024.392
	<b>Duration Deployed</b>	23 hours	4 hours	24 hours	4 hours
	<b>Line Bearing (west to east)</b>	101°	77°	56°	75°
	<b>Relative Angle to Local Faults</b>	83°	107°	122°	103°
	<b>Surface Geology</b>	Primarily loose soil and scoria. W end amidst broken basalt. E end spans small projection of underlying basaltic flow.	Primarily unconsolidated scoria and sediment. W end crosses protrusion of underlying basaltic flow. E end sits within dry stream bed.	SW crosses portion of basaltic outcrop. NE contains wash of small cinders & sediment.	Sediment and scoria.
	<b>Associated Volcanic Vent</b>	V5704		V6735	
<b>Vent Geometry</b>	Approximately circular, 1500 m basal diameter, 180 m high cone, containing 3 designated vent locations. Rim is approximately 660 m north to south by 500 m west to east.		Elongated, 2000 m basal length north to south by 1000 m basal wide west to east, 170 m high fissure vent. Fissure rim is approximately 850 m north to south by 225 m west to east.		
<b>Vent Description</b>	Crater is approximately 60 m deep, and infilled with rim collapse, cinder, and ash.		Fissure crater is approximately 80 m deep, with large multi-meter sized blocks collapsed from the rim.		
<b>Associated Fault(s)</b>	Fault A & Fault B (Fig 1A)		Fault C & Fault D (Fig 1A)		
<b>Description of Associated Fault(s)</b>	Two normal faults, forming a graben formation.		Two normal faults, forming a horst formation.		
<b>Average Azimuth of Associated Local Faults</b>	184° (varies from 172° to 200°)		178° (varies from 162° to 187°)		

**Table 3.1:** Summary of select properties of nodal seismic lines, and associated volcanic vents and faults shown in Figure 3.1A. (Billingsley, Priest, & Felger, 2007; Ulrich & Bailey, 1987)

Each seismic line consisted of 51 individual Fairfield Zland 3C 5Hz Nodal seismometers (*ZSystems Zland 1C and 3C Node User Manual*, 2014), abbreviated here-on out as “nodes”, spaced every 20 m. Each node is a self-contained, three-component (X, Y, Z orthogonal axis) seismometer, with a GPS receiver for timing, and a battery and storage system capable of providing 30 days of power, and 30 days of stored seismic data at 2000 Hz (0.5 millisecond intervals) sampling rate. Nodes in each line were positioned by hand using a measuring tape and Brunton compass to orient the line. Instruments were firmly set into the local surface materials, but not buried. Every node was oriented with the y-axis of the unit pointing to true north using a handheld Brunton compass set to the local magnetic declination of 10° 30’, based on the International Geomagnetic Reference Field model for Flagstaff, AZ during October 2017. Four metallic spikes on the bottom of the node prevented the sensor from rotating readily and further coupled it into the ground. The exact locations of each node were recorded using a differential GPS unit. After deployment, the nodes were activated and continuous data recording commenced until we deactivated the nodes for removal. Data recording durations lasted from approximately 7 hours to 24 hours depending on if a line was completed within a single working day, or was split overnight across two days. This process was repeated for each of the lines in our study region (Figure 3.1A).

The PEG seismic active source for “shots” was installed on the trailer hitch of our 2½ ton field support vehicle and provided an active seismic source by using an electric motor to raise a 40 kg cylindrical mass up compressed against an elastomer band. The PEG seismic impact source radiates energy in the frequency range between 10 Hz and 250 Hz (R.T. Clark Geophysical Equipment Co., 2014). A single shot was completed when the cylindrical mass was released and accelerated by the elastomer band into a

½-inch thick, two-foot by two-foot, aluminum plate on a cleared area of the ground beneath the PEG. We removed any surface rocks or obstructions to prevent the plate from recoiling or bouncing after shots. The PEG was then activated several times to help firmly seat the plate onto the surface for good physical connectivity of the seismic energy into the ground. Timing of the source relative to the nodes was captured at an accuracy of 1  $\mu$ s using a GPS Synchronizer unit to activate a piezoelectric trigger attached to the metal plate and connected to the synchronizer. The PEG source was shot at 40-meter intervals along the line, beginning from 110 m prior to the first seismic node and continuing to 130 m after the final seismic node (Figure 3.2A). Shot sites within the node locations were always centered 10 m from each of the nearest two nodes. At each of the 32 source locations on a line, 10 individual shots were performed and then stacked during the analysis using the shot onset times provided by the GPS-Synchronizer (Bell et al., 2018). The location for each of these shot positions were also recorded via differential GPS. To mitigate any impact on the quality of the data from the noise of any vehicles passing on very infrequently used dirt roads in the area, we would cease collection of shot data until the vehicle could no longer be heard. Once shots were completed at all 32 shot locations, the nodes were deactivated and collected for re-use at the subsequent nodal lines.

### ***3.3.2 Nodal Seismic Lines Pair 1, Vent V5704***

The first pair of nodal seismic lines, labeled as Nodal Line 1A and Nodal Line 1B in Figure 3.1A, were situated on the west side of our study area to the north and south of cinder cone vent V5704. Cinder cone V5704 is approximately 200-meter-high, roughly 1500-meter diameter circular shaped cone, slightly elongated north to south, with three closely concentrated vent locations in a north-south alignment (Billingsley,

Priest, & Felger, 2007). On its northern flank there is a possible lava flow breakout and/or wall collapse. Two surface faults, designated as Fault A and Fault B, form Graben A which lies directly to the north of Line 1A (Figure 3.1A). Graben A runs primarily north-south, at a general azimuth of between 7 and 11 degrees from North and is observable north of V5704. Fault A has a vertical separation on the order of 40 m, while Fault B shows a vertical separation of as much as 14 m (Billingsley et al., 2007).

Nodal Line 1A was located on the north side of cinder cone crater V5704, which abuts the west side of SP Crater. The location of Nodal Line 1A was positioned to the south of Graben A and oriented to be perpendicular to its trend. The nodal line runs in a west to east direction at a heading of approximately 101 degrees. The line was deployed approximately parallel to an infrequently used nearby dirt road, which it crossed around the line's midpoint. The nodal seismometers were coupled into loose soil and scoria throughout most of line. However, the western extent of the nodal line lies amidst broken basalt and the eastern extent spans a projection of the underlying lava flow. The only surface vegetation along this line consisted of sparse grass and prickly pear cactus.

Nodal Line 1B was positioned on the south side of cinder cone crater V5704, approximately 3 km south of Line 1A, and perpendicular to the inferred continuation of Graben A. The nodal line was set approximately parallel and about 50 m north of a rarely used nearby dirt road. Again, we paused data collection when vehicles were present on the road. The nodal line crossed the road at both the western and eastern extents of the line. Line 1B was situated primarily west to east, at a heading of approximately 77 degrees. The majority of the line was set on relatively unconsolidated

scoria and/or sediment. The western extent of the line was set over a narrow section of basaltic lava flow with little vegetation, with the eastern extreme set through a sparsely vegetated dry stream bed or episodic dry pond. The central portion of the line was within a relatively open and accessible section of juniper bushes. During data collection, wind gusts were minimal, and the juniper bushes were not actively moving.

### ***3.3.3 Nodal Seismic Lines Pair 2, Vent V6735***

The second pair of nodal seismic lines, Nodal Line 2A and Nodal Line 2B, were deployed in the eastern portion of the study area in the vicinity fissure vent V6735, as designated on USGS geologic map MF-1956 (Ulrich & Bailey, 1987), and south of Fault C, Fault D, Fault E, and Fault F (Figure 3.1A). Vent V6735 is an approximately 170-meter-high, elongated cinder cone built up along a suspected fissure vent, extending north to south, that is approximately 2000-meter-long and 1000-meter-wide. Additionally, there is a more defined cone of slightly lower maximum elevation attached to the southern extent and in line with the fissure vent itself. This fissure vent V6735 is located to the northeast of SP Crater and just south of the majority of the SP lava flow which appears to cover the southern extent of horst feature, Horst A, created by Fault C and Fault D, and is visible extending from the north side of the SP lava flow. Both Faults C and D have a vertical separation of 9 m (Billingsley et al., 2007). Nodal Line 2A was deployed on the north side of fissure vent V6735, with Nodal Line 2B deployed on the south side of the vent, and both set approximately perpendicular to the strikes of Fault C, Fault D, Fault E, and Horst A.

Nodal Line 2A was positioned nearly parallel to a sporadically used nearby road that traverses the same general path between the SP lava flow and the northern extent

of the fissure location (Figure 3.1A). The nodal line was located along the south side of the road in a southwest to the northeast direction at a heading of 56 degrees. The surface geology consisted of the west portion of the line crossing over a portion of either a basaltic outcrop while the middle and east portions were set on a wash of small cinders, scoria, and sediment where the topography dips down in elevation several meters. Only sparse grass and mesquite bushes were present at the surface.

Nodal Line 2B was located to the south of fissure vent V6735. The nodal line was positioned near the northern ramparts of vent V5702, which lies about 2 km south of fissure vent V6735. The line was situated on sediment and scoria. Line 2B was approximately 2.75 km south of Line 2A, and crossed a road near its eastern end. The elevation of the eastern extent of the line drops approximately 40 m from the peak of the western half of the nodal line. This nodal line was positioned at a heading of approximately 75 degrees. The surface geology for this line consisted of a sediment and scoria mixture.

### ***3.4 Data Processing and Analysis Methods***

#### ***3.4.1 Dataset and Data Processing***

The raw data from the nodes totaled 56 hours of continuous recordings of the ground motion on all three axes at 2000 Hz sampling rate. We focused solely on the vertical z-axis for our P-wave refraction analysis. Processing was done in a series of steps that were applied uniformly across the dataset. The instrument response was removed from the data using the instrument parameters provided in Table 3.1 in Ringler, Anthony, Karplus, Holland, & Wilson (2018), and used to convert the recorded amplitude to velocity. We then used the GPS Synchronizer times obtained from the

PEG to clip out individual 1 second time windows, called traces, following the recorded trigger times of each shot. For each of the nodes this equaled 10 velocity traces from each shot location. This resulted in 16,320 individual traces for each of the four nodal lines, or a total dataset of 65,280 one-second duration seismic wave traces across all four nodal lines. The trace data were organized by node and shot location number for the next steps of processing. The 10 unfiltered velocity traces from each shot, at each node, were then stacked, and used to pick the first arrivals of the P-waves. The software package PickWin® was used to plot and pick the first arrival times of the P-waves at each node location. However, despite a 1000 m long seismic line, with only a few exceptions, the first arrival could only be picked out to a distance of approximately 110 to 130 meters from the source location. This was the case regardless as to if a frequency filter was applied or not, and can be seen in example shown in Figure 3.3. These first arrival times were then used in the refraction analysis, described in Section 3.4.3.

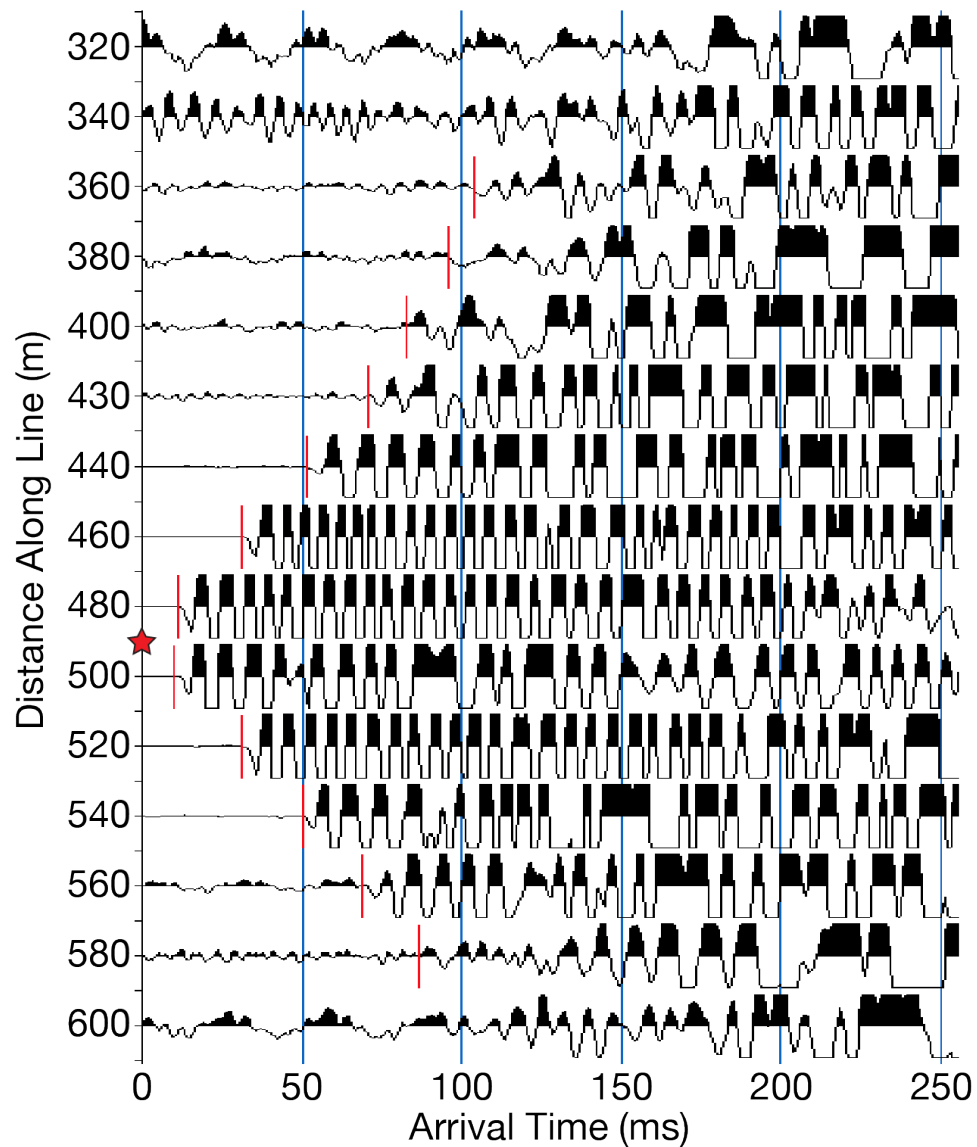


**Figure 3.3:** Example of typical seismic wave move out and first arrivals picks. Source located at 490 m, designated by red star. Receiver nodes located at each of the distances noted on y-axis. First arrival picks designated with vertical red lines. Note maximum pick distance from source to receiver was 130 m between 490 m (source) and 360 m (receiver) positions. Trace data amplitudes are normalized to maximum amplitude per trace, and clipped to prevent overlapping other traces. Trace data from nodes not shown shows only the background noise, and no perceptible source waves.

### ***3.4.2 Power Spectral Density Analysis***

Due to the lack of ability to select first arrival time picks beyond approximately 110 to 130 meters, an analysis of the power spectral density (PSD analysis) was completed. For this analysis, a five-minute period of data during an inactive timeframe was selected for analysis to evaluate the background noise. Data from nodal lines 1A and 2A (one nodal line per pair for which we had data available from a period without shots) were used for this analysis by means of the Matlab® multi-taper power spectral density estimate function, with the results shown in Figure 3.4, plot A. The earth background high noise and low noise models, which are available up to 10 Hz, are included as reference (Peterson, 1993). For these same lines (1A and 2A) a power spectral density estimate was then performed on the stacked data for 10 second clips from the data for all 51 nodes from a shot at the Shot 16 position located at 490 m along the nodal line to compare to the initial analysis of the inactive period. The results show the shot energy primarily between 10 and 200 Hz (Figure 3.4, plots B and D). This same data is then plotted in Figure 3.4 plots C and E to show the dispersion of the energy along the nodal lines, for the frequencies between 5 and 200 Hz, from the Shot 16 position. These plots show a rapid attenuation of the energy within the first +/- 100 to 150 meters which corresponds with the maximum distance for which first arrival picks were able to be obtained.

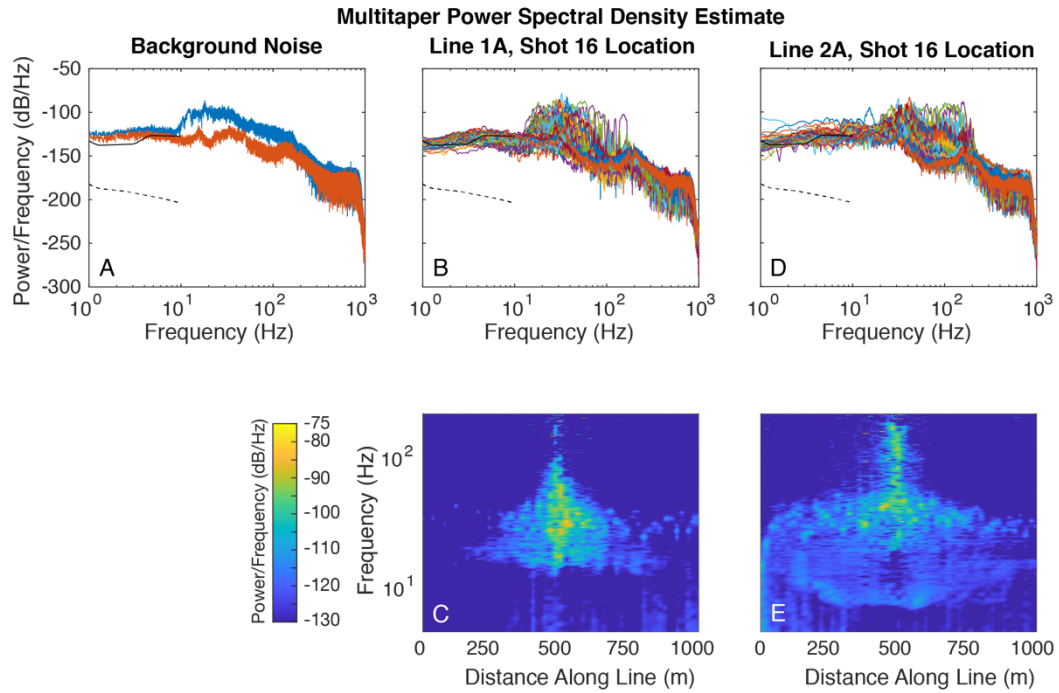


**Figure 3.4:** Power spectral density estimate plots characterizing the SFVF study area. A) Background noise for the study area using data from Line 1A (blue) and Line 2A (red). Earth background high (solid black line) and low noise (dashed black line) models are included for reference. B & D) Show the power spectral density plots for at each of the 51 nodes for a shot performed at shot location 16 (490 m position) on Lines 1A & 2A. Each of the 51 nodes is shown as a different colored line. C & E) Spectrograms showing the attenuation of the shot energy from shot location 16 (490 m position) as it moves out along both Lines 1A & 2A respectively. Power/frequency scale saturates at -130 dB as this is the point that the noise background (equivalent to the earth new high noise model) is greater than the signal.

### ***3.4.3 2-D Inversion***

A 2-dimensional (2-D) Bayesian inversion of the refracted P-wave arrival time picks was used to determine the P-wave seismic velocity structure beneath each nodal line (Huang et al., 2020). The 2-D inversion parameterizes models with a set of Voronoi cells within the model that provide for the lateral variation in interface depth and velocity along the profile. Here we constrain velocity to increase with depth, although we recognize that this assumption may not hold in all geological settings or structures. The proposed structure of Voronoi cells is interpolated linearly using the velocity at each control point and Delaunay triangles to smooth the final model velocities between the cells. The method allows for surface topography by fixing the top layer to the elevation along the surface profile (Huang et al., 2020).

The inversion uses a reversible-jump Markov chain Monte Carlo algorithm to create an ensemble of layered models that share similar misfit to the data (Green, 1995). During each iteration, Figure 3.5, a new proposed model is created by performing one of the following operations to update the current model: 1) change of control point velocity, 2) addition of a control point, 3) removal of a control point, 4) moving of a control point location, or 5) swapping of control point velocities. For the proposed model, P-wave arrival times are calculated at each receiver using a fast-marching algorithm, and compared to the observed data (Sethian, 1996). The proposed model is accepted or rejected according to the Metropolis-Hastings algorithm (Metropolis, Rosenbluth, Rosenbluth, Teller, & Teller, 1953). Specifically, if the calculated arrival times result in a smaller misfit, then the proposed model will be retained. Otherwise, the current model will be retained with a probability depending on the misfit. At regular intervals, the current model is saved to an ensemble, with the frequency with which a

model shows up in the ensemble being proportional to its posterior probability. This ensemble is used to perform the overall statistical analysis from which the final data plots are produced (Huang et al., 2020).

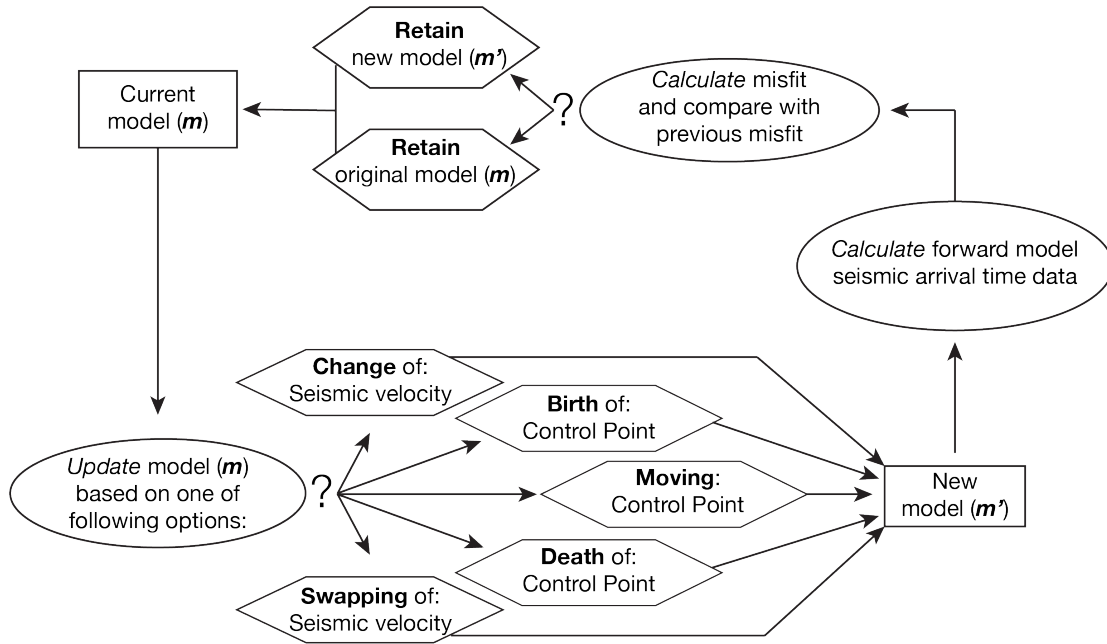


**Figure 3.5:** Schematic overview of seismic refraction reversible Markov chain Monte Carlo algorithm iteration.

The 2-D inversion of each nodal line took approximately 24 hours for each line for five 1,000,000 iteration chains, for a total of 5,000,000 iterations in each ensemble. For each run, we stipulated a set of priors, including seismic velocity, number of cells, maximum depth, and based on the geology (velocity and depths) and preferred resolution of the model (number of cells). Final runs were executed with the priors and initial conditions list in Table 3.2, which are based on preliminary test runs that showed final velocities well below 5000 m/s, and the standard deviation of the velocity increasing ( $> \pm 400$  m/s) indicating results are unreliable below depths of  $\sim 40$  m, seen in Figure 3.7 B, D, F & H. Upon completion of the prescribed 5,000,000 iterations, an

ensemble consisting of 10,000 saved iterations is created from each chain, and combined into a single ensemble of 50,000 models.

The quantity of 1,000,000 iterations in each chain was determined by initial evaluation to result in greater than the final 40% of the models having converged to a constant mean misfit of the model versus observed arrival time data, Figure 3.6, indicating stability of the posterior ensemble. The results from this ensemble are evaluated for a number items including the mean and standard deviation of the seismic velocity, the seismic velocity gradient, the mean misfit and standard deviation between the observed data and the inversion results. The resulting plots for velocity cross-section and the standard deviation from the mean velocity are shown in Figure 3.7.

<b>SFVF Nodal Seismic Refraction Lines 2-D Analysis Parameters</b>	
<b>Parameter</b>	<b>Value</b>
<b>Minimum permissible velocity</b>	200 m/s
<b>Maximum permissible velocity</b>	5000 m/s
<b>Maximum number of cells</b>	500
<b>Maximum analysis depth</b>	80 m
<b>Total number of iterations</b>	1,000,000
<b>Interval between saved iteration</b>	Model saved every 100 iterations
<b>Total number of saved models</b>	50,000 (10,000 per chain x 5 chains)
<b>Number of iterations to constant mean misfit (Figure 3.6)</b>	Line 1A: ~100,000 Line 1B: ~10,000 Line 2A: ~10,000 Line 2B: ~100,000

**Table 3.2:** List of initial conditions, constraints, and static returns for the SFVF nodal seismic line pairs 1 and 2 refraction analysis.

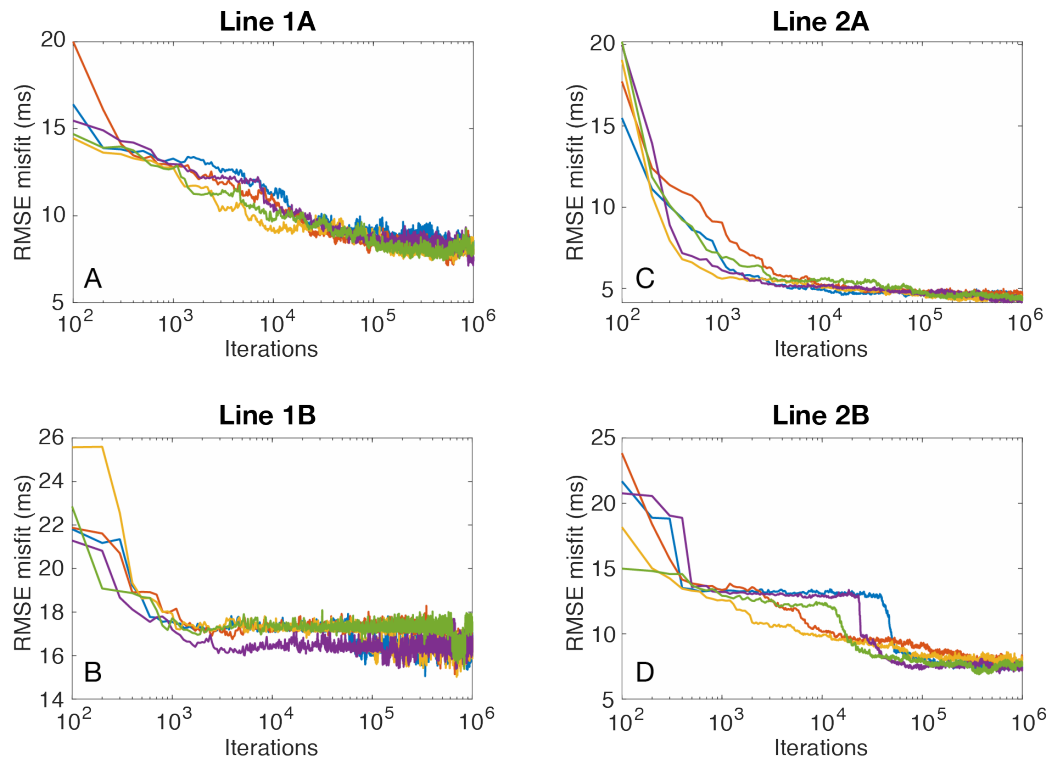


**Figure 3.6:** Mean misfit profiles from saved ensemble iterations of 2D Bayesian analysis inversions for each of the four nodal lines. Inversions were saved every 100 iterations.

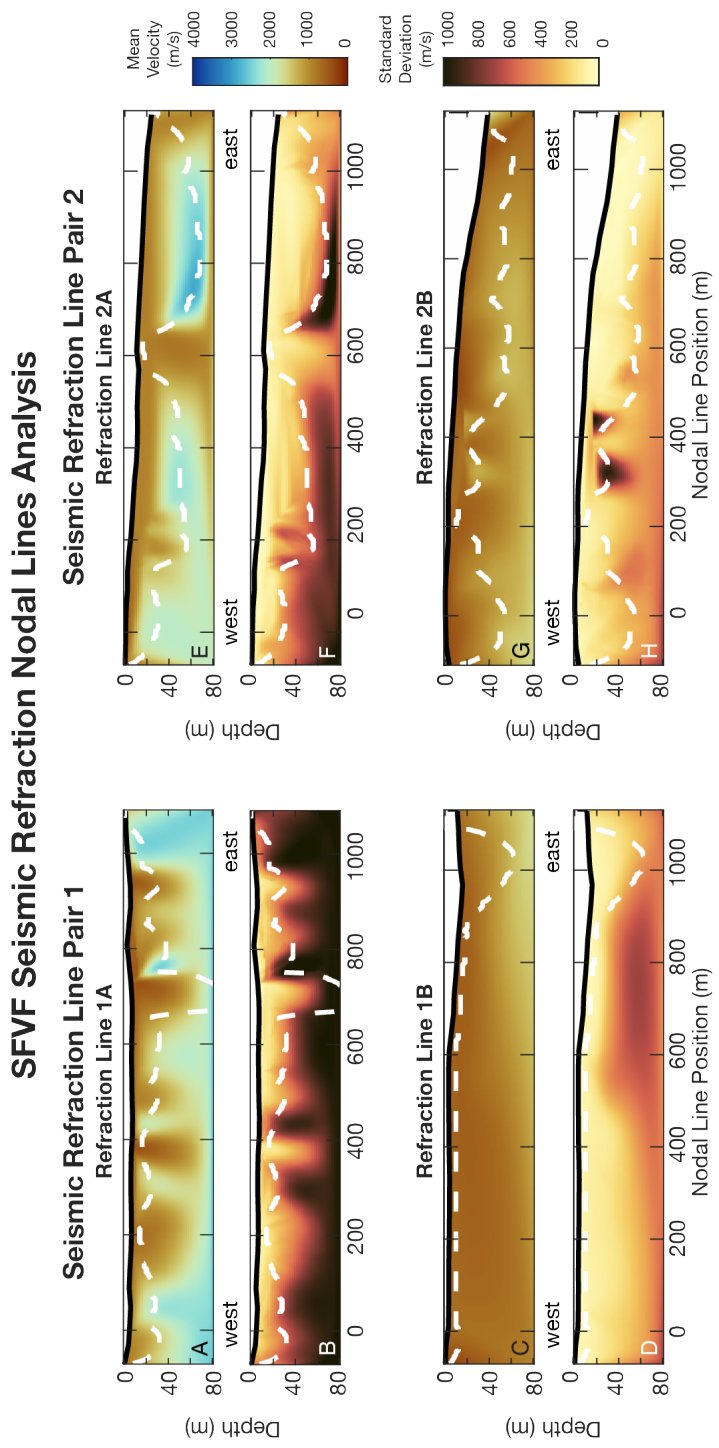


**Figure 3.7:** Results from the 2D inversion for the SFVF refraction surveys. The mean P-wave velocity of the ensemble is shown in A, C, E, and G, while the standard deviation of the ensemble is shown in B, D, F, and H for each refraction line respectively. The white dashed line indicates the deepest modelled penetration of the seismic rays recorded by the nodes. Velocity scale is the same for the four velocity panels, and the four standard deviation panels as indicated by the color bars.

### ***3.5 Results***

#### ***3.5.1 Evaluation of Seismic Velocity Profiles & Power Spectral Density***

The analysis of data from the four active seismic nodal lines in the SFVF resulted in seismic velocity profiles for approximately the upper 40 m of the sub-surface for three of the four locations and approximately the upper 10 meters of line 1B. The seismic velocity and standard deviation plots, shown in Figure 3.7, with the deepest reliable portions of the models, as determined by the deepest seismic ray penetration along each profile, indicated by the white dashed line. For each of the lines, the mean misfit and the standard deviation of the results of the inversion to the observed data are as follows: Line 1A: mean misfit = 6.1 ms, standard deviation = 8.5 ms; Line 1B: mean misfit = 9.5 ms, standard deviation = 17.1 ms; Line 2A: mean misfit = 3.2 ms, standard deviation = 4.7 ms; and for Line 2B: mean misfit = 6.3 ms, standard deviation = 8.0 ms.

The seismic velocity results shown in Fig. 3.7 do not indicate strong lateral heterogeneity in the near surface, and have little to no correlation with the position of projected surface faults. Lines to the North of the cinder cones tended to show more variability in velocity, with high velocity structure appearing at 20-40 meters depth. This possibly indicates that the overlying volcanic deposits and lava flows are thinner in this region, with bedrock closer to the surface. The southern profiles (1B and 2B) results both show relatively homogeneous velocity profiles and low velocity. We interpret this as cinder deposits that have buried the region. There is no evidence of correlation between the postulated fault systems and 2-D velocity variations observed in these seismic velocity profiles. It was expected that locations of high velocity

gradient and corresponding high standard deviation would have indicated these fault locations (Hole et al., 2006; Wang et al., 2008).

As mentioned, the recorded seismic waves were only able to penetrate the upper 10 m to 40 m beneath the surface. The maximum distance from source location to node that was recoverable was in general no more than 130 m of the 1000 m long seismic line. Power spectral density analysis, Figure 3.4, verifies that the energy from the source was attenuated below the background noise within this distance, seen in Figure 3.4 plots C and E. The background noise for these lines is shown to be between -140 and -100 dB/Hz, Figure 3.4 plot A. Source shots reach above this noise level to approximately -80 dB/Hz between 10 Hz and 200 Hz, as seen in Figure 3.4 plots B and D. However, despite the source power/frequency being sufficiently above the background noise close to the shot location, Figure 3.4 plots C and E confirm that the P-wave energy above the background noise disperses within the first 100 m to 150 m of the source location. The remaining residual energy is in the surface waves which are not analyzed in this study.

### ***3.5.2 Apollo 17 LSPE Re-evaluation***

To understand how refraction experiment geometry ties to the Apollo 17 LSPE 1-D investigation, we use our SFVF analysis methods to demonstrate how seismic array design dictates the ability to detect subsurface structure. 2-D refraction analysis has the ability to show vertical and lateral heterogeneity in the seismic velocity structure. From our analysis of the data from the 51 node, 1 kilometer long, SFVF refraction lines our results show some vertical heterogeneity along with a few locations of minimal lateral heterogeneity. Using the SFVF data to invert for 1-D models, both with the full SFVF

data set as well as a LSPE equivalent data set, we demonstrate the loss of ability to interpret any 2-D seismic structure.

As a step in this comparison, we first re-evaluated the Apollo 17 LSPE data using similar methodology to the processing of the SFVF experiment data up through the development of seismic velocity models, with the following exceptions. First, we used the LSPE P-wave arrival time picks selected by Heffels et al. (2017) when applying an updated Weiner filter method to the raw data. For their work, they used the source-to-receiver pairs from only six of the eight EPs (EP 2, 3, 4, 5, 6, & 8). These six EPs were used in their analysis because of refined locations of the LSPE geophones and these six EPs as determined from Lunar Reconnaissance Orbiter data (Haase, Gläser, Knapmeyer, Oberst, & Robinson, 2013; Haase, Wählisch, Gläser, Oberst, & Robinson, 2019). Using the same data as Heffels et al. (2017) allows us a direct comparison to their work along with their corresponding correlation to the results of the Apollo 17 LSPE analysis by Cooper et al., (1974). Second, similar to Heffels et al. (2017) and Cooper et al., (1974) we assumed that the subsurface within the Taurus Littrow study area consists of a laterally homogeneous layered seismic velocity structure of constant topographic elevation, and analyzed the data for 1-dimensional seismic velocity structure.

Using the P-wave first-arrival time picks from Heffels et al. (2017) study, we processed the data through a 1-dimensional Bayesian refraction code (Montgomery et al., 2017) that is the foundation from which our 2-dimensional code was developed. The code executes in the same iterative approach as the 2-dimensional code as described earlier, and shown in Figure 3.5, with obvious exception of not including hinge-points.

Two analyses were run. The first was using only the arrival times from EPs 2 and 3. These two EPs were in an approximate straight line from the LSPE geophones at distances varying from 236 m to 425 m, and provide the opportunity to focus on the upper 50 m of the subsurface. The second analysis used the arrival times from the six EPs used by Heffels et al. (2017), with a maximum EP to geophone distance of 2318 m, to examine deeper structure down to 600 m. The parameters set for both analyses were a minimum velocity of 0 m/s, maximum of 20 layers, and 1,000,000 iterations saving the solution every 500 iterations. For the first analysis of the upper 60 m, the maximum velocity was set to 600 m/s, and the initial velocity structure was set at 100 m/s, 300 m/s, and 500 m/s with interfaces between 10 m and 50 m. The second analysis, to a depth of 600 m, had a maximum velocity of 1500 m/s, and initial velocity structure of 100 m/s, 300 m/s, 500 m/s, and 1000 m/s with interface depths of 10 m, 50 m, and 500 m. Upon completion of the set number of iterations, an ensemble was created and saved, from which the plots of the resulting seismic velocity model and standard deviation were created.

Our analysis of the upper 60 m using EPs 2 & 3 resolved a best fit model of four velocity layers of 140 m/s, 202 m/s, 270 m/s, and 362 m/s with upper depths of 0 m, 5 m, 16 m, and 33 m. Examining the upper 600 m using EPs 2, 3, 4, 5, 6, and 8 results in a two-layer model with a upper velocity layer of 287 m/s, transitioning to a second layer of 779 m/s at a depth of 178 m. The 1-dimensional seismic velocity analysis results are shown in Figure 3.8, A and B, along with the results from the analysis by Cooper et al., (1974), and the 2-layer model from Heffels et al. (2017) for comparison.

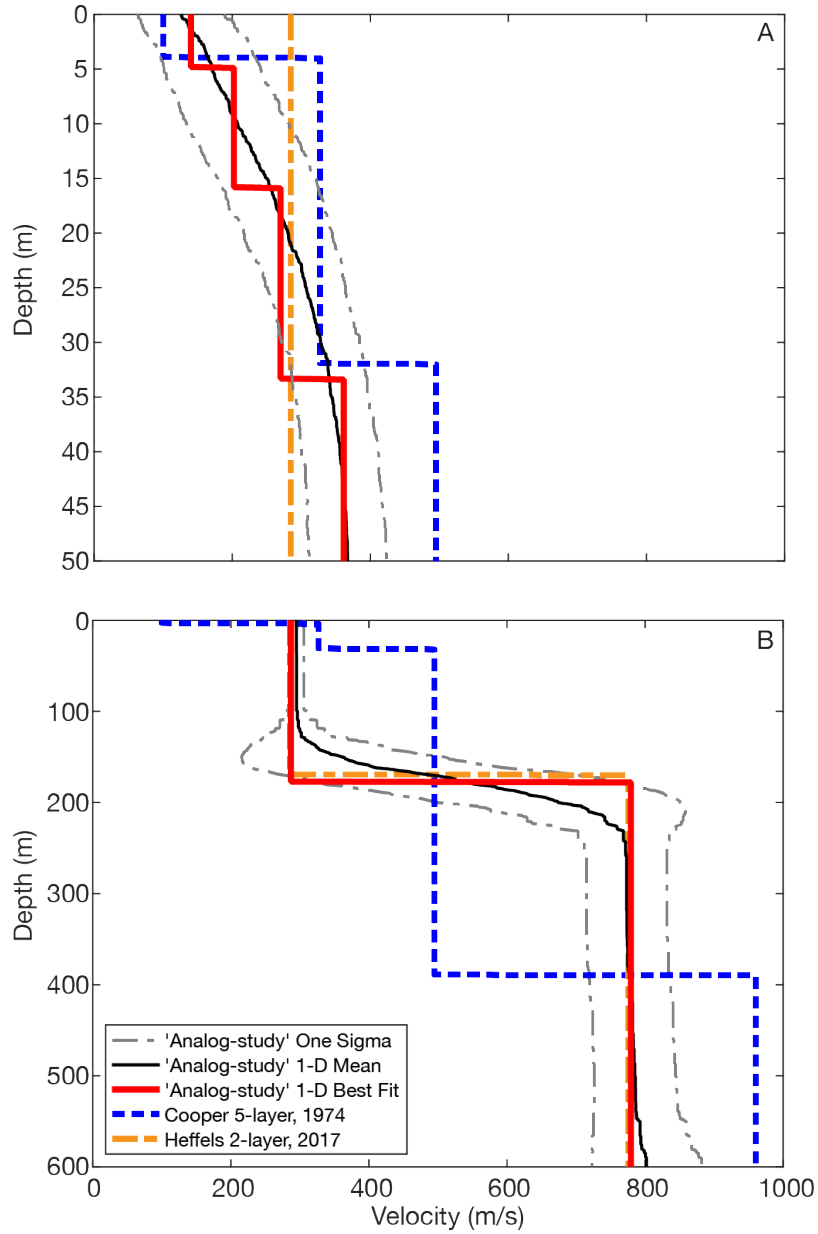


**Figure 3.8:** Plots A and B show the 1-D seismic velocity profiles for the Apollo 17 LSPE TLV data as calculated by this ‘Analog-study’; Cooper and Kovach, 1974; and Heffels et al., 2017. For this ‘Analog study’, the solid red profile is the best fit discrete steps velocity model; solid black profile is the mean velocity model; and the gray dot-dash lines are the one sigma standard deviation from the mean model. A) Upper 50 m of TLV subsurface, based results from EPs 2 & 3. B) Upper 600 m, based on results using EPs 2, 3, 4, 5, 6, & 8.

### ***3.5.3 Evaluation of SFVF Experiment as an Apollo 17 LSPE Analog***

The final portion of this study uses the SFVF fieldsite and seismic velocity analysis as an analog to the Apollo 17 LSPE setup. To do this we compare the detail of the results of the analysis of the seismic velocity structure between the full SFVF data set and a SFVF data set reduced to the equivalent of the LSPE data set. This allows for a comparison of how the analysis results, including the standard deviation, varies for the 1-D cases of full versus LSPE equivalent SFVF array data sets. For this comparison study, we essentially down-selected the actual SFVF nodal field data to represent an equivalent dataset as that created by the Apollo 17 LSPE experiment. Impacts to a seismic equivalency between the lunar and terrestrial locations include the effects of intrinsic attenuation which is much lower on the Moon, with a quality factor (Q) of 3000 to 5000, versus the higher attenuation on Earth (Dainty & Toksöz, 1981; Tittmann, Ahlberg, & Curnow, 1976). The effects of scattering are also different between the Earth and Moon, with more intense scattering on the Moon (Dainty & Toksöz, 1981; Tittmann et al., 1976). Since, we cannot match these portions of the seismic environments, we based the SFVF to LSPE equivalency on reducing the locations of SFVF sources-to-receiver pair data to those that match the number of wave cycles, based on wavelengths, between each of the EPs and geophone pairs used for the Apollo 17 LSPE experiment on the Moon to produce an analogous amount of attenuation on the waves. We use the following method relating wavelength, velocity, and frequency; starting with determining the wavelength for both the SFVF and the LSPE field sites using Eq. 1.

$$wavelength = \frac{velocity}{frequency} \quad (12)$$

### SFVF / Apollo 17 LSPE Seismic Refraction Equivalency Data Comparison

SFVF Nodal Line 1B, Node 26, Shot Location 11

Apollo 17 LSPE Geophone 1, EP 2

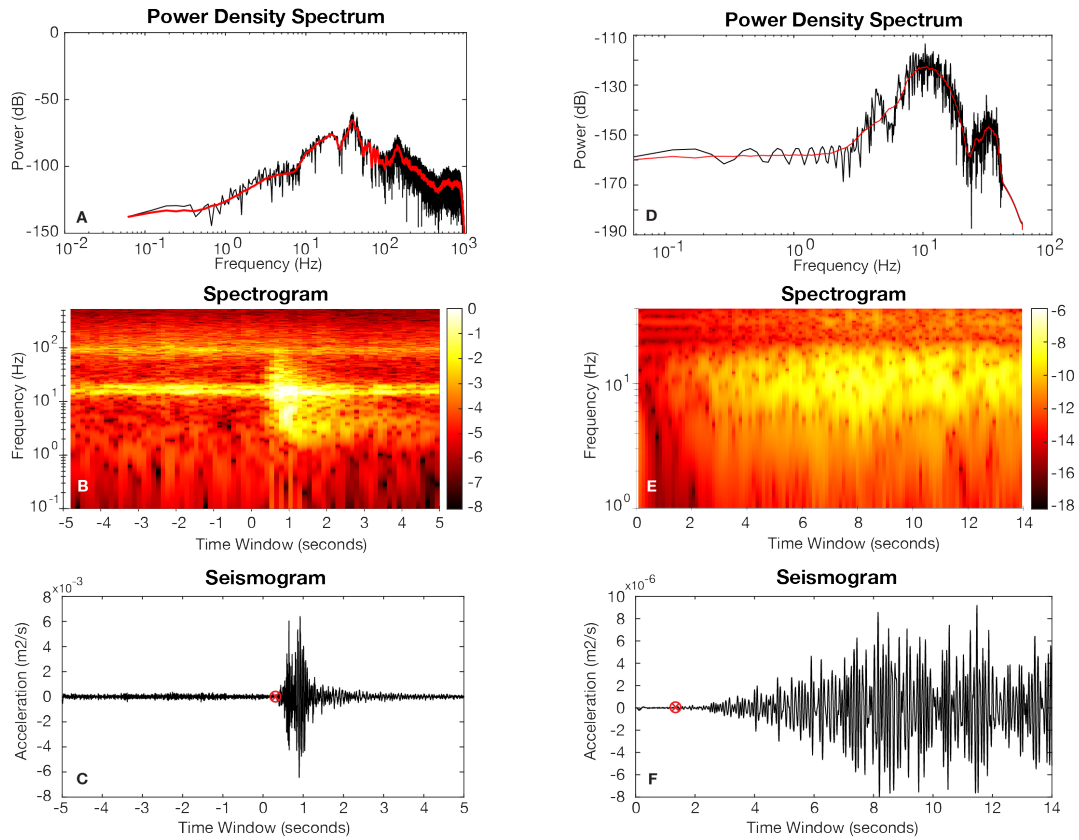


**Figure 3.9:** Comparison of typical seismic characteristics of the SFVF and the Apollo 17 LSPE data used for SFVF Apollo 17 LSPE equivalency analysis. Plots A, B, & C are SFVF data and D, E, & F are Apollo 17 LSPE data (DARTS Seismology at ISAS/JAXA, 2019). From top to bottom of each column, the figures contain representative data for Power Density Spectrum, Spectrogram, and Seismogram plots. Frequency resolution for the SFVF data is 1000 Hz, and for the LSPE data is 235 Hz. A red circle-X on the seismograms indicates examples of the picks for the P-wave first arrival.

For the calculation of the wavelengths, the velocities used were those found in the upper layer for the SFVF and LSPE seismic cross-section models. For the SFVF we used 525 m/s and for the LSPE data we used 273 m/s. The frequencies used for the wavelength equivalency calculation were determined by evaluation of source to receiver power density spectrum (PDS) and spectrogram plots. PDS, Spectrogram, and seismic trace examples plots for Line 1B shot location 11 to node 26 data pair for the SFVF, and EP1-to-geophone 1 data for the LSPE, are shown in Figure 3.10 (“DARTS Seismology at ISAS/JAXA,” 2019). The SFVF plots, Figures 3.9 A, B, & C, were constructed from a 10-second data window that includes a 5-second lead-in of background data prior to the shot at time 0 seconds. This allows for a complete PDS and spectrogram without concern of missing initial data leading up to the shot. The PDS and spectrogram plots use data from the initially processed full data sets, prior to the creating the 10 second clips, starting at time 0 seconds, used to pick arrival times. The SFVF spectrogram (Figure 3.10 B) shows a persistent frequency band at approximately 20 Hz that is attributed to the instrument (Farrell, Wu, Ward, & Lin, 2018). For the example SFVF seismogram in Figure 3.10C, we included a low-pass filter of 7 Hz, a high-pass filter of 110 Hz, and a bandpass filter of 25 to 50 Hz to remove the persistent node noise, and better display the straight summed stack of 10 shots for this source-receiver combination. This filter was not included in the bulk data processing used for picking arrival times because the phase-weighted-stacking muted the impact of the node induced noise in the final stack. The LSPE plots, Figures 3.9 D, E, & F, are created from the first 14 seconds of data after the shot (EP detonation). A lead-in window was not available, as the data sets started at the shot time of 0 seconds. From the LSPE data, the frequency peak, of 9 Hz, was selected for the analysis. The

frequency of 140 Hz corresponding to the body wave arrival was selected from the SFVF data. In reality, attenuation will actually result in a shift to lower frequencies with increased distances between source and receivers, as higher frequencies sustain more attenuation over a given distance. On the Moon the scattering provides a greater impact to this attenuation, and on the Earth intrinsic attenuation would be the stronger mechanism. Also, the increase of velocity with depth is not 1-to-1 between the SFVF and TLV inserting an additional variation between the geologic environments. However, the assumption of applying our single point selections for velocities and frequency selections result in a first-order approximation for wavelengths to calculate a basic equivalency between the SFVF and TLV LSPE data sets.

The calculated wavelengths are 3.75 m for the SFVF fieldsite, and 30.33 m for the TLV location on the Moon. The ratio of LSPE experiment wavelength to SFVF wavelength was then calculated, with the simple equation of Eq. 2, to be 0.124.

$$wavelength = \frac{wavelength_{SFVF}}{wavelength_{LPSE}} \quad (13)$$

This ratio was used to calculate the equivalent SFVF distances travelled by the same quantity of wave cycles as the between the EPs and geophones pairs in the LSPE experiment using Eq. 3.

$$Distance_{SFVF} = Distance_{LPSE} \times wavelength\ ratio \quad (14)$$

These distances were then rounded to the nearest 10 m to select the equivalent source to nodes distances from the SFVF experiment. For each nodal line, a single node

was selected as the receiver to represent all four LSPE geophones. The reason for this is twofold. First, the geometry of the LSPE did not attempt to provide the overall structure in a specific direction, resulting in essentially 32 individual EP to source data pairs. Secondly, adjusting the LSPE geophone array to the SFVF using the wavelength equivalency ratio results in no geophone being more than approximately 7 m from another receiver location. With the SFVF nodal lines geometry having receiver nodes at 20 meter intervals, the 7-meter distance essentially results in the equivalent receiver positions all being co-located. Node location 16, approximately centered on the SFVF nodal line at the 490 m position was used as the receiver for this analysis. The receiver and source locations for the SFVF LSPE equivalent datasets are provided in Table 3.3.

<i>Apollo 17 LSPE</i>				<i>SFVF</i>	
<i>Explosive Packages</i>	<i>Geophone</i>	<i>EP-geophone distance (m)</i>	<i># wavelengths EP to geophone</i>	<i>Scaled distance (m)</i>	<i>Rounded scaled distance (m)</i>
<b>EP2</b>	<b>1</b>	327.4	10.8	40.5	50
	<b>2</b>	425.6	14.0	52.7	50
	<b>3</b>	372.9	12.3	46.2	50
	<b>4</b>	367.2	12.1	45.5	50
<b>EP3</b>	<b>1</b>	236.3	7.8	29.3	30
	<b>2</b>	334.9	11.0	41.5	50
	<b>3</b>	282.9	9.3	35.0	30
	<b>4</b>	281.0	9.3	34.8	30
<b>EP4</b>	<b>1</b>	259.5	8.6	32.1	30
	<b>2</b>	162.4	5.4	20.1	30
	<b>3</b>	205.4	6.8	25.4	30
	<b>4</b>	210.9	7.0	26.1	30
<b>EP5</b>	<b>1</b>	2225.9	73.4	275.6	270
	<b>2</b>	2318.4	76.5	287.0	290
	<b>3</b>	2283.2	75.3	282.7	290
	<b>4</b>	2302.6	76.0	285.1	290
<b>EP6</b>	<b>1</b>	1200.7	39.6	148.7	150
	<b>2</b>	1236.1	40.8	153.0	150
	<b>3</b>	1192.3	39.3	147.6	150
	<b>4</b>	1138.2	37.5	140.9	150
<b>EP8</b>	<b>1</b>	169.4	5.6	21.0	30
	<b>2</b>	95.0	3.1	11.8	10
	<b>3</b>	111.9	3.7	13.9	10
	<b>4</b>	101.4	3.3	12.6	10

**Table 3.3:** Wavelength scaled distances of SFVF nodal data.

The resulting distinct distances for the SFVF configuration as related to the Apollo 17 LSPE array are summarized in Table 3.4. Due to the spacing of the receiver nodes (20 m) to sources (40 m) with an initial offset of 10 m in one direction and 30 m in the other, and lack of resolvable seismic waves beyond a distance of ~130 m. This resulted in the full length of the LSPE equivalent line analyzed being only 80 m (+50 m and -30 m from the receiving node), using only three source-to-receiver pairs for each analysis.

<i>Distinct equivalent distances (m)</i>	<i>Quantity of LSPE EP-geophone pairs at rounded distance</i>
10	3
30	8
50	5
150	4
270	1
290	3

**Table 3.4:** Quantity of Apollo 17 LSPE EP-to-geophone pairs for each of the SFVF equivalent distances, with the three data points available in the SFVF data highlighted in gray.

Two separate 1-D analysis were run on the SFVF data. The first using the full data set for each of the four nodal lines (Figure 3.10 plots A, C, E, & G). The second using only the arrival time picks for the distinct down-selected SFVF source-receiver pair distances (Figure 3.10 plots B, D, F, & H). We inverted both data sets for each of the four SFVF nodal lines using the 1-dimensional Bayesian refraction code (Montgomery et al., 2017). For each of these analyses the minimum velocity was 0 m/s, maximum velocity was 5000 m/s, maximum depth was 50 m, and a maximum of 20 layers was permitted. 1,000,000 iterations were completed with data saves at every 500<sup>th</sup> iteration as with the re-evaluation of the LSPE data, and the statistics on the resulting ensemble were completed on the final 50% of the ensemble models. Figures showing the 1-D seismic velocity profile results for both the full and LSPE equivalent data sets for each of the four SFVF nodal lines are shown in Figure 3.10. In each case for the full data sets the results show a two layer model (of varying interface depths), with the northern Lines 1A and 2A having significantly higher second layer velocities ( $\sim 2000$  m/s or greater), than more southern Lines 1B and 2B ( $< 1000$  m/s). All four LSPE equivalent models show large standard deviations due to the sparsity of equivalent data points available for the analysis.

## SFVF Apollo 17 LSPE Equivalency Seismic Refraction Data Analysis

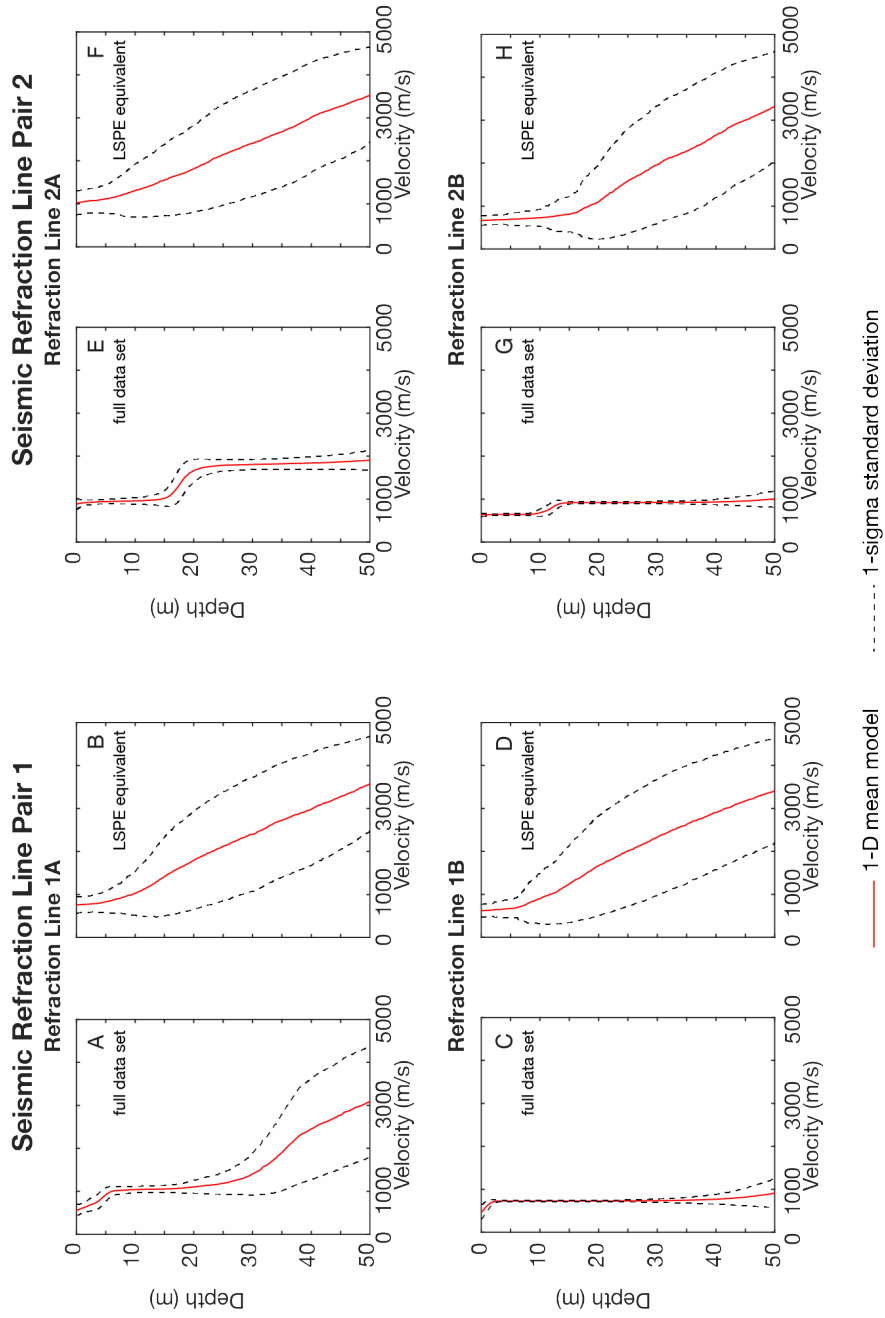


**Figure 3.10:** Four sets of plots (A-B, C-D, E-F, G-H) show the 1-D velocity profiles for the SFVF full data set (plots A, C, E, H); and the 1-D velocity profiles for the SFVF LSPE equivalent data set (plots B, D, F, H); of the four seismic refraction nodal lines (1A, 1B, 2A, 2C) shown in Figure 1A.

## **3.6 Discussion**

### **3.6.1 *SFVF 2-D Seismic Velocity Profiles***

Our refraction analysis produced reliable 2-D velocity cross-sections down to a depth of 10 m to 40 m, below which the standard deviation of the mean velocity increases. For the 2-D inversion results, Figure 3.7, it can be seen that the velocity models are essentially constructed of 2 velocities, of approximately 900 m/s and then between 2000 m/s and 3000 m/s, for Lines 1A and 2A. For Lines 1B and 2B, the southern two lines, there is primarily a single velocity of approximately 800 m/s to 900 m/s. This north to south trend in velocity profiles between the pairs of refraction lines is also seen in the 1-D velocity profiles in Figure 3.10 plot pairs A & C, and E & G. For both of the northern lines (1A & 2A), the lower velocity layer indicates a likely thinner portion of lava flow sitting atop of the higher velocity local Kaibab limestone layer, which has been shown to have a P-wave velocity as between 2600 m/s and 5800 m/s (Kring, 2017). The southern two refractions lines (1B & 2B), which are both approximately 2 km further south, do not resolve this higher velocity, instead only reaching velocities of less than 1000 m/s. This velocity indicates a thicker lava flow or multiple overlaid flows. The overall trend then is of a thinning lava flow to the north, which correlates with the known primary flow direction, from the San Francisco Mountain stratovolcano, in this area.

As stated in the results, the depth of the seismic ray penetration recovered was only 10 m for Line 1B, and down to 40 m for the other three lines. It was shown that the background noise for this area is between -140 and -100 dB/Hz in frequency range of our source shots of between 10 Hz and 200 Hz, Figure 3.4 plot A, which is similar

to the Earth background high noise model (Peterson, 1993). The shots are shown to produce a power, above the background noise, of -80 dB/Hz between 10 Hz and 200 Hz, Figure 3.4 plots B and D. Despite the source power/frequency being sufficiently above the background noise close to the shot location, Figure 3.4 plots C and E confirm that the energy above the background noise attenuates within the first 100 m to 150 m of the source location, indicating a high attenuation for this field area that correlates with the inability to resolve first-arrivals of the seismic waves beyond this distance between source and receiver node.

### ***3.6.2 Re-evaluation and Interpretation of Apollo 17 LSPE Analysis***

As part of the comparison of our SFVF nodal lines as an analog to the Apollo 17 LSPE experiment, we re-analyzed the LSPE data based on the data used in Heffels et al. (2017) analysis. The original analysis of the LSPE data by Cooper et al. (1974), incorporating all seismic arrival picks, resulted in a five layer 1-D model of the upper 1400 m. The velocities of each layer were calculated to be 100 m/s, 327 m/s, 495 m/s, 960 m/s, and 4700 m/s; with the associated upper depths of the layers being 0 m, 4 m, 32 m, 390 m, and 1385 m. These layers are shown in Figure 3.9 to a depth of 600 m. The re-evaluation of the LSPE data by Heffels et al. (2017) resulted in a two-layer model of the sub-surface seismic velocity structure using the six EPs (2, 3, 4, 5, 6, & 8), and a three-layer model using EPs 2, 3, 4, and 8. The two-layer model has velocities of 285 m/s and 775 m/s with the transition occurring at a depth of 170 m. The three-layer model resulted in velocities of 285 m/s, 580 m/s, and 1825 m/s with transitions occurring at depths of 96 m and 773 m.

Our 1-D seismic refraction analysis results, of the LSPE data used by Heffels et al. (2017), shown as the dashed black line (labelled Analog-study 1-D Model) in Figure 3.9, match very closely to the results from Heffels et al. (2017) analysis results, shown as the solid blue line in Figure 3.5 (labelled Heffels 2-layer, 2017). Our results differ from Heffels et al. (2017) in the details of the upper 60 m of the subsurface, where ours produce possible additional seismic velocity layers. Where Heffels et al. (2017) determined only a single seismic velocity of 285 m/s in the upper 60 m, our best fit model shows four velocity layers of 140 m/s, 202 m/s, 270 m/s, and 362 m/s with upper depths of 0 m, 5 m, 16 m, and 33 m. Our results are similar to findings by Nakamura, Dorman, Duennebier, Lammlein, & Latham (1975) of a regolith layer with a seismic velocity of  $\sim 100$  m/s down to a depth of around 4 m at the Apollo 11, 12, and 15 sites. This also compares well to Cooper et al. (1974) findings of a 100 m/s regolith layer down to a depth of  $\sim 4$  m from the Apollo 17 LSPE, fitting within our results 1-sigma standard deviation error of the mean velocity.

The next three layers from our analysis of this upper 60 m of the subsurface, indicate seismic velocity structure of velocities and interface depths that differ for the TLV from those previously reported by Heffels et al. (2017) or Cooper et al. (1974). Heffels et al. (2017) single layer structure of 285 m/s however, is essentially the weighted average, 288 m/s, of our four-layer velocity structure. Cooper et al. (1974) results differ with much higher step increases in velocity at shallower depths than our results, and fall outside our standard deviation of the mean velocity even when accounting for their 10% error in velocity and depth (Cooper et al., 1974). One thing that cannot be ruled out from our analysis, and may account for some of the differences in the velocity increases in the upper 60 m between the various studies, is whether these

apparent step increases are actually manifestations from a continuously increasing seismic velocity profile with depth. The reason for this is that the step increases we obtained fall within the 1 sigma limits of our mean velocity results which shows a smooth increase in velocity with depth. This would be similar to previously hypothesized smoothly increasing profile of seismic velocities in the upper lunar crust due to the structural compaction of regolith down into decreasingly fractured crustal basaltic material (Cooper et al., 1974; Gangi, 1972).

Our analysis using EPs 2, 3, 4, 5, 6, and 8 results in a two-layer model in the upper 600 m of the subsurface with a transition from a lower velocity layer of 287 m/s, to a higher velocity layer of 779 m/s, at a depth of 178 m. This nearly perfectly matches Heffels et al. (2017) 2-layer model results. It also encompasses our finer detailed model of the upper 60 m within a two sigma overlap of the two models. As for the difference of both our and Heffels et al. (2017) models with respect to the results from Cooper et al., 1974, this may be a result of the updated LSPE position data from Haase et al. (2013) and Haase et al. (2019), and increased accuracy in the arrival time picks from Heffels et al. (2017).

### ***3.6.3 SFVF Experiment as an Analog to Apollo 17 LSPE***

The final portion of our study examined the use of the SFVF data as an analog analysis to the Apollo 17 LSPE experiment results. The aim for this was to compare 1-D seismic profiles, of the upper 200 m of the subsurface, between analysis using full SFVF data set versus a reduced SFVF LSPE equivalent data set. This comparison provides insight into understanding the additional detail of the TLV subsurface

construct that may be gained with a linear active source seismic array positioned across the TLV.

Reviewing the plots in Figure 3.10, there are two primary items that stand out. The first is that the standard deviation of the mean velocity is significantly greater for the SFVF LSPE equivalent data set. As expected, this occurs at very shallow depths for the drastically reduced SFVF LSPE equivalent data set, with the total seismic paths reduced to three for the analysis. For the full data set, the increase in standard deviation increases rapidly below a depth of 25 m for Line 1A, meaning lower confidence in the solution below this depth. The other three lines have a very tight standard deviation down to 40 meters where it begins to increase. The second item that stands out is the trend in resolved velocity structure between the full data set and the LSPE equivalent data set. Between the two data sets, the resulting initial velocities near the surface are very similar, and in all cases overlap at 1-sigma standard deviation from the mean velocity. However, the velocity below the upper 5 m is unable to be constrained due to the lack of data points available for the SFVF LSPE equivalent analysis. Although these trends can be expected due to the difference in seismic wave coverage between large and small data sets, it does reinforce the likelihood of there being unresolved layers or structure within the TLV that additional source receiver pairs could help determine.

The Apollo 17 LSPE results filled a significant gap within the knowledge of the lunar seismic velocity model for the layers within the upper 2 km of the lunar surface by providing the 1-D average seismic layering beneath the TLV. However, there is still seismological content to be discovered within the TLV. From our evaluation of the Apollo 17 LSPE equivalent SFVF analysis, we show a comparative example of how

the quantity and distances of seismic sources relative to the seismic wavelength impact the ability to resolve the subsurface structure. Now that basic seismic velocities of the TLV are known, and by calculation associated wave properties, it should be encouraged that future lunar missions target specific geophysical problems in the near sub-surface with seismic arrays designed to provide the ability to resolve specific structural geometries. For example, if an SFVF equivalent geophone/seismometer line were set up on the lunar surface, across the 10 to 12-kilometer-wide TLV, with an interval of approximately 160 m between receivers, based on the SFVF to TLV wavelength ratio of 0.124, an array of 60 to 70 receivers would provide sufficient resolution to understand the details of the hypothesized graben structure that forms the valley, assuming appropriately sized sources. This type of an array would be able to provide 2-D results equivalent to the near-surface fault structure surrounding the SFVF monogenic volcanic vents of this study, and likely provide resolution of the graben feature forming the TLV.

### **3.7 Conclusions**

We completed an active seismic field study within the SFVF to examine the seismic velocities of the layers within the upper several hundred meters of subsurface. Four linear seismic arrays were grouped in two pairs, Nodal Line Pair 1 associated with cinder cone vent V5704, and Nodal Line Pair 2 associated with cinder cone vent V6735. The intent of both pairs was to examine the subsurface for structure that is indicative of fault planes that may align underneath the associated cinder cone vents, and are hypothesized to be a contributing factor in controlling the final ascent of magma to the surface, and therefore the position and alignment of the cinder cone vents in the

study area. Refraction analysis from the four seismic lines however indicated that the field area consists of highly attenuating structure that results in dispersion of the seismic energy from our source to below the background noise level within 130 m of the source location. Therefore, the executed 1000 m seismic refraction line is essentially reduced to resolving structure to depths equivalent to that examined by 130 m long lines, which in the case of this study was a maximum of approximately 40 m. This was unfortunately insufficient to resolve any of the anticipated fault structure surrounding the volcanic vents we studied, but did allow for the recognition of a thinning basaltic layer to the north, with contact on the Kaibab limestone seen in Lines 1A and 2A. The data did allow the characterization of the background noise level to be similar to the Earth background high noise model and the attenuation distance for the PEG source was quantified.

The second part of this study was the use of the data from these SFVF seismic lines as an analog to the LSPE conducted on the surface of the Moon in the TLV during Apollo 17. As part of this comparison, the Apollo 17 LSPE first seismic arrival time pick data were re-evaluated using the seismic refraction analysis code which we used to analyze our SFVF data. Our analysis of the upper 600 m matched that of Heffels et al. (2017), which confirmed our refraction analysis inversion code could reproduce previous results using the identical data. Additionally, our analysis resulted in a best fit model of four distinct velocity layers in the upper 60 m. These velocities are 140 m/s, 202 m/s, 270 m/s, and 362 m/s with upper depths of 0 m, 5 m, 16 m, and 33 m. The upper of these four layers matches well with both Nakamura et al. (1975) and with Cooper et al. (1974). The lower three velocities, however, are previously unresolved seismic velocity structure and may indicate step increases in the seismic velocity

structure, but a continuously increasing seismic velocity profile cannot be dismissed as these steps fall within the 1 sigma limits of our analysis.

The use of the SFVF data as an analog to the Apollo 17 LSPE then included a 1-D seismic velocity evaluation of the SFVF from a LSPE lunar wave-length equivalent sub-set of SFVF data. The results show corresponding initial seismic velocities, but due to a lack of data points are unable to constrain the velocity structure below the upper 5 m. However, based on our calculated SFVF to TLV wavelength equivalency ratio of 0.124, we can recommend an SFVF equivalent geophone/seismometer linear array across the TLV could be constructed of 60 to 70 equally spaced receiver stations with 36 to 41 sources. An array of this design could produce a detailed 2-D subsurface seismic velocity structure, provided sufficient seismic source energy. The source energy would need to be sufficiently above any background noise as well as attenuation properties to allow receiver stations to resolve the first arrivals of the body waves along the length of the array. These results could include resolving the hypothesized fault locations within the TLV.

Overall, the SFVF fieldsite provides a geophysical analog to the Moon; with its multiple basaltic lava flows, arrangement of cinder cone vents, and fault produced features. Provided sufficient source energy to account for high background noise and attenuation, this area can be used for conducting and optimizing seismic refraction studies in a location similar to that expected to be encountered by future lunar astronauts. The methods for conducting these studies in this lunar analog environment, along with the resulting analysis techniques, can transfer to the overall planning and execution of similar field studies to be performed on the lunar surface.

### ***3.8 Acknowledgments and Data Location***

Funding for this work was provided by the NASA PSTAR grant NNX15AL87G in support of geophysical analog studies. We would like to thank the Babbitt Ranch for providing access to the fieldsite. Thanks to Ryan Porter, John West, Shannon Rees, & Jacob Richardson for their field assistance with collecting active seismic line data. Thanks to Doyeon Kim and Ross Maguire for their help to remove the instrument response from the Apollo 17 LSPE data, and to perform the power density spectrum analysis.

## **4 Active Seismic Studies on Lunar Traverses, An Example Based on a NASA Analog Human Lunar Mission**

### ***4.1 Abstract***

Lunar surface traverses during Apollo and terrestrial analog human lunar mission simulations have commonly focused on routes to locations that prioritize surface observations and sample collection activities. Along the way, geophysical measurements are often made, but not necessarily in such a way as to optimize the crucial information geophysics can provide. In 2010, NASA simulated a high-quality multi-week human lunar rover traverse analog mission in the San Francisco Volcanic Field, AZ. The traverse route and associated science station locations were selected based on addressing surface observation and sampling tasks. Geophysical studies were not included in this simulation. We returned to the same field area and obtained data on nineteen active seismic refraction geophone lines from the science station locations accessed during the simulation. We analyzed this data to create 1-D seismic velocity profiles for each of these nineteen geophone lines. The results revealed seven distinct seismic layers evident in the study area and a nearly constant veneer of regolith at the surface, along with providing details of the first 60 m of the subsurface at the specific science station locations or sub-groupings pseudo-transect positions. However, systematic interpretation of structural types could not be determined due to the non-coherent positioning of the individual locations. This provides support for synchronizing geologic subdiscipline research requirements during lunar traverse planning and execution to optimize addressing scientific and utilization questions.

## **4.2 Introduction, Motivation, and Background**

Terrestrial volcanic fields have long been used as scientific and operational analogs for the seismic studies of features similar to those that have been and will be examined on the lunar surface (Bell et al., 2018; Bleacher et al., 2015; Esmaeili et al., 2020; Garry & Bleacher, 2011; L veill , 2010). The refinement of field techniques, data analysis methods, and interpretation of results for extrapolation to the future exploration of similar locations on the lunar surface has been performed at locations such as the San Francisco Volcanic Field (SFVF), AZ. Historically, the SFVF was first used for geologic training, testing of lunar exploration hardware and vehicles, and operational concepts for the Apollo lunar missions (Lofgren et al., 2011; Phinney, 2015). The Apollo crews and Mission Control teams executed training exercises at locations within the SFVF including Cinder Lake, Merriam Crater, and Sunset Crater (Lofgren et al., 2011; National Aeronautics and Space Administration, 1969a; National Aeronautics and Space Administration, 1970; National Aeronautics and Space Administration, 1971a; National Aeronautics and Space Administration, 1972b; Phinney, 2015). This training included preparation for active seismic experiments included on Apollo 14, Apollo 16, and Apollo 17 (National Aeronautics and Space Administration, 1971a, p. 14; National Aeronautics and Space Administration, 1972b, p. 16; National Aeronautics and Space Administration, 1973a).

The SFVF region contains a variety of geomorphologic features that are similar to those of the lunar surface and therefore it provides a significant relevance for use as a lunar analog for geologic and geophysical studies, as well as for human and robotic lunar exploration tests and simulations. Geologic features found within the SFVF with similarities to the lunar surface include lava flows, volcanic vent locations (both point

and fissure cinder vents), tectonic deformation (grabens and horsts), as well as loosely consolidated soils and cinders (Skinner & Fortezzo, 2013).

The SFVF comprises an approximately 4800 square kilometer area of the southern margin of the Colorado Plateau, which is a physiographic region located within the current borders of Utah, Colorado, New Mexico, and Arizona. Elevation of this region ranges from 450 m to greater than 3800 m. The region consists of igneous intruded metamorphic rock from the Precambrian Eon that was episodically covered by tropical seas during the Paleozoic Era resulting in layering of limestone, sandstone, siltstone, and shale, and finally uplifted as much as 3 km about 20 Ma ago (USGS, 2017).

The Cataract Creek, Mesa Butte, and Bright Angel are the three regional fault systems found within the SFVF. The Cataract Creek and Mesa Butte systems, which intersect approximately 26 km to the south of our fieldsite are a focal point of local seismic and volcanic activity (Brumbaugh, 2012). Volcanism in the area began in the mid-Tertiary period with the forming of volcanic fields at the margins of the Colorado Plateau. The interior of the plateau experienced only low volume volcanic activity during this same period. The volcanism coincides with the ignimbrite flareup that resulted from the rollback of the Farallon slab at the end of the Laramid orogeny. Historically, the SFVF has been volcanically active for the past 780 kA, with eruptions occurring at a rate of approximately every 15 kA (Conway et al., 1998). The volcanism has trended primarily along the local faulting resulting in a somewhat linear arrangements of the resulting cinder cone vents (Brumbaugh, 2012; Brumbaugh et al., 2014). This has resulted in over 600 volcanic vents, cinder cones, maars, and related lava flows (Tanaka et al., 1986). Based on the remanent magnetism from over 600 samples obtained from throughout the volcanic field, Tanaka et al. (1986) concluded

that the volcanic activity within the SFVF has been steadily migrating in a north-east and east direction. The magma source is attributed to viscous heating from shearing at the base of the lithosphere from the stress of asthenospheric flow, although the possibility of multiple heat sources cannot be completely dismissed (Tanaka et al., 1986).

Geophysical research in the SFVF has included gravimetric, magnetic, heat flow, seismicity and various reflective and refractive seismic studies as reviewed by Hendricks & Plescia (1991). An example of a large-scale active seismic refraction study of the SFVF was the Pacific to Arizona Crustal Experiment that examined the velocity structure of the upper crust (Durrani et al., 1999). Their results showed a high velocity zone in the upper crust beneath San Francisco Mountain most likely related to the volcanic activity of the SFVF (Durrani et al., 1999). Chapter 3 of this dissertation provides another example of an active seismic refraction study in the SFVF. The chapter describes the use of kilometer long active nodal seismic refraction lines to study the proximity of local faults to cinder cone vents within the SFVF (Bell et al., 2019).

Active seismic techniques use an energy source, or shot, to generate seismic waves which are then recorded by geophones or seismometers. This geophysical technique can be used to analyze the layers of the subsurface by recognizing the variations in seismic velocities between geophysically different strata. The use of active seismic refraction field methods and analysis can be used to examine structure, stratigraphy, locating resources, and determining the geologic history of the upper portion of the subsurface. For these types of experiments, seismic refraction lines of three to four times the maximum target exploration depth are required (Burger et al., 2006). These active source seismic studies require precisely known timing of the shots with respect

to the subsequent receiving of the seismic signal by each geophone or seismometer. Geophysicists can analyze the seismic data from a field survey to construct a model of the subsurface, and when linked with surface derived data or core samples of the subsurface can provide a detailed geologic understanding of the fieldsite. These studies often require acquiring seismic data from a variety of locations within a fieldsite.

To date, the only experience of conducting geophysical or geologic fieldwork by humans on another planetary body was during the Apollo lunar missions of the late 1960s and early 1970s. During these missions basic seismic fieldwork performed by crews included initiating active sources via a thumper mechanism along with deployment of geophones, seismometers, and explosive energy sources (National Aeronautics and Space Administration, 1969a, p. 11; National Aeronautics and Space Administration, 1970, p. 12; National Aeronautics and Space Administration, 1971a; National Aeronautics and Space Administration, 1972b; National Aeronautics and Space Administration, 1973a). The goals of these studies included understanding both the immediate subsurface with resolution of meters to kilometers, as well as gaining an understanding of the deeper structure of the interior of the Moon (National Aeronautics and Space Administration, 1971b; National Aeronautics and Space Administration, 1972c, p. 16; National Aeronautics and Space Administration, 1973b).

These lunar studies included the Apollo Passive Seismic Experiment (PSE), which was an array of seismometers that was deployed during the Apollo 12, 14, 15, and 16 missions to use moonquakes to understand the deep interior of the lunar structure (Latham et al., 1973). The results of these deployments were an array of four seismic stations in the form of an equilateral triangle that was approximately 1100 km on a side (Latham et al., 1973). The PSE resulted in a 1-D seismic velocity model of the lunar

interior to a depth of approximately 1000 km. Active seismic experiments included the Active Seismic Experiment (ASE), flown on both Apollo 14 and 16, and the Lunar Seismic Profiling Experiment (LSPE) which was deployed during Apollo 17 (National Aeronautics and Space Administration, 1971a; National Aeronautics and Space Administration, 1972b; National Aeronautics and Space Administration, 1973a; National Aeronautics and Space Administration, 1973b). For the ASE, the crew deployed three geophones in a line with a spacing of approximately 46 m. The source for the ASE consisted of both a crew activated “thumper”, and mortar shots that were launched after crew departure from the surface (National Aeronautics and Space Administration, 1972b). The ASE results indicated a two-layer seismic model of around 100 m/s to a depth of 8 m to 12 m followed by a layer with a seismic velocity of 250 to 300 m/s (National Aeronautics and Space Administration, 1971b; National Aeronautics and Space Administration, 1972c). The LSPE, deployed in the Taurus-Littrow Valley, consisted of a small geophone array of four geophones in the form of an equilateral triangle of approximately 100 m on a side, with one geophone in the center. Eight explosive packages (EP) deployed around the Taurus-Littrow Valley during the crew’s rover’s traverses, and the discarded lunar model ascent stage were used as active sources for this experiment (National Aeronautics and Space Administration, 1973b). The LSPE results showed a structure of rapidly increasing velocity from 100 m/s at the surface to 4.7 km/s at a depth of 1.4 km (Cooper et al., 1974), with discreet steps near the surface (Heffels et al., 2017; Kovach, Robert & Watkins, Joel, 1973a, 1973b). However, the locations of these seismic studies were largely based on the serendipitous location of the actual landing site, lunar rover traverse paths, and mission durations. This did not provide for synchronizing seismic

data with geologic sampling locations to, upon analysis, provide for a more detailed model of the full geologic picture of the fieldsite. And at best, the layer cake seismic velocity models are limited by the station spacing, inversion tools, and other complexities in the data analysis, and are poorly correlated with the local geology at the lunar landing sites.

Beginning in 1997, the NASA Desert RATS test team took advantage of the lunar analog features of the SFVF region to test updated concepts for conducting geologic field science tasks on the lunar surface and to develop hardware to facilitate crew execution of these tasks, including spacesuit design evolution (Ross et al., 2013). These tests evolved in complexity and test objectives until the most elaborate of this series of field tests was conducted in 2010. In 2010 the NASA Desert RATS team combined the operational aspects of field geology into a multi-week simulated human lunar mission using a combination of advanced communication and navigation concepts, robotic operations, conceptual pressurized crew rovers, a habitable base/science lab element, and a mission control operations and science team (Eppler & Bleacher, 2013). For the primary portion of this simulation, two conceptual lunar rovers (Rover A & Rover B) were employed to transport two teams, each consisting of two crewmembers, on a traverse through the SFVF that included Black Point Lava Flow and encircled the SP crater (Hörz et al., 2013; Ross et al., 2013). The scientific objectives of the field simulations included a full-scale geologic sampling and observational study of the region covered during the rover traverse (Gruener, Lofgren, Bluethmann, & Abercromby, 2013; Hörz et al., 2013; Skinner & Fortezzo, 2013). During this traverse, the crews would periodically stop at positions termed science stations, where they would egress the rover cabin to performed simulated extravehicular activities (EVA)

or Moon-walks in this case (Gruener et al., 2013; Hörz et al., 2013). In all, the crews collected a total of 461 samples, 161.2 kg, from 38 science stations (Gruener et al., 2013).

Full priority of the traverse route, along with the locations of the science stations, was given to geologic field observation, surface analysis, and sample acquisition (Gruener et al., 2013; Hörz et al., 2013; Skinner & Fortezzo, 2013). Therefore, geophysical studies, particularly active seismic studies, were not included as part of the NASA Desert RATS 2010 lunar mission simulation. For this study we returned to the SFVF and performed active seismic refraction experiments at locations that coincide with science stations on the traverse routes the rovers followed in 2010. We also collected magnetic and GPR datasets along the traverse route that are not the focus of the study here. The SFVF study's seismic refraction experiments would be equivalent to lunar surface science operations, such as if similar experiments had been conducted along the Apollo 15, 16 or 17 rover traverse routes to seismically characterize the near-subsurface in detail at discrete points.

Our fieldsite is an approximately 50 km<sup>2</sup> portion of the SFVF centered on the SP Crater cinder cone, Figure 4.1. It is characterized by numerous cinder cone volcanoes, lava flows, rilles, and faults (Tanaka et al., 1986). This site constitutes a significant portion of the 2010 NASA Desert RATS simulation, including 19 of the science stations locations. Science stations are locations along the rover traverse path where the crews egressed the vehicles and performed geologic observations and sampling. Figure 4.1 shows an overview of our study site within the SFVF, including the simulated lunar mission science station locations, and our geophone line positions.

The ability to interpret key geophysical characteristics of the near surface, as well as understanding the impact from prioritizing of geological versus seismic, or other geophysical, tasks will be of key importance to successfully executing future lunar surface science operations and accomplishing efficient data collection and analysis. For our study we performed active seismic refraction lines at 19 science station locations commensurate with how the Apollo geophone lines were collected. We use 115-meter-long high-frequency linear geophone array lines to characterize the subsurface stratigraphy and seismic velocity structure of the upper 30 m to 60 m of the subsurface.

The results of the seismic refraction analysis inform on the impact of performing geophysical observations at these NASA simulated lunar mission locations, on increasing the overall geologic understanding of the field area. This will offer insight into the possible results on the option of using non-prioritized, non-idealized, geophysical study locations along a traverse route designed for geologic field observations and sampling. Additionally, of primary importance for this study is the use of seismic analysis to highlight key geophysical field operations issues and best practices for executing future lunar surface traverse science operations that include conducting geophysical research.

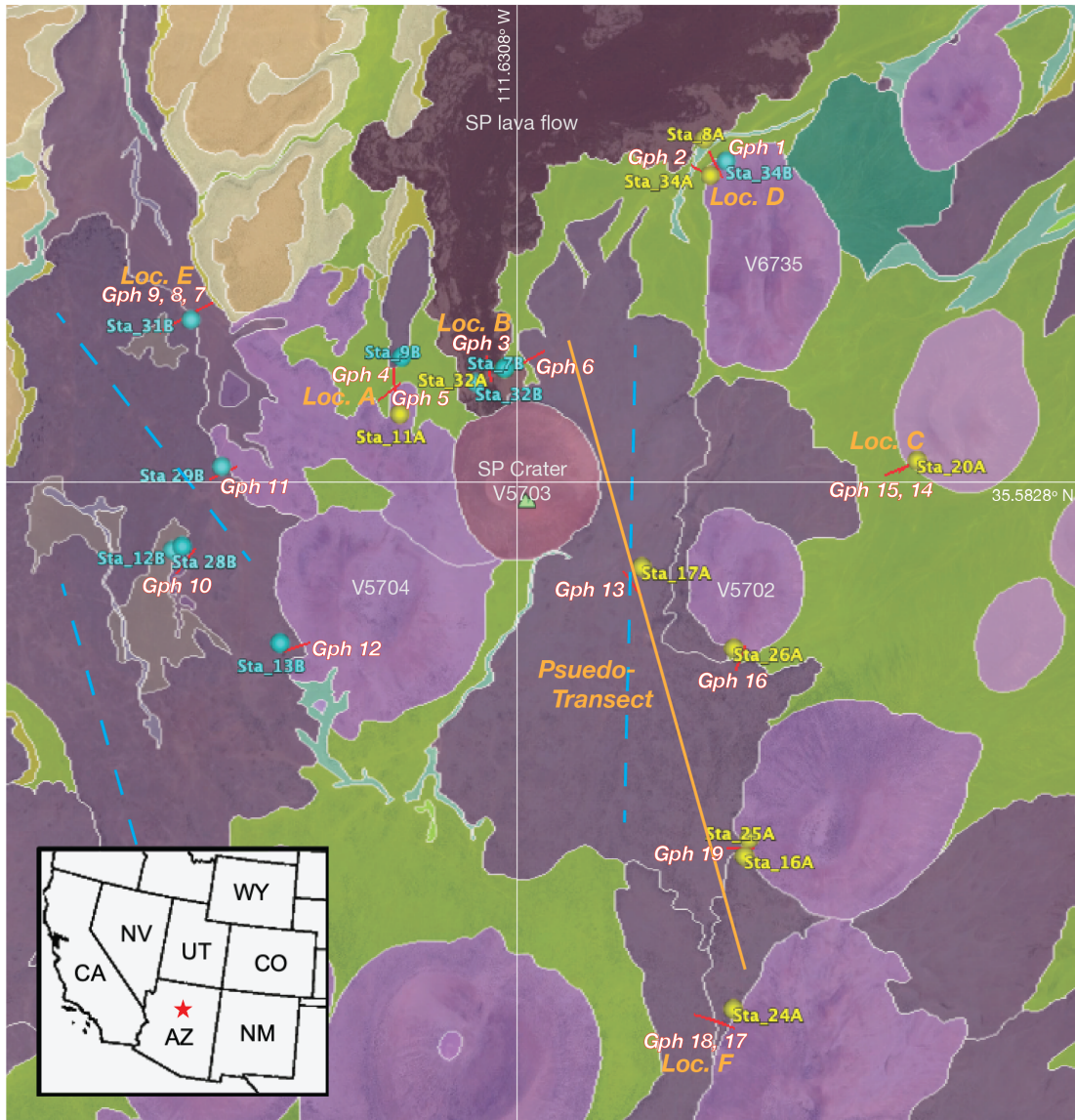


**Figure 4.1:** Overview of SFVF field area, showing geologic units as defined by Skinner & Fortezzo (2013) for the NASA Desert RATS lunar rover traverse simulation. Map modified to show science stations (blue and yellow dots, geophone lines from this study (red lines denoted as Gph #), geographic grouping locations (denoted as Loc. A thru F), pseudo-transect grouping alignments (orange line), and suggest ideal geophysical transects (dashed blue lines). Locations A-F, and pseudo-transect and suggested transect lines, are discussed in the Sections 4.6 & 4.7, and Figure 4.7.

### 4.3 Experimental Setup and Data

For this study, we conducted a series of active source seismic profiles similar to the active source experiments on Apollo 14 and 16. Our geophone lines consisted of a 115-meter line of twenty-four 4.5 Hz vertical-component geophones, spaced every 5 m, (Figure 4.2) with data collection on a multi-channel Geometrics ES-3000 datalogger. We used an active source that consisted of a manually slung 4.5-kg sledge hammer striking an approximately 0.5-meter square by 1-centimeter thick aluminum metal plate, producing seismic waves with a frequency content of 10-250 Hz. The ray paths of these seismic waves refract at velocity discontinuities and are recorded upon arrival at the geophones, illustrated by Figure 4.4C.

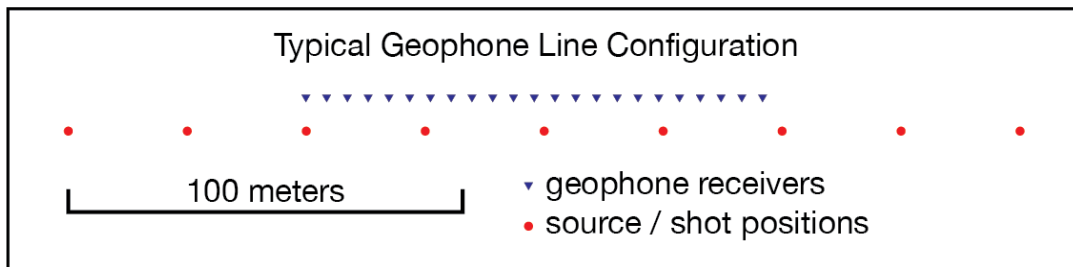


**Figure 4.2:** Geometry of typical geophone line array employed. Geophones indicated at blue triangles. Source locations indicated as red dots.

The active source experiment was repeated at 19 locations adjacent to science station locations explored during the 2010 NASA Desert RATS lunar simulation rover traverse (Figure 4.1). Prior to the field season, we selected line positions based on the criteria that 1) the line was to start within 100 m of a science station, and 2) the line was oriented to overlie as many of the accessible geologic units as possible as mapped by the geologic precursor evaluations for the NASA lunar mission simulation preparation (Skinner & Fortezzo, 2013). In the field these initial location selections were modified as needed to accommodate terrain and field observations of the area.

Photographs, which can be found in the appendix, were taken of each of the geophone lines.

The ES-3000 recording system was used to collect 1 second of data at a sampling rate of 62.5  $\mu$ s and powered in the field by 12V marine batteries (Geometrics, 2012). The geophones were coupled to the ground by pressing them into the local surface via an underlying 10 cm metal spike. When working on lava flows, sometimes it was necessary to wedge a geophone into a nearby crack or add soil to provide a coupling surface. In general, sources of noise were minimal, consisting primarily of wind and nearby field team members. There were some rarely traveled dirt roads in the area, and we would pause performing data collection until any vehicles were out of earshot. The recording time and shot source time was captured by a piezoelectric trigger attached to the hammer that initiated recording upon a manual strike of the hammer against the metal plate. The metal plate was typically placed onto the local regolith, and where the surface was too hard, we would either add some soil, or tap the plate into place to avoid a bounce or ricochet from the hammer blow. The seismic “shots” of the sledgehammer were conducted at 30-meter intervals with usual offset distances of up to 60 m prior to the first geophone and 65 m beyond the final geophone, depending on the specific terrain of a given geophone line (Figure 4.2). This resulted in a maximum source to receiver distance of 180 m in the array geometry. In total, there were usually nine shot locations, but based on terrain there were some geophone lines with only seven or eight source locations possible (Table 4.1). A GPS unit was used to record the locations for the first and last shot locations along the geophone line (Table 4.1). In all except one case 15 shots were conducted at each source location (Table 4.1). The exception was first line performed, Study Geophone Line #1, for which 10 shots per

source location was acceptable. The quantity of 15 shots per source location was selected in the field, via visual examination of the wave on the field computer to provide a sufficient signal-to-noise ratio on the final stack to positively select the recorded P-wave onset.

The initial portion of data processing occurred in the field, during the data collection, where the Geometrics® exploration seismograph software automatically stacked the seismic traces from the sequential shots at each seismic source location along the geophone line. The final dataset consisted of the results from 2,370 individual shots at 161 shot locations along 19 geophone lines, each with 24 geophones, for a total of 3,864 seismic traces after the automatic stacking.

Using the resulting stacked data traces, P-wave arrival travel times were manually selected, or picked, for each of the combinations of seismic source to geophone wave traces, for a total of between 168 and 216 (7 to 9 source locations) maximum picks per geophone line. Figure 4.3 shows a typical seismic wave move-out plot from a source location to the geophones that was used for picking the first arrival times. Most combinations were able to be picked, but some of the body wave arrivals from the further shots could not be resolved. Of the 3,864 possible picks 3,447, or 89%, were able to be selected, and are shown in Figure 4.4A, along with the best fit general seismic model accounting for all picks. Table 4.1 includes the percentage of picks able to be selected for each of the geophone lines.

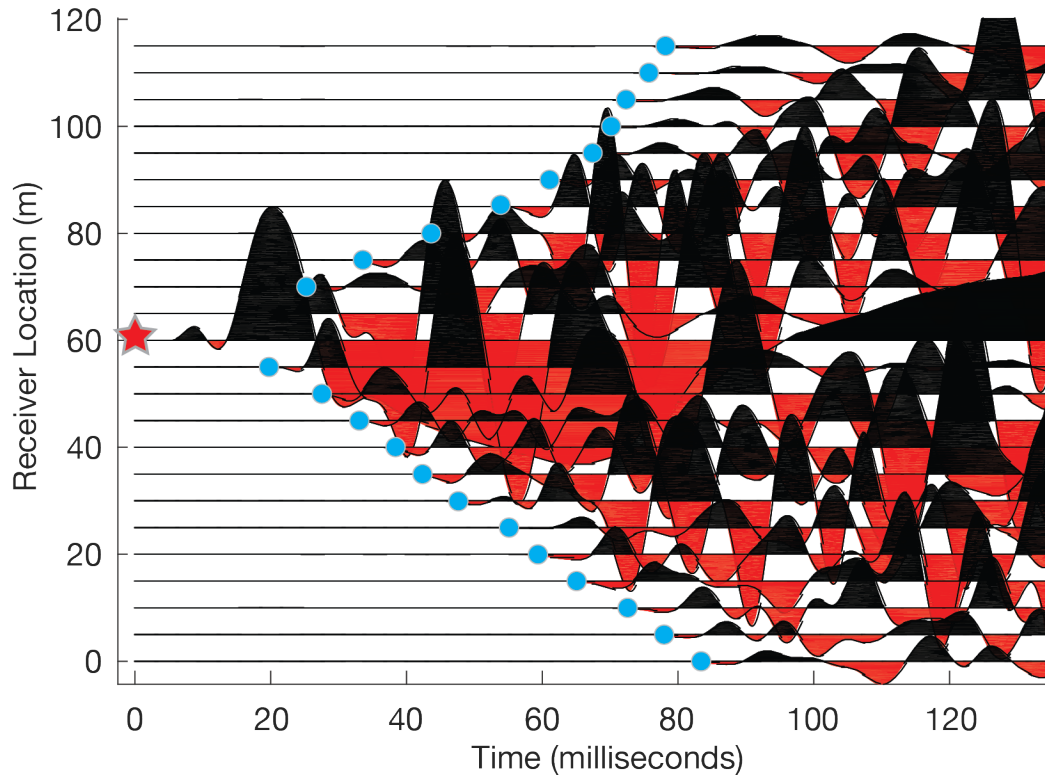


**Figure 4.3:** Example seismic wave move-out plot of seismic wave arrivals for each of the 24 geophone receivers for study geophone line #7. Individual waves are normalized against their maximum. Y-axis indicates location of the 24 geophone receivers (0 m equal to first geophone). X-axis indicates time from shot occurrence. Red star is location of shot. Blue circles indicate example picks of first arrivals. On individual waves, black fill indicates positive and red fill indicates negative arrivals.

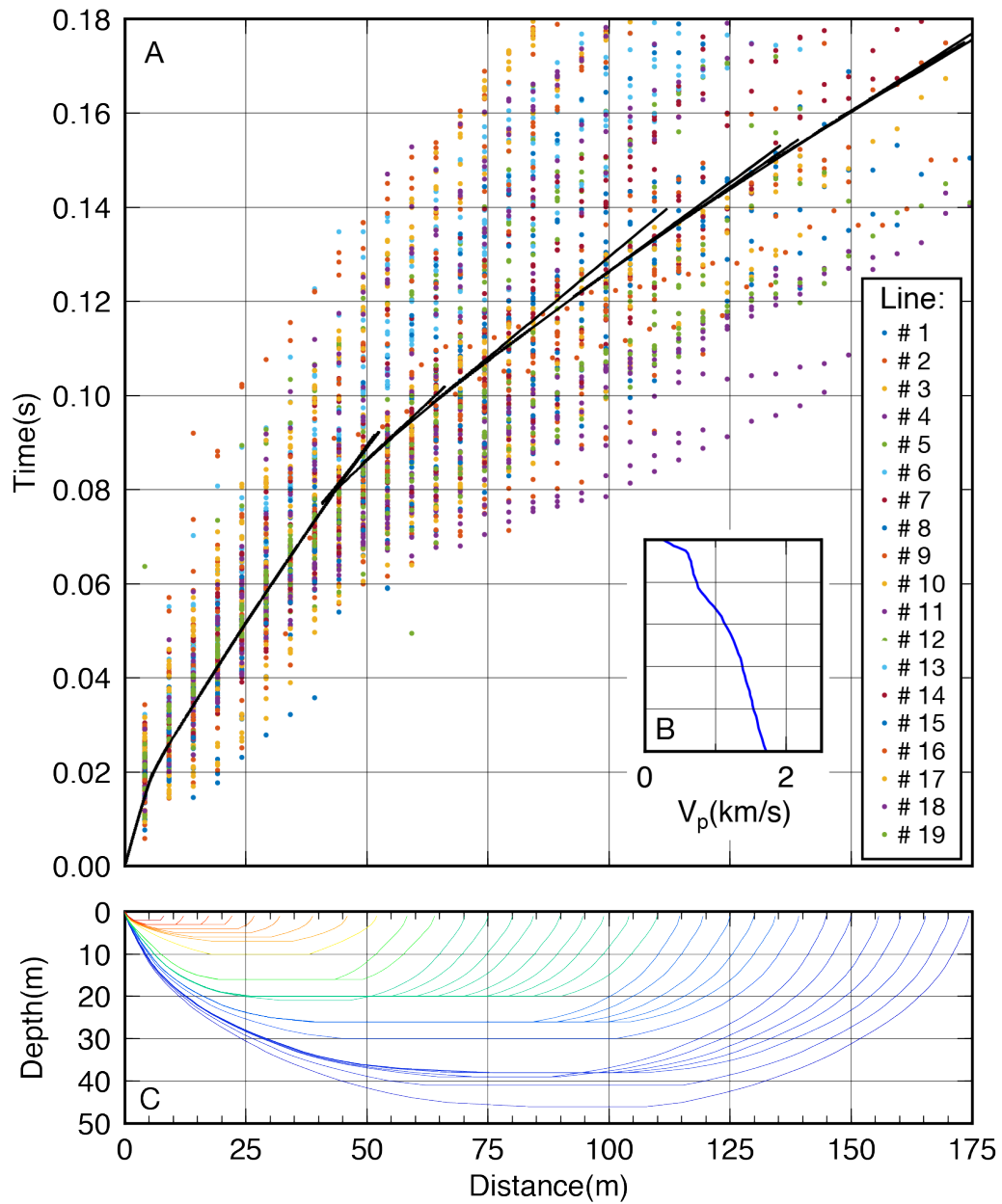


**Figure 4.4:** Travel time picks, average velocity model, and example seismic ray paths. A) Plot of all 3,447 travel time picks from all nineteen geophone lines, along with best fit travel time model. Scatter of arrival time picks is representative of the range of subsurface structure encountered across the nineteen geophone line locations. B) Seismic velocity model of best fit travel time model from A. C) Theoretical seismic ray paths for the P-waves traveling in model B. Note rays bottom at between 40 and 50 m, providing confidence in the velocity models to 50 m depth.

**Table 4.1:** Details of geophone lines. Left to right, the line number as designated in this study, latitude & longitude of first and last source location, maximum offset distance (negative distance) from first geophone, maximum offset distance (positive distance) from final geophone, maximum change in elevation between first and last source locations, and the percentage of first arrival picks that were able to be selected.

Study Geophone Line #	Start Latitude	Start Longitude	End Latitude	End Longitude	Neg. Offset (m)	Pos. Offset (m)	Max. Source Delta Elev. (m)	% Picks Made
1	35 36' 16.1"	111 36' 53.0"	35 36' 19.5"	111 36' 55.1"	-60	+65	31	83%
2	35 36' 16.7"	111 36' 59.6"	35 36' 14.6"	111 36' 55.8"	-60	+65	24	79%
3	35 35' 24.3"	111 38' 03.2"	35 35' 28.5"	111 38' 09.0"	-60	+35	10	80%
4	35 35' 25.3"	111 38' 32.6"	35 35' 25.3"	111 38' 32.3"	-30	+35	15	99%
5	35 35' 21.4"	111 38' 32.4"	35 35' 19.0"	111 38' 35.9"	-60	+35	14	83%
6	35 35' 28.3"	111 37' 51.7"	35 35' 28.1"	111 37' 51.5"	-30	+35	4	100%
7	35 35' 41.9"	111 39' 30.5"	35 35' 40.1"	111 39' 34.6"	-60	+65	10	91%
8	35 35' 40.1"	111 39' 34.5"	35 35' 38.3"	111 39' 38.6"	-60	+65	7	85%
9	35 35' 38.3"	111 39' 38.5"	35 35' 36.3"	111 39' 42.4"	-60	+65	7	94%
10	35 34' 39.7"	111 39' 34.1"	35 34' 36.8"	111 39' 36.4"	-60	+65	5	91%
11	35 34' 59.2"	111 39' 26.5"	35 34' 00.7"	111 39' 22.3"	-60	+65	13	97%
12	35 34' 16.1"	111 39' 03.4"	35 34' 17.1"	111 38' 59.1"	-60	+65	37	75%
13	35 34' 34.2"	111 37' 20.6"	35 34' 31.1"	111 37' 17.9"	-60	+65	3	92%
14	35 35' 01.7"	111 35' 55.5"	35 35' 03.5"	111 35' 51.5"	-60	+35	12	99%
15	35 35' 01.8"	111 35' 55.5"	35 35' 00.3"	111 35' 59.8"	-60	+65	3	55%
16	35 34' 12.5"	111 36' 46.8"	35 34' 16.0"	111 36' 45.1"	-60	+35	16	99%
17	35 32' 44.4"	111 36' 53.4"	35 32' 43.3"	111 36' 49.1"	-60	+35	13	99%
18	35 32' 44.5"	111 36' 53.3"	35 32' 45.5"	111 36' 57.8"	-60	+65	3	100%
19	35 33' 27.0"	111 36' 47.8"	35 33' 27.0"	111 36' 43.3"	-60	+35	20	100%

#### ***4.4 1-D Seismic Inversion***

The P-wave refraction travel time picks from each seismic profile in the SFVF were analyzed using a 1-D seismic Bayesian inversion method (Montgomery et al., 2017) to determine the one-dimensional subsurface seismic structure beneath each geophone line. This code assumes all sources and geophones are at the same elevation, which is not the true case for our lines. However, for the purposes of this study, to evaluate inclusion of geophysical field studies on lunar surface traverses we are accepting the impacts to the resulting models from not taking this into account. The 1-dimensional Bayesian refraction inversion code constructs an ensemble of models from

which we can determine the most likely P-wave seismic velocity structure in the upper 60 m of the subsurface at one-sigma uncertainty level. For the analysis, it is assumed there is increasing velocity with depth (Montgomery et al., 2017).

The processing uses a reversible-jump Markov chain Monte Carlo methodology to create an ensemble of layered models (Green, 1995). To initiate the code, we specified the following priors for the final runs. The velocity range from 0 to 4,000 m/s was selected to encompass the expected seismic velocities for the area (Burger et al., 2006). A maximum depth of 60 m was chosen based on the expected maximum resolved depth for an active source refraction line being approximately one-third to one-fourth the total source line length, which, in all but two cases, was 210 m or 240 m for our study (Burger et al., 2006). Based on an initial quick-look analysis these velocity and depth ranges were acceptable as the standard deviation in mean velocity begins increasing by a depth of 50 m. A maximum of 20 discrete layers were permitted in the model, which is well above the resulting quantities for the models. The initial velocity model, which is simply a starting point from which the inversion quickly deviates to best fit models, was a six-layer profile with velocities of 200, 450, 600, 750, 900, and 4000 m/s at corresponding upper depths of 0 m, 10 m, 20 m, 30 m, 40 m, and 60 m. We set our inversions to run for 1,000,000 iterations to provide a satisfactory quantity of models from which to create the ensemble.

For each iteration, Figure 4.5, of the algorithm, a new model is formed based on changing one parameter from the previous model. At the beginning of each iteration, one of the following modifications will be performed: addition or removal of a layer,

change in depth of a layer, or changing a layer's seismic velocity. Then, using the new

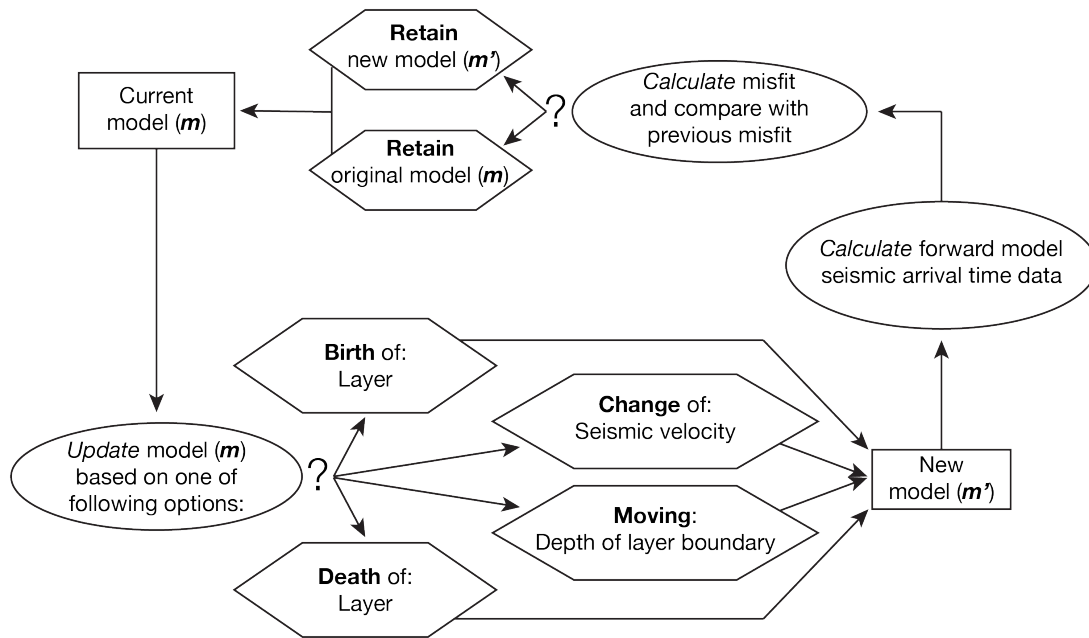


**Figure 4.5:** Schematic overview of seismic refraction Markov chain Monte Carlo inversion algorithm iteration.

model, the P-wave arrival times at each geophone are calculated using a fast-marching algorithm. The arrival times are compared to the recorded data and the proposed model is then either accepted or rejected according to the Metropolis-Hastings algorithm (Metropolis et al., 1953; Sethian, 1996). In other words, the new proposed model is retained if it results in a smaller misfit between the modeled and recorded seismic wave arrival times. If the misfit is higher, then the new proposed model will be retained with a probability depending on the misfit. Throughout the processing the current model is saved to an ensemble at an interval of once every 500 iterations. The frequency with which the parameters of a given model appear in the ensemble is proportional to its posterior probability. The final ensemble consisted of 2000 saved iterations, and is used to calculate the overall final statistical analysis (Montgomery et al., 2017). The ensemble includes the discrete velocity structure (velocity and depth of each layer) from each of the saved iterations. The results captured in the ensemble are used to

evaluate for the mean and standard deviation of the seismic velocity profile, and determine the most probable depths for discrete step changes in seismic velocities.

#### ***4.5 Results***

For each of the nineteen geophone lines, we describe the surface context and physiographic area surrounding each of the locations in Table 4.2. The descriptions of the locations vary in combinations of colluvium, scoria, ash, cinders, pebbles, cobbles, and boulder sized basalt. Impacts of weathering on the basalt ranges from smooth and rounded to rough and blocky. Some locations contain basaltic outcroppings. Vegetation combinations include sparse grass, low brush, and juniper trees. The physiographic groupings range from on or near cinder cones, to locations on open lava flows, to portions of washes.

**Table 4.2:** Surface context and physiographic location descriptions for the nineteen geophone line locations. Color coded by physiographic descriptions.

Study Geophone Line #	Surface Description	Physiographic Description
1	northern end: weathered cinder & colluvium; minimal grass southern end: northern slope of V6735, blocky basalt w/ colluvium; denser grass & low-lying brush; uphill to south	Cinder cone edge
2	mix of soil, ash, cinder, pieces of basalt, possibly on lava flow from V6735; grass & a few small junipers at south-eastern end; south-eastern end: uphill on northern slope of V6735	Cinder cone edge
3	SP lava flow; grass covered with cinders, blocky basalt, & weathered basalt pebbles & cobbles; fairly flat	SP lava flow
4	ash, cinders and colluvium; grass & low-lying brush; set axially on a possible small alluvial fan from saddle between SP & V5704; uphill to the south	Lower saddle of SP & V5704
5	ash, cinders and colluvium; grass & low-lying brush; set perpendicular across a possible small alluvial fan from saddle between SP & V5704; fairly flat	Lower saddle of SP & V5704
6	ash, cinders, pebbles, and colluvium; western end in a wash; eastern end: elevated over a rise from the wash; grass; flat	Wash on lava flow
7	wash of colluvium and ash; low & sparse grass; eastern end at base of ~ 6m Kaibab limestone rise; flat	Wash on a lava flow
8	wash of colluvium and ash; low & sparse grass; western end slight rise out of wash with taller grass & larger rough cobble & boulder sized pieces of basalt mixed in; flat	Wash on a lava flow
9	larger rough cobble & boulder sized pieces of basalt mixed in the colluvium and ash/soil; multi-meter (1-3m) sized vertical basaltic outcrops; likely part of a lava flow; flat	Wash on a lava flow
10	colluvium of ash, and rough pebble, cobble, & boulder sized basalt; line intersects through area of large vertical outcrops of basalt (few to 10+ m wide x few to 10+ m high); grass; flat	Lava flow w/ basalt formations
11	colluvium of ash and rough pebble & cobble sized basalt; eastern end rises up towards outcrops of basalt (meter sized); grass	Lava flow w/ basalt formations
12	western side of V5704; ash, cinders, rough pebble & cobble sized basalt; grass, and very few juniper	Cinder cone edge
13	ash, cinders, & pebble sized basalt; likely middle of old lava flow; grass; flat	Lava flow
14	ash, cinders, & rough pebble sized basalt; grass; eastern end rises onto cinder cone	Cinder cone edge
15	cinders & rough pebble sized basalt; grass; flat	Lava flow adjacent to cinder cone
16	northern end: cinders & rough pebble sized basalt; southern end: colluvium, cinders, rough pebble, cobble, & boulder sized basalt; grass, some low brush & juniper; northern end rises onto cinder cone	Cinder cone edge
17	colluvium, soil, cinders, rough pebble & cobble sized basalt; eastern end: rises slightly onto cinder cone; grass, low brush, and juniper;	Cinder cone edge
18	colluvium, ash, cinders, rough pebble, cobble & boulder sized basalt; grass, few low brush and juniper; flat	Lava flow adjacent to cinder cone
19	cinders & rough pebble sized basalt; eastern end: rises onto cinder cone; grass, sparse juniper	Cinder cone edge

Using the velocity profiles ensembles created from the seismic refraction analysis, we created the histogram seen in Figure 4.6 to determine the various specific velocity layers revealed from the nineteen geophone line locations. This results in seven distinct seismic velocity layers with statistical characteristics and geophysical interpretation provided in Table 4.3.

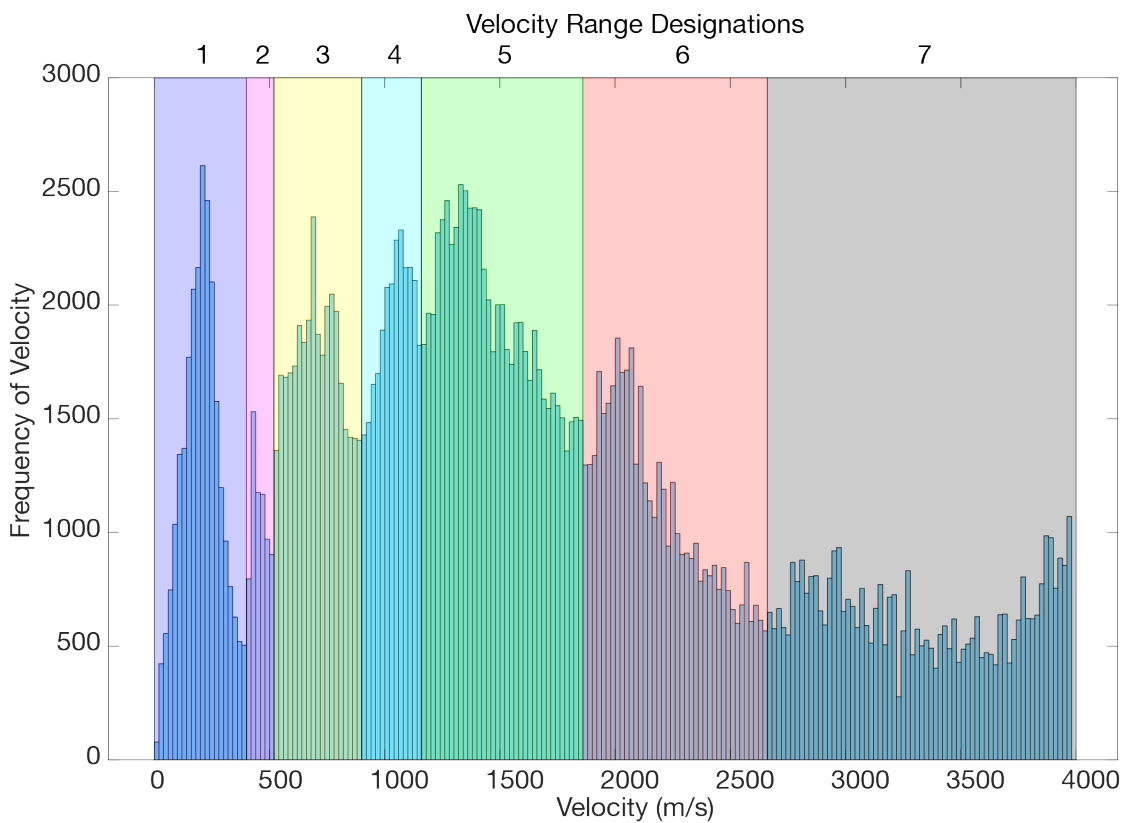


**Figure 4.6:** Histogram of velocities from all 19 geophone line refraction analysis ensembles. Velocity ranges shown by colored regions and designated as 1 thru 7. Statistical details and interpretations listed in Table 4.3. Velocity range designations and colors match those used in the Figure 4.7 mean seismic velocity plots, and used for interpretations and discussion in Section 4.6.

**Table 4.3:** Statistical details and interpretation of seismic velocity layers. All values in m/s. Column definitions are, *Range*: seismic layer designation; *Min. & Max. Vel.*: minimum and maximum velocities of layer; *Mean*: mean of the velocity range; *SD*: standard deviation of the velocity range; *Median*: median of the velocity range; *Mode*: mode of the velocity range; *Interpretation*: geophysical interpretation of the velocity range with descriptions provided in the section 4.6 Interpretation and Discussion; *Reference Velocity Range*: expected P-wave seismic velocity based on previous studies; \*Watkins, 1965; \*\*Kring, 2017.

Range	Min. Vel.	Max. Vel.	Mean	SD	Median	Mode	Interpretation	Reference Velocity Range
1	0	400	206	83	208	211	Regolith	~240 To 370+*
2	400	520	458	32	456	430	Cinder	-
3	520	900	707	103	704	690	Fracture lava	~750 To 1200*
4	900	1160	1038	71	1043	1050	Fractured to consolidated transition	
5	1160	1860	1481	195	1460	1330	Consolidated lava group 1	<1550*
6	1860	2660	2189	219	2148	2010	Consolidated lava group 2	-
7	2660	4000	3411	442	3417	3990	Country rock (Kaibab limestone)	4167 +/- 1129**

The plotted results for the 1-D mean velocity and standard deviation of the mean for all 19 geophone lines are shown in Figure 4.7. The profiles are arranged to illustrate any geographical coherency with respect to adjacent positions, or pseudo-transect based on nearly linear, serendipitous, arrangement of the geophone line positions along a specific lava flow as mapped in Figure 4.1. This arrangement provides for easier interpretation of trends with respect to geographical locations. The individual 1-D seismic profiles are labelled by this study's geophone line number. Traceability to line designations used in the field, and to the NASA Desert RATS simulation science stations, can be found in the appendix along with photographs of each of the lines.

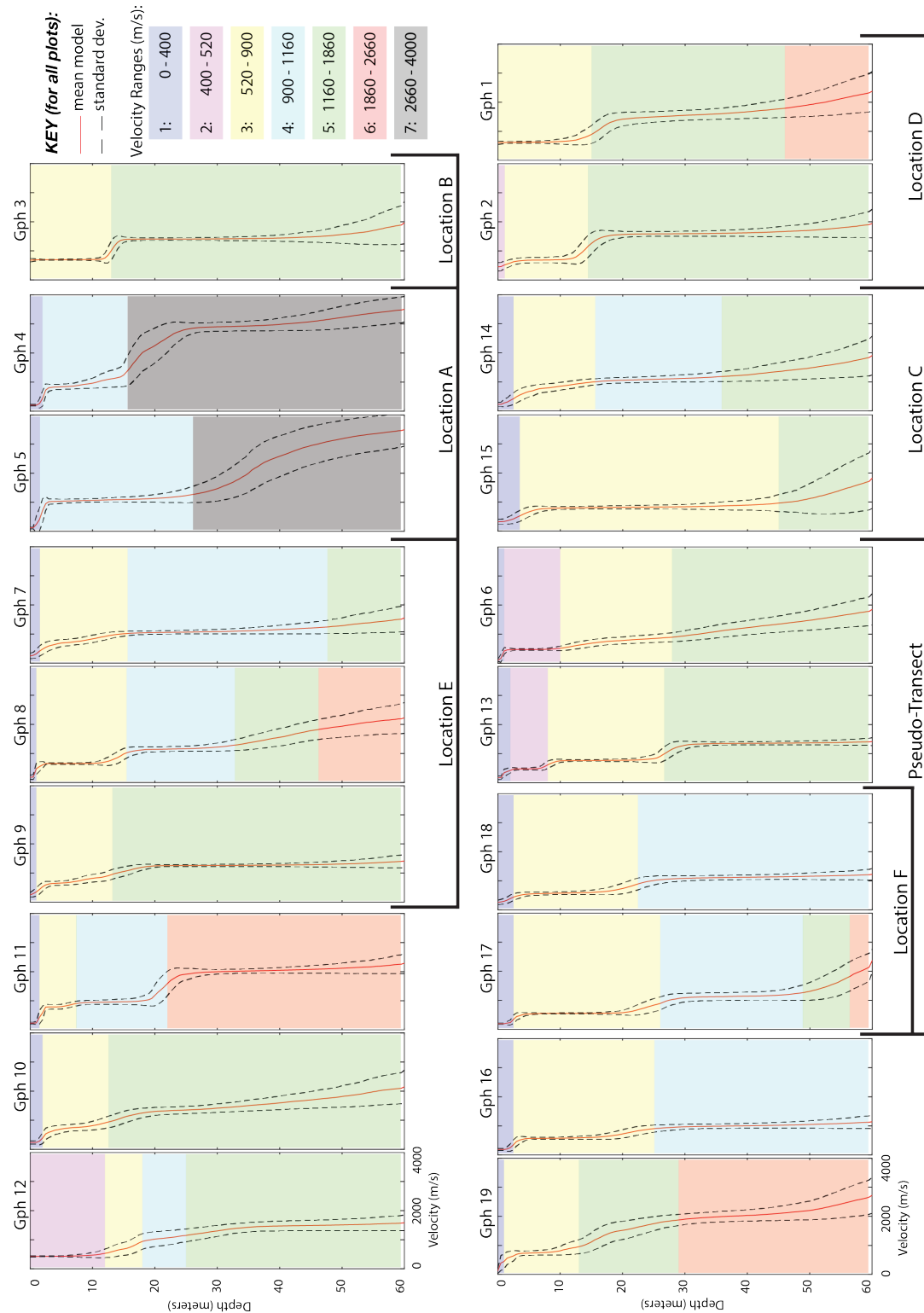


**Figure 4.7:** Study geophone line #'s (Gph) 1 thru 19, 1-D seismic velocity profiles of mean and standard deviations for the mean velocity organized according to geographic locations along one pseudo-transect, six geographic location groups (Location A thru F), or individual positions. Depth and velocity scales are the same for all plots.

## ***4.6 Interpretation and Discussion***

Our refraction analysis reveals seven distinct seismic velocity ranges, as shown in Figure 4.6, and defined in Table 4.3. The initial six of these ranges are clearly evident with the peaks and valleys in the histogram shown in Figure 4.6, with the statistical details for each range provided in Table 4.3. We interpret velocity range 1, an ultra-slow zone with a mean velocity of 206 m/s, to be equivalent to a regolith layer consisting of unconsolidated colluvium, ash, scoria, and cinders from the surrounding cinder cone vents. This layer is fairly ubiquitous across the surface of our field area, and consistent with observed basaltic ash velocities between 240 and 370 m/s (Watkins, De Bremaecker, Loney, Whitcomb, & Godson, 1965). From examination of the 1-D velocity profiles in Figure 4.7, the regolith layer is typically in the upper 1 m to 3 m, with the exception of four locations, across the locations analyzed. Of the four locations the regolith layer is absent from; Gph 1, 2, 3, & 12; three of these are on the edges of cinder cones, and the fourth is on the young SP lava flow. Our interpretation is that the edges of the cinder cones aid in the removal of any accumulated regolith via fluvial processes. For the SP lava flow, we interpret the lack of a regolith layer to be a result of its elevated surface of greater than 10 m above the surrounding region it sits on combined with the blockiness of the flow resulting in any regolith formed or deposited onto it being transported into the voids of the lava flow itself.

Velocity range 2 is defined between 400 to 520 m/s. We interpret this range to be primarily cinder, possibly including ash and filling an upper highly fractured basalt layer. This may be a transitional composition between range 1 and range 3, and is above observed basaltic ash velocities of 240 and 370 m/s, and the velocities of fractured lava which are known to begin at 750 m/s (Watkins et al., 1965). Rationale for this

interpretation is from the four locations where it is present. Of these, location Gph 2 was located on a possible flow of lava from cinder cone V6735 but was noted to have a surface of ash and cinders. Gph 6 & 13 were located on a lava flow, with noted ash, cinders, and pebble sized basalt at the surface. The fourth location, Gph 12 was previously noted to be at the edge of a cinder cone, but this location is abutted by a lava flow covered with ash, cinders, and smooth cobbles.

Velocity range 3 is bounded between 520 to 900 m/s. We interpret this velocity layer to consist of primarily fractured basaltic lava flow, which is consistent to previously collected in-situ velocity range of 750 to 1200 m/s (Watkins et al., 1965). All but Gph 4 & 5 see this velocity layer in the 1-D profiles. The primary indication of the interpretation of this velocity layer is based on the profile from Gph 3 on the SP lava flow, near the base of SP Crater. The 1-D velocity profile for Gph 3 consists of an initial layer of this velocity range (range 3), to a depth of approximately 13 m. This depth is thicker than, but approximately matches, the visually apparent height of the SP flow on which Gph 3 was set. This lava flow is observed to consist of large fractured blocky basaltic.

Velocity range 4 is a tight range of 900 to 1160 m/s. Our interpretation of this velocity layer is that it is likely a transitional layer from the fractured basalt of velocity range 3, to consolidating lava flows of velocity ranges 5 & 6. It is also possible that it is simply a less fractured portion of the lava flow based on the 750 to 1200 m/s range for fractured lava flows as defined Watkins, 1965. About half of the nineteen locations have a notable layer of velocity range 4. Overlapping standard deviations of the mean velocities between this range 4 and the next, range 5, provide evidence that this is a transitional layer into consolidated basalt.

Velocity ranges 5 and 6, are interpreted to be layers of increasing consolidation of lava flows. Velocity range 5 encompasses velocities from 1160 to 1860 m/s, and velocity range 6 bounded from 1860 to 2660 m/s. These two velocity ranges likely are two unique layers, as their standard deviation of mean velocities do not overlap, indicating a distinct transition of the structures forming the two layers. It is possible that velocity range 5 is still consists of basaltic lava flow, which is expected to be less than 1550 m/s (Watkins et al., 1965), while velocity range 6 may be more of a transitional layer of a more complicated construction based on its higher velocity.

Finally, velocity range 7 includes any velocities above 2660 m/s, and has a mean of 3411 m/s, and is interpreted to indicate country rock. The country rock consists of the basement sedimentary rock in the area, primarily the Kaibab limestone, which has a previously documented seismic velocity of 4167 m/s with a standard deviation of +/- 1129 m/s (Kring, 2017). We see this velocity layer only in Gph 4 & 5, Location A on Figure 4.1, with 1-D velocity profiles shown in Figure 4.7. This layer is likely limestone based on the close proximity of these lines to the location of Kaibab limestone visually observed to the northeast of the Gph 4 & 5 locations. Below 50 m these two velocity profiles, at Location A, both have mean velocities that approach, and standard deviation of the mean velocity that exceeds, the analysis prior maximum velocity of 4,000 m/s. Therefore, it is possible that the actual maximum velocity of these two profiles is greater than 4,000 m/s. Resolving this discrepancy will not however ultimately affect the velocity range groupings or designations for the overall study, as the minimum velocity for this grouping will remain the same.

Along with Location A, we identify five additional geophone lines locations and one potential pseudo-transect, all of which are shown on Figure 4.1, with their 1-D

seismic velocity profiles shown in Figure 4.7. The first is Location B, Gph 3 set on the SP lava flow. Gph 3 shows a very distinct 2-layer model where we have already discussed the depth of the top layer, of velocity range 3, being slightly larger than the visually noticeable topographic height for this lava flow. We suggest that this indicates a possible buildup around the perimeter of the lava flow, post-emplacment, and/or the lava flow itself having thermally eroded the ground beneath during emplacment. The second layer, beginning at a depth of 13 m is in velocity range 5, which we interpret is likely an older lava flow of consolidated material.

Location D, consisting of Gph 1 & 2 are nearly in parallel on the northern extent of cinder cone V6735. These both show a velocity range 3 layer of fractured basalt to a consistent depth of approximately 15 m, at which point we interpret a layer of consolidated lava to begin. The primary difference near the surface is a layer of regolith being apparent on Gph2.

Location E, is a series of three geophone lines, Gph 9, 8, & 7, from west to east. Here there is a consistent regolith layer followed by a fractured basalt layer, velocity range 3, to a depth of about 15 m. At this depth Gph 9 jumps to the higher velocity range 5, interpreted as a consolidated lava flow layer, which coincides with its position on the edge of a lava flow. For Gph 8 & 7, however, the next layer consists of the slower velocity range 4, is likely a result of their location in a wash of lower elevation than Gph 9, likely off the lava flow of higher seismic velocity seen by Gph 9.

The final location is Location F, which includes Gph 18 & 17, west to east. These two lines were performed in series from the edge of a cinder cone, with Line 17 rising

slightly onto the cone. These two show a consistent 2 to 3 meter regolith layer followed by the transitional layer, velocity range 4. They apparently skip a fractured basalt layer.

The one pseudo-transect consists of the point analysis from Gph 17, 18, 13 & 6, with Gph 17 & 18 simultaneously grouped together, positioned south to north along what appears to be the same lava flow. By connecting the seismic layers between the analysis of the individual geophone lines we can provide an interpretation of larger scale variation of the layer thicknesses along this specific lava flow versus the point interpretations at the individual geophone line locations. We interpret the results to show a consistent 2 to 3 meter thick upper layer of regolith along this transect. This layer sits atop a variable 15 to 20 meter thick fractured lava flow. A layer of cinder and colluvium, possibly filling highly broken basalt is seen between the regolith and fractured lava in the northern two profiles, Gph 13 & 6. This may indicate two distinct overlapping lava flows at the northern portion of this lava flow.

Overall, a variety of units were geophysically explored by conducting active seismic refraction lines at the 19 locations adjacent to the NASA simulation science stations. The results for our 1-D analysis is a best fit average of the structure beneath each of the geophone lines. However, there are several details which we do not account for in the 1-D seismic analysis. These details contribute to the variation of the misfit, or standard deviation, seen from one 1-D velocity profile to another, as seen in Figure 4.7. It can be seen that between the lines some, such as Gph 9, Gph 12, Gph 16, Gph 18, and Gph 13 have a very narrow standard deviation for the entire depth of the analysis, indicating a well constrained and consistent data set in both the forward and reverse ray path directions of their refraction lines. Other lines show more deviation from the mean at shallower depths, for example Gph 3, Gph 5, and Gph 15. One of the

primary items we do not account for is any 2-D heterogeneity of the subsurface along the seismic refraction lines. Instead, we assume a homogeneous layering of seismic strata beneath each of the geophone lines. Based on the variation in 1-D velocity structure between the geophone line locations, there likely exists some heterogeneity at each location because of the multiple overlapping lava flows, and cinder cone constructs. These 2-D variations in the subsurface can result in a difference in the travel times for the forward and reverse shot directions between the same locations which will increase the uncertainty in the 1-D velocity profile analysis. Additionally, we do not account for the effects of the topography of the terrain in the analysis. For 15 of the lines, the maximum elevation change along the line shot positions is less than 16 m. For the other 4 lines the maximum elevation change ranges from 20 m to 37 m. The elevation change would result in seismic waves arriving earlier from one direction (forward), and later from the other direction (reverse) than expected for a level surface. Finally, refraction analysis requires the assumption of a continual increase of velocity with depth (Burger et al., 2006). It is possible for lower level lava flows, or buried regolith layers, to consist of more vesicular or variable density lava that would result in layers of slower velocity. However, this possibility might be countered by compaction and in-fill of the lower layers as additional layers were emplaced on top. Therefore, the use of increasing velocity with depth is an acceptable assumption, and required for this seismic refraction analysis. Otherwise, seismic reflection and surface wave analysis is required to resolve layers with reduced seismic velocity with depth.

From a geophysical study perspective, the selected geophone line locations resulting from the position of the NASA simulation science stations were primarily at contacts between the geologic units mapped for the NASA simulated lunar traverse, as

seen in Figure 4.1 (Skinner & Fortezzo, 2013). A 2-D analysis, which we did not perform, is required to examine any seismic variability between the specific surface geologic units. We suggest that a similar application of targeted locations on the Moon would produce increased understanding of specific geophysical questions or features. Examples of this would be to target collecting multiple data points of specific lunar volcanic field features, such as the cinder cone structure, or to prescribe transect points, such as suggested by dashed blue lines in Figure 4.1, along a traverse route to examine individual lava flows for their thicknesses and layers.

In addition, this study can be used to underscore important considerations and best practices for executing geophysical studies as part of human lunar surface science traverses analogous to that simulated by NASA in 2010. These items involve both the operations by the crew, as well as the coordination of information between the crew and mission control.

From a historical standpoint of lunar surface science, the execution of our geophone line operations is very analogous to the active seismic experiment (ASE) operations performed during Apollo 14 and 16. For both of these Apollo missions a geophone line, of three geophones intervals of 46 m, was deployed. An astronaut activated source comprised the use of a thumper device that contained 21 small explosive charges. During thumper operations one crewmember would fire the thumper. The other crewmember was instructed to remain still from 20 or 10 seconds prior to a thumper firing, through 5 or 10 seconds after a thumper firing (times for Apollo 14 and 16 respectively). This was based on Apollo 14 operations where realtime data, to Mission Control scientists, indicated that the movement of the second crewmember generated seismic energy that obstructed the observation of the thumper

firings (National Aeronautics and Space Administration, 1971b). Thumper firings were executed at predetermined intervals, usually about 4.6 (Apollo 14) or 4.75 (Apollo 16) meters apart, between geophone 3 to geophone 1.

There were several issues that occurred during these Apollo ASE lunar surface operations that are worth discussing, and comparing to our field experience (National Aeronautics and Space Administration, 1971b; National Aeronautics and Space Administration, 1972c). During Apollo 14, there were multiple source locations where the thumper failed to fire (National Aeronautics and Space Administration, 1971b). During Apollo 16, two attempts were required at one source location. From the data, this was determined to be an operator error of not properly arming the thumper versus being an equipment malfunction (National Aeronautics and Space Administration, 1972c). These types of failures can be compared to issues we had with executing shots during our fieldwork. For example, our shot issues included improperly executed hammer blows (glancing or bounced hammer strike) resulting in poor quality seismic waves. Also, the trigger, attached to the hammer which was used to indicate the time of shot occurrence, would occasionally fail to signal a shot. These issues were noted by the team member at the recording computer and relayed to the person conducting the shot. In both the Apollo and our SFVF cases, realtime feedback, to the person conducting the shot, allows for a repeat of the shot, preventing the loss of a data point, with the impact being the use of additional time. However, in the case where each shot source is a consumable, this could result in the loss of a future shot opportunity.

A second issue occurring during Apollo 14, of which we saw similar instances, had to do with the coupling of the geophone into the surface. During Apollo 14, although there was no issue with implanting the geophones into the regolith, the middle

geophone (#2) did pull out of the ground, possibly because of the elastic memory of the connecting cable. This issue was noted by the crewmember when beginning thumper operations at the geophone 3 location. However, based on a decision by Mission Control scientists it was not resolved until the crewmember reached geophone 2 due to time constraints. (National Aeronautics and Space Administration, 1971b) We experienced similar issues with geophones in the SFVF. Our issues included geophones needing to be re-implanted to provide better coupling, being accidentally pulled out of the ground by the field team walking up the line, and failed geophone sensors. In most cases each of these issues were noticed during the first few shots by the team member at the recording computer. This permitted the anomalous geophone to be troubleshot and the problem corrected. The primary impact was a loss of time to correct the issue and to repeat any affected shots. Sufficient spare components and instrument redundancy can help reduce data loss in these cases, but the criticality for this capability will need to be weighed against impacts to the mission timeline, mass, power, and data capacity.

For our field operations in the SFVF, the primary impact to issues was loss of time for problem recognition, troubleshooting, resolution, and repeating of failed actions. We had sufficient field days scheduled to absorb this time without reducing the planned amount of data collection. However, this is not always the case in terrestrial field operations, and is a significant issue for human spaceflight mission plans. For lunar EVA operations, increasing the time required to complete a task can have significant impacts to accomplishing mission objectives. This is highlighted by the crew of Apollo 14 not having the time to re-implant the geophone 2 until the thumper operations coincided with the location of the geophone (National Aeronautics and Space

Administration, 1971b). From a geophysical science perspective, the geophone would have ideally been re-implanted when the issue was recognized and prior to additional data collection. However, the time it would have taken for this was apparently deemed to be beyond what was acceptable to not impact the execution of additional tasks during the extravehicular activity (EVA).

From a data analysis standpoint, there are two items of note from the Apollo 14 and 16 ASE with respect to picking first arrivals of the seismic waves. The first is that the seismic signal received from a thumper firing within 9 m of a geophones saturated the dynamic range of the sensor. The second is that the seismic signal received beyond 41 m to 46 m from a thumper firing introduce significantly more error when picking the first arrival (National Aeronautics and Space Administration, 1971b; National Aeronautics and Space Administration, 1972c). Both of these issues result in difficulty resolving and picking first arrivals. At the time, the unknown properties of the lunar surface resulted in a best estimate for sizing of the thumper explosive charges and capability of the geophones (National Aeronautics and Space Administration, 1971b; National Aeronautics and Space Administration, 1972c). However, current knowledge of the lunar surface should provide for updated geophone and seismic source technology that can result in acceptable data from near as well as further locations. An option could include conducting multiple shots at further locations for stacking of seismic waves. This could be coupled with realtime feedback to the crew to verify when the data quality standard is met, either per source location or to create a standard shot quantity based on the actual field conditions. This would be equivalent to our use of the first and second geophone lines, Gph 1 & 2, in the SFVF to determine a standard shot stack quantity for each source location. Considerations here will include the impact

to the EVA timeline to use this method, as well as quantities (and mass) of equipment required.

For both off-nominal problem recognition through resolution, and nominal operations, fieldwork on the Moon will present trade-offs, similar to terrestrial fieldwork, of the value of time spent weighed against the need to perform other tasks. The impacts of these trade-offs are heightened within the context of the fixed duration of a space mission and especially an EVA. It is recommended that the benefit and priorities of nominal science tasks be clearly defined prior to lunar missions or EVA execution. Earth based scientists providing support to lunar surface science activities will need to adjust their mode of operations from the less rigid constraints of terrestrial fieldwork, where realtime finalization of plans often occur in the field and data priorities can be more flexible. For these support scientists, pre-mission options will need to be outlined, with clear gates. Also, crib sheets to address possible off-nominal situations will need to be developed. These items will help to provide quick, concise, and effective support from Mission Control to the crew to maximize the data return of the surface science activities.

#### ***4.7 Conclusions***

In this study we examine the results from adding an active seismic refraction study to a previously executed NASA simulated human lunar traverse mission in the SFVF of the Arizona desert. The locations of the seismic data were driven purely by the positions used for geologic observations and sampling during the earlier simulated mission. 1-D seismic velocity profiles, to a depth of 60 m, for nineteen locations in the field area were created based on the refraction analysis of the seismic data. Examination

of the results of the seismic refraction lines augment the previous geologic observations by providing constraints on seismic velocity ranges that enable the defining of seven different layers present throughout our field area. We provide interpretation of the various seismic layers. These layer definitions help to constrain unit thickness for each of the 1-D profiles. These seismic velocity profiles and interpretations indicate a fairly ubiquitous veneer of regolith with a thickness of 1 m to 3 m across most of the field area. Beyond the identification of field area specific subsurface seismic layers (including velocities and thicknesses) and identifying an area wide regolith layer, the analysis primarily provides point solutions of subsurface structure for each specific location. The lack of targeting the data to address specific geophysical questions prohibit identification of structural trends or generalizing characteristics of specific features or structures.

In addition to the seismic analysis results and interpretation, geophysical studies are maximized through proper pre-mission (pre-field deployment) planning of data sampling locations, similar to conducting surface geologic observations and sample collection. This study provides an increase in the understanding of applying terrestrial active seismic fieldwork methods, anomaly resolution, and standard practices to lunar surface seismic studies and by extension other geophysical research. Use of terrestrial analogs is recommended for evolving standard geophysical field operations flexibility to accomplish similar scientific goals within the more structured approach required for human lunar mission operations. Finally, for lunar missions, we suggest use of traverse plans which provide balanced prioritization of complementary geophysical and geologic tasks to address the investigations of a mission, and maximize the scientific return.

#### ***4.8 Acknowledgements***

Funding for this work was provided by the NASA PSTAR grant NNX15AL87G in support of geophysical analog studies. I would like to thank the Babbitt Ranch for providing access to the fieldsite. Also, many thanks to Ryan Porter, Kelsey Young, and Don Pettit for assisting in collecting the seismic refraction line data used in this study, and Mong-Han Huang for help with the refraction analysis.

## **5 Conclusions and Application to Human Lunar Exploration**

### ***5.1 Overview***

My dissertation research uses the San Francisco Volcanic Field (SFVF), AZ and Lava Beds National Monument (LBNM), CA as lunar surface exploration analog sites to characterize the subsurface structure of lava tubes, cinder cones, and lava flows through the use of magnetic and seismic geophysical methods. This work demonstrates that analysis of magnetic anomalies can be used to approximate the morphologic structure and location of terrestrial lava tubes, and be similarly used for the Moon. Using seismic refraction methods, I identify local subsurface fault structure that shows alignment with the positions of monogenetic volcanic vents, and provide an analog to applying linear seismic arrays to study similar lunar features. Finally, I use the addition of active seismic field methods and analysis to a previously executed simulated human lunar rover traverse mission to provide geophysical data and interpretation that highlight the importance of balancing geophysical and geologic objectives for lunar surface missions. This balance should be optimized in a strategic fashion to get sufficient data coverage and resolution to address predefined geologic and geophysical questions within the context of mission constraints such as crew and/or robotic limitations and mission duration. The execution of the active seismic fieldwork provides the opportunity to examine the parallels of terrestrial and the Apollo lunar missions' field methods related to anomaly resolution and best practices to apply to lunar surface geophysical exploration. In the following section I summarize my results from Chapters 2 thru 4 and include operational considerations for conducting similar

studies on the lunar surface. This is followed by concluding thoughts on the evolution of terrestrial field geophysics for human lunar surface exploration.

## ***5.2 Summary of Conclusions with Operational Considerations***

### ***5.2.1 Chapter 2 Summary & Lunar Surface Survey Considerations***

Chapter 2 examined the ability to use the results of ground level magnetic surveys to visualize and decipher magnetic anomalies produced by terrestrial lava tubes as an analog to performing similar studies on the lunar surface. Lava tubes are found in basaltic lava flows on terrestrial planets, and impact lava flow processes. In the future, exploration of lava tubes on the Moon will be able to provide access to geologic settings that have likely remained unaltered since emplacement billions of years ago. Additionally, lunar lava tubes are good candidates to provide protection for astronauts against thermal extremes, meteoroid impacts, and radiation they would encounter on the Moon's surface. However, at present, the primary method for locating lava tubes either on Earth or other planetary bodies is through the visual identification and alignment of collapse pits. This chapter demonstrated the use of ground level magnetometry to map terrestrial magnetic anomalies produced by lava tubes in the Lava Beds National Monument, and relate these anomalies to the locations and geometry of the lava tubes.

The results of this study show that where the magnetic anomaly is above the background variation, the maximum negative anomaly along a lava tube follows the magnetic signature of a simple cylindrical model, specifically relating to a non-dimensional geometric ratio of height, width, and depth. Additionally, the resulting two-dimensional ground level magnetic gradient informs on the location of the lava

tube perimeter. This model and gradient information, when coupled with an independent determination of the local magnetic properties and lava tube ceiling thickness can be used to envelope the width and height of a lava tube. Finally, results were extended to demonstrate the application of these methods to predict the magnetic anomaly of a lunar lava tube, formed prior to the extinction of the lunar dynamo, provided constraints on the geometry and magnetic properties. These methods have direct application to aid in the prospecting and evaluation of lunar lava tubes for additional robotic or human scientific investigation or for human utilization.

From a lunar surface operations perspective this study relates to both scientific and prospecting activities. Although the science and prospecting objectives have different motivations, they essentially are tied together with regards to the actual surface activities required to accomplish them. These activities are to conduct a fine resolution, close grid spacing, surface survey to examine magnetic anomalies for signatures indicating the existence, or informing on the geometry of lava tubes within a basaltic formation. For this terrestrial based study of lava tubes, the survey was conducted by personnel walking the pre-determined survey grid while carrying a magnetometer. While this is a fairly inexpensive solution to obtain the required magnetic data on Earth, having a suited crewmember on the Moon's surface delegated to similar activities is an unacceptable solution. The primary reasons for the unacceptability of this solution is that crew members' time during space missions is finite, extravehicular activity (EVA or spacewalk) time is even more finite, and to utilize this time to have a crewmember perform a repetitive task such as this, while subjecting them to the rigors and hazards of an EVA, would be a poor choice.

Therefore, a more acceptable solution could consist of a human-robotic partnership. This partnership could consist of an initial human reconnaissance of an area of interest as part of other surface EVA activities, followed by a deployment of a magnetometer capable robotic vehicle to perform the actual close grid survey. The robotic vehicle would be capable of performing surface, or extremely low altitude, surveys. It is recommended that these robotic vehicles be capable of significantly higher travel rates, on the order of 10,000's of meters a day, than have been employed by planetary robotic operations to date. Due to the availability of crewmembers on location to provide "rescue assistance" to the robotic vehicle, the additional risks encountered by conducting the surveys at these higher velocities could be accepted with crewmember provided contingency options being available. In this way, a crew-robotic partnership could result in increased data coverage to address both scientific and crew utilization objectives of lunar exploration.

### ***5.2.2 Chapter 3 Summary & Considerations for Crew-Robotic Synergy***

Chapter 3 provides results of using 2-D seismic refraction analysis to examine the upper subsurface beneath lava flows in the San Francisco Volcanic Field (SFVF) to distinguish vertical displacement of the stratigraphic layers that would be indicative of fault locations, and compare these fault locations relative to cinder cone vent positions. Unfortunately, due to high attenuation in the field area, only the upper 10 to 40 meters of the subsurface seismic structure could be modelled, resulting in an inability to resolve seismic structure that would be indicative of fault locations. However, an understanding of the variability of the lava flow thickness, the background seismic noise, and attenuation characteristics for our energy source were able to be examined.

Additionally, terrestrial locations such as the SFVF are analogs for similar near-surface features that are found on the Moon. For this second part of the study I applied the terrestrial seismic refraction field methods to examining lunar equivalent field studies. The Apollo 17, Taurus-Littrow Valley (TLV), Lunar Seismic Profiling Experiment (LSPE) data was used to extend the terrestrial field seismic refraction methods to a lunar application and examine the SFVF results as an analog to lunar studies. First, the LSPE data was re-examined using 1-D seismic analysis methods similar to those used for processing the SFVF data. The results of this analysis were in agreement with previous LSPE studies. Using wavelength equivalent criteria to then down-select the quantity of SFVF data points to an Apollo 17 LSPE equivalency, the SFVF data was reprocessed for a qualitative comparison to the full data set as an analog to what an LSPE layout in the SFVF would produce. The results produce models for each of the nodal lines that provided the initial near-surface seismic velocities down to about 5 m, but below this point produced a poorly constrained model of the seismic velocity structure due to the low number of available data points. However, from this Apollo 17 LSPE to SFVF comparison it can be suggested that a properly scaled SFVF style geophone/seismometer linear array study across the TLV could produce a detailed subsurface seismic model revealing various 2-D heterogeneity and faulting, provided it is executed with sources having sufficient energy to be acquired by the most distant receivers placed on the array.

The SFVF fieldsite; with its basaltic lava flows, cinder cone vents, and local fault structure; provides a geophysical analog for conducting lunar analog seismic studies. The SFVF location is especially favorable for examining and refining field techniques for execution on the lunar surface. From the perspective of executing an active source

nodal seismometer deployment on the lunar surface, there are some takeaways from the fieldwork performed in support of this study. In the SFVF the site selection and deployment of the seismometer nodes was a manual activity supported by a chase vehicle. This was followed by the execution of seismic shots from a vehicle transported propelled energy generator (PEG), described in Chapter 3. Shot locations for the PEG often required site preparation to maximize coupling of energy from the propelled mass to the ground. One important item of note is that the lack of active realtime data evaluation in the field resulted in being blind to the quality of the data being collected and resulted in the analysis results being insufficient to address the primary hypothesis of the study.

The execution of similar activities to create an active source nodal seismic line across large distances on the Moon's surface will require augmentation to provide for crew input into nodal and source site selections while minimizing crew time, specifically EVA time. A possible scenario for this would be for the crew to use a rover for transportation of the nodes as well as a crew controlled robotic arm for node deployment and pick-up. This same rover could also carry a crew controlled robotic seismic source generator. The rover in this scenario could be either pressurized or unpressurized. Assuming high confidence in the robotic node deployment hardware, a pressurized rover would be preferred to maximize the crew utilization by minimizing EVA induced fatigue, while an unpressurized rover with the crew EVA would provide the crew with quick access to hardware in the event of a failed installation or other issue. In either scenario, three passes of the nodal line would be required for a temporary deployment. The first pass of the line would be for node deployment, and include details such as proper node orientation, sub-meter location accuracy (both

relative and absolute), and operational verification to meet minimum array configuration requirements. A return pass would consist of executing the seismic shots recommended to include automated synchronized timing across the array, and ideally realtime confirmation to verify acquisition of required data. The third pass would be for node deactivation and retrieval. By the end of the field deployment in the SFVF, the team was able to conduct these equivalent steps within a seven-hour period, with the shots accounting for three hours and forty minutes of this time. With the proposed crew directed robotic modifications, these activity times would be significantly reduced, which would suggest the capability to execute multiple SFVF equivalent nodal lines within a day. The on-site ability of the crew to select locations, deal with obstacles, and address off-nominal situations greatly enhances the ability for increased data return.

### ***5.2.3 Chapter 4 Summary & Considerations for Lunar Geophysics***

Chapter 4 revisits the San Francisco Volcanic Field fieldsite, but this time from the perspective of inserting active seismic refraction studies into a simulated human lunar rover mission traverse route that was prioritized for geologic surface observations and sample collection activities, not geophysical studies. This traverse route strategy is similar to the Apollo missions where the lunar rover traverses were dictated primarily to optimize the return of surface observations and geologic sample collection. Traditionally, terrestrial analog mission simulations have followed this same pattern resulting in the de-prioritization or omission of geophysical studies including seismic activities. Arguably, one of the highest fidelity of these terrestrial human mission simulations occurred in the SFVF in 2010 as part of the NASA Desert Research and Technology Studies (RATS) test series.

For the study presented in Chapter 4, 19 locations, science stations visited by the crews of the 2010 NASA RATS simulation, were selected on which to conduct active seismic refraction activities using 115-meter-long geophone lines. From the refraction data, 1-D seismic velocity profiles to a depth of 60 m were created. The goal was to examine the analysis results, from these non-geophysically prioritized field locations, for subsurface structural trends that could be applied to the field area or particular structure. The analysis showed seven distinct velocity layers were present, and revealed a fairly consistent upper regolith layer within the field area. Additionally, co-located, or alignments, of the geophone line positions allowed for geographic specific interpretations from the seismic profiles.

From a seismic field operations perspective, this study provided comparable fieldwork methods, anomaly resolution, and standard practices as those experienced during the Apollo 14 and 16 missions active seismic experiment tasks. The results show that even within a monogenetic volcanic field there is substantial geophysical and geologic complexity at the outcrop scale. These analog relationships increases the ability to understand issues and best practices for conducting lunar surface seismic studies tasks and by extension other geophysical research. Overall, the results provide rationale for providing balanced prioritization within planetary traverse plans for targeted locations to address geophysical and geologic study objectives. Ideally traverses can be planned for geophysical, observational, and sampling studies to be used in conjunction, to increase overall geologic understanding.

### **5.3 Continued Research: Human Lunar Surface Exploration**

Future human lunar surface geophysical studies will require an adaptation of terrestrial field geophysics activities for application on space exploration missions. This will include the adjustment or scaling of scientific requirements to account for the difference in geophysical properties between the Earth and Moon. Some examples of these modifications were included in this dissertation with respect to translation of both magnetics and seismic terrestrial studies to lunar surface environments.

In addition, and just as importantly, the understanding and evolution of terrestrial field methods, anomaly resolution, and standard practices for application to lunar surface fieldwork will be critical to the success of future human space exploration. This evolution will feed into all aspects of missions including planning; prioritization; training; communications; procedures and protocols; mission control support; and the design of vehicles, hardware, and systems for efficiently executing lunar science operations.

With regards to this evolution, there is significant historic and current experience on which to draw upon including the missions of Apollo, Space Shuttle, and International Space Station; along with Earth based lunar analog simulations such as the NASA Desert RATS test series. Finally, continued documenting of terrestrial geophysical/geologic fieldwork methodology, asset management, and data acquisition as they relate to overall objectives, preplanned field expectations, minimum data requirements, and unexpected field opportunities is of prime importance to inform on the establishing of a standard for planning, training, and executing human lunar surface science operations.

## Appendices

A.1 The following is included on this appendix for each of the nineteen geophone lines completed in the San Francisco Volcanic Field.

First page, per geophone line:

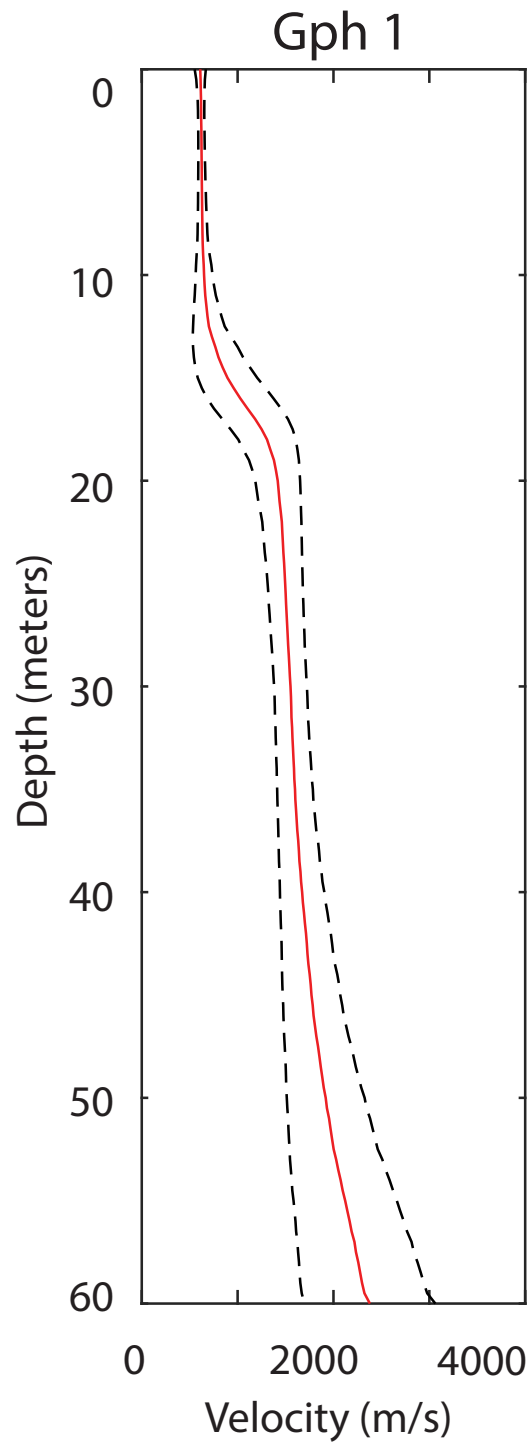
- 1) Study geophone line number: geophone line designation for this study
- 2) NASA 2010 Science Station: science station(s) at the geophone location
- 3) Field nomenclature: pre-2016 field season designation for the geophone line
- 4) Field geophone line number: 2016 field season line designation
- 5) Position: latitude and longitude for each picture (photos credit: E. Bell)
- 6) Direction of view for each picture
- 7) Field pictures of line location

Second page, per geophone line:

- 8) Mean seismic velocity profile (shown with red line), and the one-sigma standard deviation (shown with black dashed lines) for the geophone line

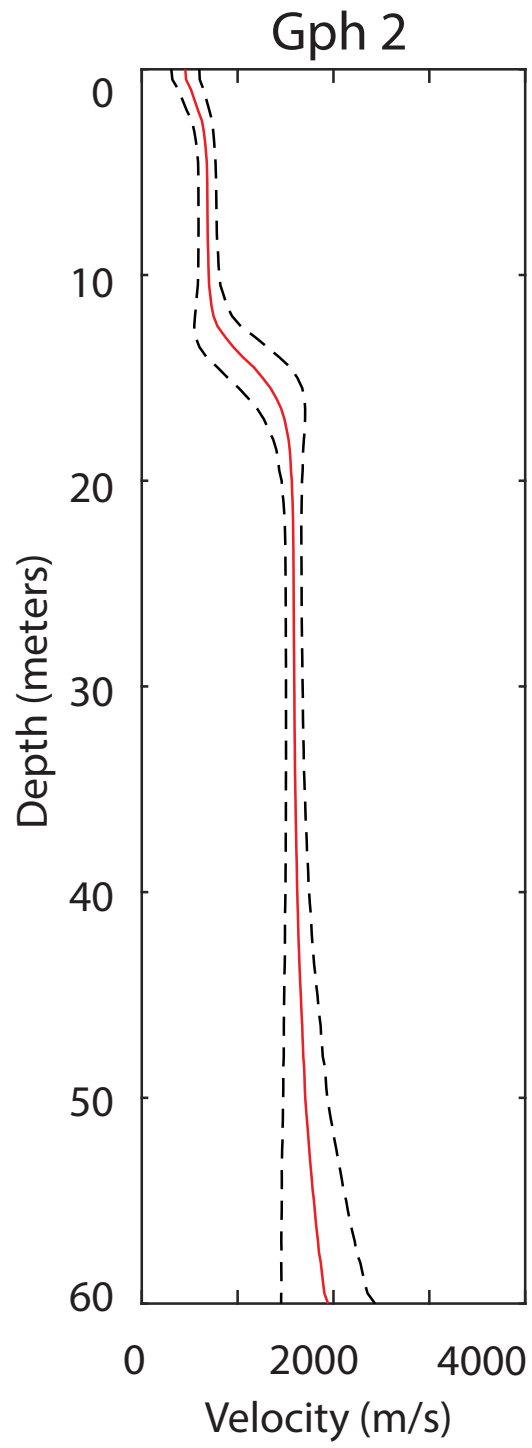
Study geophone line number:	1		
NASA 2010 Science Station:	34B		
Field nomenclature:	G1F		
Field geophone line number:	02		
Position:		Position:	
35.60542219		35.60447495	
-111.6153111		-111.6146944	
Looking south		Looking north	
			

Mean Velocity Profile:



Study geophone line number:	2		
NASA 2010 Science Station:	34A		
Field nomenclature:	G1E		
Field geophone line number:	03		
Position:		Position:	
35.60465273		35.60405829	
-111.6165528		-111.6154861	
Looking southeast		Looking northwest	
			

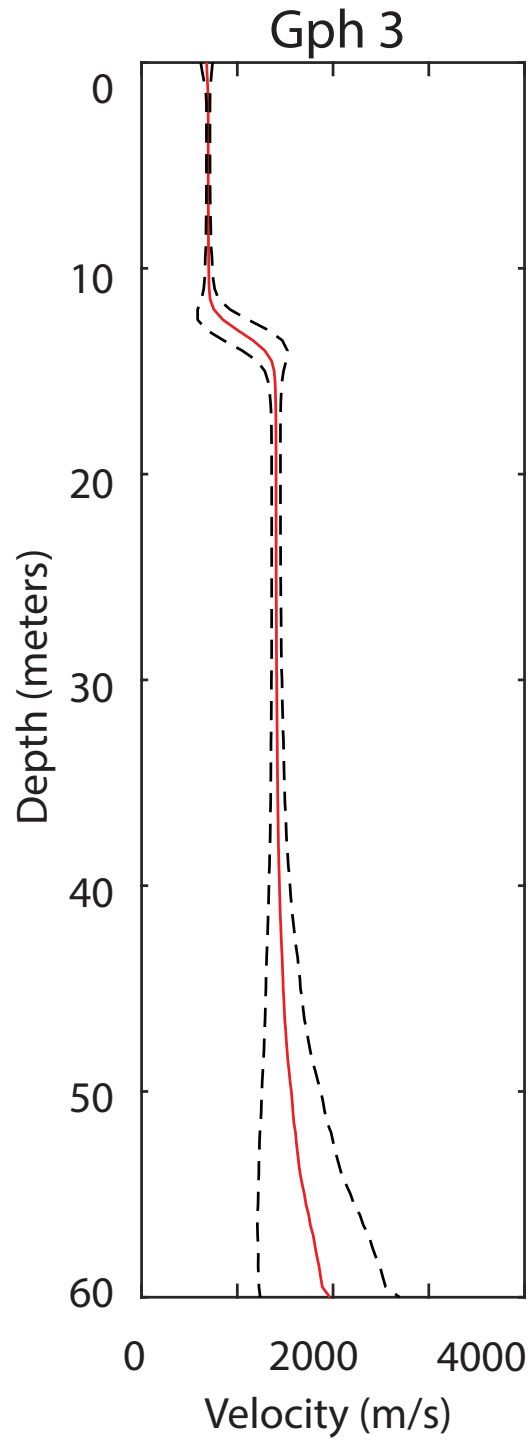
Mean Velocity Profile:



Study geophone line number:	3		
NASA 2010 Science Station:	32B		
Field nomenclature:	32B		
Field geophone line number:	04		
Position:		Position:	
35.59126943		35.59021943	
-111.63445		-111.6342027	
Looking south		Looking north	



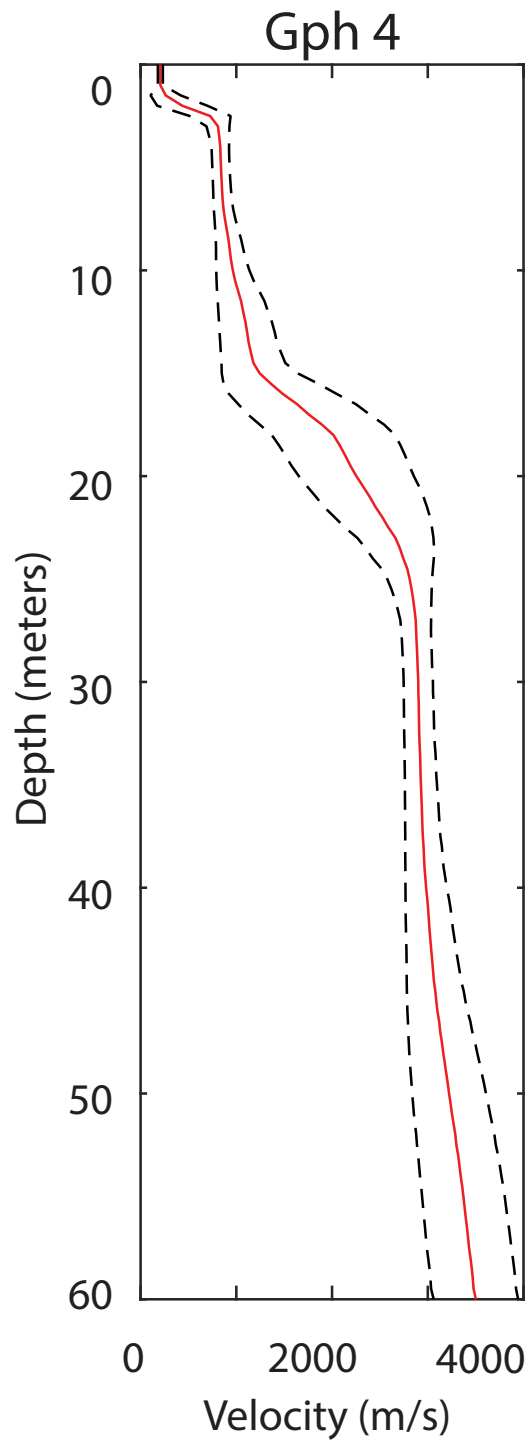
Mean Velocity Profile:



Study geophone line number:	4		
NASA 2010 Science Station:	9B		
Field nomenclature:	G2F		
Field geophone line number:	05		
Position:		Position:	
35.59035832			
-111.6423805			
Looking south			



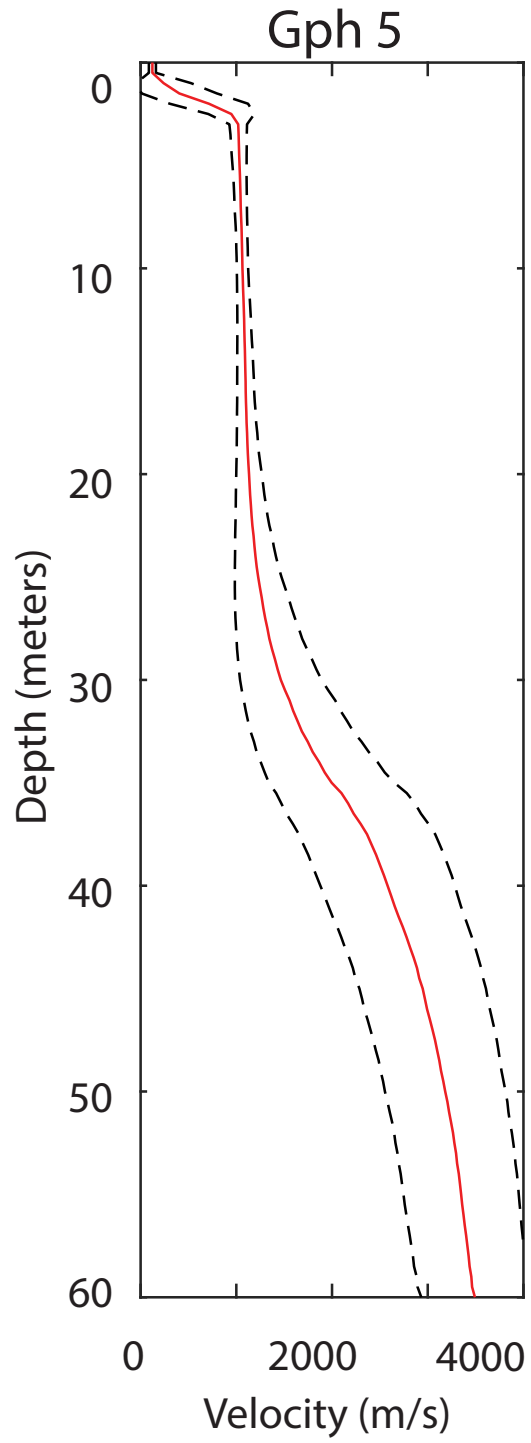
Mean Velocity Profile:

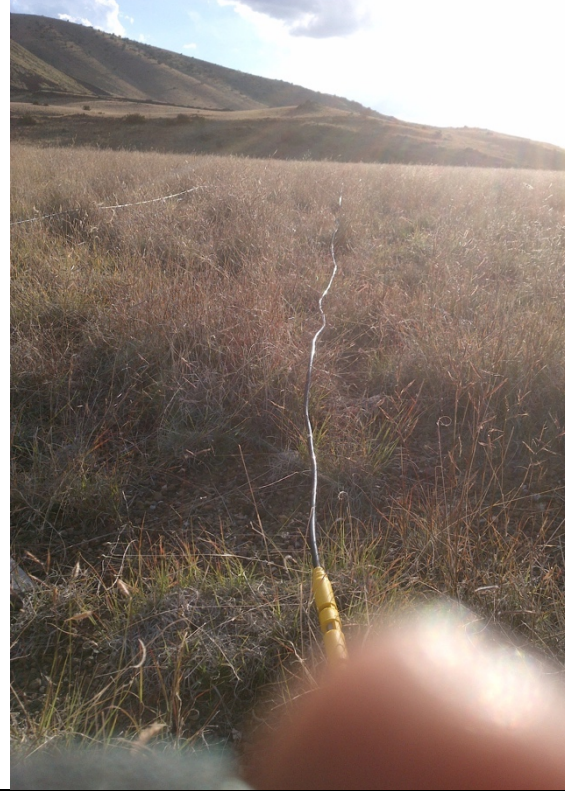


Study geophone line number:	5		
NASA 2010 Science Station:	11A		
Field nomenclature:	11A		
Field geophone line number:	06		
Position:		Position:	
35.58927219			
-111.6423249			
Looking west			

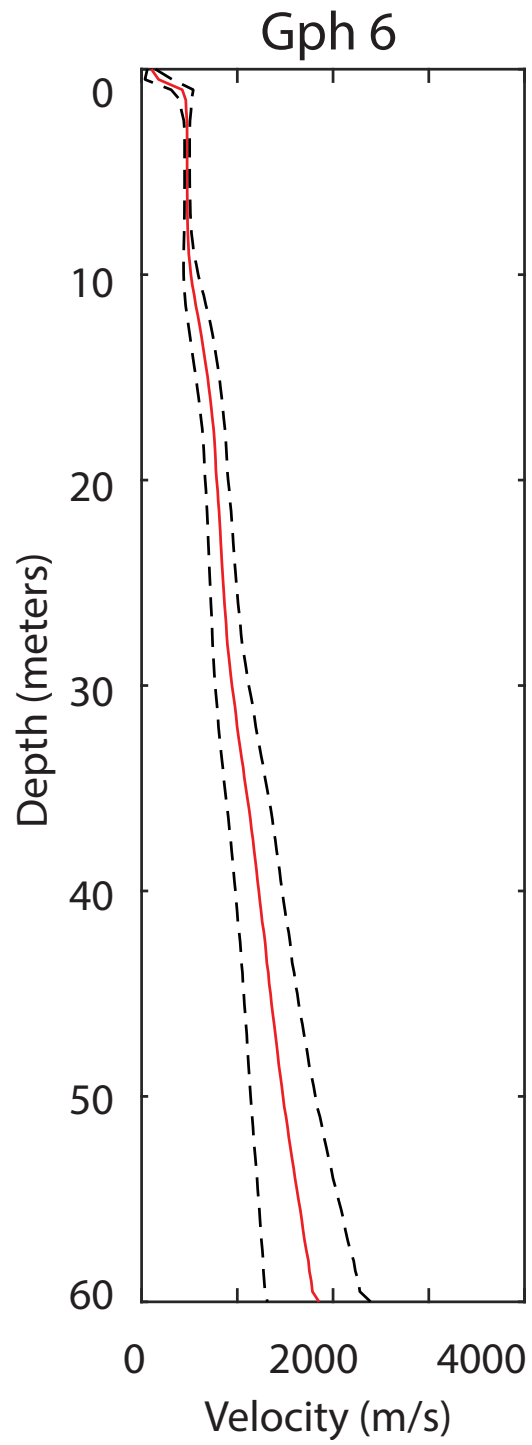


Mean Velocity Profile:



Study geophone line number:	6		
NASA 2010 Science Station:	32A & 7B		
Field nomenclature:	G2A		
Field geophone line number:	07		
Position:		Position:	
35.5911805		35.59170269	
-111.6310305		-111.6299055	
Looking northeast		Looking southwest	
			

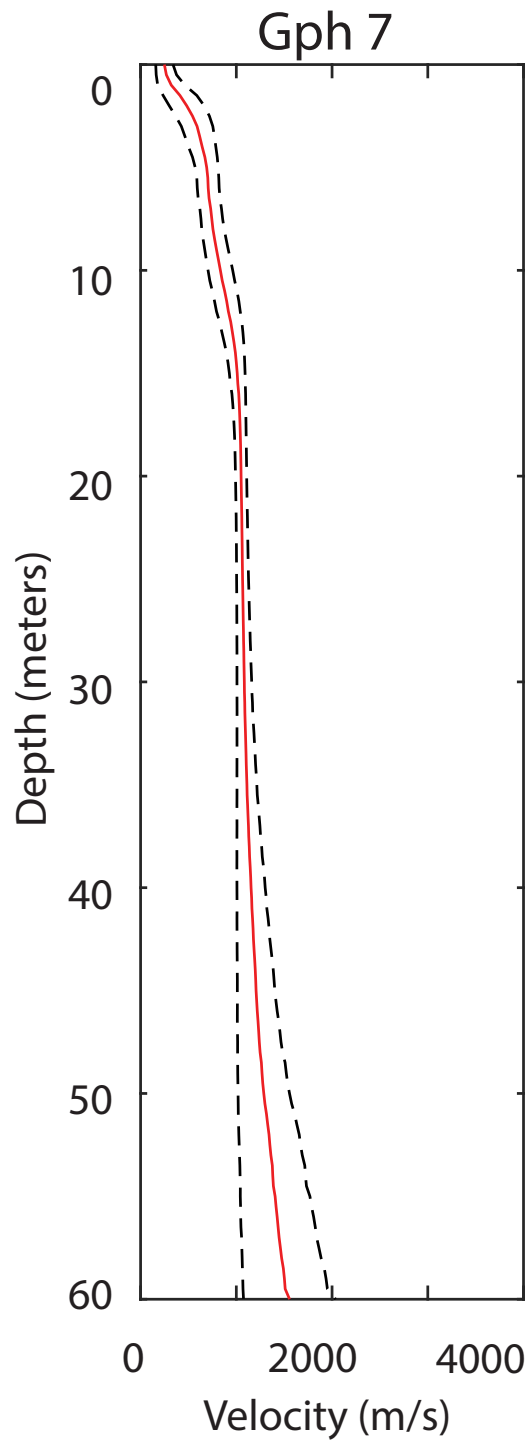
Mean Velocity Profile:



Study geophone line number:	7		
NASA 2010 Science Station:	31B		
Field nomenclature:	G3C		
Field geophone line number:	08		
Position:		Position:	
35.59446939		35.59496108	
-111.6596027		-111.6584555	
Looking east		Looking west	



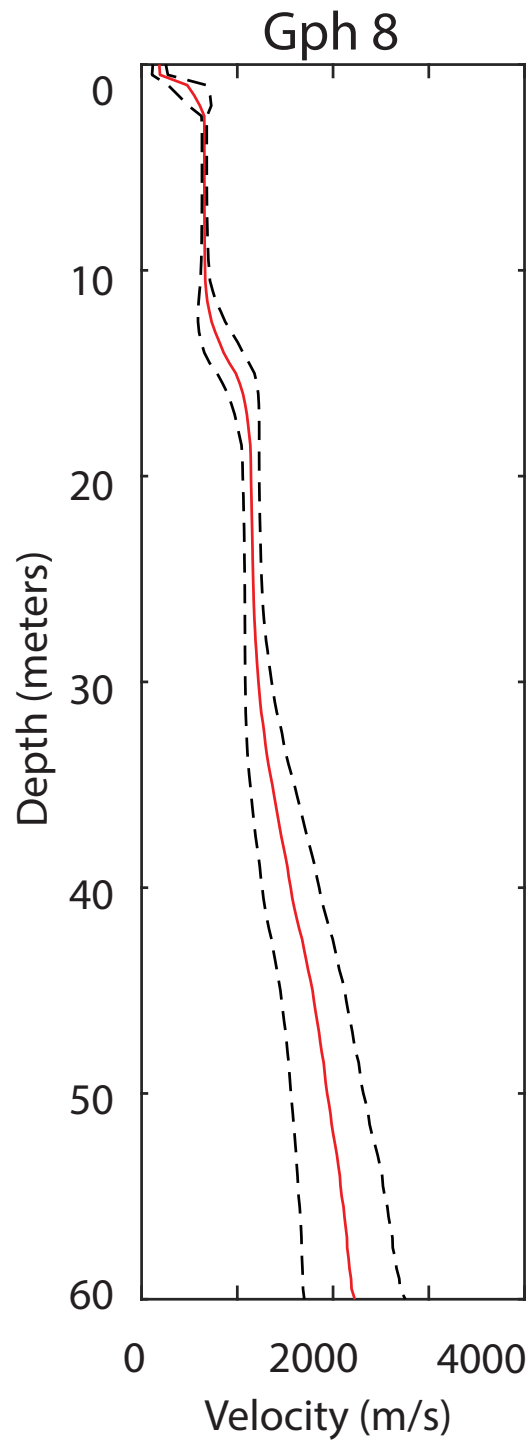
Mean Velocity Profile:



Study geophone line number:	8		
NASA 2010 Science Station:	31B		
Field nomenclature:	G3F		
Field geophone line number:	09		
Position:		Position:	
35.59395273		35.5944916	
-111.6607111		-111.6595777	
Looking east		Looking west	



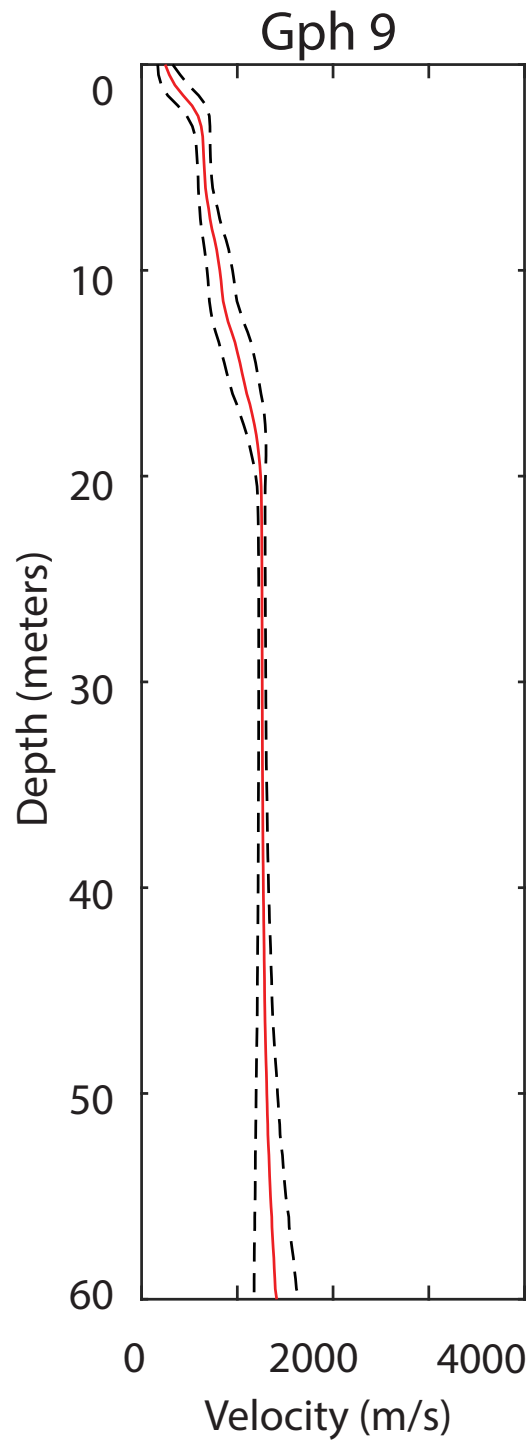
Mean Velocity Profile:



Study geophone line number:	9		
NASA 2010 Science Station:	31B		
Field nomenclature:	G3G		
Field geophone line number:	10		
Position:		Position:	
35.59397494			
-111.6606889			
Looking west			

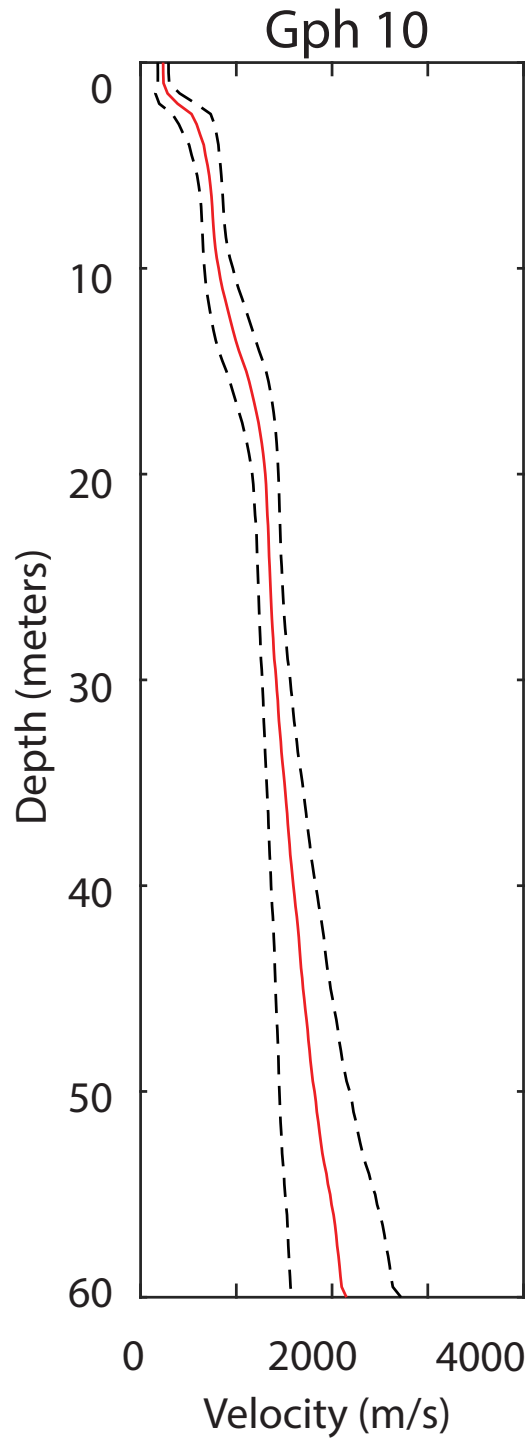


Mean Velocity Profile:



Study geophone line number:	10		
NASA 2010 Science Station:	12B & 28B		
Field nomenclature:	G4C		
Field geophone line number:	11		
Position:		Position:	
35.57771942		35.57687771	
-111.6594694		-111.66025	
Looking south		Looking north	
			

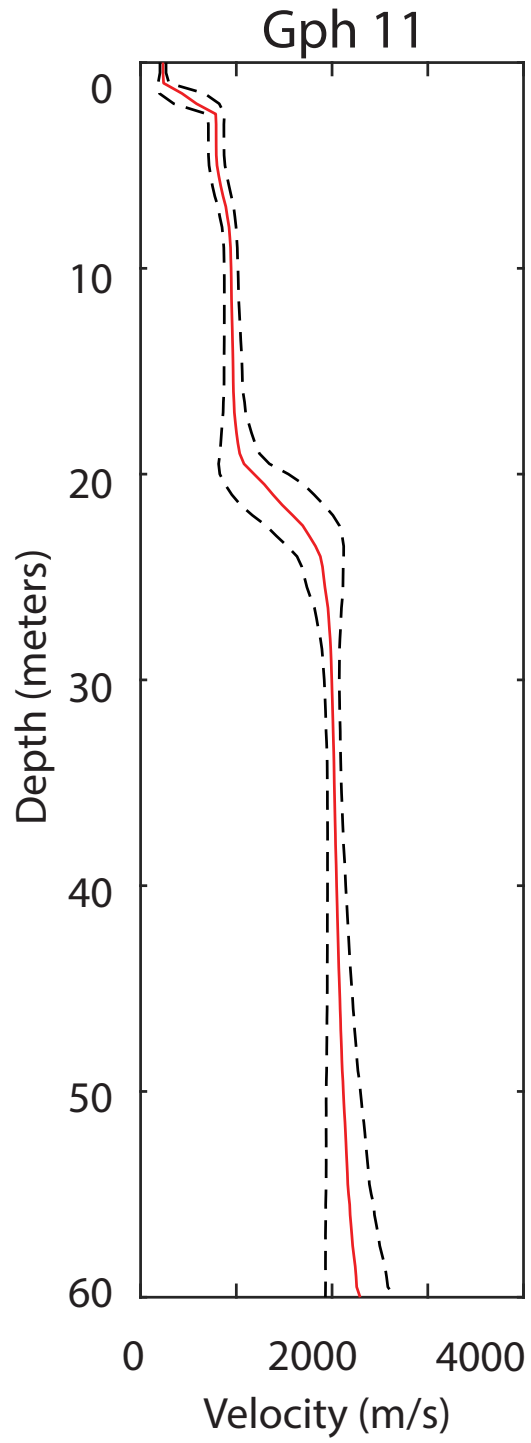
Mean Velocity Profile:



Study geophone line number:	11		
NASA 2010 Science Station:	29B		
Field nomenclature:	G4A		
Field geophone line number:	12		
Position:		Position:	
35.58311384		35.58353889	
-111.6573638		-111.6562055	
Looking east		Looking west	



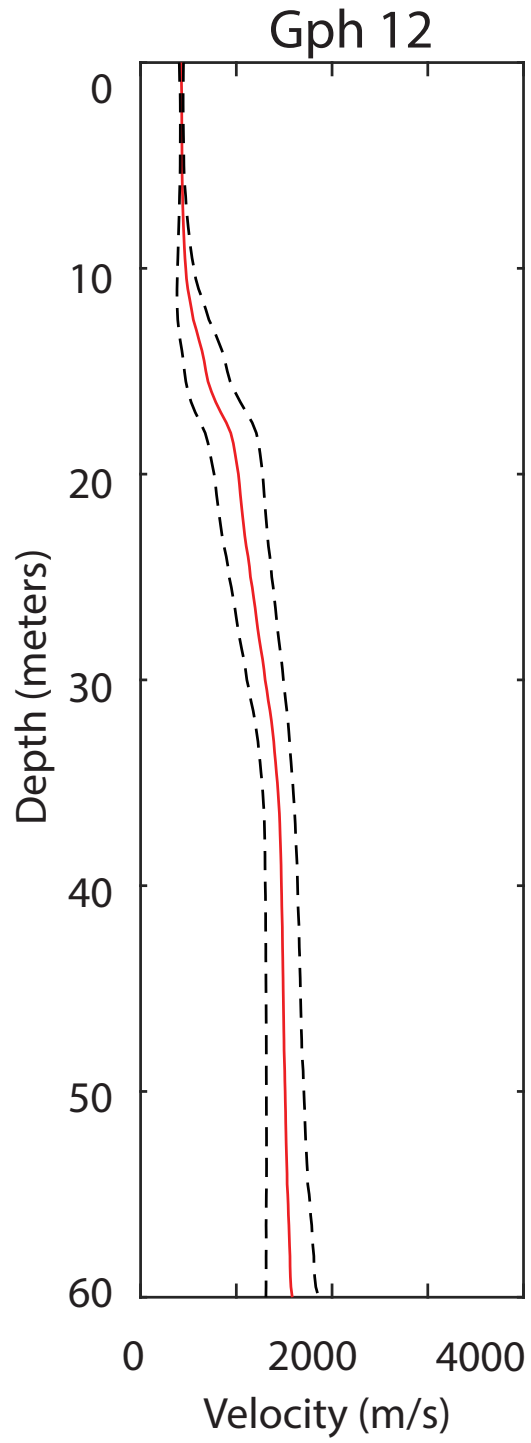
Mean Velocity Profile:



Study geophone line number:	12		
NASA 2010 Science Station:	13B		
Field nomenclature:	G4F		
Field geophone line number:	13		
Position:		Position:	
35.57112772		35.57144162	
-111.6509666		-111.6497444	
Looking east		Looking west	



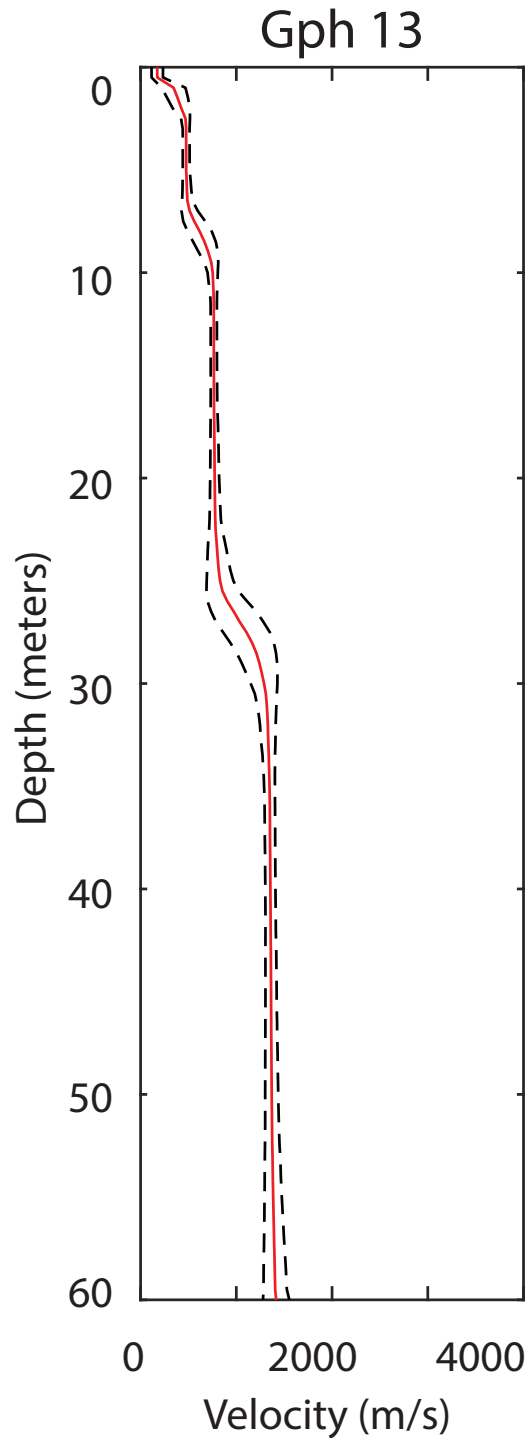
Mean Velocity Profile:



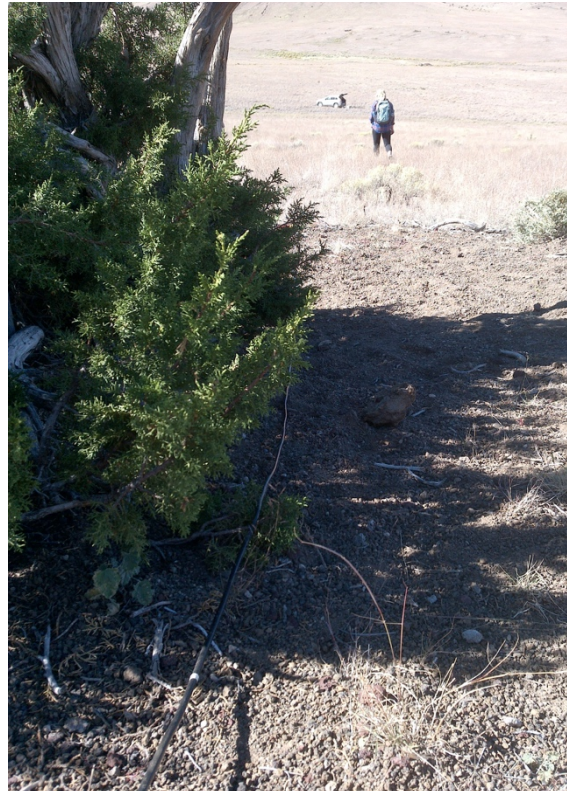
Study geophone line number:	13		
NASA 2010 Science Station:	17A		
Field nomenclature:	G5C		
Field geophone line number:	14		
Position:		Position:	
35.57615829		35.57530275	
-111.6223833		-111.6216278	
Looking south		Looking north	



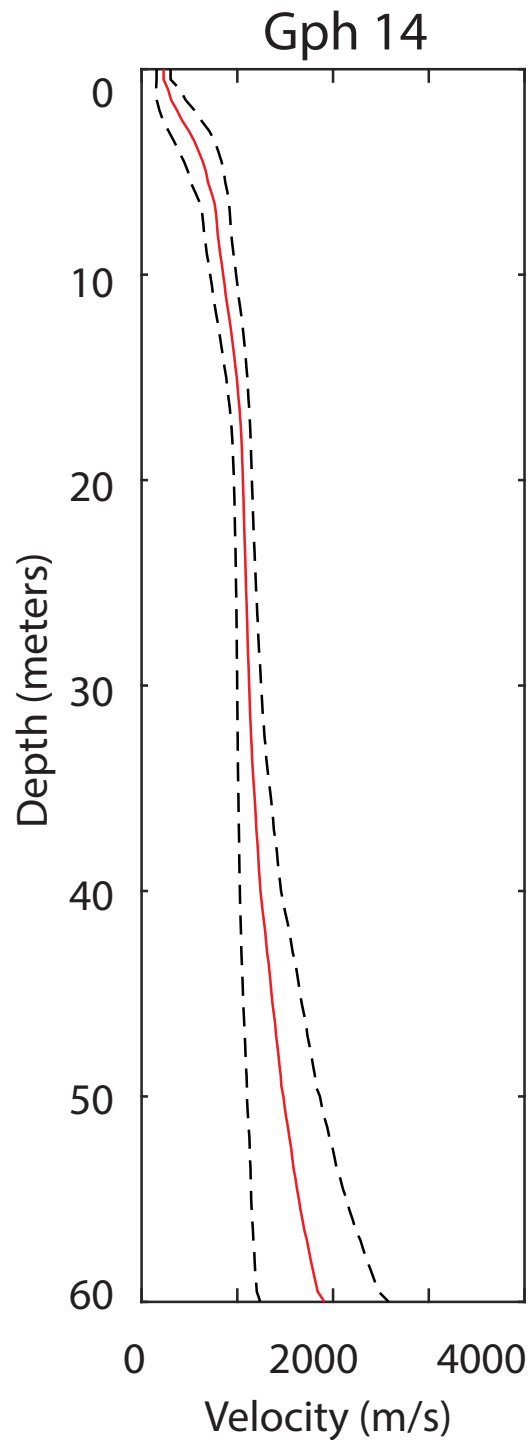
Mean Velocity Profile:



Study geophone line number:	14		
NASA 2010 Science Station:	20A		
Field nomenclature:	G6C		
Field geophone line number:	16		
Position:		Position:	
35.58378607		35.58437021	
-111.5987625		-111.597703	
Looking east		Looking west	



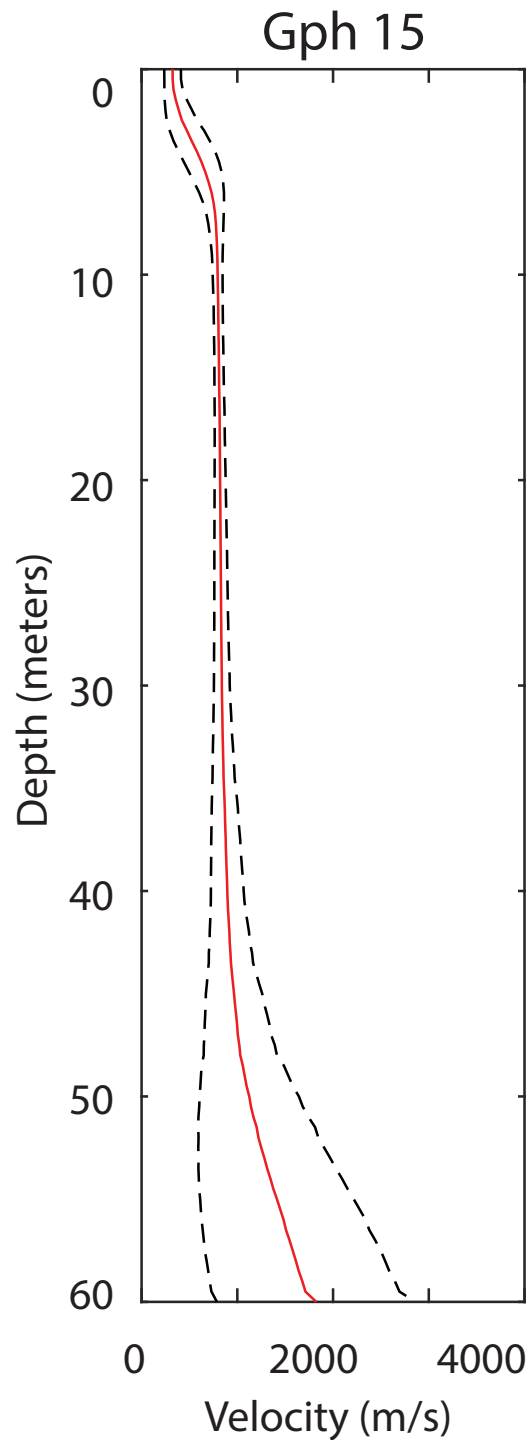
Mean Velocity Profile:



Study geophone line number:	15		
NASA 2010 Science Station:	20A		
Field nomenclature:	G6B		
Field geophone line number:	17		
Position:		Position:	
35.58342674		35.58382764	
-111.5999369		-111.5987737	
Looking east		Looking west	



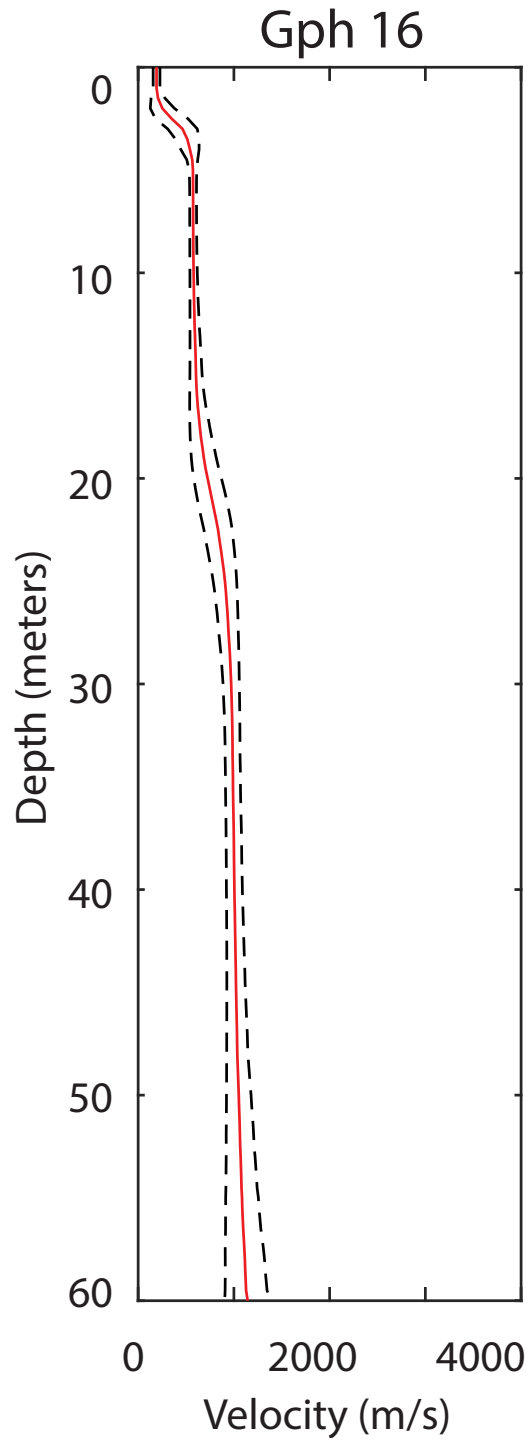
Mean Velocity Profile:



Study geophone line number:	16		
NASA 2010 Science Station:	26A		
Field nomenclature:	G5F		
Field geophone line number:	18		
Position:		Position:	
35.57112437		35.57014829	
-111.6125231		-111.613001	
Looking south		Looking north	



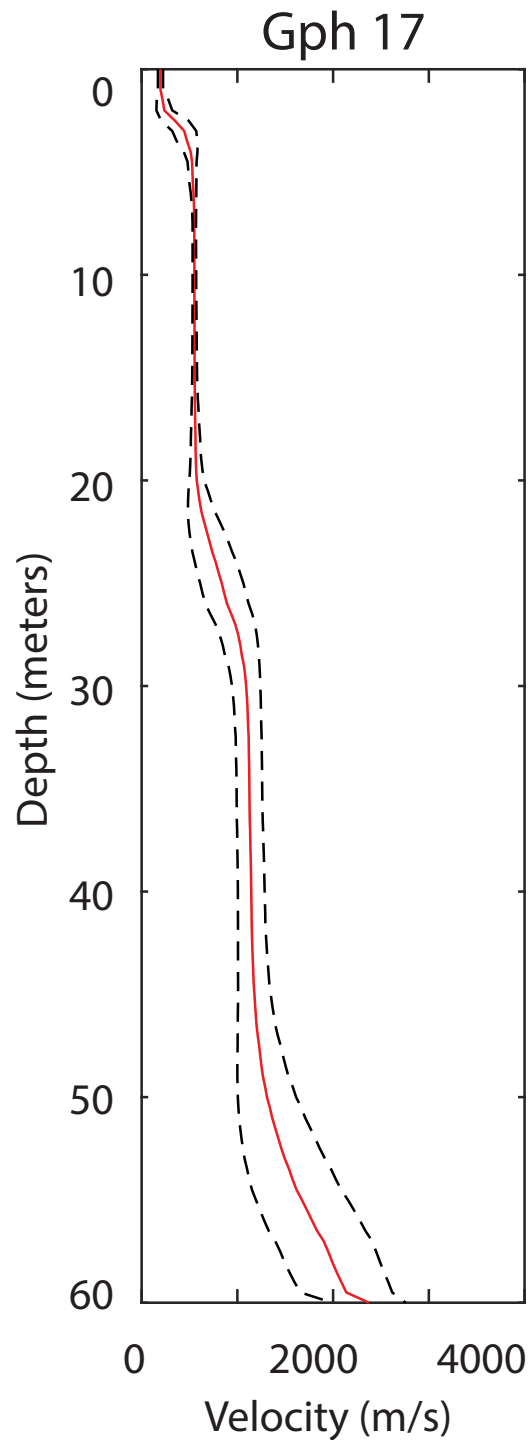
Mean Velocity Profile:



Study geophone line number:	17		
NASA 2010 Science Station:	24A		
Field nomenclature:	G8E		
Field geophone line number:	19		
Position:		Position:	
35.54567004		35.54534993	
-111.6148503		-111.6136334	
Looking east		Looking west	



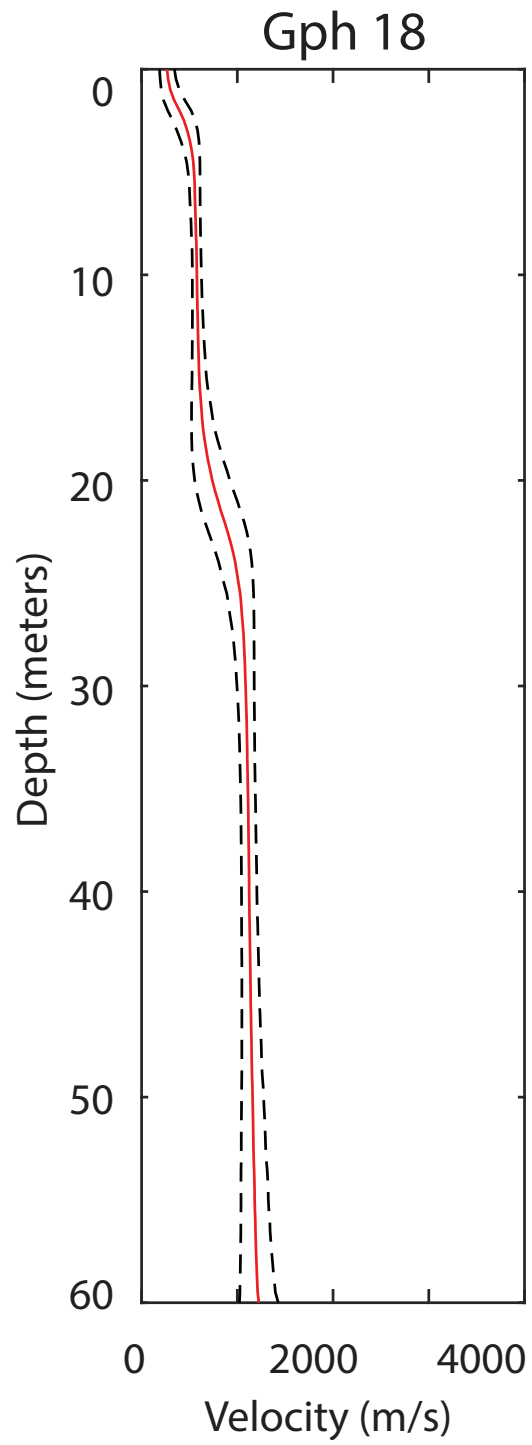
Mean Velocity Profile:



Study geophone line number:	18		
NASA 2010 Science Station:	24A		
Field nomenclature:	G8F		
Field geophone line number:	20		
Position:		Position:	
35.54597572		35.5456832	
-111.6160477		-111.6147929	
Looking east		Looking west	

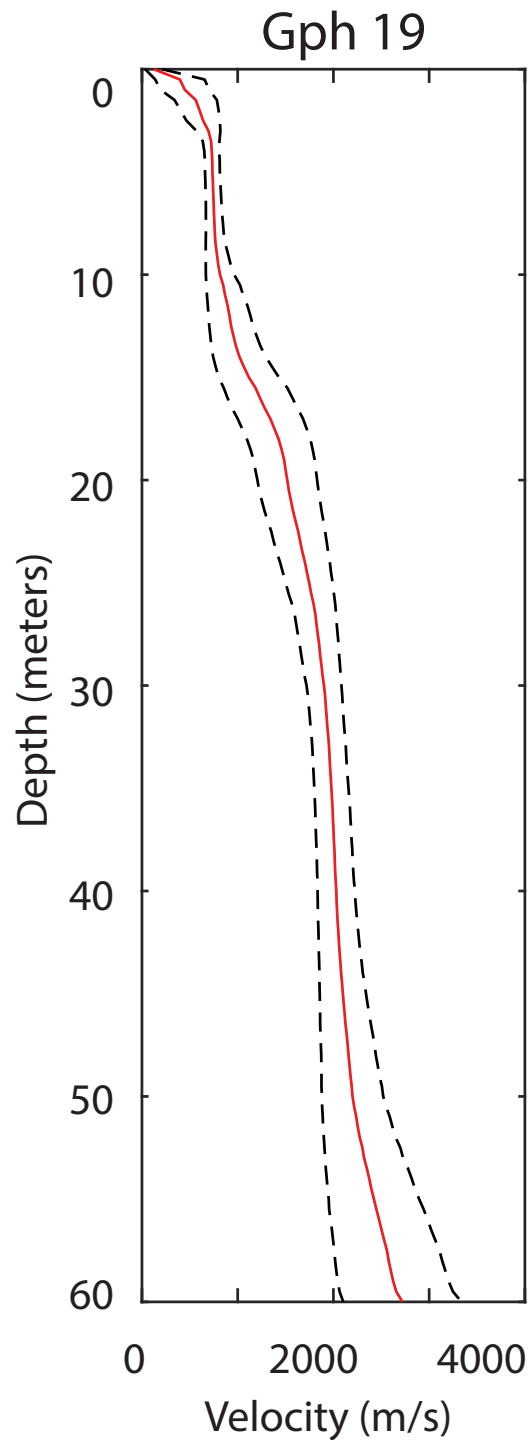


Mean Velocity Profile:



Study geophone line number:	19		
NASA 2010 Science Station:	16A & 25A		
Field nomenclature:	G8B		
Field geophone line number:	21		
Position:		Position:	
35.55750621		35.55750528	
-111.6132937		-111.6120104	
Looking east		Looking west	
			

Mean Velocity Profile:



## Bibliography

- Arnold, C. (1986). *Inside the Caves*. Charles L. Arnold.
- Bell, E., Schmerr, N., Bleacher, J., Porter, R., Young, K., Richardson, J., ... Rees, S. (2019). *Geophysical Characterization of a Volcanic Cinder Cone Field, an Analog to Lunar Exploration*. 50, 2868.
- Bell, E., Schmerr, N., Young, K., Bleacher, J., Esmacili, S., Garry, W. B., ... Whelley, P. (2020). *MAGNETIC SIGNATURES OF TERRESTRIAL LAVA TUBES AS ANALOGS FOR LUNAR*. 2294. Retrieved from <https://www.hou.usra.edu/meetings/lpsc2020/pdf/2294.pdf>
- Bell, E., Schmerr, N., Young, K., Whelley, P., Garry, W. B., Kruse, S., ... Jazayeri, S. (2018). *CHARACTERIZATION OF LAVA TUBES WITH MAGNETOMETRY*. 2412. Retrieved from <https://www.hou.usra.edu/meetings/lpsc2018/pdf/2412.pdf>
- Bell, Ernest, Schmerr, N. C., Bleacher, J. E., Porter, R. C., Young, K., Richardson, J. A., ... Pettit, D. R. (2018, December 14). *Using Earth Analogs of the Moon to Study Volcanic Fields and Prepare for Human Lunar Geophysical Exploration*. Presented at the AGU Fall Meeting 2018. Retrieved from <https://agu.confex.com/agu/fm18/meetingapp.cgi/Paper/460945>
- Billingsley, G. H., Priest, S. S., & Felger, T. J. (2007). *Geologic Map of the Cameron 30' x 60' Quadrangle, Coconino County, Northern Arizona*. 1.
- Binder, A. B. (1998). Lunar Prospector: Overview. *Science*, 281(5382), 1475–1476. <https://doi.org/10.1126/science.281.5382.1475>

- Bird, P. (1979). Continental delamination and the Colorado Plateau. *Journal of Geophysical Research: Solid Earth*, 84(B13), 7561–7571.  
<https://doi.org/10.1029/JB084iB13p07561>
- Blair, D. M., Chappaz, L., Sood, R., Milbury, C., Bobet, A., Melosh, H. J., ... Freed, A. M. (2017). The structural stability of lunar lava tubes. *Icarus*, 282, 47–55.  
<https://doi.org/10.1016/j.icarus.2016.10.008>
- Bleacher, J. E., Eppler, D. B., Needham, D. H., Evans, C. A., Skinner, J. A., & Feng, W. (2015). Geologic Investigations Spurred by Analog Testing at the 7504 Cone-Sp Mountain Area of the San Francisco Volcanic Field. *AGU Fall Meeting Abstracts*, 31, P31A-2037.
- Bleacher, Jacob E., Orr, T. R., de Wet, A. P., Zimbelman, J. R., Hamilton, C. W., Brent Garry, W., ... Williams, D. A. (2017). Plateaus and sinuous ridges as the fingerprints of lava flow inflation in the Eastern Tharsis Plains of Mars. *Journal of Volcanology and Geothermal Research*, 342, 29–46.  
<https://doi.org/10.1016/j.jvolgeores.2017.03.025>
- Bongiolo, A. D. B. e S., Souza, J. D., Ferreira, F. J. F., & Castro, L. G. D. (2013). GRAV MAG PRISM: A MATLAB /OCTAVE PROGRAM TO GENERATE GRAVITY AND MAGNETIC ANOMALIES DUE TO RECTANGULAR PRISMATIC BODIES. *Revista Brasileira de Geofísica*, 31(3), 347–363.  
<https://doi.org/10.22564/rbgf.v31i3.310>
- Braden, S. E., Stopar, J. D., Robinson, M. S., Lawrence, S. J., van der Bogert, C. H., & Hiesinger, H. (2014). Evidence for basaltic volcanism on the Moon within the past 100 million years. *Nature Geoscience*, 7(11), 787–791.  
<https://doi.org/10.1038/ngeo2252>

- Brenguier, F., Coutant, O., Baudon, H., Doré, F., & Dietrich, M. (2006). High resolution seismic tomography of a Strombolian volcanic cone. *Geophysical Research Letters*, 33(16). <https://doi.org/10.1029/2006GL026902>
- Brumbaugh, D. S. (2012). Seismicity of the San Francisco Volcanic Field of Northern Arizona. *Journal of Earth Science and Engineering*, 2, 722–728.
- Brumbaugh, Hodge, B. E., Linville, L., & Cohen, A. (2014). Analysis of the 2009 earthquake swarm near Sunset Crater volcano, Arizona. *Journal of Volcanology and Geothermal Research*, 285, 18–28. <https://doi.org/10.1016/j.jvolgeores.2014.07.016>
- Budetta, G., & Negro, C. D. (1995). Magnetic field changes on lava flow to detect lava tubes. *Journal of Volcanology and Geothermal Research*, 65(3–4), 237–248. [https://doi.org/10.1016/0377-0273\(94\)00108-S](https://doi.org/10.1016/0377-0273(94)00108-S)
- Burger, H., Sheehan, A., & Jones, C. H. (2006). *Introduction to applied geophysics: Exploring the shallow subsurface (Vol. 550)*. New York, NY: WW Norton.
- Calvari, S., & Pinkerton, H. (1998). Formation of lava tubes and extensive flow field during the 1991-1993 eruption of Mount Etna. *Journal of Geophysical Research: Solid Earth*, 103(B11), 27291–27301. <https://doi.org/10.1029/97JB03388>
- Calvari, S., & Pinkerton, H. (1999). Lava tube morphology on Etna and evidence for lava flow emplacement mechanisms. *Journal of Volcanology and Geothermal Research*, 90(3–4), 263–280. [https://doi.org/10.1016/S0377-0273\(99\)00024-4](https://doi.org/10.1016/S0377-0273(99)00024-4)
- Cebriá, J. M., Martín-Escorza, C., López-Ruiz, J., Morán-Zenteno, D. J., & Martiny, B. M. (2011). Numerical recognition of alignments in monogenetic volcanic areas: Examples from the Michoacán-Guanajuato Volcanic Field in Mexico

- and Calatrava in Spain. *Journal of Volcanology and Geothermal Research*, 201(1–4), 73–82. <https://doi.org/10.1016/j.jvolgeores.2010.07.016>
- Chappaz, L., Sood, R., Melosh, H. J., Howell, K. C., Blair, D. M., Milbury, C., & Zuber, M. T. (2017). Evidence of large empty lava tubes on the Moon using GRAIL gravity: Evidence of Lunar Lava Tubes From GRAIL. *Geophysical Research Letters*, 44(1), 105–112. <https://doi.org/10.1002/2016GL071588>
- Connor, C. B. (1987). *STRUCTURE OF THE MICHOAC, & N-GUANAJUATO VOLCANIC FIELD, MEXICO*. 10.
- Connor, C. B. (1990). Cinder cone clustering in the TransMexican Volcanic Belt: Implications for structural and petrologic models. *Journal of Geophysical Research: Solid Earth*, 95(B12), 19395–19405. <https://doi.org/10.1029/JB095iB12p19395>
- Connor, C. B., Condit, C. D., Crumpler, L. S., & Aubele, J. C. (1992). Evidence of regional structural controls on vent distribution: Springerville Volcanic Field, Arizona. *Journal of Geophysical Research*, 97(B9), 12349. <https://doi.org/10.1029/92JB00929>
- Conway, F. M., Connor, C. B., Hill, B. E., Condit, C. D., Mullaney, K., & Hall, C. M. (1998). Recurrence rates of basaltic volcanism in SP cluster, San Francisco volcanic field, Arizona. *Geology*, 26(7), 655. [https://doi.org/10.1130/0091-7613\(1998\)026<0655:RROBVI>2.3.CO;2](https://doi.org/10.1130/0091-7613(1998)026<0655:RROBVI>2.3.CO;2)
- Conway, F. Michael, Ferrill, D. A., Hall, C. M., Morris, A. P., Stamatakos, J. A., Connor, C. B., ... Condit, C. (1997). Timing of basaltic volcanism along the Mesa Butte Fault in the San Francisco Volcanic Field, Arizona, from  $^{40}\text{Ar}/^{39}\text{Ar}$  dates: Implications for longevity of cinder cone alignments.

- Journal of Geophysical Research: Solid Earth*, 102(B1), 815–824.  
<https://doi.org/10.1029/96JB02853>
- Cooper, M. R., Kovach, R. L., & Watkins, J. S. (1974). Lunar near-surface structure. *Reviews of Geophysics*, 12(3), 291. <https://doi.org/10.1029/RG012i003p00291>
- Cournède, C., Gattacceca, J., & Rochette, P. (2012). Magnetic study of large Apollo samples: Possible evidence for an ancient centered dipolar field on the Moon. *Earth and Planetary Science Letters*, 331–332, 31–42.  
<https://doi.org/10.1016/j.epsl.2012.03.004>
- Crow, R., Karlstrom, K., Asmerom, Y., Schmandt, B., Polyak, V., & DuFrane, S. A. (2011). Shrinking of the Colorado Plateau via lithospheric mantle erosion: Evidence from Nd and Sr isotopes and geochronology of Neogene basalts. *Geology*, 39(1), 27–30. <https://doi.org/10.1130/G31611.1>
- Crown, D. A., Berman, D. C., Scheidt, S. P., & Hauber, E. (2019). GEOLOGY OF ALBA MONS, MARS: RESULTS FROM 1:1M-SCALE GEOLOGIC MAPPING. David A. *Lunar and Planetary Science Conference*, 2.
- Cushing, G. E., Titus, T. N., Wynne, J. J., & Christensen, P. R. (2007). THEMIS observes possible cave skylights on Mars. *Geophysical Research Letters*, 34(17). <https://doi.org/10.1029/2007GL030709>
- Dainty, A. M., & Toksöz, M. N. (1981). Seismic codas on the Earth and the Moon: A comparison. *Physics of the Earth and Planetary Interiors*, 26(4), 250–260.  
[https://doi.org/10.1016/0031-9201\(81\)90029-7](https://doi.org/10.1016/0031-9201(81)90029-7)
- DARTS Seismology at ISAS/JAXA. (2019). Retrieved January 15, 2019, from <https://www.darts.isas.jaxa.jp/planet/seismology/apollo/ASE.html>

- de Silva, S., & Lindsay, J. M. (2015). Chapter 15—Primary Volcanic Landforms. In H. Sigurdsson (Ed.), *The Encyclopedia of Volcanoes (Second Edition)* (pp. 273–297). Amsterdam: Academic Press. <https://doi.org/10.1016/B978-0-12-385938-9.00015-8>
- DeDecker, J. (2014). *EVALUATION OF LAVA TUBE FORMATION MECHANISMS USING THREEDIMENSIONAL MAPPING AND VISCOSITY MODELING: LAVA BEDS NATIONAL MONUMENT, CALIFORNIA* (Master of Science). University of North Carolina, Chapel Hill, NC.
- Dickinson, W. R. (2002). The Basin and Range Province as a Composite Extensional Domain. *International Geology Review*, *44*(1), 1–38. <https://doi.org/10.2747/0020-6814.44.1.1>
- Doell, R. R., Grommé, C. S., Thorpe, A. N., & Senftle, F. E. (1970). Magnetic Studies of Lunar Samples. *Science*, *167*(3918), 695–697.
- Dolginov Sh., Eroshenko E. G., Zhuzgov L. N., & Pushkov N. V. (1966). Measurements of the Magnetic Field in the Vicinity of the Moon by the Artificial Satellite Luna10. *Kodlady, Akad Nauk USSR*, *170*, 574–577.
- Dolginov, Sh. Sh., Yeroshenko, E. G., Zhuzgov, L. N., & Pushkov, N. V. (1963). INVESTIGATION OF THE MAGNETIC FIELD OF THE MOON. *AIAA Journal*, *1*(2), 514–516. <https://doi.org/10.2514/3.1589>
- Dragoni, M., Piombo, A., & Tallarico, A. (1995). A model for the formation of lava tubes by roofing over a channel. *Journal of Geophysical Research: Solid Earth*, *100*(B5), 8435–8447. <https://doi.org/10.1029/94JB03263>
- Duda, R. O., Hart, P. E., & Stork, D. G. (1973). *Pattern Classification and Scene Analysis: Part I Pattern Classification*. John Wiley & Sons, Inc.

- Durrani, B. A., Doser, D. I., Keller, G. R., & Hearn, T. M. (1999). Velocity Structure of the Upper Crust under the San Francisco Volcanic Field, Arizona. *Bulletin of the Seismological Society of America*, 89(1), 239–249.
- Dyal, P., & Gordon, D. (1973). Lunar surface magnetometers. *IEEE Transactions on Magnetism*, 9(3), 226–231. <https://doi.org/10.1109/TMAG.1973.1067650>
- Eppler, D., & Bleacher, J. (2013). NASA's 2010 Desert Research and Technology Studies Mission Objectives and Results. *Acta Astronautica*, 90(2). [https://doi.org/10.1016/S0094-5765\(13\)00222-1](https://doi.org/10.1016/S0094-5765(13)00222-1)
- Esmacili, S., Kruse, S., Jazayeri, S., Whelley, P., Bell, E., Richardson, J., ... Young, K. (2020). Resolution of Lava Tubes with Ground Penetrating Radar: The TubeX project. *Journal of Geophysical Research: Planets*, n/a(n/a), e2019JE006138. <https://doi.org/10.1029/2019JE006138>
- Farrell, J., Wu, S., Ward, K. M., & Lin, F. (2018). Persistent Noise Signal in the FairfieldNodal Three-Component 5-Hz Geophones. *Seismological Research Letters*, 89(5), 1609–1617. <https://doi.org/10.1785/0220180073>
- Ferreira, F. J. F., de Souza, J., de B. e S. Bongioiolo, A., & de Castro, L. G. (2013). Enhancement of the total horizontal gradient of magnetic anomalies using the tilt angle. *GEOPHYSICS*, 78(3), J33–J41. <https://doi.org/10.1190/geo2011-0441.1>
- Flowers, R. M. (2010). The enigmatic rise of the Colorado Plateau. *Geology*, 38(7), 671–672. <https://doi.org/10.1130/focus072010.1>
- Frankel, C. (1996). *Volcanoes of the Solar System*. Cambridge University Press.
- Gangi, A. F. (1972). The lunar seismogram. *The Moon*, 4(1–2), 40–48. <https://doi.org/10.1007/BF00562913>

- Garrick-Bethell, I., & Weiss, B. P. (2010). Kamacite blocking temperatures and applications to lunar magnetism. *Earth and Planetary Science Letters*, 294(1–2), 1–7. <https://doi.org/10.1016/j.epsl.2010.02.013>
- Garry, W. B., Whelley, P., Shiro, B., Rowland, S., & Bleacher, J. (2017). *ANALYSIS OF A LAVA TUBE WITH LIDAR ON MAUNA LOA VOLCANO, HAWAI'I*. 25–3. Retrieved from <https://gsa.confex.com/gsa/2017CD/webprogram/Paper292954.html>
- Garry, W. Brent, & Bleacher, J. E. (2011). *Analogs for Planetary Exploration*. Geological Society of America.
- Gay, S. P. (1965). STANDARD CURVES FOR MAGNETIC ANOMALIES OVER LONG HORIZONTAL CYLINDERS. *GEOPHYSICS*, 30(5), 818–828. <https://doi.org/10.1190/1.1439656>
- GEM Systems, Inc. (2008). *GEM GSM-19 v7.0 Instruction Manual*. Retrieved from [https://userpage.fu-berlin.de/geodyn/instruments/Manual\\_GEM\\_GSM-19.pdf](https://userpage.fu-berlin.de/geodyn/instruments/Manual_GEM_GSM-19.pdf)
- Geometrics. (2012). *Operations and Reference Manual for Geometrics Seismograph Models: SmartSeis ST GEODE, Stratavisor NZ ES-3000*.
- George, O., McIlrath, J., Farrell, A., Gallant, E., Tavarez, S., Marshall, A., ... Kruse, S. (2014). High-Resolution Ground-Based Magnetic Survey of a Buried Volcano: Anomaly B, Amargosa Desert, NV. *Statistics in Volcanology*, 1, 1–23. <https://doi.org/10.5038/2163-338X.1.3>
- Greeley, R. (1971a). Lava tubes and channels in the lunar Marius Hills. *The Moon*, 3(3), 289–314. <https://doi.org/10.1007/BF00561842>
- Greeley, R. (1971b). *Observations of actively forming lava tubes Hawaii*. National Aeronautics and Space Administration, TM X-62,014.

- Greeley, R. (1971c, March). *Observations of Actively Forming Lava Tubes and Associated Structures, Hawaii*. NASA Technical Memorandum X-62014.  
Retrieved from  
<https://ntrs.nasa.gov/archive/nasa/casi.ntrs.nasa.gov/19710009490.pdf>
- Greeley, R. (1972). Additional observations of actively forming lava tubes and associated structures, Hawaii. *Modern Geology*, 3, 157–160.
- Greeley, R. (1987). The role of lava tubes in Hawaiian volcanoes. *US Geologic Survey Professional Paper 1350(2)*, 1589–1602.
- Green, P. J. (1995). Reversible jump Markov chain Monte Carlo computation and Bayesian model determination. *Biometrika*, 82(4), 711–732.
- Gruener, J. E., Lofgren, G. E., Bluethmann, W. J., & Abercromby, A. F. (2013). NASA Desert RATS 2010: Preliminary results for science operations conducted in the San Francisco Volcanic Field, Arizona. *Acta Astronautica*, 90(2), 406–415. <https://doi.org/10.1016/j.actaastro.2011.12.006>
- Haase, I., Gläser, P., Knapmeyer, M., Oberst, J., & Robinson, M. S. (2013). *Improved Coordinates of the Apollo 17 Lunar Seismic Profiling Experiment (LSPE) Components*. Presented at the Lunar and Planetary Science Conference (LPSC), The Woodlands, Texas, USA. Retrieved from  
<https://elib.dlr.de/86084/>
- Haase, Isabel, Wählisch, M., Gläser, P., Oberst, J., & Robinson, M. S. (2019). Coordinates and Maps of the Apollo 17 Landing Site. *Earth and Space Science*. <https://doi.org/10.1029/2018EA000408>

- Halliday, W. (1998). "Pit Craters", lava tubes, and open vertical volcanic conduits in Hawaii: A problem in terminology. *International Journal of Speleology*, 27(1), 113–124. <https://doi.org/10.5038/1827-806X.27.1.12>
- Haruyama, J, Kaku, T., Shinoda, R., Miyake, W., Kumamoto, A., Ishiyama, K., ... Howell, K. C. (2017). *DETECTION OF LUNAR LAVA TUBES BY LUNAR RADAR SOUNDER ONBOARD SELENE. 2.*
- Haruyama, Junichi, Hioki, K., Shirao, M., Morota, T., Hiesinger, H., van der Bogert, C. H., ... Pieters, C. M. (2009). Possible lunar lava tube skylight observed by SELENE cameras. *Geophysical Research Letters*, 36(21). <https://doi.org/10.1029/2009GL040635>
- Head, J. W. (1976). Lunar volcanism in space and time. *Reviews of Geophysics*, 14(2), 265–300. <https://doi.org/10.1029/RG014i002p00265>
- Head, J. W., & Wilson, L. (2017). Generation, ascent and eruption of magma on the Moon: New insights into source depths, magma supply, intrusions and effusive/explosive eruptions (Part 2: Predicted emplacement processes and observations). *Icarus*, 283, 176–223. <https://doi.org/10.1016/j.icarus.2016.05.031>
- Heffels, A., Knapmeyer, M., Oberst, J., & Haase, I. (2017). Re-evaluation of Apollo 17 Lunar Seismic Profiling Experiment data. *Planetary and Space Science*, 135, 43–54. <https://doi.org/10.1016/j.pss.2016.11.007>
- Heldmann, J. L., Colaprete, A., Elphic, R. C., Mattes, G., Ennico, K., Fritzler, E., ... Stoker, C. R. (2015). Real-time science operations to support a lunar polar volatiles rover mission. *Advances in Space Research*, 55(10), 2427–2437. <https://doi.org/10.1016/j.asr.2014.07.037>

- Hemingway, D. J., & Tikoo, S. M. (2018). Lunar Swirl Morphology Constrains the Geometry, Magnetization, and Origins of Lunar Magnetic Anomalies. *Journal of Geophysical Research: Planets*, 123(8), 2223–2241.  
<https://doi.org/10.1029/2018JE005604>
- Hendricks, J. D., & Plescia, J. B. (1991). A review of the regional geophysics of the Arizona Transition Zone. *Journal of Geophysical Research: Solid Earth*, 96(B7), 12351–12373. <https://doi.org/10.1029/90JB01781>
- Hinze, W. J., & Hood, P. J. (1998). MAGNETIC ANOMALY MAP OF NORTH AMERICA. *Geophysics: The Leading Edge of Exploration*, 19–21.
- Hole, J. A., Ryberg, T., Fuis, G. S., Bleibinhaus, F., & Sharma, A. K. (2006). Structure of the San Andreas fault zone at SAFOD from a seismic refraction survey. *Geophysical Research Letters*, 33(7).  
<https://doi.org/10.1029/2005GL025194>
- Hon, K., Kauahikaua, J., Denlinger, R., & Mackay, K. (1994). Emplacement and inflation of pahoehoe sheet flows: Observations and measurements of active lava flows on Kilauea Volcano, Hawaii. *Geological Society of America Bulletin*, 106(3), 351–370. [https://doi.org/10.1130/0016-7606\(1994\)106<0351:EAIOPS>2.3.CO;2](https://doi.org/10.1130/0016-7606(1994)106<0351:EAIOPS>2.3.CO;2)
- Hong, I.-S., Yi, Y., & Kim, E. (2014). Lunar Pit Craters Presumed to be the Entrances of Lava Caves by Analogy to the Earth Lava Tube Pits. *Journal of Astronomy and Space Sciences*, 31(2), 131–140.  
<https://doi.org/10.5140/JASS.2014.31.2.131>
- Hood, L. L., Zakharian, A., Halekas, J., Mitchell, D. L., Lin, R. P., Acuña, M. H., & Binder, A. B. (2001). Initial mapping and interpretation of lunar crustal

magnetic anomalies using Lunar Prospector magnetometer data. *Journal of Geophysical Research: Planets*, 106(E11), 27825–27839.

<https://doi.org/10.1029/2000JE001366>

Horz, F. (1985). Lava Tubes: Potential Shelters for Habitats. In *Lunar Bases and Space Activities of the 21st Century* (1st ed., pp. 405–412). Lunar and Planetary Institute. Retrieved from

[https://www.lpi.usra.edu/publications/books/lunar\\_bases/FrontMatter.pdf](https://www.lpi.usra.edu/publications/books/lunar_bases/FrontMatter.pdf)

Hörz, F., Lofgren, G. E., Gruener, J. E., Eppler, D. B., Skinner, J. A., Fortezzo, C. M., ... Bell, E. R. (2013). The traverse planning process for D-RATS 2010. *Acta Astronautica*, 90(2), 254–267. <https://doi.org/10.1016/j.actaastro.2012.02.008>

Huang, M.-H., Hudson-Rasmussen, B., Burdick, S., Nelson, M., Lekic, V., Fauria, K., & Schmerr, N. (2020). Bayesian seismic refraction inversion for critical zone science and near-surface applications. *Geochemistry, Geophysics, Geosystems*.

Humphreys, E. D. (1995). *Post-Laramide removal of the Farallon slab, western United States*. 4.

Humphreys, E., Hessler, E., Dueker, K., Farmer, G., Erslev, E., & Atwater, T. (2003). How Laramide-age hydration of North American lithosphere by the Farallon slab controlled subsequent activity in the western United States. *International Geology Review*, 7(45), 575–595.

Hurwitz, D. M., Head, J. W., & Hiesinger, H. (2013). Lunar sinuous rilles: Distribution, characteristics, and implications for their origin. *Planetary and Space Science*, 79–80, 1–38. <https://doi.org/10.1016/j.pss.2012.10.019>

- Jawin, E. R., Valencia, S. N., Watkins, R. N., Crowell, J. M., Neal, C. R., & Schmidt, G. (2019). Lunar Science for Landed Missions Workshop Findings Report. *Earth and Space Science*, 6(1), 2–40. <https://doi.org/10.1029/2018EA000490>
- Jones, C. H., Mahan, K. H., Butcher, L. A., Levandowski, W. B., & Farmer, G. L. (2015). Continental uplift through crustal hydration. *Geology*, 43(4), 355–358. <https://doi.org/10.1130/G36509.1>
- Kaku, T., Haruyama, J., Miyake, W., Kumamoto, A., Ishiyama, K., Nishibori, T., ... Howell, K. C. (2017). Detection of Intact Lava Tubes at Marius Hills on the Moon by SELENE (Kaguya) Lunar Radar Sounder: Intact Lunar Lava Tube Detection by LRS. *Geophysical Research Letters*, 44(20), 10,155-10,161. <https://doi.org/10.1002/2017GL074998>
- Keating, G. N., Valentine, G. A., Krier, D. J., & Perry, F. V. (2008). Shallow plumbing systems for small-volume basaltic volcanoes. *Bulletin of Volcanology*, 70(5), 563–582. <https://doi.org/10.1007/s00445-007-0154-1>
- Keszthelyi, L., & Self, S. (1998). Some physical requirements for the emplacement of long basaltic lava flows. *Journal of Geophysical Research: Solid Earth*, 103(B11), 27447–27464. <https://doi.org/10.1029/98JB00606>
- Keszthelyi, Laszlo. (1995). A preliminary thermal budget for lava tubes on the Earth and planets. *Journal of Geophysical Research: Solid Earth*, 100(B10), 20411–20420. <https://doi.org/10.1029/95JB01965>
- Kiefer, W. S., Macke, R. J., Britt, D. T., Irving, A. J., & Consolmagno, G. J. (2012). The density and porosity of lunar rocks. *Geophysical Research Letters*, 39(7). <https://doi.org/10.1029/2012GL051319>

- Kirsten, T., & Horn, P. (1974). Chronology of the Taurus-Littrow region III: Ages of mare basalts and highland breccias and some remarks about the interpretation of lunar highland rock ages. *Proceedings of the Fifth Lunar Conference, Supplement 5, Geochimica et Cosmochimica Acta*, 2, 1451–1475. Retrieved from [http://articles.adsabs.harvard.edu/cgi-bin/nph-iarticle\\_query?1974LPSC....5.1451K&defaultprint=YES&filetype=.pdf](http://articles.adsabs.harvard.edu/cgi-bin/nph-iarticle_query?1974LPSC....5.1451K&defaultprint=YES&filetype=.pdf)
- Klitgord, K. D., Huestis, S. P., Mudie, J. D., & Parker, R. L. (1975). An Analysis of Near-Bottom Magnetic Anomalies: Sea-Floor Spreading and the Magnetized Layer. *Geophysical Journal International*, 43(2), 387–424. <https://doi.org/10.1111/j.1365-246X.1975.tb00641.x>
- Kovach, Robert & Watkins, Joel. (1973a). Chapter 10. Lunar Seismic Profiling Experiment. In *Apollo 17: Preliminary Science Report*.
- Kovach, Robert & Watkins, Joel. (1973b). The structure of the lunar crust at the Apollo 17 site. *Proceedings of the Fourth Lunar Science Conference*, 3, 2549–2560. [https://doi.org/10.1016/0006-2952\(75\)90018-0](https://doi.org/10.1016/0006-2952(75)90018-0)
- Kring, D. A. (2017). *Guidebook to the Geology of Barringer Meteorite Crater, Arizona (a k a Meteor Crater). Second edition (2nd ed.)*. Lunar and Planetary Institute.
- Larson, C., & Larson, J. (1990). *Lava Beds Caves*. ABC Publishing.
- Latham, G., Ewing, M., Dorman, J., Nakamura, Y., Press, F., Toksöz, N., ... Lammlin, D. (1973). Lunar structure and dynamics—Results from the apollo passive seismic experiment. *The Moon*, 7(3–4), 396–421. <https://doi.org/10.1007/BF00564643>

- Le Corvec, N., Spörli, K. B., Rowland, J., & Lindsay, J. (2013). Spatial distribution and alignments of volcanic centers: Clues to the formation of monogenetic volcanic fields. *Earth-Science Reviews*, *124*, 96–114.  
<https://doi.org/10.1016/j.earscirev.2013.05.005>
- Levander, A., Schmandt, B., Miller, M. S., Liu, K., Karlstrom, K. E., Crow, R. S., ... Humphreys, E. D. (2011). Continuing Colorado plateau uplift by delamination-style convective lithospheric downwelling. *Nature*, *472*(7344), 461–465. <https://doi.org/10.1038/nature10001>
- Léveillé, R. (2010). A half-century of terrestrial analog studies: From craters on the Moon to searching for life on Mars. *Planetary and Space Science*, *58*(4), 631–638. <https://doi.org/10.1016/j.pss.2009.04.001>
- Liu, K., Levander, A., Niu, F., & Miller, M. S. (2011). Imaging crustal and upper mantle structure beneath the Colorado Plateau using finite frequency Rayleigh wave tomography. *Geochemistry, Geophysics, Geosystems*, *12*(7).  
<https://doi.org/10.1029/2011GC003611>
- Liu, L., & Gurnis, M. (2010). Dynamic subsidence and uplift of the Colorado Plateau. *Geology*, *38*(7), 663–666. <https://doi.org/10.1130/G30624.1>
- Lofgren, G., Horz, F., & Eppler, D. (2011). Geologic field training of the Apollo astronauts and implications for future manned exploration. *Geological Society of America Special Papers*, *483*, 33–48.
- Mallozzi, A. (2019). *Magnetic and electromagnetic surveying of lava tubes at Lava Beds National Monument, California* (Master of Science, Carleton University). Carleton University, Ottawa, Ontario.  
<https://doi.org/10.22215/etd/2019-13878>

- McGetchin, T. R., & Head, J. W. (1973). Lunar Cinder Cones. *Science, New Series*, 180(4081), 68–71.
- McQuarrie, N., & Chase, C. G. (2000). *Raising the Colorado Plateau*. 4.
- McQuarrie, N., & Oskin, M. (2010). Palinspastic restoration of NAVDat and implications for the origin of magmatism in southwestern North America. *Journal of Geophysical Research: Solid Earth*, 115(B10).  
<https://doi.org/10.1029/2009JB006435>
- Meglich, T. M., Williams, M. C., Hodges, S. M., & DeMarco, M. J. (2003). *SUBSURFACE GEOPHYSICAL IMAGING OF LAVA TUBES, LAVA BEDS NATIONAL MONUMENT, CA*. 13.
- Metropolis, N., Rosenbluth, A. W., Rosenbluth, M. N., Teller, A. H., & Teller, E. (1953). Equation of State Calculations by Fast Computing Machines. *The Journal of Chemical Physics*, 21(6), 1087–1092.
- Mickus, K. L., & Durrani, B. (1996). Gravity and magnetic study of the crustal structure of the San Francisco volcanic field, Arizona, USA. *Tectonophysics*, 267(1–4), 73–90. [https://doi.org/10.1016/S0040-1951\(96\)00087-X](https://doi.org/10.1016/S0040-1951(96)00087-X)
- Minty, B. R. S., Milligan, P. R., Luyendyk, T., & Mackey, T. (2003). Merging airborne magnetic surveys into continental-scale compilations. *GEOPHYSICS*, 68(3), 988–995. <https://doi.org/10.1190/1.1581070>
- Miyamoto, H., Haruyama, J., Kobayashi, T., Suzuki, K., Okada, T., Nishibori, T., ... Masumoto, K. (2005). Mapping the structure and depth of lava tubes using ground penetrating radar. *Geophysical Research Letters*, 32(21).  
<https://doi.org/10.1029/2005GL024159>

- Montgomery, L. N., Schmerr, N., Burdick, S., Forster, R. R., Koenig, L., Legchenko, A., ... Solomon, D. K. (2017). Investigation of Firn Aquifer Structure in Southeastern Greenland Using Active Source Seismology. *Frontiers in Earth Science*, 5. <https://doi.org/10.3389/feart.2017.00010>
- Morgan, P., & Swanberg, C. A. (1985). On the Cenozoic uplift and tectonic stability of the Colorado Plateau. *Journal of Geodynamics*, 3(1–2), 39–63. [https://doi.org/10.1016/0264-3707\(85\)90021-3](https://doi.org/10.1016/0264-3707(85)90021-3)
- Moucha, R., Forte, A. M., Rowley, D. B., Mitrovica, J. X., Simmons, N. A., & Grand, S. P. (2008). Mantle convection and the recent evolution of the Colorado Plateau and the Rio Grande Rift valley. *Geology*, 36(6), 439. <https://doi.org/10.1130/G24577A.1>
- Moucha, R., Forte, A. M., Rowley, D. B., Mitrovica, J. X., Simmons, N. A., & Grand, S. P. (2009). Deep mantle forces and the uplift of the Colorado Plateau. *Geophysical Research Letters*, 36(19). <https://doi.org/10.1029/2009GL039778>
- Nagata, T., Fisher, R. M., & Schwerer, F. C. (1974). Some characteristic magnetic properties of lunar materials. *The Moon*, 9(1–2), 63–77. <https://doi.org/10.1007/BF00565393>
- Nakamura, Y., Dorman, J., Duennebier, F., Lammlein, D., & Latham, G. (1975). Shallow lunar structure determined from the passive seismic experiment. *The Moon*, 13(1–3), 57–66. <https://doi.org/10.1007/BF00567507>
- Nakamura, Y., Latham, G. V., & Dorman, H. J. (1982). Apollo Lunar Seismic Experiment—Final summary. *Journal of Geophysical Research*, 87(S01), A117. <https://doi.org/10.1029/JB087iS01p0A117>

- National Aeronautics and Space Administration. (1969a). *Apollo 11 Mission Operations Report* (No. M-932-69-11). Retrieved from [https://www.hq.nasa.gov/alsj/a11/A11\\_MissionOpReport.pdf](https://www.hq.nasa.gov/alsj/a11/A11_MissionOpReport.pdf)
- National Aeronautics and Space Administration. (1969b). *Apollo 11 Mission Report* (No. MSC-05161). Retrieved from [https://www.hq.nasa.gov/alsj/a11/A11\\_MissionReport.pdf](https://www.hq.nasa.gov/alsj/a11/A11_MissionReport.pdf)
- National Aeronautics and Space Administration. (1970). *Apollo 12 Mission Report* (No. MSC-01855). Retrieved from [https://www.hq.nasa.gov/alsj/a12/A12\\_MissionReport.pdf](https://www.hq.nasa.gov/alsj/a12/A12_MissionReport.pdf)
- National Aeronautics and Space Administration. (1971a). *Apollo 14 Mission Report* (No. MSC-04112). Retrieved from <https://www.hq.nasa.gov/alsj/a14/A14MRntrs.pdf>
- National Aeronautics and Space Administration. (1971b). *Apollo 14 Preliminary Science Report* (No. SP-272). Retrieved from <https://www.hq.nasa.gov/alsj/a14/as14psr.pdf>
- National Aeronautics and Space Administration. (1971c). *Apollo 15 Mission Report* (No. MSC-05161). Retrieved from <https://www.hq.nasa.gov/alsj/a15/ap15mr.pdf>
- National Aeronautics and Space Administration. (1972a). *Apollo 15 Preliminary Science Report*. Retrieved from <https://www.hq.nasa.gov/alsj/a15/as15psr.pdf>
- National Aeronautics and Space Administration. (1972b). *Apollo 16 Mission Report* (No. MSC-07230). Retrieved from [https://www.hq.nasa.gov/alsj/a16/A16\\_MissionReport.pdf](https://www.hq.nasa.gov/alsj/a16/A16_MissionReport.pdf)

- National Aeronautics and Space Administration. (1972c). *Apollo 16 Preliminary Science Report* (No. SP-315). Retrieved from <https://www.hq.nasa.gov/alsj/a16/as16psr.pdf>
- National Aeronautics and Space Administration. (1973a). *Apollo 17 Mission Report* (No. JSC\_07904).
- National Aeronautics and Space Administration. (1973b). *Apollo 17 Preliminary Science Report* (No. SP-330). Retrieved from <https://www.hq.nasa.gov/alsj/a17/as17psr.pdf>
- National Aeronautics and Space Administration. (1973c). *Apollo 17 Preliminary Science Report* (No. NASA SP330).
- National Geophysical Data Center. (2020). National Centers for Environmental Information Geomagnetic Calculators. Retrieved May 26, 2020, from U.S. Department of Commerce website: <https://www.ngdc.noaa.gov/geomag/calculators/magcalc.shtml#igrfwmm>
- National Park Service. (2017). *Lava Beds*. Retrieved from <https://www.nps.gov/labe/planyourvisit/upload/GEOLOGY.pdf>
- Negro, C. D., & Ferrucci, F. (1998). Magnetic history of a dyke on Mount Etna (Sicily). *Geophysical Journal International*, 133(2), 451–458. <https://doi.org/10.1046/j.1365-246X.1998.00517.x>
- Nelson, S., Davidson, J., & Sullivan, K. (1992). New age determinations of central Colorado Plateau laccoliths, Utah: Recognizing disturbed K-Ar systematics and re-evaluating tectonomagmatic relationships. *Geological Society of America Bulletin*, 104(12), 1547–1560.

- Parsons, T., & McCarthy, J. (1995). The active southwest margin of the Colorado Plateau: Uplift of mantle origin. *Geological Society of America Bulletin*, 107(2), 139. [https://doi.org/10.1130/0016-7606\(1995\)107<0139:TASMOT>2.3.CO;2](https://doi.org/10.1130/0016-7606(1995)107<0139:TASMOT>2.3.CO;2)
- Pederson, J. L., & Mackley, R. D. (2002). Colorado Plateau uplift and erosion evaluated using GIS. *GSA TODAY*, 7.
- Peterson, D., Holcomb, R., Tilling, R., & Christiansen, R. (1994). *Development of lava tubes in the light of observations at Mauna Ulu, Kilauea Volcano, Hawaii*. 56, 343–360.
- Peterson, D. W., & Swanson, D. A. (1974a). Observed formation of lava tubes. *Studies in Speleology*, 2(6), 209–222.
- Peterson, D. W., & Swanson, D. A. (1974b). *Peterson and Swanson 1974—Observed formation of lava tubes.pdf*.
- Peterson, J. (1993). *Observations and Modeling of Seismic Background Noise* (No. 93–322). U.S. Department of the Interior, U.S. Geological Survey. Retrieved from U.S. Department of the Interior, U.S. Geological Survey website: <https://pubs.usgs.gov/of/1993/0322/ofr93-322.pdf>
- Phinney, W. (2015). *Science Training History of the Apollo Astronauts* (No. NASA/SP-2015-626). Retrieved from <https://ntrs.nasa.gov/api/citations/20190026783/downloads/20190026783.pdf>
- Pieri, D. C., & Baloga, S. M. (1986). Eruption rate, area, and length relationships for some Hawaiian lava flows. *Journal of Volcanology and Geothermal Research*, 30(1–2), 29–45. [https://doi.org/10.1016/0377-0273\(86\)90066-1](https://doi.org/10.1016/0377-0273(86)90066-1)

- Piombo, A., Di Bari, M., Tallarico, A., & Dragoni, M. (2016). Thermal anomaly at the Earth's surface associated with a lava tube. *Journal of Volcanology and Geothermal Research*, 325, 148–155.  
<https://doi.org/10.1016/j.jvolgeores.2016.06.019>
- Porter, R., Hoisch, T., & Holt, W. E. (2017). The role of lower-crustal hydration in the tectonic evolution of the Colorado Plateau. *Tectonophysics*, 712–713, 221–231. <https://doi.org/10.1016/j.tecto.2017.05.025>
- Reynolds, P., Brown, R. J., Thordarson, T., & Llewellyn, E. W. (2016). The architecture and shallow conduits of Laki-type pyroclastic cones: Insights into a basaltic fissure eruption. *Bulletin of Volcanology*, 78(5), 36.  
<https://doi.org/10.1007/s00445-016-1029-0>
- Ringler, A. T., Anthony, R. E., Karplus, M. S., Holland, A. A., & Wilson, D. C. (2018). Laboratory Tests of Three Z-Land Fairfield Nodal 5-Hz, Three-Component Sensors. *Seismological Research Letters*, 89(5), 1601–1608.  
<https://doi.org/10.1785/0220170236>
- Roberts, C. E., & Gregg, T. K. P. (2019). Rima Marius, the Moon: Formation of lunar sinuous rilles by constructional and erosional processes. *Icarus*, 317, 682–688.  
<https://doi.org/10.1016/j.icarus.2018.02.033>
- Robinson, M. S., Ashley, J. W., Boyd, A. K., Wagner, R. V., Speyerer, E. J., Ray Hawke, B., ... van der Bogert, C. H. (2012). Confirmation of sublunarean voids and thin layering in mare deposits. *Planetary and Space Science*, 69(1), 18–27. <https://doi.org/10.1016/j.pss.2012.05.008>

- Ross, A., Kosmo, J., & Janoiko, B. (2013). Historical synopses of desert RATS 1997–2010 and a preview of desert RATS 2011. *Acta Astronautica*, *90*(2), 182–202. <https://doi.org/10.1016/j.actaastro.2012.02.003>
- Rowland, S. K., & Walker, G. P. (1990). Pahoehoe and aa in Hawaii: Volumetric flow rate controls the lava structure. *Bulletin of Volcanology*, *52*(8), 615–628. <https://doi.org/10.1007/BF00301212>
- Roy, M., Jordan, T. H., & Pederson, J. (2009). Colorado Plateau magmatism and uplift by warming of heterogeneous lithosphere. *Nature*, *459*(7249), 978–982. <https://doi.org/10.1038/nature08052>
- R.T. Clark Geophysical Equipment Co. (2014). *PEG-40kg Brochure*. Retrieved from <https://rtclark.com/wp-content/uploads/2015/05/PEG-40kg-Brochure-2014.pdf>
- Runcorn, S. K., Collinson, D. W., O'Reilly, W., Stephenson, A., Greenwood, N. N., & Battey, M. H. (1970). Magnetic Properties of Lunar Samples. *Science*, *167*(3918), 697–699.
- Sakimoto, S. E. H., Crisp, J., & Baloga, S. M. (1997). Eruption constraints on tube-fed planetary lava flows. *Journal of Geophysical Research: Planets*, *102*(E3), 6597–6613. <https://doi.org/10.1029/97JE00069>
- Sauro, F., Pozzobon, R., Massironi, M., De Berardinis, P., Santagata, T., & De Waele, J. (2020). Lava tubes on Earth, Moon and Mars: A review on their size and morphology revealed by comparative planetology. *Earth-Science Reviews*, *209*, 103288. <https://doi.org/10.1016/j.earscirev.2020.103288>
- Schmitt, Harrison H. (1973). Apollo 17 Report on the Valley of Taurus-Littrow. *Science*, *182*(4113), 681–690. JSTOR. Retrieved from JSTOR.

- Schmitt, H.H., Petro, N. E., Wells, R. A., Robinson, M. S., Weiss, B. P., & Mercer, C. M. (2017). Revisiting the field geology of Taurus–Littrow. *Icarus*, 298, 2–33. <https://doi.org/10.1016/j.icarus.2016.11.042>
- Self, S., Thordarson, Th., Keszthelyi, L., Walker, G. P. L., Hon, K., Murphy, M. T., ... Finnemore, S. (1996). A new model for the emplacement of Columbia River basalts as large, inflated Pahoehoe Lava Flow Fields. *Geophysical Research Letters*, 23(19), 2689–2692. <https://doi.org/10.1029/96GL02450>
- Sethian, J. A. (1996). A fast marching level set method for monotonically advancing fronts. *Proceedings of the National Academy of Sciences*, 93(4), 1591–1595. <https://doi.org/10.1073/pnas.93.4.1591>
- Settle, M. (1979). The structure and emplacement of cinder cone fields. *American Journal of Science*, 279(10), 1089–1107. <https://doi.org/10.2475/ajs.279.10.1089>
- Sigurdsson, H., Houghton, B., McNutt, S., Rymer, H., & Stix, J. (2015). *The Encyclopedia of Volcanoes*. Elsevier.
- Sine, C. R., Wilson, D., Gao, W., Grand, S. P., Aster, R., Ni, J., & Baldrige, W. S. (2008). Mantle structure beneath the western edge of the Colorado Plateau. *Geophysical Research Letters*, 35(10). <https://doi.org/10.1029/2008GL033391>
- Skinner, J. A., & Fortezzo, C. (2013). The role of photogeologic mapping in traverse planning: Lessons from DRATS 2010 activities. *Acta Astronautica*, 12.
- Sobel, I. (2014). *History and definition of the sobel operator*. Retrieved from [https://www.researchgate.net/publication/239398674\\_An\\_Isotropic\\_3x3\\_Image\\_Gradient\\_Operator](https://www.researchgate.net/publication/239398674_An_Isotropic_3x3_Image_Gradient_Operator)

- Spencer, J. E. (1996). Uplift of the Colorado Plateau due to lithosphere attenuation during Laramide low-angle subduction. *Journal of Geophysical Research: Solid Earth*, 101(B6), 13595–13609. <https://doi.org/10.1029/96JB00818>
- Spudis, P. D., Wilhelms, D. E., & Robinson, M. S. (2011). The Sculptured Hills of the Taurus Highlands: Implications for the relative age of Serenitatis, basin chronologies and the cratering history of the Moon. *Journal of Geophysical Research: Planets*, 116(E12). <https://doi.org/10.1029/2011JE003903>
- Srnka, L. J., Hoyt, J. L., Harvey, J. V. S., & McCoy, J. E. (1979). A study of the Rima Sirsalis lunar magnetic anomaly. *Physics of the Earth and Planetary Interiors*, 20(2–4), 281–290. [https://doi.org/10.1016/0031-9201\(79\)90051-7](https://doi.org/10.1016/0031-9201(79)90051-7)
- Stauber, D. A. (1982). Two-dimensional compressional wave velocity structure under San Francisco Volcanic Field, Arizona, from teleseismic *P* residual measurements. *Journal of Geophysical Research: Solid Earth*, 87(B7), 5451–5459. <https://doi.org/10.1029/JB087iB07p05451>
- Tanaka, K. L., Shoemaker, E. M., Ulrich, G. E., & Wolfe, E. W. (1986). Migration of volcanism in the San Francisco volcanic field, Arizona. *Geological Society of America Bulletin*, 97(2), 129. [https://doi.org/10.1130/0016-7606\(1986\)97<129:MOVITS>2.0.CO;2](https://doi.org/10.1130/0016-7606(1986)97<129:MOVITS>2.0.CO;2)
- Thompson, G. A., & Zoback, M. L. (1979). Regional geophysics of the Colorado Plateau. *Tectonophysics*, 61(1–3), 149–181. [https://doi.org/10.1016/0040-1951\(79\)90296-8](https://doi.org/10.1016/0040-1951(79)90296-8)
- Tien-when, L., & Inderwiesen, P. (1994). *Fundamentals of seismic tomography*. Society of Exploration Geophysicists.

- Tikoo, S. M., Weiss, B. P., Shuster, D. L., Suavet, C., Wang, H., & Grove, T. L. (2017). A two-billion-year history for the lunar dynamo. *Science Advances*, 3(8), e1700207. <https://doi.org/10.1126/sciadv.1700207>
- Tittmann, B. R., Ahlberg, L., & Curnow, J. (1976). *Internal friction and velocity measurements*. 7, 3123–2132. Retrieved from <http://adsabs.harvard.edu/pdf/1976LPSC....7.3123T>
- Tsunakawa, H., Takahashi, F., Shimizu, H., Shibuya, H., & Matsushima, M. (2015). Surface vector mapping of magnetic anomalies over the Moon using Kaguya and Lunar Prospector observations. *Journal of Geophysical Research: Planets*, 120(6), 1160–1185. <https://doi.org/10.1002/2014JE004785>
- Ulrich, G., & Bailey, N. (1987). *Geologic Map of the SP Mountain Part of the San Francisco Volcanic Field, North-Central Arizona*. Department of the Interior, USGS.
- USGS. (2017). Geologic Provinces of the United States: Colorado Plateau Province. Retrieved July 17, 2017, from <http://geomaps.wr.usgs.gov/parks/province/coloplat.html>
- Valentine, G. A., & Gregg, T. K. P. (2008). Continental basaltic volcanoes—Processes and problems. *Journal of Volcanology and Geothermal Research*, 177(4), 857–873. <https://doi.org/10.1016/j.jvolgeores.2008.01.050>
- Valentine, G., & Krogh, K. (2006). Emplacement of shallow dikes and sills beneath a small basaltic volcanic center – The role of pre-existing structure (Paiute Ridge, southern Nevada, USA). *Earth and Planetary Science Letters*, 246(3–4), 217–230. <https://doi.org/10.1016/j.epsl.2006.04.031>

- Valentine, Greg A., & Connor, C. B. (2015). Chapter 23—Basaltic Volcanic Fields. In H. Sigurdsson (Ed.), *The Encyclopedia of Volcanoes (Second Edition)* (pp. 423–439). Amsterdam: Academic Press. <https://doi.org/10.1016/B978-0-12-385938-9.00023-7>
- Valerio, A., Tallarico, A., & Dragoni, M. (2008). Mechanisms of formation of lava tubes. *Journal of Geophysical Research: Solid Earth*, 113(B8). <https://doi.org/10.1029/2007JB005435>
- van Wijk, J. W., Baldrige, W. S., van Hunen, J., Goes, S., Aster, R., Coblenz, D. D., ... Ni, J. (2010). Small-scale convection at the edge of the Colorado Plateau: Implications for topography, magmatism, and evolution of Proterozoic lithosphere. *Geology*, 38(7), 611–614. <https://doi.org/10.1130/G31031.1>
- Wagner, R. V., & Robinson, M. S. (2014). Distribution, formation mechanisms, and significance of lunar pits. *Icarus*, 237, 52–60. <https://doi.org/10.1016/j.icarus.2014.04.002>
- Walker, G. P. L. (1973). Mount Etna and the 1971 eruption—Lengths of lava flows. *Philosophical Transactions of the Royal Society of London*, 107–118.
- Wang, F., Duan, Y., Yang, Z., Zhang, C., Zhao, J., Zhang, J., ... Liu, B. (2008). Velocity structure and active fault of Yanyuan-Mabian seismic zone—The result of high-resolution seismic refraction experiment. *Science in China Series D: Earth Sciences*, 51(9), 1284–1296. <https://doi.org/10.1007/s11430-008-0098-0>
- Waters, A., Donnelly-Nolan, J., & Rogers, B. (2010). Selected Caves and Lava-Tube Systems In and Near Lava Beds National Monument, California. *U.S. Geological Survey Bulletin 1673*.

- Watkins, J., De Bremaecker, J., Loney, R., Whitcomb, J., & Godson, R. (1965). *Investigation of In-Situ Physical Properties of Surface and Subsurface Site Materials by Engineering Geophysical Techniques*. U.S. Department of the Interior, U.S. Geological Survey. Retrieved from U.S. Department of the Interior, U.S. Geological Survey website:  
<https://ntrs.nasa.gov/api/citations/19660026676/downloads/19660026676.pdf>
- Watters, T. R., Robinson, M. S., Beyer, R. A., Banks, M. E., Bell, J. F., Pritchard, M. E., ... Williams, N. R. (2010). Evidence of Recent Thrust Faulting on the Moon Revealed by the Lunar Reconnaissance Orbiter Camera. *Science*, 329(5994), 936–940. <https://doi.org/10.1126/science.1189590>
- Weber, R. C., Lin, P.-Y., Garnero, E. J., Williams, Q., & Lognonne, P. (2011). Seismic Detection of the Lunar Core. *Science*, 331(6015), 309–312. <https://doi.org/10.1126/science.1199375>
- Weitz, C. M., & Head, J. W. (1999). Spectral properties of the Marius Hills volcanic complex and implications for the formation of lunar domes and cones. *Journal of Geophysical Research: Planets*, 104(E8), 18933–18956. <https://doi.org/10.1029/1998JE000630>
- Wendel, J. (2017). Lunar Lava Tubes Could Offer Future Moon Explorers a Safe Haven. *EOS*, 98. <https://doi.org/10.1029/2017EO070477>
- Whelley, P., Garry, W. B., Young, K., Kruse, S., Esmaili, S., Jazayeri, S., ... Richardson, J. (2018). *LIDAR SURVEYS OF LAVA TUBES IN LAVA BEDS NATIONAL MONUMENT*. Presented at the Geologic Society of America Annual Meeting, Indianapolis, Indiana. <https://doi.org/10.1130/abs/2018AM-322466>

- Williams, D. A., O'Brien, D. P., Schenk, P. M., Denevi, B. W., Carsenty, U., Marchi, S., ... Davison, T. M. (2014). Lobate and flow-like features on asteroid Vesta. *Planetary and Space Science*, *103*, 24–35.  
<https://doi.org/10.1016/j.pss.2013.06.017>
- Wilson, L. (2009). Volcanism in the Solar System. *Nature Geoscience*, *2*(6), 389–397. <https://doi.org/10.1038/ngeo529>
- Wilson, L., & Head, J. W. (1981). Ascent and eruption of basaltic magma on the Earth and Moon. *Journal of Geophysical Research: Solid Earth*, *86*(B4), 2971–3001. <https://doi.org/10.1029/JB086iB04p02971>
- Wilson, L., & Keil, K. (1996). Volcanic eruptions and intrusions on the asteroid 4 Vesta. *Journal of Geophysical Research: Planets*, *101*(E8), 18927–18940.  
<https://doi.org/10.1029/96JE01390>
- Wolfe, E., Lucchitta, B., Reed, V., Ulrich, G., & Sanchez, A. (1975). Geology of the Taurus-Littrow valley floor. *Lunar and Planetary Science Conference*, *6*, 2463–2482. Retrieved from  
<http://adsabs.harvard.edu/pdf/1975LPSC....6.2463W>
- Wolfe, E. W., Bailey, N. G., Lucchitta, B. K., Muehlberger, W. R., Scott, D. H., Sutton, R. L., & Wilshire, H. G. (1981). *The Geologic Investigation of the Taurus-Littrow Valley: Apollo 17 Landing Site*.
- Wood, C. A. (1980). Morphometric evolution of cinder cones. *Journal of Volcanology and Geothermal Research*, *7*(3–4), 387–413.  
[https://doi.org/10.1016/0377-0273\(80\)90040-2](https://doi.org/10.1016/0377-0273(80)90040-2)
- Xu, W., Van der Voo, R., Peacor, D. R., & Beaubouef, R. T. (1997). Alteration and dissolution of fine-grained magnetite and its effects on magnetization of the

ocean floor. *Earth and Planetary Science Letters*, 151(3–4), 279–288.

[https://doi.org/10.1016/S0012-821X\(97\)81854-7](https://doi.org/10.1016/S0012-821X(97)81854-7)

Zhao, J., Huang, J., Kraft, M. D., Xiao, L., & Jiang, Y. (2017). Ridge-like lava tube systems in southeast Tharsis, Mars. *Geomorphology*, 295, 831–839.

<https://doi.org/10.1016/j.geomorph.2017.08.023>

*ZSystems Zland 1C and 3C Node User Manual*. (2014). Fairfield Nodal.